12-13-2013

Engineering Analysis of Minimally Invasive Mitral Valve Repair

Thuy Pham
pham.m.thuy@gmail.com

Engineering Analysis of Minimally Invasive Mitral Valve Repair

Thuy Pham, PhD

University of Connecticut, 2013

Surgical treatment for severe functional MR often involves mitral annuloplasty to improve leaflet apposition and ultimately downsize the dilated mitral valve. However, the high rate of operative mortalities of up to 6 ~12% have limited the more expanded use of this procedure. Recently, minimally invasive percutaneous transvenous mitral annuloplasty (PTMA) approaches using entirely catheter-based methods have been developed to reduce procedural morbidity and mortality. One of the approaches is to utilize the proximal location of the coronary sinus (CS) to the mitral annulus (MA) to percutaneously deploy a PTMA device within CS vessel. When the device contracts, it indirectly reshapes the MA and decreases MR. Although the approach has been shown to be promising in several animal studies, device dysfunction and fatigue fracture have been reported in human clinical trials. In this research, integrated experimental and computational studies were performed to apply quantitative analysis to study the biomechanical tissue-stent interaction (TSI) between PTMA device and CS vessel. Both human and animal CS tissue properties were characterized experimentally and implemented into finite element (FE) simulation. Realistic patient-specific geometries of the CS vessel were obtained from clinical imaging data and reconstructed into three-dimensional (3D) FE model. By incorporating proper tissue material properties and realistic 3D patient-specific geometries, FE simulation of the device deployment into the vessel could be achieved to investigate TSI and the associated biomechanics involved in the system. Quantitative understanding of the biomechanics in PTMA intervention is clearly an enabling step for science-based design of the devices.

Engineering Analysis of Minimally Invasive Mitral Valve Repair

Thuy Pham

B.S., University of Connecticut, 2008

A Dissertation

Submitted in Partial Fulfillment of the

Requirements for the Degree of

Doctor of Philosophy

at the

University of Connecticut

2013

APPROVAL PAGE

Doctor of Philosophy Dissertation

Engineering Analysis of Minimally Invasive Mitral Valve Repair

Presented by

Thuy Pham, B.S.

Major Advisor _____

Wei Sun

Associate Advisor _____

George Lykotrafitis

Associate Advisor _____

Donald Peterson

Associate Advisor _____

Charles Primiano

Associate Advisor _____

Quing Zhu

University of Connecticut

2013

Preface

As cardiovascular disease remains the number one killer in the United States, it is very fortunate to be able to contribute my time and knowledge to the field of cardiovascular disease research and treatment. I am very grateful that I have had the opportunity to study and formulate a method to provide engineering analytical insights to one of the new promising techniques in treating mitral valve disease.

This work would not be completed without the helps and supports from many wonderful individuals. First, I would like to thank my great advisor, Dr. Wei Sun, who, not only provided financial supports, had shared his immense and valuable knowledge with me during my doctoral study. Not only have I gained confidence in technical skills, my success also comes from adopting his positive attitudes towards challenges and perseverance in research.

I would like to express many thanks to my associate advisors, Dr. George Lykotrafitis, Dr. Charles Primiano, Dr. Donald Peterson, and Dr. Quing Zhu for their supports and guidance during my doctoral study. In particular, Dr. Primiano, who brought invaluable clinical insights to this engineering research project. I would also like to thank our collaborators Dr. John Elefteriades from Yale University Medical School for his explanations of cardiovascular diseases and demonstration of a variety of stents for treatments of cardiovascular diseases as well as Dr. Susheel Kodali from Columbia University Medical Center for his explanations of transcatheter aortic valve implantation from a clinical perspective. I would like to specially acknowledge my pre-doctoral fellowship from the National Institute of Health.

To all my current and past colleagues at the University of Connecticut: Kewei Li, Eric Sirois, Qian Wang, Caitlin Martin, Dave Kaputa, Huijuan Xu, Joseph Caldaren, Joseph Mummert, Haofei Liu, Shamik Bhattacharya and many others, I greatly appreciate your collaborations and helps on all aspects from making suture lines for biaxial testing to implement programming code. Without these helps, it would be much difficult to complete this work. Also daily working life would not be that enjoyable and memorable without your surroundings and positive working attitudes.

Last but not least, I am very grateful to my parents Minh Pham and Loan Le, sister Tram Pham and very best friends, MinhXuan Nguyen, Ngoc Bui and Hien Le for not giving up on me always stand by my side and provide continuous supports throughout my years of study and research. They all give me the mindset to look forward, the power to stay strong and the strength not to look back. They are an endless resource and purpose.

I dedicate this dissertation to all of wonderful family members, colleagues and friends.

Thuy Pham

October 20, 2013

Contents

List of Tables

List of Figures

1 Introduction*

Cardiovascular disease remains to be the number one killer in the United States. Among various types of cardiovascular disease, valvular heart disease is a significant cause of morbidity and mortality. In the United States, it is estimated that approximately 85,000 heart valve related procedures are performed annually. Valvular heart disease is responsible for about 22,144 deaths per year [1]. The two most common valvular heart diseases are aortic stenosis and mitral valve regurgitation. Structurally, mitral valve is more complex than aortic valve, which result in under-treatment and consequently high rate of mortality. In this dissertation, my research effort primarily focuses on the study of mitral valve function and the modeling of the associated mitral valve intervention techniques. Thus, I will begin this chapter with a brief introduction of the heart and its four valves, then the normal mitral valve structure and function, followed by main clinical issues and current clinical treatment techniques for mitral valve disease. Then, I will give a brief overview of current mitral valve biomechanical studies, which will lead to the motivation of my research on the modeling of minimally invasive mitral valve repair.

---

* Some of the contents of this chapter are taken from:

W. Sun, C, Martin and **T Pham**, "Computational Modeling of Heart Valve Function and Intervention ", ***Annual Review of Biomedical Engineering,*** accepted.

1.1 The heart and heart valves

The heart has four major valves: the aortic, mitral, tricuspid and pulmonary valves. As illustrated in in Figure 1-1, the tricuspid valve is located between the right atrium and right ventricle. The pulmonary or pulmonic valve is between the right ventricle and the pulmonary artery. The mitral valve is between the left atrium and left ventricle. The aortic valve is between the left ventricle and the aorta. These valves share a common function which is to ensure unidirectional flow of blood in and out of the heart. Biomechanically, these four valves are primarily passive structures i.e., they open and close due to the differential blood pressure on each side of the valve leaflets. Closure of the valve is achieved by coaptation of the leaflets (or cusps). Proper coaptation of the leaflets prevents backflow of blood. Diseases of the valve often involve improper closure of the leaflets; and the two most common heart valve diseases are stenosis and regurgitation. Stenosis is narrowing of the valve orifice which results in constriction of the blood flow. Regurgitation, on the other hand, is dilation of the valve orifice which results in blood leaks back through the valve in the opposite direction. Other valvular diseases are rheumatic diseases which results in valve leaflet prolapse, or billowing of the leaflets, and sometimes cause regurgitation. The mitral and aortic valves are frequently affected by diseases because they are located on the left side of the heart, where hemodynamic conditions are highly dynamics and deemed to frequent alternations. The study in this dissertation will mainly focus on the mitral valve function and the modeling of the associated mitral valve intervention techniques.

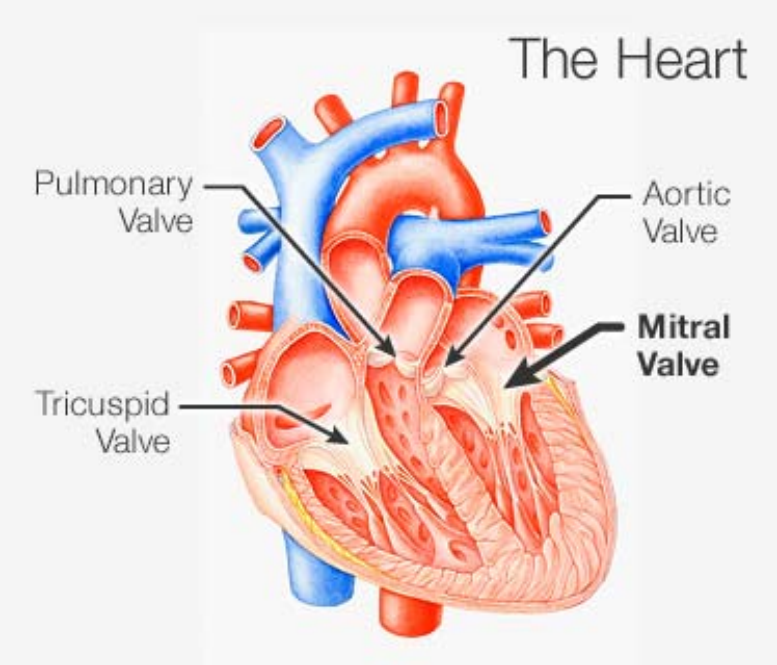

Figure 1-1: Anatomical structure of the heart and the heart valves (adopted from www.webmed.com)

1.2 Mitral valve structure and function

The mitral valve (MV) is a complex yet elegantly structured cardiac valve that consists of four anatomic components working congruently during a cardiac cycle: an annulus, two leaflets, approximately 25 chordae tendineae, two papillary muscles, and the underlying left ventricular myocardium (Figure 1-2). The mitral annulus (MA) of MV serves as a fulcrum for the leaflets. It is subdivided into lateral (anterior) and septal (posterior) portions that separated by the two trigones [2]. A lateral portion is mainly composed of cardiac muscles, while a stiff and dense fibrous section runs along the septal section. This fibrous tissue is shared by the non-coronary aortic valve leaflet, often called aortic-mitral curtain, where its left and right are formed by denser fibrous interleaflet triangles or trigones. This region is less prone to dilation compared to the muscular septal portion, which often undergo mitral repair by resecting extra tissues.

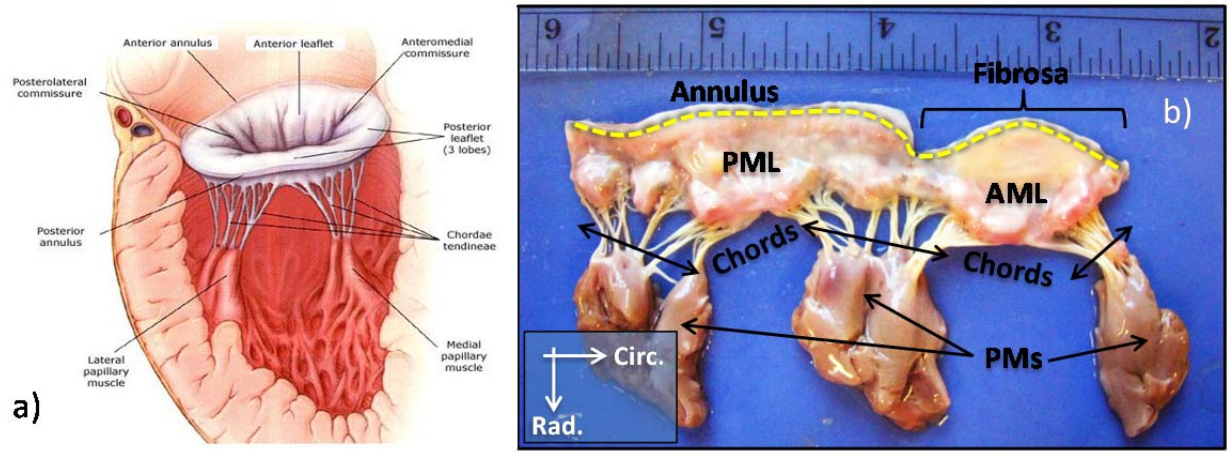

Figure 1-2: The anatomy of human mitral valve within a) the left heart and b) dissected from explanted heart showing mitral annulus, mitral leaflets, chords and papillary muscles. (Fig. a) is adapted from http://www.heart-valve-surgery.com.

The MV has two leaflets, the larger anterior (AML) and the smaller posterior mitral leaflet (PML) that are connected by the anterior and posterior commissural leaflet portions (Fig. 1-2b). The two leaflets detach during diastole and coapt or meet during systole to prevent regurgitation. Both AML and PML have two zones, the smooth that runs radial from the annulus to mid belly section and the rough zones that ends at the leaflet free-edge, where rough zone corresponds to the insertion (bumpy) locations of chordae tendineae. Histology of the microstructure of the MV leaflet revealed that it is composed of the atrialias, spongiosa, fibrosa and ventricularis layers. Similar to aortic and other valve leaflet constituents, the main components of MV layers include the extracellular cells, interstitial fibroblasts and connective fibers. The atrialis comprises of a thin layer of endothelium and elastin/collagen fibers. The spongiosa layer is mainly consists of extracellular matrix inconsisting of proteoglycans (PGs) and glyosaminglycans (GAGs). The GAGs and PGs provide cushion to withstand compressive tension [3] and promote sliding of collagen bundles [4], particularly proteoglycans which bind to the surface of collagen fibrils to transfer load from fibril to the matrix to relieve the fibril stress [5]. The fibrosa is the thickest layer of the MV leaflet and is the main load-bearing layer, consisting of GAGs/PGs and abundant circumferential aligned collagen fibers from where the leaflets exhibiting its strength and stiffness under high systolic pressure

loading. The stiffness of collagen fibrils of porcine AML was estimated to be 95.5 ± 25.5 MPa from biaxial loading tension of > 20 N/m [6], compared to ~ 1 GPa stiffness of collagen strength found in normal tendon. The ventricularis layer has elastin and collagen fibers with endothelial cell lining, where the chordae tendineae (chords) are attached to. The structure and material properties at these attachment regions were found to vary greatly due to the regional variations of collagen fiber angle and degree of alignment that affect the stress distribution of the entire mitral valve leaflets [7]. The fibrous chords are mainly composed of collagen bundles, which grant chord its stiffness and minimal extension that restraining the leaflets from pillowing into the left atrium (LA) during systole. There are three types of chords which are named in many ways, they are preferred as basal, marginal and strut chords herein. The basal chords originate from the base of the leaflets and marginal chords from free-edge zone. While both basal and marginal chords are multiple and vary in size, there are only two strut chords that attach at mid-length of the ventricular surface of the AML. The chords can originate either from the two major papillary muscles (on the anterolateral and posterolateral walls) or multiple small musclebundles attaching to the ventricular wall. Normal MV function involves a proper force balance between each of its components working congruently during a cardiac cycle.

Hemodynamics of the MV is highly complex that involves changes in pressure, and spatial and temporal orientation of all components. Mitral valve opens during the diastolic filling cycle where the annulus and leaflets are in resting and passive state. At late diastole, after left atrial systole, the pressure in the LV begins to rise above the pressure of the left atrium, causing the mitral valve to begin closing. As the pressure in the left ventricle rises rapidly during systole, the two leaflets begin to coapt. The mitral valve leaflets experience large deformation during valve closure [8] that could bulge toward the left atrium. However, bulging of the mitral valve leaflet is prevented by the tension of the chordae tendineae. It has been shown that rupture of the chordae tendineae leads to malcoaptation of leaflets and consequently valve regurgitation [9]. Contraction and motion of active muscles in the left atrial [10], mitral annulus [11] and papillary muscles [12, 13] are also important for valve closure during systole. Therefore, a balance of the mitral valve apparatus during systole enables proper leaflet closing.

1.3 Main clinical issues and current clinical treatment techniques for mitral valve disease

Heart valve disease is a significant cause of morbidity and mortality. In the United States, it is estimated that approximately 85,000 valve related procedures are performed annually. Heart valve disease is responsible for about 22,144 deaths per year [1]. In the past two decades, major advances have been made towards our understanding of the natural history of valvular heart disease. These advances have resulted in enhanced diagnostics, as well as interventional cardiology and surgical procedures, and have increased patient survival. However, valve procedures still have an overall in-hospital mortality rate of 4.22%, a figure that is much higher than that for many other cardiac procedures, including: coronary bypass graft surgery, percutaneous coronary intervention, and defibrillator implantation.

The two most common presentations of valve disease are aortic stenosis and mitral valve regurgitation. Mitral regurgitation (MR) is an abnormal leakage of blood from the left ventricle (LV) back into the left atrium during systole (Figure 1-3). Pathological alterations affecting any mitral valve component, such as mitral annulus (MA) dilatation, papillary muscle displacement, leaflet calcification and myxomatous disease can lead to altered mitral valve function and cause MR [14].

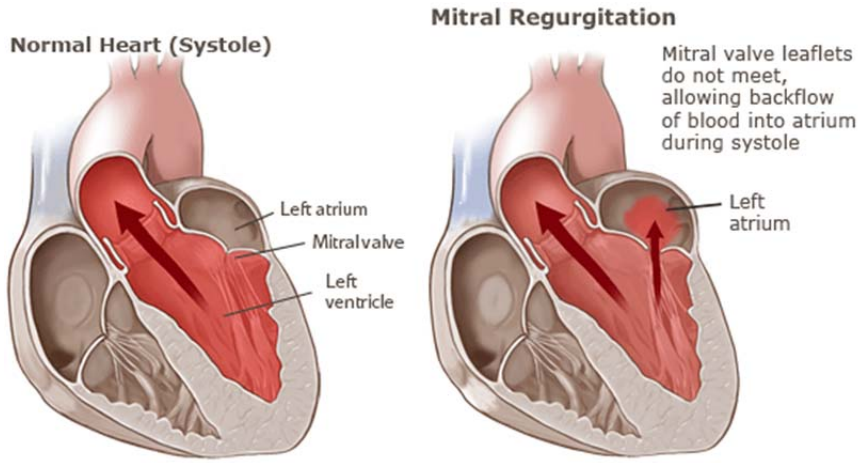

Figure 1-3: (a) a normal mitral valve function during systole and b) mitral valve with MR - an abnormal leakage of blood from the leftventricle back into the left atrium during systole. (adopted from http://uvahealth.com)

MR is one of the most common valvular lesions with a prevalence of 1 to 2% among adults [15], and this prevalence rises up to 13.2% beyond the age of 75 [16]. Moderate to severe MR occurs in up to 19% of patients after myocardial infarction and in 15% of patients with dilated cardiomyopathy [17, 18]. In these patients with functional MR, a combination of changes in left ventricular and mitral annulus (MA) geometry/function induces leaflet malcoaptation and regurgitation. Functional MR represents a major clinical challenge, often poorly recognized and undertreated, and is associated with high mortality [19].

Standard treatment techniques for MR are MV repair or replacement. The MV repair, benefited from improved understanding of MV mechanics and function, is now a preferable surgical approach to valve replacement. Common MV repair techniques include triangular or quadrangular resection, slide annuloplasty, ring annuloplasty, chordal cutting and transposition [20], artificial chord use [21, 22] and, recently, percutaneous technologies[23]. Surgical annuloplasty has been a commonly used treatment technique for severe functional MR intending to improve leaflet apposition by posterior annular correction. However, the reported operative mortalities of up to 6 ~12% have limited the more expanded use of this procedure [24-27].

1.4 Current biomechanical analysis of mitral valve function and intervention

The MV's primary function is essentially mechanical - preventing backflow of blood back to the left atrium during systole. Thus, biomechanics plays a central role in its function. Biomechanical analysis, encompassing experimental characterization of tissue properties, constitutive modeling of experimental data and computational simulations of tissue behavior, is playing an increasingly important role in enhancing our understanding of the normal MV physiological function, etiology of MV diseased states, surgical and interventional planning, and in the design and evaluation of artificial MV implants. In this section, I will give a brief review of methods of testing methods, modeling and computational simulation techniques.

1.4.1 Review of the state of the art of the biaxial testing method

Testing methods to characterize MV tissue properties usually include *uniaxial* and *biaxial* studies of material properties of MV, and *pressure-inflation* tests of structural properties of MV. As shown the following chapters, I have been using the biaxial testing method extensively to obtain MV tissues mechanical properties, thus its testing setup and theories behind the data analysis are briefly summarized here.

Illustrated on Figure 1-4 is a typical setup of a biaxial testing device. Biaxial experiments are generally performed a square piece of planar soft tissue, with the sample of about 10-25 mm of lateral length. The specimen is mounted to the biaxial device in trampoline-like fashion using thin threads, which allows the edges to expand freely in the lateral direction. Testing is generally performed with the specimen completely immersed in phosphate buffered normal saline (pH 7.4) at room or body (37 °C) temperature. The central target region must be sufficiently small and located away from the outer edges to avoid the tethering effects. Thus, in the central target region the stress and strain field is generally considered homogeneous.

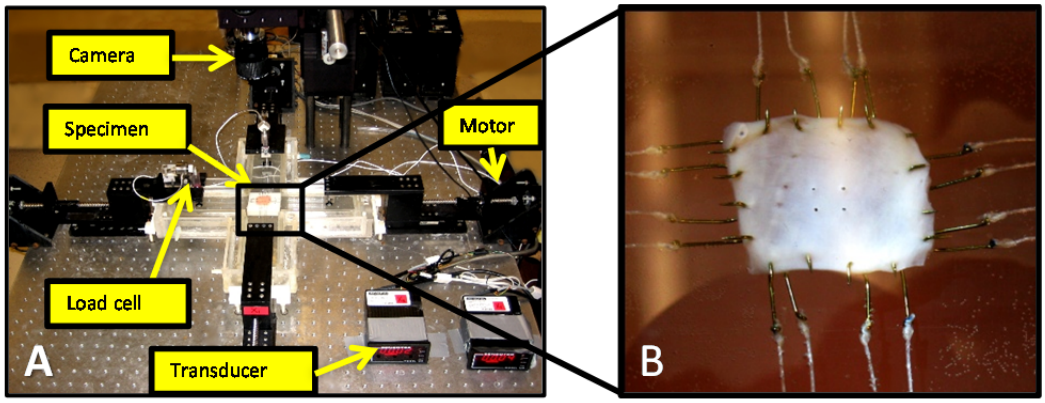

Figure 1-4: a) The biaxial testing system with an actual testing setup, showing the camera, the two load cells, the two signal conditioners and the four motors; b) A representative specimen is submerged in an appropriate physiologic solution, marked with four black graphite particles (optical markers for strain measurement) and attached to the device via four hooks at each side.

The following is a brief summary of the most important aspects of the kinematics of a biaxial mechanical test [28]. Consider deformation of membrane tissues under a biaxial stress state, including non-zero in-plane shear stresses. For this case, let Ω_0 and Ω be the (fixed) reference and deformed configurations of the continuous body, respectively. Consider the general mapping $\chi : \Omega_0 \to \mathbf{R}^3$, which transforms a material point $\mathbf{X} \in \Omega_0$ to a position $\mathbf{x} = \chi(\mathbf{X}) \in \Omega$ in the deformed configuration. For planar homogeneous deformations that occur during a biaxial test, this mapping reduces to

$$x_1 = \lambda_1 X_1 + \kappa_1 X_2, \quad x_2 = \lambda_2 X_2 + \kappa_2 X_1, \quad x_3 = \lambda_3 X_3 \tag{1.1}$$

where λ_i are the axial stretch ratios and κ_i measures of in-plane shear. λ_i and κ_i are also components of the deformation gradient tensor **F**, which for deformation described in eqn. 1.1 is $\mathbf{F} = \mathrm{Grad}(\mathbf{x})$ or

$$\mathbf{F} = \begin{bmatrix} \frac{\partial x_1}{\partial X_1} & \frac{\partial x_1}{\partial X_2} & \frac{\partial x_1}{\partial X_3} \\ \frac{\partial x_2}{\partial X_1} & \frac{\partial x_2}{\partial X_2} & \frac{\partial x_2}{\partial X_3} \\ \frac{\partial x_3}{\partial X_1} & \frac{\partial x_3}{\partial X_2} & \frac{\partial x_3}{\partial X_3} \end{bmatrix} = \begin{bmatrix} \lambda_1 & \kappa_1 & 0 \\ \kappa_2 & \lambda_2 & 0 \\ 0 & 0 & \lambda_3 \end{bmatrix} \tag{1.2}$$

where the out-of-plane stretch $\lambda_3 = h/H$ is the ratio of deformed (h) to the undeformed thickness (H) of specimen. **F** is a critical mathematical quantity since it completely describes the deformation state. Since soft tissues are composed primarily of water and have negligible permeability [29], they can be considered incompressible so that J=det**F**=1. From **F** the right Cauchy-Green deformation tensor is defined as $\mathbf{C}=\mathbf{F}^T \cdot \mathbf{F}$, from which the components of the in-plane Green-Lagrange strain tensor $\mathbf{E} = \frac{1}{2}(\mathbf{C} - \mathbf{I})$, where **I** is the identity tensor. **E** is the most common finite strain measure in the soft tissue literature due to the simplicity of the constitutive formulations. In practice the components of **E** are computed more directly using:

$$\mathbf{E} = \frac{1}{2}(\mathbf{F}^T\mathbf{F} - 1) = \frac{1}{2}\begin{bmatrix} \lambda_1^2 + k_2^2 - 1 & \lambda_1 k_1 + \lambda_2 k_2 & 0 \\ \lambda_1 k_1 + \lambda_2 k_2 & \lambda_2^2 + k_1^2 - 1 & 0 \\ 0 & 0 & \lambda_3^2 - 1 \end{bmatrix} \tag{1.3}$$

The components of **F** are determined optically to avoid any mechanical interference with the specimen.

As mentioned above, biaxial testing of biological tissues is performed using thin specimens (no more than ~3 mm, usually <1 mm) and acted on by only in-plane loads. A state of plane stress is thus assumed so that the components t_{i3} (i=1,2,3) of the Cauchy stress **t** (force/deformed area) are 0. During actual experiments one can directly measure only the initial specimen dimensions, so that the Lagrangian stresses **T** (force/unit original cross-sectional area) are used for convenience. The components of **T** are computed from the measured axial forces **P** using

$$T_{11} = \frac{P_1}{hL_2}, \quad T_{22} = \frac{P_2}{hL_1} \tag{1.4}$$

where h is the specimen thickness and L_i are the specimen lengths. Since experimentally applied loads are normal to the edges, $T_{12}=T_{21}=0$. The 2nd Piola-Kirchhoff stress tensor **S** is the most commonly utilized stress tensor for soft tissue constitutive theories, and is determined using $\mathbf{S=T\bullet F^{-1}}$. The Cauchy stress tensor **t** is determined using **t=F•T**/J, which in component form is given by (with $T_{12}=T_{21}=0$):

$$t_{11} = \lambda_1 T_{11}, \; t_{22} = \lambda_2 T_{22}, \; t_{12} = \kappa_1 T_{22}, \; t_{21} = \kappa_2 T_{11} \tag{1.5}$$

In the case where there is negligible shear strain (i.e. $E_{12}\sim 0$), the normal components of the two stress tensors are related by:

$$S_{11} = T_{11}/\lambda_1, \; S_{22} = T_{22}/\lambda_2 \tag{1.6}$$

1.4.2 Review of constitutive models of heart valve mechanical properties

Linear elastic models. Early attempts to describe valve tissue properties relied on the linear elastic material model, following the generalized Hooke's law [30, 31]

$$\boldsymbol{\sigma_{ij}} = \boldsymbol{C_{ijkl}\epsilon_{kl}}\ , \tag{1.7}$$

where $\boldsymbol{\sigma_{ij}}$is the stress tensor, $\boldsymbol{\epsilon_{kl}}$ is the strain tensor and $\mathbf{C_{ijkl}}$ is the fourth order elasticity tensor. Linear elastic models are appropriate when the stress-strain relationship is indeed linear, and are typically restricted to relatively small deformations. Linear elastic material properties were chosen for various reasons [32-34], but mainly to simplify the simulation process in order to achieve numerical convergence in FE simulation solutions. Over the physiological range of pressures, valve tissues have been shown to exhibit a relatively linear stress-strain relationship [35]. However, for a FE simulation of valve deformation from the undeformed state to a deformed state, the valve material response is clearly nonlinear and the use of nonlinear material models is essential for any realistic valve simulations.

Fung-elastic model The Green-strain based exponential model proposed by Fung [29] is probably the most commonly used hyperelastic model for characterizing the mechanical response of soft tissues [29, 36]. A two-dimensional Fung-type strain energy function W can be expressed as:

$$W = \frac{c}{2}[e^{Q} - 1], \tag{1.8}$$

$$Q = A_1E_{11}^2 + A_2E_{22}^2 + 2A_3E_{11}E_{22} + A_4E_{12}^2 + 2A_5E_{11}E_{22} + 2A_6E_{22}E_{12}$$

where c and A_i are material constants, $\boldsymbol{E}$ is the Green strain tensor. Note that Eqn. (1.8) has other variants that could be easily treated as a subset or expansion of this model [37]. Eqn. (1.8) is often used to model planar biaxial mechanical responses of valve tissues [38] and should be implemented with plane stress elements, such as shell or membrane elements. One problem with Eqn. (1.8) is that the transverse shear stiffness in the 13 and 23 directions are undetermined due to the lack transmural response definitions in this model. As shown by Sun *et al.* [37], valve peak stress is insensitive to change of TSS values for the valve closure simulation. However, to simulate valve opening, the tissue bending response is critical, and without accurate transverse shear stiffness values, the use of Eqn. (1.8) may give inaccurate results. The

details on the FE implementation of Eqn. (1.8) can be found in Sun and Sacks [37]. The 3D Fung model has not been widely used to model valve functions. Labrosse *et al.* [39, 40] has successfully utilized a 3D Fung model in simulation of native AV deformation.

Strain invariant-based fiber-reinforced hyperelastic model. Weiss *et al.* [41] and Holzapfel [42] presented a computational framework to implement strain invariant-based models that can accommodate the effects of one or two families of elastic fibers. To use this class of models, typically, the valve tissues are assumed to be composed of a matrix material with two families of imbedded fibers, each of which with a preferred direction. The deviatoric strain invariant $\bar{I}_1$ is used to describe the matrix material; and $\bar{I}_{4i}$ is used to describe the properties of the fiber families. One example of such models proposed by Holzapfel *et al.* [42] can be expressed as

$$W=C_{10}(\bar{I}_1-3)+\frac{k_1}{2k_2}\sum_{i=1}^{2}\left[\exp\left\{k_2\left[\kappa\bar{I}_1+(1-3\kappa)\bar{I}_{4i}-1\right]^2\right\}-1\right]+\frac{1}{D}(J-1)^2,\ i=1,2 \qquad (1.9)$$

where, C_{10}, k_1, k_2 and D are material constants. Particularly, C_{10} describes the matrix material and D enforces near incompressibility. In addition, a dispersion parameter, κ, is used to describe the distribution of the fiber orientation. Local coordinate systems should be defined for each leaflet to include fiber orientations. There are several variations of the model that have been applied to heart valve simulations. Prot *et al.* [43] implemented the Holzapfel material model into the analysis of healthy and pathological human mitral valves. Wang *et al.* [44, 45] simulated AV and MV functions with a variation of the material model. Similarly, in the study by Stevanella *et al.* [46], the MV dynamics were simulated where leaflet properties were characterized through a transversely isotropic model proposed by May-Newman and Yin [47], while the same material model was used by Conti *et al.* [48] and Auricchio *et al.* [49] to simulate AV biomechanics.

1.4.3 Review of computational studies of MV function and intervention

Kunzelman and co-workers were among the pioneers in developing 3D FE models of the normal [31] and pathologically altered [50, 51] MV. Their MV model, albeit limited by symmetric geometry

based on the excised porcine MV, included all the essential components of a MV. The model has been used extensively to analyze various MV repair procedures [50, 52, 53]. Although various designs of annuloplasty rings including: undersized, rigid, semi-rigid, flexible, D-shape and dog bone shaped, are commercially produced, the optimal shape is uncertain. Kunzelman *et al.* developed static FE models of the normal and dilated MV to simulate the effects of flexible and rigid annuloplasty rings [50]. Subsequently, Maisano *et al.* [54] and Votta *et al.* [34] showed that dog bone-shaped annuloplasty with selective reduction in the septolateral dimension is more effective than a conventional prosthesis for treating leaflet tethering in functional MR. These studies however excluded or simplified the LV geometry. Wong *et al.* [55] reconstructed a 3D FE model incorporating the LV, annulus and chordae tendineae from 3D cardiac MRI images of sheep. They successfully simulated the MR scenario and observed that the stress reduction with the saddle-shape MA was slightly greater than that of the asymmetric rings. More recently, research groups have begun to construct *in vivo* patient-specific MV models using clinical Echo [56, 57] and MRI [46, 58]. For instance, 3D Echo images were used by Xu *et al.* [56] to reconstruct MV models to predict leaflet and chordal stresses. MV geometries were perturbed to examine how MV leaflet coaptation area, non-coapted leaflet area and inter-leaflet coefficient of friction, affect leaflet and chordal stress distribution. Their results indicated that mitral valve repair techniques that increase or preserve noncoapted leaflet area might decrease stresses and thereby enhance repair durability. Similarly, Stevanella *et al.* [46] utilized cardiac MRI to develop patient-specific MV models of one healthy subject and one patient with ischemic MR. Their diseased model captured actual regurgitant characteristics and revealed abnormal tensions in the annular region and subvalvular apparatus.

One of the inaccuracies in MV modeling is the bulging of anterior leaflet into the atrium, which could be due to incorrect assumptions about chordal length, chordal origins and insertion points at the mitral leaflets. Such structure details are not distinguishable in the current clinical MRI or TEE images due to their poor spatial resolution. Multi-slice CT images offer much better spatial resolution, e.g., 64-

slice CT of 0.625mm. CT images were used to reconstruct patient-specific MV models in the study by Wang and Sun [45]. In the study, the MV models incorporated not only the mitral leaflet thickness, but the papillary muscle locations, chordal origins, and chordal insertion points, as shown in Figure 1-5. Dynamic motions of the mitral annulus and papillary muscles were obtained from middle systole and middle diastole; and were prescribed as boundary conditions for the FE simulation. Simulation results were validated by comparing FE deformed MV geometries with the CT images at systole and a close match was obtained (Figure 1-5c) [45]. Significant bulging of the mitral leaflets was not observed at peak transmitral pressure [45]. As there is evidence of muscle fibers and innervation in mitral leaflets [59], Skallerud *et al.* [60] applied a simple active stress component into modeling the porcine mitral valve, which resulted in a significant reduction in the leaflet bulging.

Percutaneous catheter-based Edge-To-Edge (ETE) repair using MitralClip has grown rapidly in Europe during the past years. Over 10,000 MitraClips have been implanted worldwide to date [61]. MV mechanics under ETE repair conditions are thus of great interest. Using idealized geometries of the MV and LV, Radealli *et al.* [62] and Fiore *et al.* [63] were able to provide a good estimation of the pressure drop across the ETE repaired valve and assess the leaflet stress pattern from the 8-mm ETE suture [64]. Consistent with clinical observations, FE simulations confirmed that using an annuloplasty ring in conjunction with ETE is favorable if mitral annular dilation is present, because it could reduce leaflet stresses [65, 66]. Dal Pan *et al.* [67] employed a parametric study of the ETE technique to investigate stress and strain distributions on leaflets at various suture positions and extension lengths as well as dilated annulus dimensions. The study provides useful analyses for technique improvement and optimization.

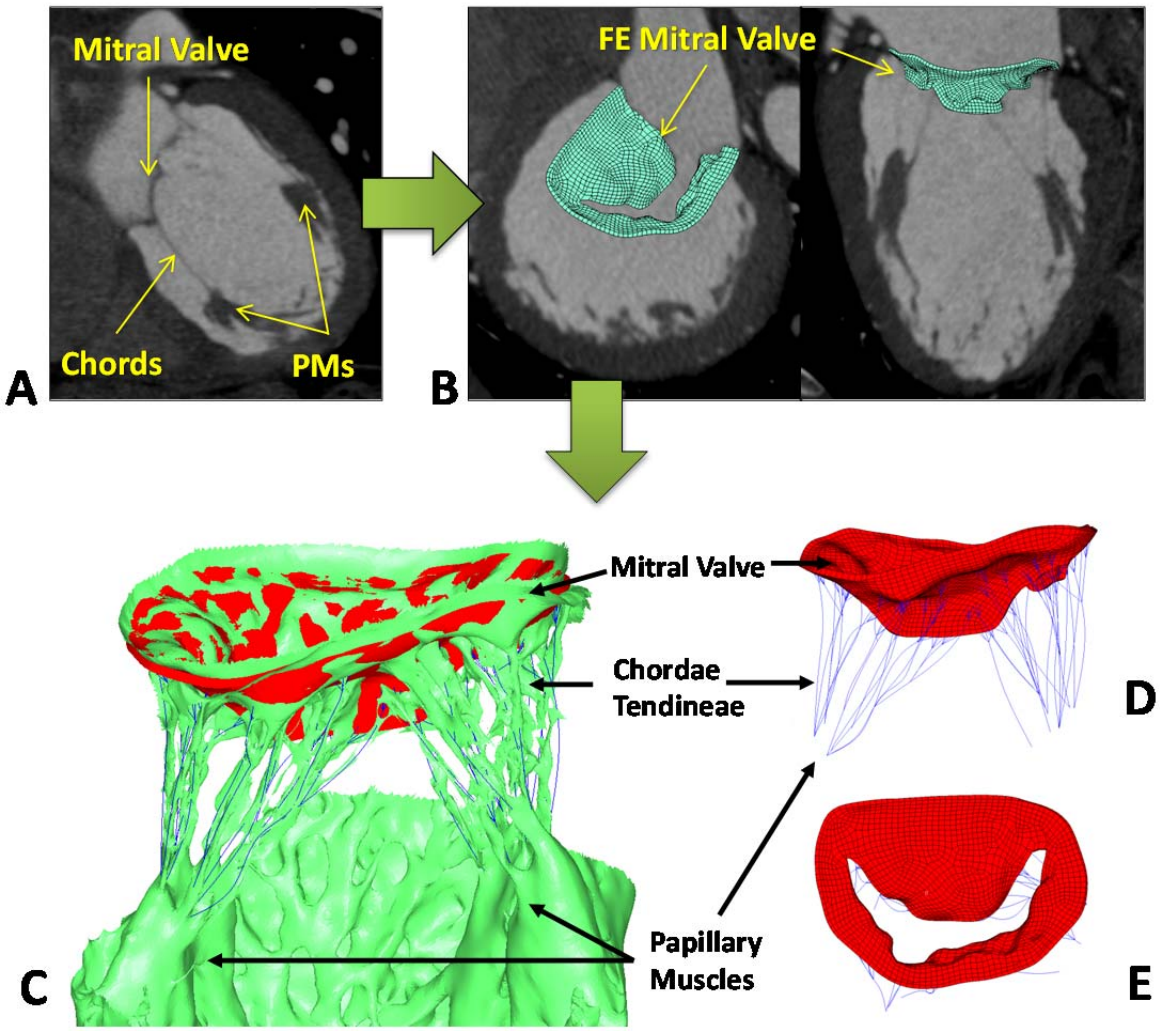

Figure 1-5: (A) The CT long-axis two chamber view of a close mitral valve (MV) showing a good visualization of chords and papillary muscles (PMs); **(B)** the short-axis and long-axis views of the reconstructed finite element (FE) MV model overlapped with the CT images; **(C)** the overlapping of geometries of the close MV valve from the CT scans (green) and the simulated result (red) after applied a pressure demonstrates a good match; open MV valve geometry and the anatomical locations of chordae tendineae with chordal origins and papillary muscles are shown in the **(D)** long-axis & **(E)** short-axis views.

There are relatively few FSI studies on MV structural and hemodynamic function. Kunzelman *et al.* [68] developed a fully-coupled FSI model using the LS-DYNA (Livermore Software Technology Corporation, Livermore, CA). The model was substantially enhanced from their previous models [31] by incorporating a fiber-reinforced hyperelastic material model for the leaflets, non-uniform leaflet

thickness, branched chords and fluid flow. The simulation results agreed well with physiological data reported in the literature. By varying the parameters of the fiber model, the authors also investigated effects of pathological changes. More recently, Ma *et al.* [69] developed a FSI MV model using the immerse boundary method. The model was generated from MRI data of a healthy patient. Linear elastic material models were used for both leaflets and chords. From the simulation results, the authors concluded that the differences in the thicknesses of the leaflets play an important role in maintaining the physiological curvature of the MV leaflet during its dynamic motion. Neither Kunzelman *et al.* [68] nor Ma *et al.* [69] incorporated the left atrium and LV into their models. Dahl *et al.* [70], however, reported a FSI study on the MV behavior during LV filing with the realistic left atrium and left ventricle obtained from echocardiography. Although limited by performing a 2D simulation with prescribed rigid wall motions (thus, not a coupled FSI), their results underscored the importance of incorporating the asymmetric leaflet geometry and left atrium to obtain accurate MV flow fields.

1.5 Emerging percutaneous mitral valve repair methods

A number of new approaches to percutaneous treatment are now developing rapidly. Percutaneous edge-to-edge mitral valve repair using the MitraClip ® system is the only endovascular approach that demonstrates as a viable treatment option for severe MR patients when compared with standard surgical repair in a randomized trial. Over 10,000 MitraClips have been implanted worldwide to date [61]. However, a considerable number of patients with functional MR will present with extensive annulus dilatation and minimal vertical leaflet coaptation that potentially preclude them from this beneficial technology for anatomical reasons [71].

Recently, since 2006, there have been several new minimally invasive transcatheter devices to treat MR utilizing the coronary sinus (CS), because of the advantage of proximity of the CS location to the MA, as a conduit to deliver a device that partially encircles the mitral annulus. Illustrated in Figure 1-6 is one of PTMA devices. This PTMA device is consisted of a 12F-outer-diameter guide catheter and dilator, a 9F delivery catheter, and a nickel-titanium alloy (Nitinol) implant. The implant itself is

composed of three sections: a distal self-expanding anchor, a springlike "bridge," and a proximal self-expanding anchor. The proximal and distal self-expanding anchors, once embedded within the coronary sinus (CS), will expand and position at the CS ostium and the great cardiac vein (GCV) ends, respectively. The bridge element can be shortened. Hence, it will pull the proximal and distal anchors together, displacing the posterior annulus anteriorly and reducing the mitral annulus diameter in the septal-lateral distance.

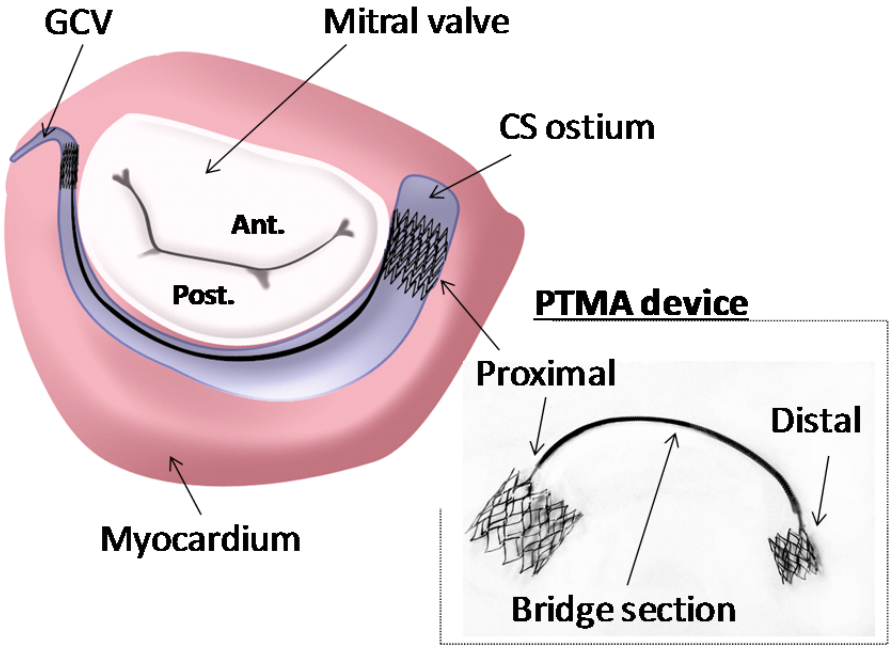

Figure 1-6: Illustration of a PTMA device deployed into the CS vessel, which is adjacent to the mitral valve posterior annulus. "Ant." for the anterior mitral leaflet and "Post." for the posterior mitral leaflet.

Several animal and human clinical trials using various PTMA devices have recently been conducted [27, 72, 73]. Although early clinical efficacy was demonstrated, device dysfunction and fatigue fracture were reported in these studies. The first-in-human clinical trial of the PTMA Monarc device, by Edwards Lifesciences as showed in Figure 1-6, in five patients was conducted by Webb *et al.* [72] in 2006. In this study, device fracture at the bridge section was reported in three patients and severe MR grade recurrence was observed after bridge separation. In addition, although no severe injury of CS was detected, compression of surrounding artery (i.e., left circumflex artery) was reported [72-76]. Because

the PTMA device is directly in contact with the CS, the biomechanical interaction between the device and the tissue could be a critical factor for device ending results.

For three percutaneous devices reported in 2006 and 2007, the results were all suboptimal. The CARILLON device (Cardiac Dimensions, Kirkland, Washington), which consists of distal and proximal anchors (Nitinol and titanium) and joined by a Nitinol ribbon connector, could reduce the dilated annulus by manually pulling the proximal anchor toward the CS ostium. Duffy et al. [73] observed that the distal anchor of a Carillon PTMA device did not hold tension during device traction in two of five temporarily implanted patients. Due to the difficulty in anchoring to the CS wall, a second generation device was developed with a twist at the distal anchor. The device was implanted in humans for up 6 months of follow-up [77]. A total of 30 out of 40 patients successfully received the device with an average of 23% MR reduction. However, three patients suffered from CS perforation and dissection.

Another device, Viacor (Viacor, Wilmington, Massachusetts), consists of up to three rigid Nitinol rods. Various rod sizes and stiffness are used to achieve the desired MR reduction. The issues with this device were associated with fracture, migration and delivery failures due to the vast difference in CS structures and geometries [27, 78]. Dubreuil et al. [79] reported temporary placements of a Viacor PTMA device in patients with an ischemic MR and MA dilation. They found that the MA diameter after the device implantation remained large compared to the surgical annuloplasty results.

Following the study by Webb et al. [72], A more recent study in 2010 on the second generation Monarc PTMA device reported a reduction in MR by ≥ 1 grade at 12 months in 50% of 22 implanted patients [80]. Unsuccessful implantations were associated with the lack of appropriately-sized devices (n = 13), inaccurate device positioning resulting in no MR reduction (n = 4), device migration (n = 1) and fracture of the proximal anchor (n = 4).

Currently only one device (Carillon, Cardiac Dimensions, LLC) remained in clinical trials. Despite the early failure and challenges encountered in these indirect approach techniques, the CS route remains highly attractive due to its simplicity. Thus, evaluation and knowledge of the CS structure and anatomy both before and during the implant procedure is critical.

Another minimally invasive mitral valve technique, called direct annuloplasty approach, involves direct implantation of a minimally invasive device into the mitral annulus, which is more similar to the surgical annuloplasty ring. So far two companies Mitralign and Guided Delivery Systems have developed devices using a direct approach. Although the direct approach has an advantage of avoiding coronary compression, it is more challenging than the indirect approach where the mitral annulus is assessing directly. Percutaneous mitral repair and replacement techniques are still in early development phase, and much more experimental and clinical trials are anticipated.

1.6 Motivation of the dissertation

Percutaneous transvenous mitral annuloplasty technique is still at its infant stage. The underlying biomechanical interaction between venous and mitral tissue and PTMA device is largely unknown. Device fatigue failure, as reported by Webb et al. [72], reflects the pressing need for a clear understanding of the biomechanical environments that the devices experienced. Unfortunately, up to today, there is no comprehensive study on the biomechanics of PTMA procedure in the literature.

Quantification of the mechanical properties of the CS vessel is critical for estimating the tissue-implant biomechanical interaction and for understanding device failure mechanisms. Although the anatomical studies of the CS have been well reported [81-83], there is a dearth of study on the mechanical properties of the tissue. One of objectives of this dissertation research is to quantify the CS structural (Chapter 2) and material (Chapter 3) properties and compare them among different species, i.e., porcine, ovine and human, to elucidate the biomechanical difference between these species, which may explain the discrepancy between animal and human clinical trials. To evaluate the cinching effect, via the contractive force of a PTMA device applied to the CS, on the change of mitral annulus area and the amount of MR, an ex vivo whole heart experiment study (Chapter 4) is needed. Building upon the experimental data, a computational analysis can be performed to quantify the stresses and strains that are on the CS tissue and PTMA stents. PTMA device deployment process requires two essential steps, 1) development of the anchoring stent, and 2) device contraction to reduce MR. Thus, the PTMA stent fatigue study should be conducted at the anchoring stents (Chapter 5) and the whole device with the bridge (Chapter 6).

The overall goal of this dissertation is to investigate the biomechanics involved in the transcatheter repair of functional MR using the coronary sinus annuloplasty approach. Using a combined innovative experimental and computational approach, the biomechanics of PTMA can be effectively investigated. The objectives of this dissertation are:

- Establish quantitative dataset for tissue structural and material properties and geometries related to the PTMA intervention.

- Provide engineering analysis of stress and deformation of mitral tissues undergoing PTMA intervention using computational methods.
- Predict PTMA device failure modes and provide insights for implant design improvement

Successful completion of the proposed work will establish a computational simulation procedure, not only applicable to Monarc PTMA, also to other future devices using the indirect coronary sinus approach. The procedure includes collection of experimental data and constitutive modeling techniques to characterize the mechanical properties of mitral tissue, and finite element modeling of mitral valve geometry (based on clinical cardiac images), which will enable the simulation of PTMA device deployment and device-tissue interactions, and prediction of PTMA failure modes. Such biomechanical simulations will allow one to virtually assess and predict results of PTMA intervention, which is unprecedented in academia and the heart valve industry.

2 Characterization of Structural Properties of Porcine Coronary Sinus Vessel*

In the next two chapters, the three experimental studies used to characterize the biomechanical properties of the coronary sinus vessel will be introduced. The experimental characterization of tissue biomechanical properties is challenging and important that provides information necessary to formulate constitutive relations as well as solving many boundary condition and initial value problems in biomechancs. The most common experimental methods for quantifying mechanical properties of soft tissues include tensile uniaxial test, planar biaxial test and inflation tests. Because the coronary sinus vessel serves as a conduit for the deployment of the PTMA device for the treatment of functional mitral regurgitation, characterization of CS structural response is an important step toward an understanding of tissue-device interaction in the PTMA intervention. In this chapter, structural characterization of the porcine CS vessel using pressure-inflation test and constitutive modeling using a four-fiber family model will be introduced.

* The contents of this chapter are published partially in:
T. Pham and W. Sun, Characterization of mechanical properties of coronary sinus for percutaneous transvenousmitral annuloplasty, **Acta Biomaterialia 6**(11): 4336-4344 (2010).

2.1 Introduction

2.1.1 Anatomy and structure of coronary sinus vessel

Coronary sinus is a large venous vessel that returns deoxygenated blood from the left heart and drains into the right atrium. It begins at the termination of the great cardiac vein (GCV), marked by the valve of Vieussens internally and the small oblique vein or vein of Marshall (OV) externally. Located in the sulcus of the atrioventricular groove, CS runs along the posterior side of the annulus of the left atrium and ends at the Thebesian valve, where it marks the CS ostium [81-83].

A study by Valle-Fernadez et al. [84] showed that there are dynamic changes in the relationship between CS/GCV and the MA. From 56 patient computed tomography angiographies, the distance between CS/GCV and MA progressively increased over the first 4 to 5 cm of the CS/GCV trajectory and decreased afterward ($p < 0.001$). The CS/GCV was larger in phase 40% (end-of-systole) than in phase 75% (mid-diastole) and was smallest in phase 0% (end-of-diastole). El-Maasarany et al. [85] showed that there are three patterns for the CS/GCV and MA relation (described as six regions, each 36 degree wide): 1) pattern A: CS was widely separated from the MA at 9.4, 10.6, 9.9, 9.1, 6.6 and 5.8 regions, 2) pattern B: CS was widely separated from the annulus at its ostium and became closer distally towards the GCV at 11.6, 11.1, 10.6, 9.8, 8.3 and 7.0 mm, and 3) pattern C: a non-consistent pattern.

These findings indicate that there is a highly variation in the CS/GCV/MA geometries and dynamic changes. Several studies also noted the coronary artery traverses between the CS/GCV and the MA [84]. Therefore, patient selection for the PTMA technique to reshape the MA using CS approach needs a detailed prospective imaging evaluation.

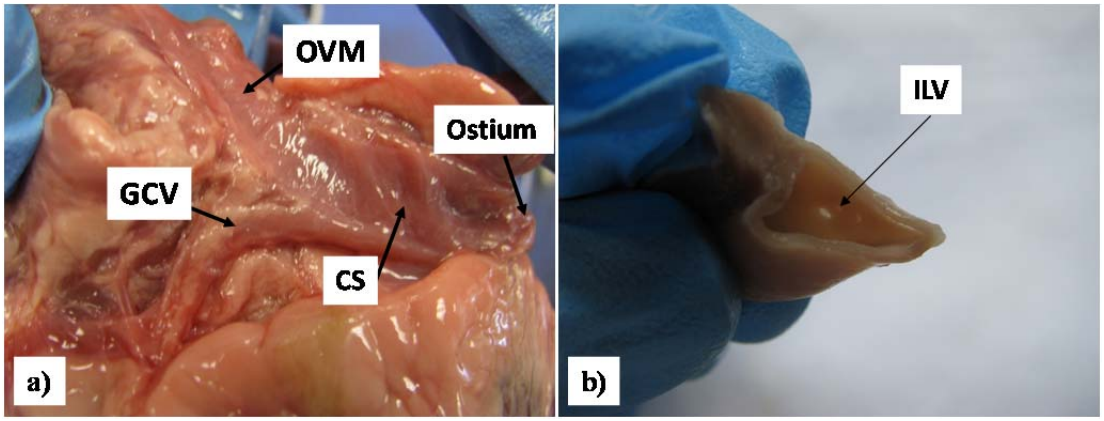

Figure 2-1: The major tributaries of the CS, with a) of the great cardiac vein (GCV) and the oblique vein of Marshall (OVM), b) the inferior left ventricular vein (VA).

2.1.2 Porcine versus human models

Porcine hearts were studied in various medical applications due to their similarity in structures with human hearts. Similar to human CS vessel, porcine CS vessel has the same major tributaries, which are the great cardiac vein (GCV), the oblique vein of Marshall (OV) that descends along the lateral and inferior wall of the left atrium and joins the GCV to form the CS, and the inferior left ventricular vein (VA) that drains from the diaphragmatic surface of the left ventricle (see Figure 2-1). However, we noticed that there is a distinct difference between porcine and human coronary sinus. Unlike human OV which is small [81, 83], porcine OV's diameter is as large as the CS's diameter (see Figure 2-1a) and there is no obvious landmark that separates this vessel from the CS. Illustrated in Figure 2-2b is the CS cut along its long axis. The internal surface of the CS resembles the right atrial endocardium, other than the endothelium of a vein. The free wall of the CS is surrounded by a striated myocardial fiber (SMF) cuff that runs obliquely starting from the OV. Superior to this SMF sheet is a thin layer of connective tissues, which also surrounds the OV (Figure 2-2a). The anterior part of the CS is attached to the left atrial appendage (LAA), and the barrier between the LAA and CS can also be identified, see long-dashed line in Figure 2-2c.

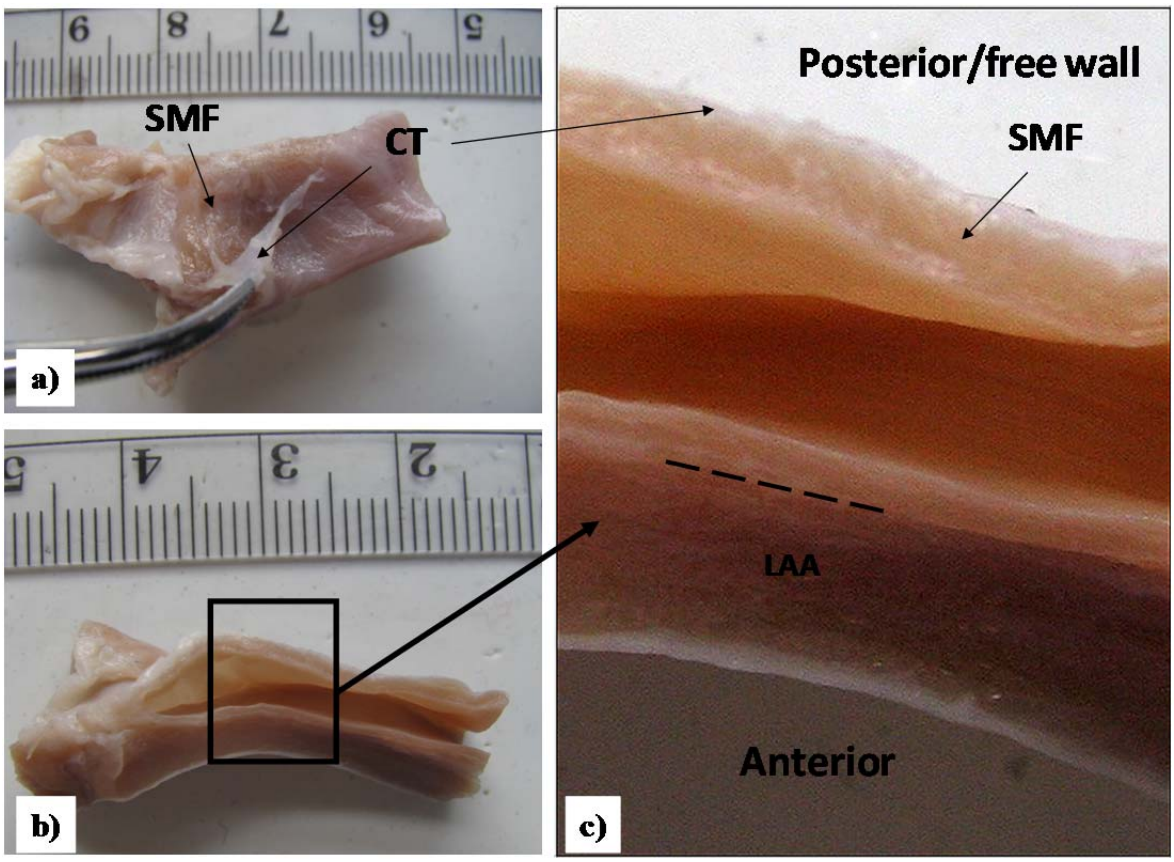

Figure 2-2: – a) Coronary sinus (CS) vessel fixed in 10% formalin in 2 days, with its connective tissue (CT) being peeled off exposing the striated myocardial fiber (SMF) layer, b) axial view and c) its closer view of the CS's inner wall with distinctive layers of SMF, CT, and left atrial appendage (LAA). The long-dashed line indicates the barrier between CS wall and LAA.

In this chapter, we reported, to our knowledge, the first biomechanical characterization of the CS vessel using a porcine model. A pressure-diameter inflation test was performed on the CS vessel at its intact, in-service configuration, e.g. CS was not dissected from its surrounding myocardium, to quantify its in vitro mechanical responses. A structure-based strain energy function (SEF) was utilized to characterize the nonlinear hyperelastic properties of the vessel wall. In addition, the microstructure of the CS through histology was studied to elicit its structure and relate it to its mechanical properties.

2.2 Materials and Methods

2.2.1 Pressure-inflation experiment

Coronary sinus is a large venous vessel that returns deoxygenated blood from the left heart and drains into the right atrium. It begins at the termination of the great cardiac vein (GCV), marked by the valve of Vieussens internally and the small oblique vein or vein of Marshall (OV) externally. Located in the sulcus of the atrioventricular groove, CS runs along the posterior side of the annulus of the left atrium and ends at the Thebesian valve, where it marks the CS ostium [81-83]. In this study, we focused on the material characterization of the CS ostium region about 10 mm from the Thebesian valve since it is the region that is directly in contact with the proximal anchor stent of the PTMA device. Porcine hearts were used in this study because of similarity between porcine and human hearts for mitral valve related applications [86].

A total of seven fresh porcine hearts, typical of 6 - 9 months old with a weight range of 400 - 500 g, were obtained from a local abattoir. Upon delivery with ice, they were subjected to vessel pressure-inflation testing within 48 hours. Prior to testing, the hearts were separated from excess tissues (e.g. aorta arch, fat) and blood clumps. The right atrium was incised to expose the CS ostium and a small section about 5 mm from the CS ostium was detached from the left atrial appendage (LAA) for the purpose of connecting the plastic cannula to the CS for the inflow pressure. The plastic cannulas were varied in sizes to fit with various CS diameters (e.g. 4, 6, & 8 mm). The other end of the CS (at the junction of the CS-GCV) was secured with a surgical forceps. To ensure pressure stabilization, all other branches of CS vessel were occluded with ligatures. Then the whole heart was submerged in a small plexi-glass tank (21L x 18W x 18H mm, 2.8 mm thick), and the front side of the tank was replaced with a thin (0.35 mm thick) clear plastic sheet for the purpose of imaging. The tank was filled with Ca^{2+}-free saline solution at room temperature. The heart was stabilized by resting on a sponge placed at the bottom of the tank. The cannula at the CS ostium end was connected to the pressure gauge, which was linked by a flexible plastic tube to

the water tank where a hand-operated pump was used to apply pressure to the CS. The ultrasound probe (7.5 MHz transducer of RT320, General Electronic Inc.) was projecting perpendicular to the CS at the clear plastic sheet side of the tank to collect 2D cross-sectional images of the CS, see Fig. 2-3a. Since the water tank is clear, ultrasound wave traveled through the tank, the water and to tissue and traveled back to the probe. All data were recorded at the cross section about 10 mm from the CS ostium.

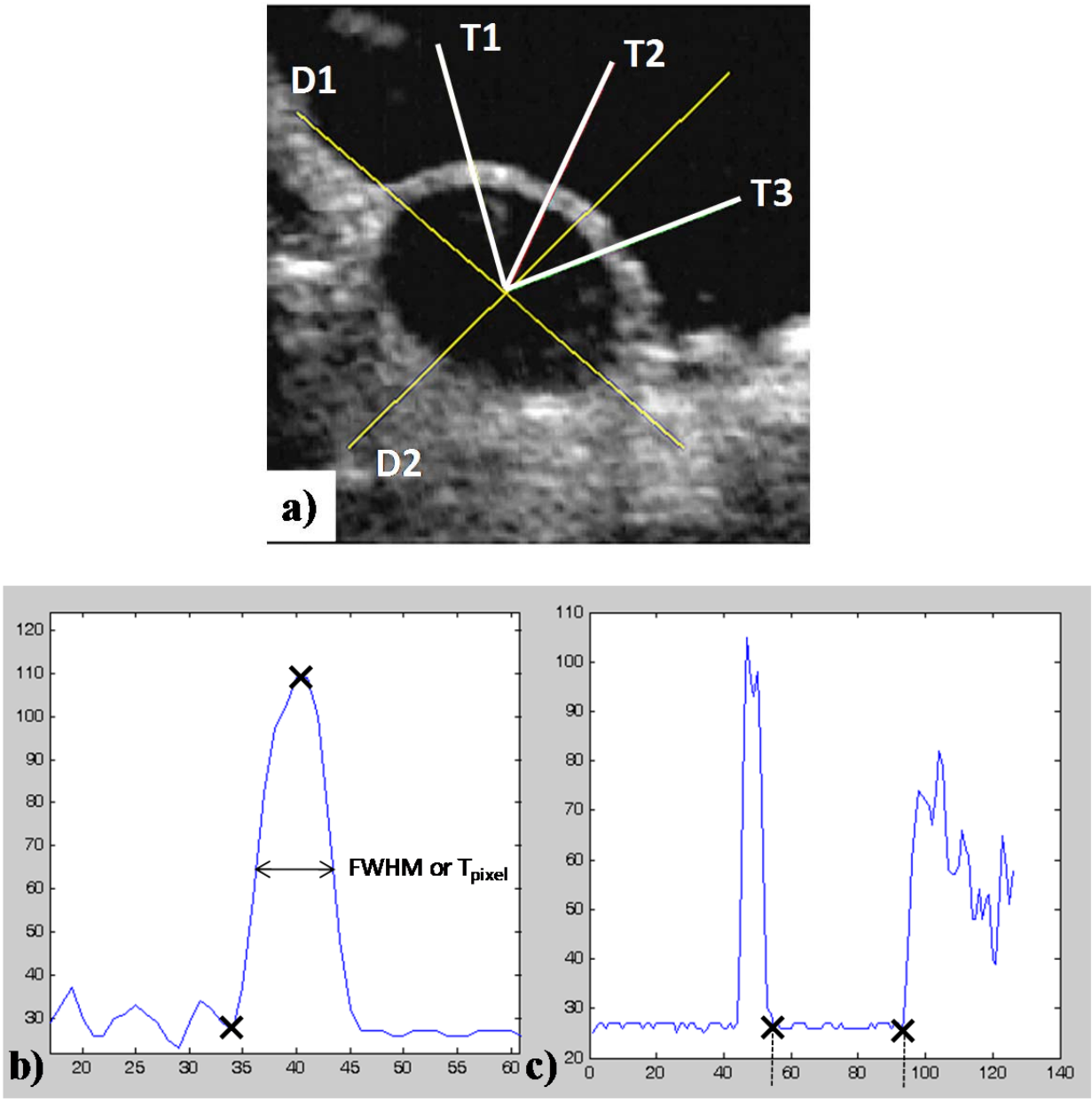

Figure 2-3: A) An ultrasound image of cross section of the inflated CS vessel, with two line segments D1 and D2 for measuring diameters and three line segments T1, T2, and T3 for thickness measurements; B) thickness measurements using the FWHM method (to obtain T_{pixel}, or thickness in pixel—width of the half amplitude of the peak), and C) diameter measurements (distance between the two crosses—in pixel), both processed by the Matlab *improfile* function.

Each specimen was subjected to preconditioning by inflating up to 80 mmHg and then venting the pressure back to 0 mmHg. This process was repeated 20 times to minimize hysteresis. Testing was then conducted by increasing pressure from 0 to 80 mmHg in increments of 5 mmHg per second. At each pressure, a 2D ultrasonic image of the CS cross-section was taken immediately using a custom-made image capturing software. A total of 17 images were taken for each heart, and inner diameter and CS wall thickness data were measured using an image post-processing code written in Matlab (Mathworks, Natick, MA). Utilizing ultrasound images to capture the cross-sections of CS geometry during the inflation test allows a direct measurement of tissue thickness. This method may provide a more accurate estimation of circumferential stretch and stress using Eqns 2.1-2.3 below, compared to other methods that used the derived thickness based on markers on the surface of vessel, particularly when the vessel is curved and partially imbedded in surrounding tissues.

2.2.2 Ultrasound Image Analysis

All images were imported into the Matlab program and analyzed using a Matlab function called *improfile*. Briefly, the image processing technique involved identifying boundaries of tissues from the change of impedance of the medium when the ultrasound wave travels from water to tissue and from tissue to water. The change of impedance resulted in the change of the image intensity, where high (white) and low (black) intensity determine the tissues and water, respectively. The *improfile* function will identify the intensity values along a line or a multiline path specified by the user, performing interpolation to find the intensity value for each pixel, and graphing these intensity values. Both diameter and thickness values were determined by detecting the pixel-value along line segments (Fig. 2-3b & c).

For diameter measurements, two line segments were drawn across the anterior-posterior and superior-inferior view on the vessel. As CS is partially imbedded in the myocardium, the inflated vessel circumference at low pressure may not be circular. Therefore, two measurements of diameters were

recorded and averaged. A center point was determined from an intersection of these two lines. Thickness was measured by drawing three lines, which originate from the center point and each goes separately through three different sections across the thickness, see Fig. 2-3a. Thickness measurement was estimated using a basic image analysis technique called Full-Width Half-Maximum (FWHM) [87]. Real measurements of tissues using a non-rotating thickness gauge (Mitutoyo, Model 7301) determined that FWHM provided a good approximation of thickness. Basically, FWHM is the full width of the section (across CS wall) at the half maximum value (intensity value). Three measurements of thickness were averaged to obtain the mean. Units in pixel were converted to lengths according to ultrasound image calibration.

2.2.3 Histology

Each CS vessel was removed from the heart and fixed in formalin for 24 hours prior to the histology process. Cross-sections through the thickness of both anterior and posterior CS sections were examined. Each sample was sliced into 6 μm piece in both circumferential and longitudinal directions using a cryostat microtome and then stained with the Verhoeff Van-Gieson (VVG) stain. Thus, the black strands are elastic fibers and the bright red materials are the collagen fibers. Muscle fibers can also be distinguished with a duller red or light brown color. Histological images were obtained through an Olympus220 digital camera that coupled to an OlympusCX41 light microscope and analyzed using LabView software (National Instruments, Austin, TX).

2.2.4 Constitutive modeling

The pressure-radius data were utilized to characterize CS mechanical properties using a four-fiber family SEF [88]. For a segment of CS with initial and deformed axial lengths of L and l, respectively, with the assumption of tissue incompressibility, the vessel wall volume, V, is a constant during the inflation. Thus, we have

$$V = (B^2 - A^2)\pi L = (b^2 - a^2)\pi l\,, \tag{2.1}$$

where A and B denote initial, unloaded inner and outer radii, respectively, a and b denote deformed, loaded inner and outer radii, respectively. Following the method presented in Wicker *et al.* [88], the associated mean stretch ratios in the CS circumferential and axial directions were computed as

$$\lambda_\theta = \frac{(a+b)/2}{(A+B)/2}, \qquad \lambda_z = \frac{l}{L} = \frac{(B^2-A^2)}{(b^2-a^2)}\,. \tag{2.2}$$

Note that both of the initial and deformed lengths were not experimentally measured in this study. Instead, using the Eqn. 2.1 and the assumption of tissue incompressibility, the axial stretch was calculated using the Eqn. 2.2 above. The mean circumferential (σ_θ) and axial (σ_z) Cauchy stresses [89] can be calculated using the pressure-radius experimental data in the deformed configurations,

$$\sigma_\theta = \frac{Pa}{h}, \qquad \sigma_z = \frac{\pi a^2 P}{\pi h(2a+h)}, \tag{2.3}$$

where, P is the luminal pressure (outer pressure was assumed to be approximately zero), $h = b - a$ is the thickness, and $\pi a^2 P$ accounts for the luminal pressure acting over the projected inner cross-sectional area of the CS.

We assumed that the CS behaves as a hyperelastic material following the concept of pseudoelasticity [29], the four-fiber family model W is expressed as

$$W = \frac{c}{2}(I_1 - 3) + \sum_{\mathrm{k}=1}^{4}\left\{\frac{c_1^k}{4c_2^k}\exp\left[c_2^k\left(\left(\lambda^k\right)^2 - 1\right)^2\right] - 1\right\}, \tag{2.4}$$

where c, c_1^{k}, and c_2^{k} are the material parameters, the superscript k represents the k^{th} fiber families. For the fiber families k = 1 and 2 represent axially (0˚) and circumferentially (90˚) oriented fibers, respectively, and fiber families k = 3 and 4 represent diagonally oriented fibers, see Fig. 2-4. Note that these fiber families do not reflect the physical fibers, instead they are the virtual fibers representing all fibers oriented in four directions throughout the vessel wall. The parameter I_1 is the first invariant of the right Cauchy–Green tensor, $\lambda^k = \sqrt{\lambda_z^2 cos^2\alpha_0^k + \lambda_\theta^2 sin^2\alpha_0^k}$ is the stretch of k^{th} fiber family, α_0^k represents the angle between the fiber family and the CS axial direction, with $\alpha_0^1 = 0$, $\alpha_0^2 = 90$, and $\alpha_0^3 = -\alpha_0^4$. For Eqn. 2.4,

$c_1^1 = c_1^2$, $c_2^1 = c_2^2$, $c_1^3 = c_1^4$, and $c_2^3 = c_2^4$ are typically assumed [88, 90, 91], therefore, a total of six parameters is needed to be determined.

Finally, the associated mean circumferential and axial Cauchy stresses are [91],

$$\sigma_\theta = \lambda_\theta \frac{\partial W}{\partial \lambda_\theta}, \qquad \sigma_z = \lambda_z \frac{\partial W}{\partial \lambda_z} \ . \tag{2.5}$$

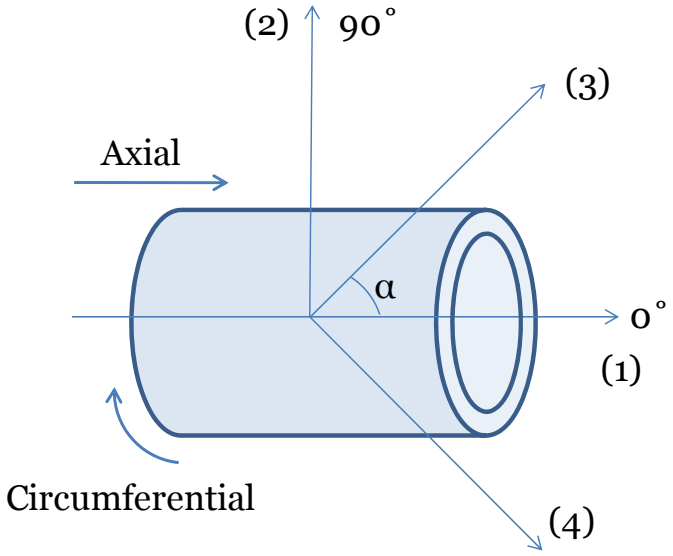

Figure 2-4: Schematic of the vessel fiber orientation, with k = 1 and 2 are 0° (axial) and 90° (circumferential) oriented fibers, respectively; and k = 3 and 4 are diagonally oriented fibers.

The constitutive model was fit to the individual experimental pressure-diameter data, yielding six optimal parameters for each dataset. In addition, the mean response of seven pressure-diameter data was obtained and fitted. The material parameters of the mean response (P_Mean_Exp_Data) and the mean values of the optimal material parameters (P_Mean_Para) were compared. The goodness of the fit was determined using the R-square value based on the Levenberg-Marquardt nonlinear regression algorithm using SYSTAT 10 (Systat Software Inc., Chicago, IL). Variation of test data was presented in terms of standard errors.

2.3 Results

2.3.1 Mechanical responses of the coronary sinus

Initial and maximum dilated diameters and thicknesses of seven specimens were listed Table 2.1. The mean pressure versus the inner diameter response of seven CS's was illustrated in Fig. 2-5. The CS exhibited a S-shape curve, typical for blood vessels [89]. Below a pressure of 10 mmHg, the CS did not exhibit obvious dilatation. However, between a pressure range of 10 to 30 mmHg, there was a rapid extension of the CS diameter. As the pressure increased above 30 mmHg, the wall became progressively less distensible and nearly stayed flat at the high pressures. At 30 mmHg pressure, the CS could be dilated approximately up to 60%, and at 80mmHg, up to about 88%. The CS vessel wall thickness decreased with the applied pressure (see Fig. 2-5b), as one would expect.

Table 2-1. Initial and maximum dilated diameters and thickness of seven specimens.

Specimen	D_0	D	T_0	T	D/D_0	T/T_0
1	4.90	12.50	1.37	0.71	2.55	0.52
2	3.11	6.55	0.56	0.55	2.11	0.98
3	5.04	10.09	1.12	0.63	2.00	0.56
4	8.54	11.72	1.06	0.62	1.37	0.58
5	7.06	10.86	1.54	1.02	1.54	0.66
6	4.22	7.59	1.54	1.15	1.80	0.75
7	6.00	10.95	1.42	0.63	1.83	0.44
Mean	5.55	10.04	1.23	0.76	1.88	0.64

D_o is the initial diameter, D is the maximum distended diameter; T_o is the initial thickness, and T is the thickness at maximum pressure, 80 mmHg. All measurements are in mm.

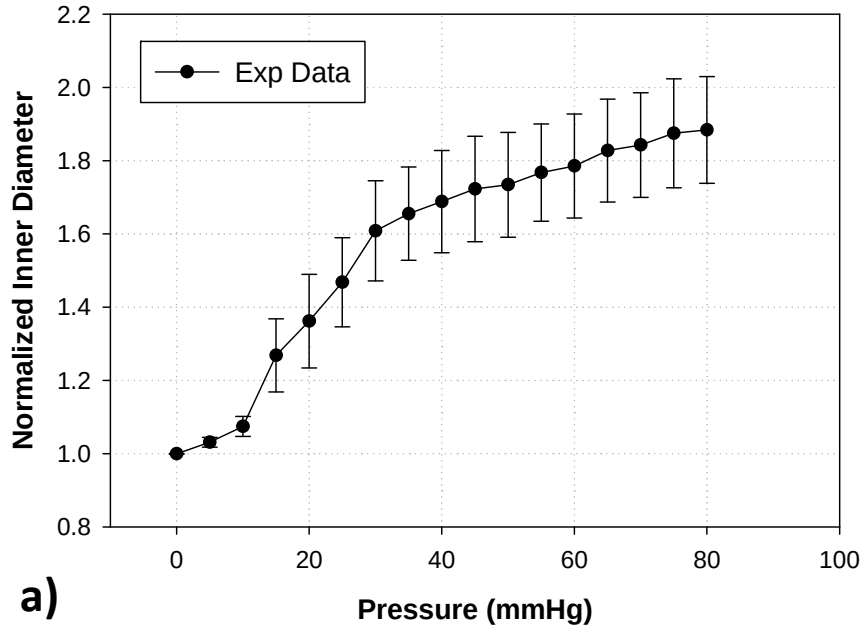

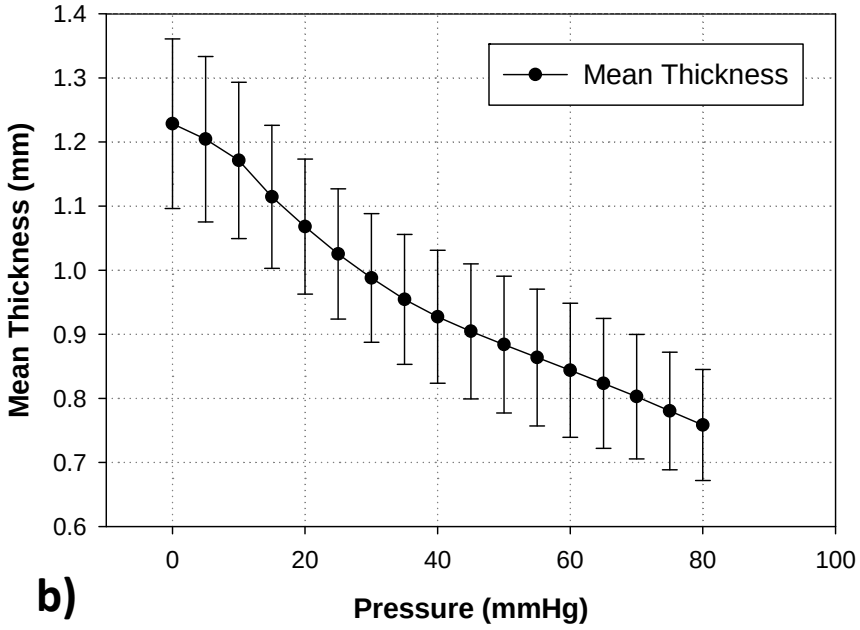

Figure 2-5: a) The normalized pressure versus inner diameter experimental result from seven porcine CS's inflated to a maximum pressure of 80 mmHg, b) the thickness change of the anterior section of the CS vessel. Data was expressed in terms of mean and standard error.

The mean stress versus stretch curves of the CS obtained from the pressure-inflation experiments can be seen in Fig. 2-6 for both axial and circumferential directions. The maximum stress values were 35.5 ± 4.64 kPa and 75.95 ± 9.34 kPa for the axial and circumferential, respectively, under the 80 mmHg pressure. The response in the axial direction showed an initial contraction which ceased at about 10 mmHg and followed by an extension at higher pressures.

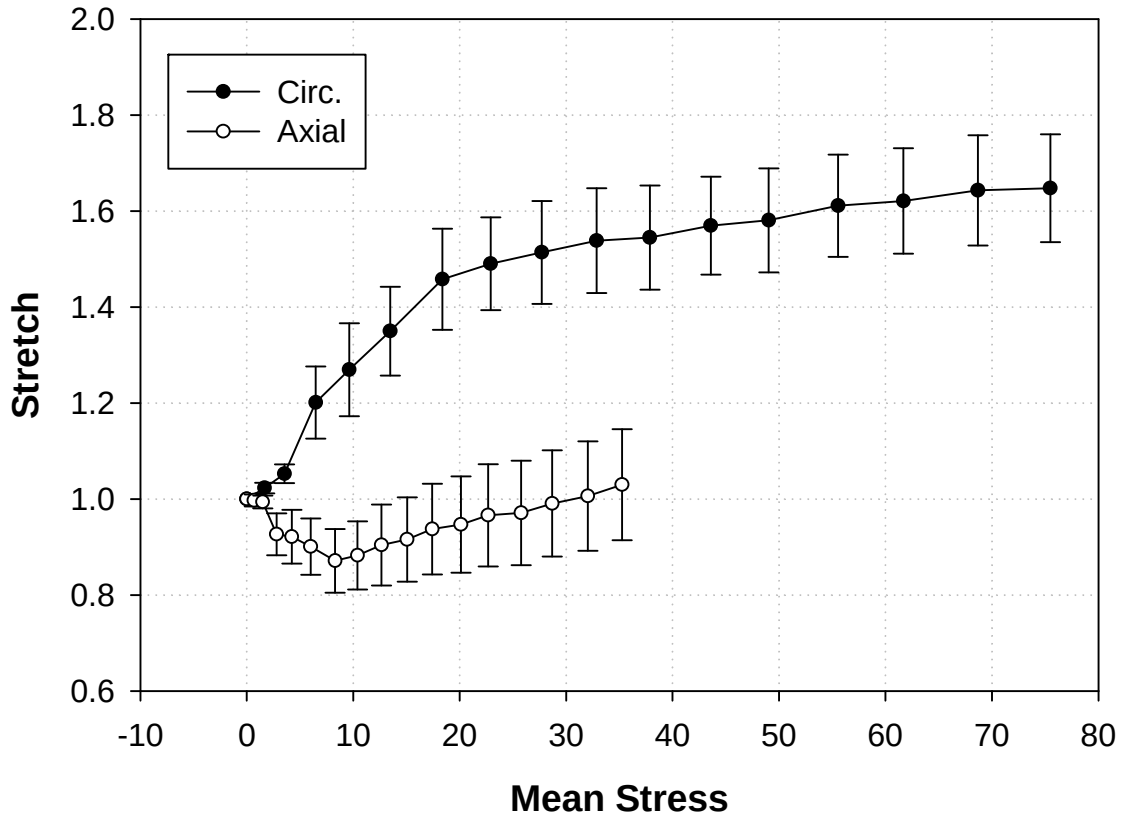

Figure 2-6: Stretch-stress curves of the CS obtained from the pressure-inflation tests. The upper curve represents the response in the circumferential (Circ.) direction and the lower curve is for the axial direction. Data was expressed in terms of mean and standard error.

2.3.2 Microstructure of CS vessel wall

The circumferentially-cut sections of the posterior (or the free wall) and the anterior (or a section attached to the LAA) CS vessel were illustrated in the Fig. 2-7. The posterior CS sections were covered by a layer of SMFs oriented circumferentially (see Fig. 2-7a). Within the CS wall, unlike other vessel wall, it was mainly composed of SMFs, with a small content of smooth muscle cell (SMC). The SMCs were only observed in bundles in the outer layer of the anterior section of the CS vessel (see Fig. 2-7b, arrow). The SMF orientations were similar in both anterior and posterior sections where they aligned in the circumferential direction in the luminal layer and realigned into transverse direction in the media layer. Collagen and elastin fibers were found throughout the vessel wall (see Fig. 2-7c & d), collagen fibers were slightly scattered in the SMF layer. Elastin fibers were aligned in the axial direction in the luminal layer and realigned into the circumferential direction in the media layer of the CS wall. Crimping of the collagen fibers were also observed in the axial direction in the CS luminal layer (see Fig. 2-7c).

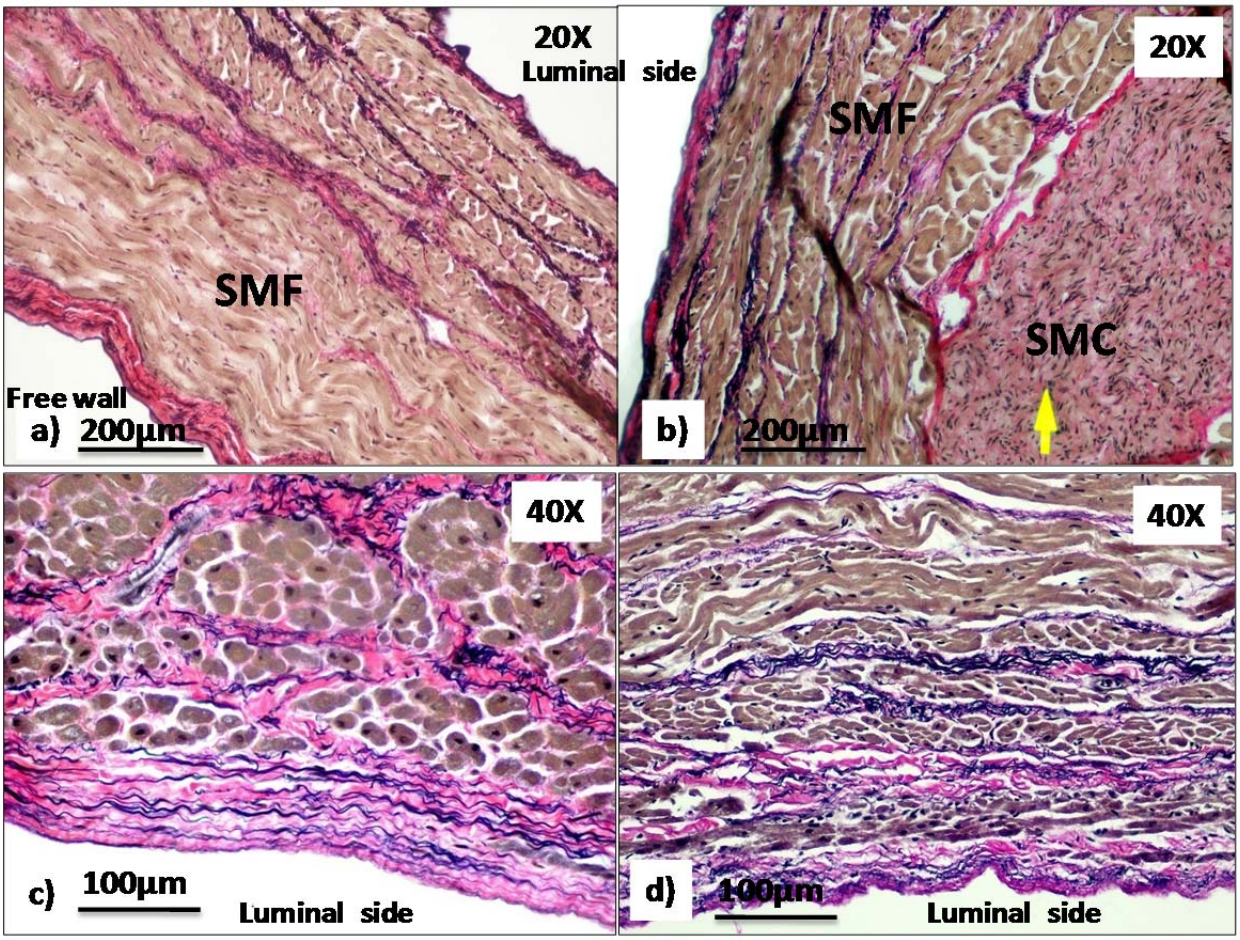

Figure 2-7: Circumferential-cut sections of a) the posterior (free wall) and b) the anterior wall of the CS. Close-up views of the CS at the luminal layer in the c) axial and d) circumferential axes. The arrow indicates smooth muscle cells (SMCs).

2.3.3 Constitutive Modeling

Material parameters and R-square values of seven individual specimens obtained from the four-fiber family model fit were summarized in Table 2. The model could capture the tissue response well with the mean R-square value of 0.914 ± 0.036. The parameters of P_Mean_Para and P_Mean_Exp_Data were also listed in Table 2.2.

Table 2-2. Material parameters for the four-fiber family model.

Specimen	Material parameters						R^2
	c (kPa)	$c_1^{1,2}$ (kPa)	$c_2^{1,2}$	$c_1^{3,4}$ (kPa)	$c_2^{3,4}$	α_0	
1	0.00E+00	3.94E-22	1.12E-07	31.36	0.51	31.60	0.996
2	1.85E+00	3.25E-21	1.36E-08	2.21	0.23	60.34	0.800
3	1.57E+01	1.16E-17	1.00E-02	1.66	0.66	46.29	0.816
4	8.97E+00	3.50E-21	2.31E+00	28.40	1.34	58.76	0.998
5	1.64E+01	2.76E-20	2.43E+00	5.43	3.37	49.18	0.970
6	4.30E+00	1.00E-05	1.00E-02	1.17	1.40	70.81	0.823
7	3.01E+00	2.71E-21	1.00E-02	2.51	1.22	53.17	0.995
Mean_Para	7.18E+00	1.43E-06	6.82E-01	10.39	1.25	52.88	0.914
Standard Error	2.52E+00	1.43E-06	4.36E-01	5.07	0.39	4.68	0.036
Mean _Exp_Data	1.30E+00	2.23E-17	1.87E-08	28.88	0.91	42.03	0.998

Illustrated in Fig. 2-8 was a comparison between the fits of two parameter sets. The fit was excellent for the P_Mean_Exp_Data parameters in both circumferential (solid line) and axial (long-dash line) directions. In contrast, the P_Mean_Para did not produce a desirable fit. It underestimated the axial direction and largely overestimated the fibers in the circumferential direction.

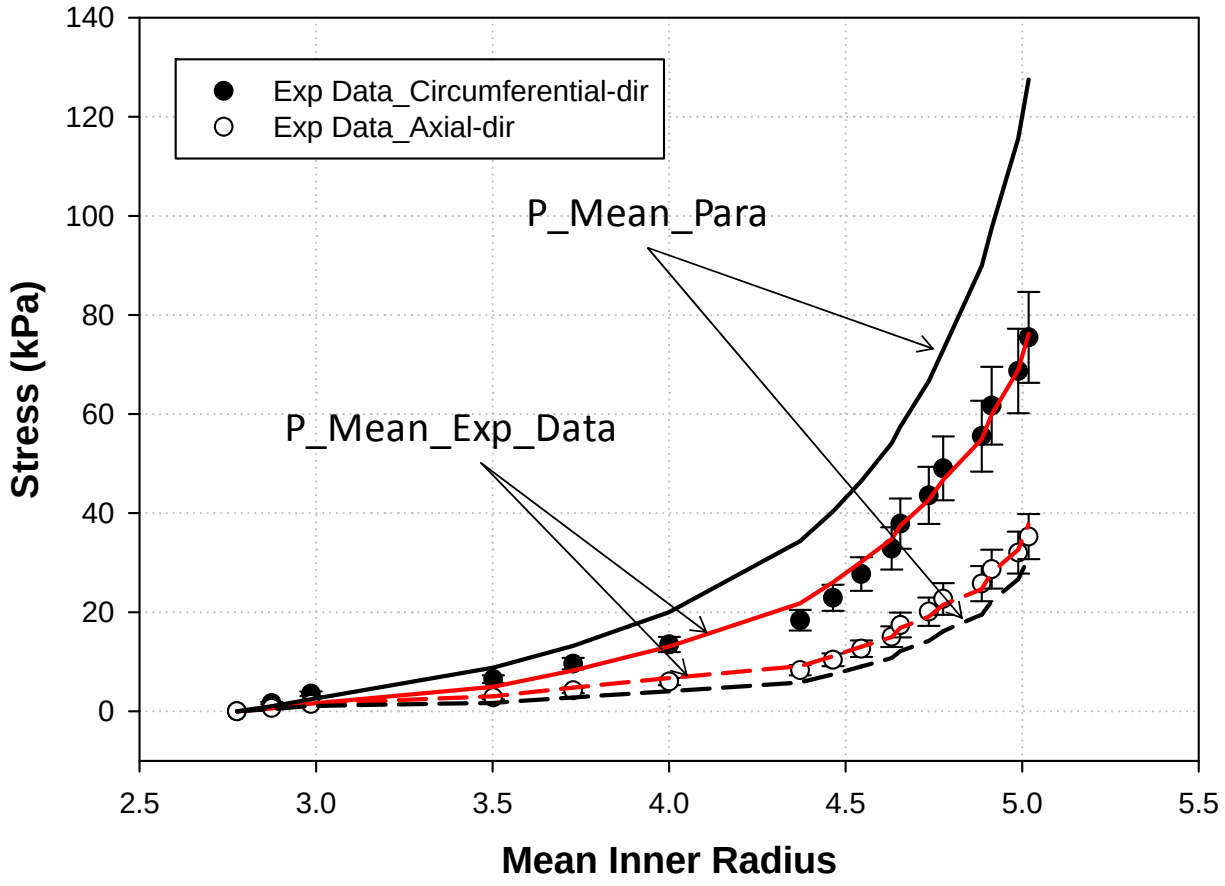

Figure 2-8: Fits of the mean experimental data of all seven specimens (P_Mean_Exp_Data) and mean parameters obtained from averaging individual parameters (P_Mean_Para). Solid lines are the circumferential fits and long-dash lines represent the axial. Fitting results show that parameters obtained from averaging experimental data (P_Mean_Exp_Data) provided a better fit. Data was expressed in terms of mean and standard error.

2.4 Discussion

Although mechanical properties of arteries have been studied extensively, there are relatively fewer studies on the mechanical properties of venous tissues [29, 89], and to our knowledge, none on the CS vessel. This is probably because the CS has seldom been treated as a load bearing tissue. Recent applications of PTMA devices for the treatment of MR utilize the CS as a hosting conduit for deployment and function of the devices. It is, thus, important to quantify the CS mechanical properties so that the CS tissue-device interaction can be better understood and the device failure as observed in Webb et al. [72] could be avoided in the future.

In this study, we observed that the CS pressure-diameter response is generally similar to many artery and vein responses [92-95]. The CS was very distensible at low pressures and became much stiffer when over physiologic pressure (see Fig. 2-5a). However, the difference between CS vessel and other vessels observed from our histological study was the presence of the high content of SMF in the CS wall, with a relatively lower content of collagen, elastin and smooth muscle cells. Apparently, the structural constituents of the CS were very different to that of a typical vein or artery, in which the collagen, elastin and smooth muscle cells are the premier constituents. Similar findings of SMF layers covering the CS were reported in the anatomical studies of human CS [81, 82]. It was argued that the CS vessel might be a small cardiac chamber that joins the other four chambers at the level of the crux cordis [81]. The histological structure obtained from this study appeared to concur that the CS may not be a cardiac vein, but rather a structural extension of the right atrial chamber because of the high content of SMF in the vessel wall.

The four-fiber family model is an extension of Holzapfel's two-fiber family model [90], which has been successfully utilized to model various blood vessel tissues [96-99]. In general, this model can capture the CS mechanical responses well. The model and the associated parameters obtained in this study can be implemented in numerical simulations to further investigate the tissue-implant mechanical interactions. The material constants of the model obtained from fitting of the experimental data might not

be unique. Multiple other sets of material constants may result in the same goodness of the fit. The issue of determinability of constitutive models has recently been discussed in Criscione 2004 and 2008 [100, 101]. A new set of kinematic tensor basis proposed by Criscione [100] might have the potential to overcome the covariance or coalignment issues inherent in the kinematical variables of strain invariant or Green strain based formulations.

Typically, the modeling approach with tissue micro-structure considerations, based on the pioneering work by Lanir 1979 [102], has employed either discrete [90, 103] or statistical distribution functions [104, 105] to describe orientations of tissue fibers. The four-fiber family model utilized the isotropic term for the tissue matrix substance and the anisotropic terms for the fibers at four assumed fiber directions. For the isotropic term, the parameter c represents the relative contribution of extracellular matrix (ECM). The mean value of 1.3kPa obtained in this study suggested the isotropic ECM played a significant role in CS wall responses. For anisotropic fiber responses, we observed that $c^{1,2}$ was close to zero. It indicated that axial and circumferential fibers have negligible contributions. However, fibers in the diagonal direction, represented by $c^{3,4}$, appeared to be responsible for most of overall tissue mechanical responses. Since we did not perform quantitative histology on the CS wall, a definitive correlation between the model predicted and actual fiber architectures cannot be established.

The response in the axial direction varied from contraction to extension at low to high stress, respectively. As showed in Fig. 2-6, the initial decrease in axial stretch at low stress occurred simultaneously with the dramatic increase in the circumferential stretch. This behavior might be due to the tissue incompressibility, or volume preservation. However, as the CS wall consists of complex multi-layer nonlinear, anisotropic tissue structures, the coupling between axial and circumferential directions could be more complex than that due to the tissue volume preservation.

In our estimation of the CS wall stress, we utilized the ideal cylindrical model. However, the CS wall has an oval shape due to the partial attachment to surrounding myocardium (see Fig. 2-3a). During the inflation tests, the averaged minor to major axis ratio of the CS vessel was 0.48 at 5 mmHg, 0.7 at 20mmHg, 0.85 at 50 mmHg and 0.93 at 80 mmHg. Using the cylindrical model in data analysis is a way

to represent the averaged stress in an oval shape. A precise estimation of stress in an oval shape should be as follows: Let m and n equal the semi-axes of an oval shape, with n > m. The minimal and the maximum stresses in the oval shape are $\sigma_{min} = \frac{Pm}{h}$ and $\sigma_{max} = \frac{Pn}{h}$, respectively, and the stress in between at the point (x, y) can be obtained by $\sigma(x,y) = \frac{P}{h}\left(y\frac{\partial x}{\partial s} + x\frac{\partial y}{\partial s}\right)$, where s is the arc length on the oval shape. By the cylindrical model, we used $\sigma = \frac{P(m+n)}{2h}$, which is the mean value between the maximum and minimal stresses. Thus, the maximum error we could have with the cylindrical model is $\sigma_{err} = \frac{P(n-m)}{2h}$, which is located at the minor and major axes of the oval shape. Based on the minor to major axis ratios during the inflation test, the maximum errors in the stress estimation were 26% at 5 mmHg, 15% at 20 mmHg, 7.5% at 50 mmHg and 3.5% at 80 mmHg. To convert them into actual stress values, they were 0.63, 1.78, 3.39 and 2.63 kPa at 5, 20, 50 and 80 mmHg, respectively.

There are some limitations in this study. First, the sample size is small. We only performed experiments on seven porcine hearts. A larger number of specimens may provide a more statistical power in analyzing the data. Also, the extrapolation of the porcine CS mechanical properties to the human CS is currently unknown. A study of human CS tissue properties is currently ongoing in our lab. We hope that in the near future we could compare human and porcine data, and use them to explain why PTMA devices respond differently in animal and human clinical trials [27, 72, 73, 106-108]. Lastly, we only studied passive behaviors of the CS vessel. The *in vivo* observation by Barcelo *et al.* [81] using cine digital CS angiography showed the reduction of the CS's diameter during the cardiac cycle, where the maximal diameter was observed at the ventricular systole, intermediate diameter during diastole and the minimal diameter at the atrial systole. This diameter change may be caused by active contraction of myocardial fibers or simply by the pressure change during the cardiac cycle. The further investigation on this phenomenon is also necessary.

2.5 Summary

In this Chapter, we presented a study of biomechanical characterization of porcine coronary sinus. Under a 80 mmHg pressure-only loading condition, the CS vessel exhibited a S-shape pressure-radius response and could be dilated up to 88%. The model fitting results indicated that the four-fiber family model could capture the experimental data well. From the histology study, we observed abundant SMFs covering the CS and also within the CS vessel wall, while smooth muscle cells are very low in content. The elastin and collagen fibers are highly concentrated in the luminal and outer layers of the CS wall, but sparsely distributed in the medial layer. In future studies, we will conduct finite element analysis of the interaction between the CS vessel and the proximal stent, utilizing the mechanical properties of the CS vessel obtained in this study. We may also conduct the mechanical characterization of human CS using cadaver tissues. Nonetheless, this study represents one of early steps towards a complete understanding of the PTMA intervention and analysis of device failures observed in current clinical trials.

3 Comparison of Biaxial Mechanical Properties of Coronary Sinus Tissue from Porcine, Ovine and Aged Human*

In this chapter, the material property characterization of the CS vessel using planar biaxial testing method will be introduced. Pre-clinical studies of PTMA devices often use animal models (i.e. porcine, ovine and canine) to obtain either acute or short-term animal trial outcomes. However, compare to pre-clinical animal studies, human clinical outcomes were sub-optimal. To investigate underlying causes of the discrepancy between the animal and human results, in this chapter, the CS tissue properties of human were compared to ones of porcine and ovine and human models. The CS tissues were subjected to multi-protocol biaxial tests and characterized by the Fung-type elastic model. Histological analysis was also performed to compare the difference in tissue microstructure among porcine, ovine and aged human CS tissues.

---

* The contents of this chapter were partially published in
T. Pham and W. Sun, Comparison of biaxial mechanical properties of coronary sinus tissues from porcine, ovine and aged human species, **Journal of the Mechanical Behavior of Biomedical Materials 6**: 21-29 (2012).

3.1 Introduction

Quantification of the mechanical properties of the CS vessel is critical for estimating the tissue-implant biomechanical interaction and for understanding device failure mechanisms. Although the anatomical studies of the CS have been well reported [81-83], there is a dearth of study on the mechanical properties of the tissue. Recently, Pham and Sun [109] reported the diameter-pressure relation of porcine CS from a vessel inflation experiment. There are two limitations in the paper: 1) the experiment was conducted under relatively simple pressure inflation loading conditions, and 2) only the porcine CS was examined. Due to complex tissue-device interactions, quantification of tissue behaviors under multi-axial loading conditions may be needed. Moreover, a study of CS tissue properties from different species (i.e., porcine, ovine and human) may be helpful in understanding the outcomes among animal trials and human studies, and establishing a proper animal model to evaluate the device efficacy.

3.2 Materials and Methods

3.2.1 Materials

The human cadaver CS tissues were selected from an age group of 86.5 ± 9.7 years old. Human cadaver hearts were obtained from Cardinal Biologicals, Inc. (Tyler, TX; n = 2) and National Disease Research Interchange (NDRI, Philadelphia, PA; n = 8). The use of human tissues was approved by the Institutional Review Board at the University of Connecticut. The hearts were fresh frozen within a post-mortem recovery interval (15.32 ± 6.51 hours) and remained frozen until delivery on the next day. All hearts were stored in a -80˚C freezer and were taken out individually for testing within 3 months. Porcine hearts (n = 10, 6 - 9 months old with a weight range of 418.60 ± 71.81 g) from the Animal Technologies, Inc. (Tyler, TX) and sheep hearts (n = 10, 1 year old, 280.08 ± 28.17 g) from the Brother Quality, Inc. (Stafford Springs, CT) were obtained fresh and stored in a -80˚C freezer until testing within 2 weeks.

Following the two-stage slow thawing method proposed by Bia et al. to void tissue damages [110], each heart was held at room temperature (20˚C) for 30 minutes and then submerged in a 37˚C water bath until totally defrosted. The entire CS vessel could be removed from the heart because only the anterior section of the vessel is partially embedded in the myocardium, as shown in Fig. 3-1. After carefully procuring the vessel and removing the excess tissues (e.g. fat and loose connective tissues), a square specimen, about 15 mm in length, and at a region near the CS ostium end (or the proximal section), was excised for testing, see Fig. 3-1. The tissue thickness was measured at six regions with a thickness gauge (Mitutoyo, Model 7301) and the average value was recorded. Four small graphite markers were placed at the center on the inner surface of the posterior (i.e., myocardium-free) section of the CS vessel to demarcate a small quadrilateral for strain calculation.

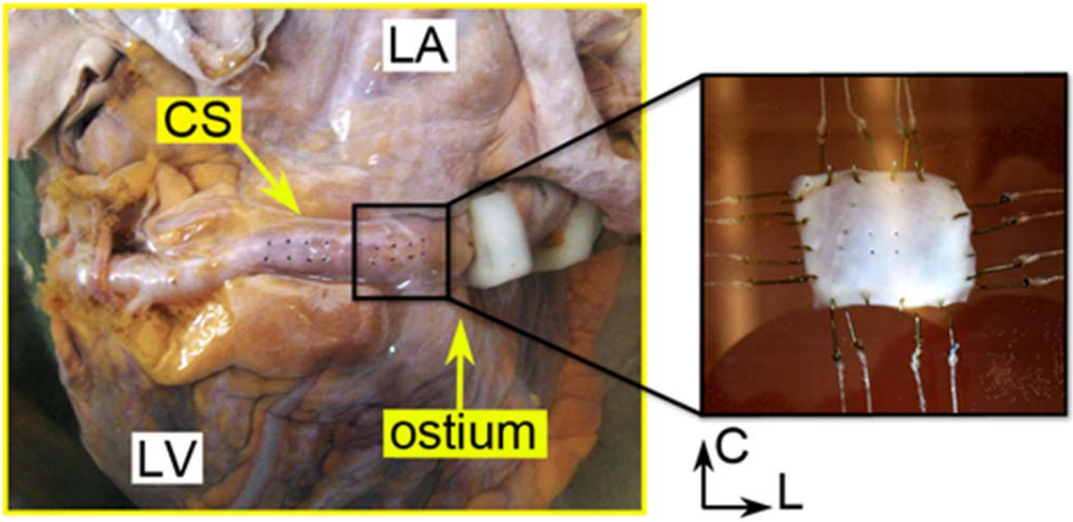

Figure 3-1: The anatomy of the intact coronary sinus (**CS**) vessel showing the excised location for biaxial testing. The image on the right shows the CS specimen mounted in the biaxial machine bath. **C** - circumferential, **L** - longitudinal, **LA** - left atrium, **LV** - left ventricle.

3.2.2 Planar Biaxial Mechanical Testing of CS tissues

Details on planar biaxial mechanical testing techniques and methods of analysis adopted in this study can be found in Sacks and Sun 2003 [38]. Briefly, all specimens were mounted in a trampoline

fashion, and the vessel circumferential and longitudinal directions were aligned with the primary axes of the biaxial test fixtures. Human tissue samples were tested in a Ca^{2+}-free phosphate buffered saline (PBS) solution at 37°C. Due to their young age and relatively high muscle content, animal tissue samples were tested in a Ca^{2+}-free and glucose-free Tyrode solution (mM: NaCl 136.9, KCl 2.7, MgCl2 1.05, NaHCO3 11.9, NaHPO4 0.47, EGTA 2.0, and 0.1M papaverine) at 37°C. Using Ca^{2+}-free solution is to minimize the active contraction of muscle fibers in order to obtain the passive mechanical properties of the CS vessel. Adding EGTA, a chelating agent with a high affinity for Ca^{2+}, would actively remove the intracellular Ca^{2+} concentration. The similar protocols have been used in studies of passive blood vessel mechanical properties [111-115]. As reported by Tritthart *et al.* [116], exposing Ca^{2+}-free solution several times in succession could have a comparable result as to the EDTA-containing solution. A stress-controlled test protocol was utilized [117], wherein the ratio of the normal Lagrangian stress components $T_{11} : T_{22}$ was kept constant with $T_{12} = T_{21} = 0$. Maximum load was applied without causing tears at the edges of the specimens. Preconditioning was performed to minimize tissue hysteresis. Each tissue specimen was preconditioned for at least 40 continuous cycles with $T_{11} : T_{22} = 1 : 1$. Seven successive protocols were performed using ratios $T_{11} : T_{22} = 1 : 0.3$, 1 : 0.5, 1 : 0.75, 1 : 1, 0.75 : 1, 0.5 : 1, and 0.3 : 1. This range was chosen for extensive coverage of the in-plane strain state [38]. All specimens were cryopreserved [110] after biaxial testing and stored at -80°C.

3.2.3 Histology

The structural constituents of the CS vessel, primarily elastin, collagen, and muscle fibers, were analyzed across the thickness. After thawing and removing the cryoprotectant agent following a protocol proposed by Bia et al. [110], tissue specimens were fixed in 10% formalin for 24 hours. Each sample was dehydrated through a process of varied alcohol concentrations, embedded in paraffin, and sectioned at 5 μm in thickness. Samples were then mounted on microscope slides and dried. After deparaffinization, slides were then stained with Verhoeff Van-Gieson (VVG). Elastic fibers could be visualized as black

strands, collagen fibers as red, muscle fibers as a duller red or light brown color. Histological images were obtained from an Olympus U-TVO.5xC digital camera coupled to an Olympus BX40 light microscope.

3.2.4 Constitutive Modeling

The coronary sinus tissue was assumed to be homogeneous, non-linear hyperelastic and anisotropic. Therefore, the Fung-type elastic model [29] was used to characterize the biaxial experimental data. The in-plane second Piola-Kirchhoff stresses, *S*, were derived from a strain energy function *W*,

$$S_{ij} = \frac{\partial W}{\partial E_{ij}} \tag{3.1}$$

where E_{ij} is the Green-Lagrange strain tensor and *W* is expressed as:

$$W = \frac{c}{2}\left(e^{Q} - 1\right) \tag{3.2}$$

and *Q* as:

$$\mathrm{Q} = A_1E_{11}^2 + A_2E_{22}^2 + 2A_3E_{11}E_{22} + A_4E_{12}^2 + 2A_5E_{11}E_{12} + 2A_6E_{22}E_{12} \tag{3.3}$$

with *c* and $A_{1\text{-}6}$ are material parameters.

The constitutive model was fit to the seven stress-controlled protocols for each individual specimen to obtain the material parameters. The goodness of the fit was determined by the R-square value based on the nonlinear regression Levenberg-Marquardt algorithm in SYSTAT 10 (Systat Software Inc., Chicago, IL). Each parameter set was tested for convexity using the method in Sun and Sacks 2005 [118]. Variation of the parameters is presented in terms of the standard deviation.

3.2.5 Data Analysis

The mechanical properties of the human CS were quantified and compared to those of ovine and porcine CS tissues. The tissue stiffness was investigated by means of the secant modulus at a low stress value of 15 kPa and a high stress value of 50 kPa. One of the human CS specimens (Specimen 2) has a maximum testable stress below 35 kPa in both the circumferential and longitudinal directions, therefore, was omitted in the stiffness analysis at 50 kPa.

To quantify the degree of anisotropy (DA) among the specimens, the ratio of circumferential to longitudinal strains at 15 and 50 kPa stresses from the equibiaxial protocol ($T_{11} : T_{22} = 1 : 1$) was used. Thus, DA = $E_{22} : E_{11}$. A DA value of 1 indicates an isotropic tissue response, whereas other values represent various degrees of anisotropy. In addition, the relationship between age and 1) thickness, 2) stiffness, and 3) maximum equibiaxial strain in human specimens were also investigated.

3.2.6 Statistical Analysis

Differences between means were determined using the analysis of variance (ANOVA) test followed by the Holm-Sidak test and the Dunn's Method test for pair-wise multiple comparisons. The Independent two-sample t-test was used to determine significant differences in anisotropy. Non-parametric tests, including the Wilcoxon signed-rank test and Mann-Whitney rank sum test, were used for non-normal distributed sample groups. Correlation was determined using the Pearson's correlation coefficient (r), and p-values were calculated based on the aforementioned statistical tests. All values of measurement are presented as a mean ± standard deviation. A probability value less than 0.05 was considered statistical significant, with high significance indicated by $p < 0.001$. Statistical analyses were performed using SigmaPlot (V11.0, Systat Software Inc., San Jose, CA).

3.3 Results

3.3.1 Patient characteristics and specimen thickness

Table 3.1 lists characteristics of human hearts investigated in this study, including patient age, gender, cause of death, primary disease, and risk factors. The thickness of all CS specimens was determined. Human (0.74 ± 0.16 mm) and ovine (0.78 ± 0.12) were not significantly different ($p = 0.537$). However, porcine CS (1.24 ± 0.18) was significantly thicker than human ($p < 0.001$) and ovine ($p < 0.001$).

Table 3-1. Anamnesis of patients.

	Specimens										
	1	2	3	4	5	6	7	8	9	10	Mean ± SD
Age (yrs)	69	88	78	96	95	79	98	87	80	95	86.5 ± 9.70
Sex	M	F	M	F	F	F	F	F	F	M	-
PMR (hr)	22	11	10	21	7	11	18	8	21.5	23.7	15.32 ± 6.51
Cause of death	HB	Alz	CPA	CPA	RA	CPA	RA	Alz	ukn	NC	-
Primary disease	HB	CAD	CA	ukn	ukn	Hyp	ukn	ukn	PKD	n	-
Risk factors											
Hypertension	y	n	y	n	n	y	n	n	n	n	-
Cholesterol	n	n	n	n	n	n	n	n	n	n	-
Diabetes	y	ukn	n	n	n	ukn	y	n	n	n	-
GERD	n	y	n	n	n	n	n	n	n	n	-
Pneumonia	n	n	n	n	y	n	n	n	n	n	-
Dementia	n	n	n	n	n	n	n	y	n	n	-
Atherosclerosis											
Coronary	n	y	n	n	n	n	n	n	n	n	-

PMR = post-mortem recovery time, **Alzheimer's** = Alz, **CA** = cardiac arrest, **CAD** = Coronary artery disease, **CHF** = Chronic heart failure, **CPA** = Chronic pulmonary aspergillosis, **COPD** = Chronic obstructive pulmonary disease, **GERD** = Gastroesophageal reflux disease, **HB** = Heart blockage, **Hyp** = Hypertension, **NC** = Natural causes (old age), **RA** = Respiratory arrest, **PKD** = Polycystic Kidney Disease, **ukn** = unknown.

3.3.2 Biaxial mechanical behavior

Individual equi-biaxial responses for ten human CS vessels are plotted in Fig. 3-2-A&B. There was a large variation in mechanical responses in both circumferential and longitudinal directions within the human samples, particularly the circumferential response which varied the most from a minimum strain of 0.18 in Spec 6 to a maximum of 0.45 in Spec 7. At low stress, the circumferential direction was

very extensible, while the longitudinal direction stiffened more rapidly at low strain. At high stress above 20 kPa, the tissue response in both directions exceeded the typical "toe" region and exhibited rapid stiffening.

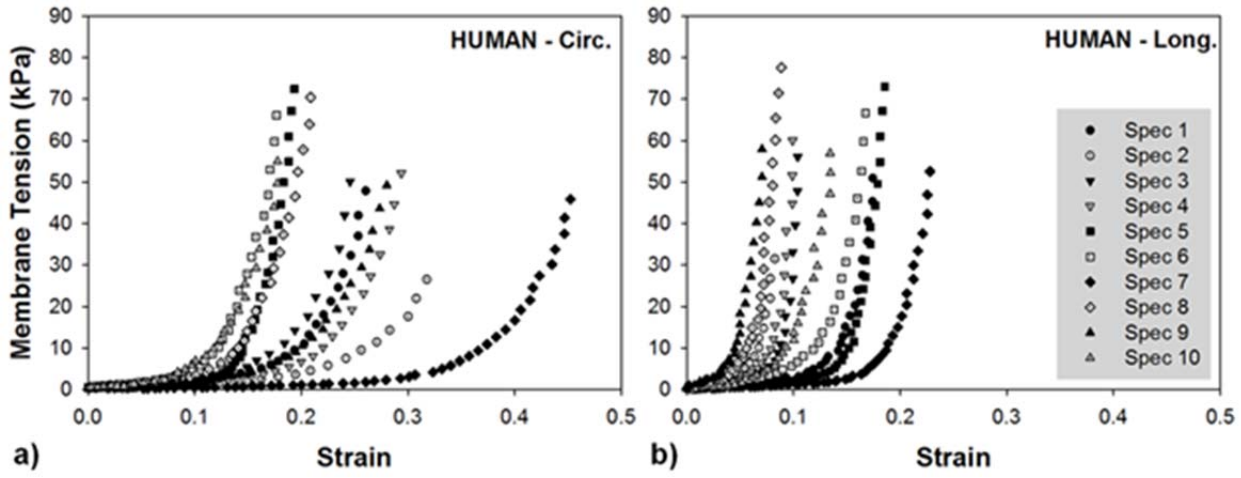

Figure 3-2: Equibiaxial results of ten human coronary sinus specimens in a) the circumferential (**Circ.**) and b) longitudinal (**Long.**) directions.

To compare the stress-strain responses of human, ovine and porcine specimens, mean response curves for each species are plotted in Fig. 3-3. All tissues exhibited the nonlinear stress-strain behavior of a typical blood vessel. However, a more gradual transition from low to high stiffness regions was observed in ovine and porcine, while human CS had a more pronounced rapid stiffening effect at the transitional region in both directions.

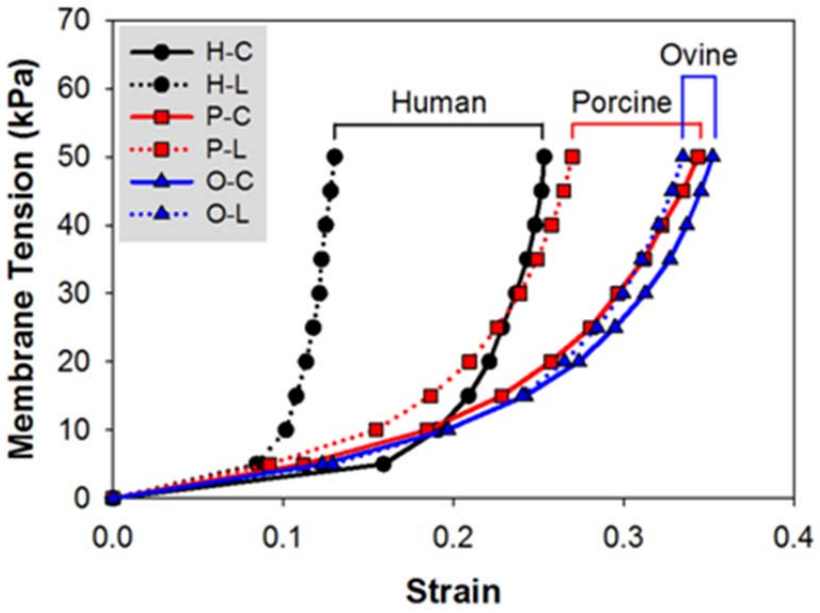

Figure 3-3: Mean equibiaxial responses of human (**H**), porcine (**P**) and ovine (**O**) CS tissues in the circumferential (**C**) and longitudinal (**L**) directions.

Differences in tissue properties among the species were examined by means of the secant moduli at stress levels of 15 and 50 kPa. In Fig. 3-4, a statistically significant difference was found between human and ovine ($p < 0.001$ at 15 kPa and $p = 0.001$ at 50 kPa) and between human and porcine ($p = 0.002$ at 15 kPa and $p = 0.003$ at 50 kPa) in the longitudinal direction. Ovine and porcine tissues did not differ at either stress level ($p = 0.449$ at 15 kPa and $p = 0.437$ at 50 kPa). For the circumferential response, only human and porcine tissues were significantly different at 50kPa, with $p = 0.024$.

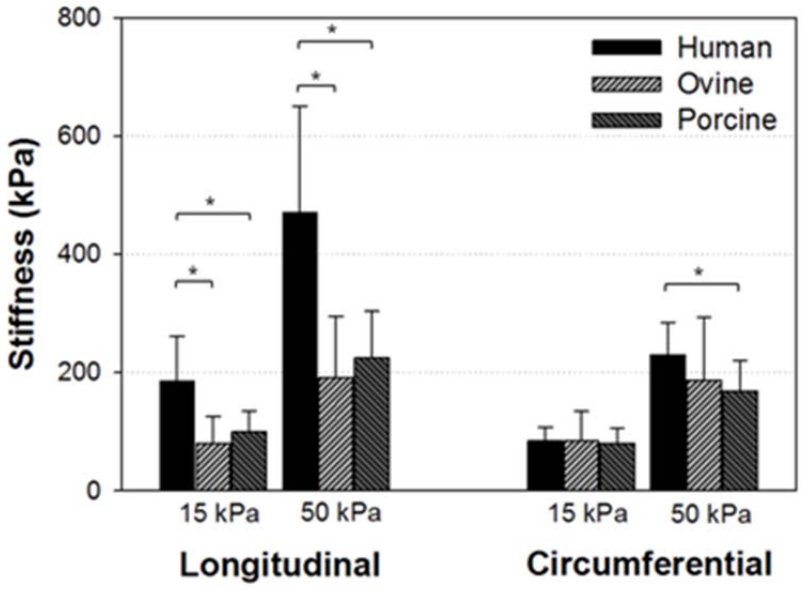

Figure 3-4: Tissue stiffness computed at membrane tensions of 15 and 50 kPa, comparing between human, ovine, and porcine tissues. (*) indicates the statistical significant difference between the two pairs. Data are presented as mean and standard deviation.

The DA value by means of the strain ratio at a stress of 50 kPa was determined. The anisotropy of human tissues (0.59 ± 0.26) was greater than those of porcine (0.78 ± 0.15) and ovine (1.02 ± 0.37). Ovine tissue exhibited a nearly isotropic response, which can be seen in Fig. 3-3. To further analyze the tissue anisotropy, a paired-t test was used to quantify the association between the two directions of each species. Human and porcine exhibited a statistically significant anisotropy with $p = 0.004$ and $p = 0.002$, respectively, while ovine tissues did not show anisotropy, $p = 0.618$.

Statistical analysis did not reveal any correlation between age and thickness, stiffness, and maximum strain in human specimens. Though there was not enough data to group the results based on medical conditions, equibiaxial data did show that stress-strain curves of three hypertensive patients were shifted to the left of the data range (Fig. 3-2).

3.3.3 Constitutive Modeling

The constitutive parameters for each species are summarized in Table 3-2. The Fung-type elastic model was able to capture the CS planar biaxial mechanical behavior well with the high R-square (R^2) value of 0.95 ± 0.03 for human, 0.93 ± 0.09 for porcine and 0.93 ± 0.05 for ovine. Representative curve fitting plots of human, ovine and porcine CS are shown in Fig.3-5.

Table 3-2. Fung model parameters for human, ovine and porcine CS specimen. Data are presented as mean ± standard deviation.

Specimen	C	A1	A2	A3	A4	A5	A6	R^2
Human	0.47 ± 0.28	28.62 ± 12.94	76.10 ± 30.76	1.99 ± 7.69	48.80 ± 16.52	-0.10 ± 4.08	-2.79 ± 8.66	0.95 ± 0.03
Ovine	6.22 ± 3.07	9.22 ± 8.77	12.28 ± 14.31	0.45 ± 3.86	10.82 ± 12.43	-0.25 ± 1.12	-0.24 ± 1.78	0.93 ± 0.05
Porcine	7.99 ± 10.17	4.17 ± 2.29	9.85 ± 6.45	1.59 ± 2.43	6.84 ± 2.97	-0.14 ± 0.56	0.20 ± 0.44	0.93 ± 0.09

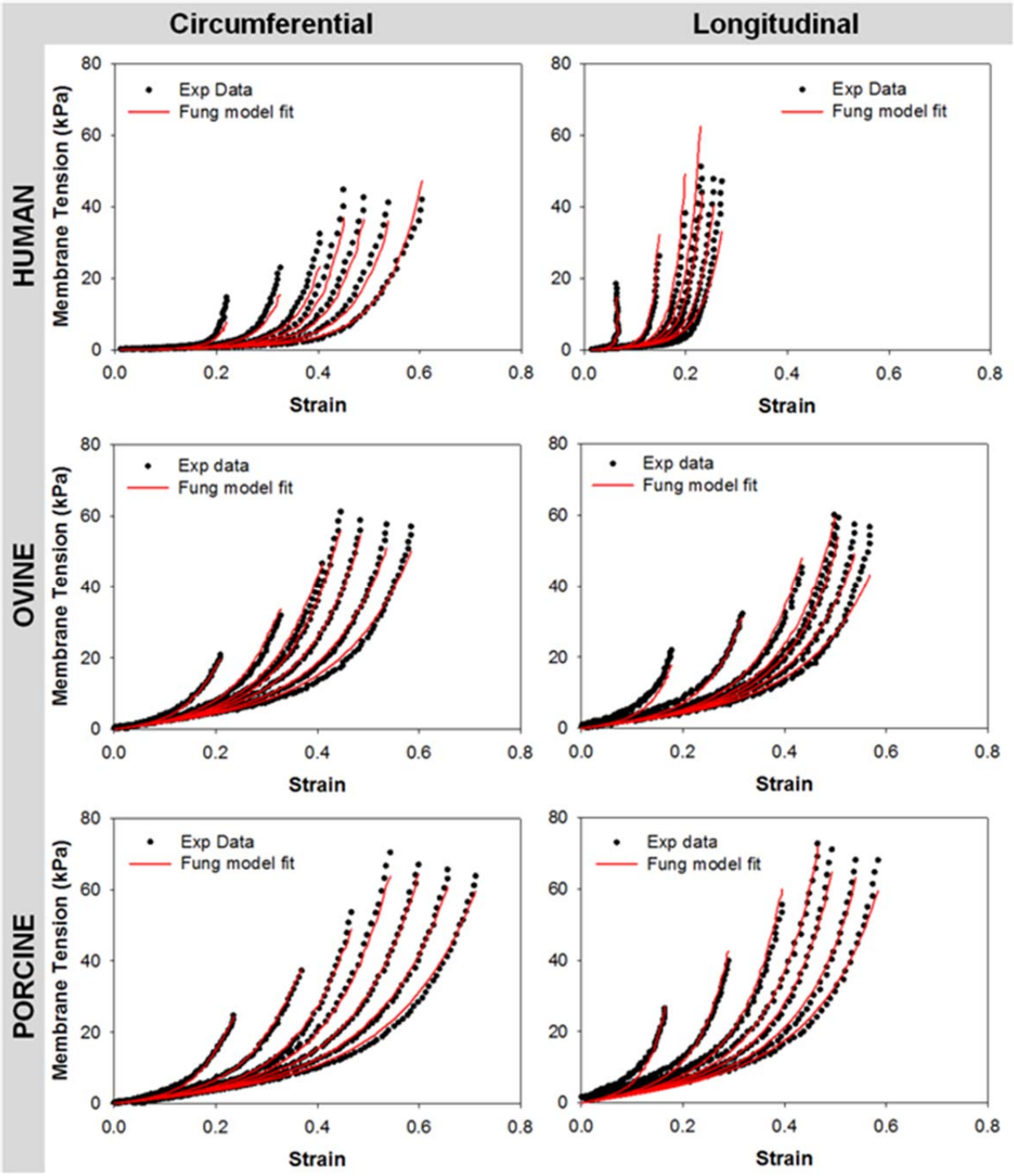

Figure 3-5: Representative stress-strain response data for human (top row), ovine (middle row) and porcine (bottom row) CS tissues (dot lines) fitted with Fung elastic model (red lines). **CIRC** - circumferential direction, **LONG** – Longitudinal direction.

3.3.4 Histology

Differences in the microstructure between human, ovine and porcine specimens can be seen in Fig. 3-6. In Fig. 3-6, the circumferential histology images of CS posterior section of each species showed differences in the content of striated muscle fibers (SMFs) and elastic constituents. The intima layer of aged human CS tissues was composed of a highly dense network of collagen fibers which intertwined with longitudinal elastin fibers. It was prominently thicker than those of younger ovine and porcine tissues. The decrease in wall media in human tissues was accompanied by a significant decrease in the SMFs and a noticeable increase in collagen fibers. Elastin were found to be abundant in both the internal elastic lamina and the media but organized in multiple fragmented layers. In contrast, elastin fibers as well as collagen were less developed in younger ovine and porcine tissues.

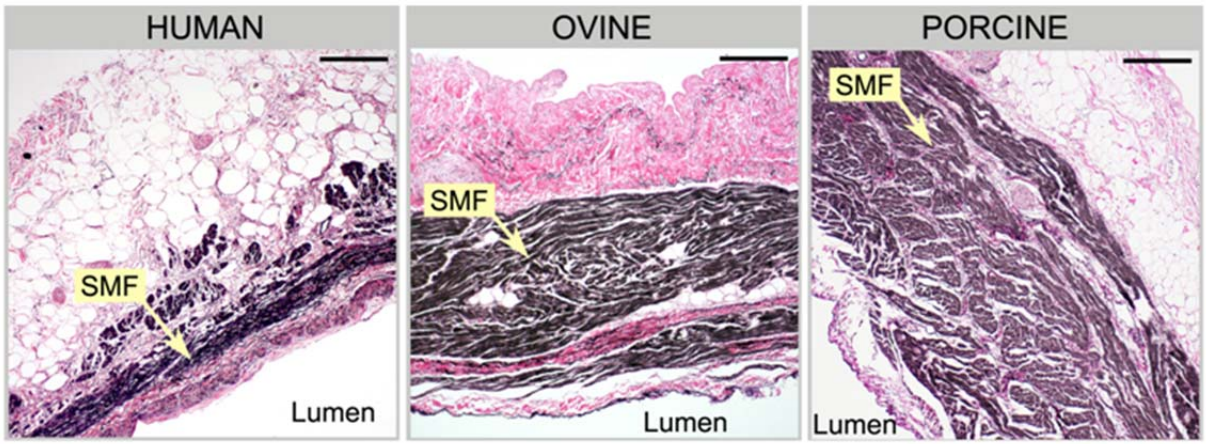

Figure 3-6 – The cross-section histological results of human, ovine, and porcine posterior CS sections in the circumferential direction. Human CS is thinner with less striated myocardial fibers (**SMF**) and exhibits a higher elastin/collagen contents than ovine and porcine CS in the intima layer. Black fibers - elastin, pink fibers - collagen, brown fibers - striated myocardial fibers. (x100 Magnification, bar length is 200 μm).

Studies on the CS anatomy reported a continuous cuff of striated muscle surrounding the external wall of the CS vessel [81, 82]. Similar structure was observed in all specimens. However, in human CS tissues, the striated muscle cuff is scarcely distributed around the posterior wall, that is the free-wall

region of the CS. In contrast, the muscle cuff covered the posterior sections and accounted for the majority of the wall thickness in both ovine and porcine tissues. The anterior section of the CS wall for human, ovine, and porcine tissues was composed mainly of the striated muscle fibers with dispersed elastin and collagen fibers.

3.4 Discussion

3.4.1 Anatomical differences

Several anatomical differences of the coronary venous vasculature between human, porcine and ovine species were observed. First, the oblique vein of Marshal (OVM) of the left atrium is found in human while the left precaval vein (LPV) is seen in both porcine and ovine, see Fig. 3-7. Both the OVM and LPV are remnants of the left superior vena cava. The LPV is completely patent and its diameter is larger than that of the OVM, but they both have the same function, which is to drain blood into the coronary sinus. The porcine LPV is found to be the largest and appears to be a continuation of the CS. The larger LPV, in some cases, resulted in a reduction of CS length and a wider junction of the LPV, GCV and CS. This could possibly prompt stent slippage due to lack of anchoring if positioned near the junction. Second, the GCV was observed to be narrowest in porcine, and the ovine GCV was smaller but similar in size to the human GCV. For the distal anchor of the PTMA device to be deployed, the GCV diameter needs to be equal or larger than 3 mm [80]. The porcine GCV appeared to be smaller than 3 mm in diameter and might not be suitable for the distal anchor deployment. Lastly, a high variation in the location of the left circumflex artery (LCX) was observed in all species, suggesting a careful imaging assessment prior to the procedure is necessary to reduce LCX perforation and impingement in the coronary flow in all species.

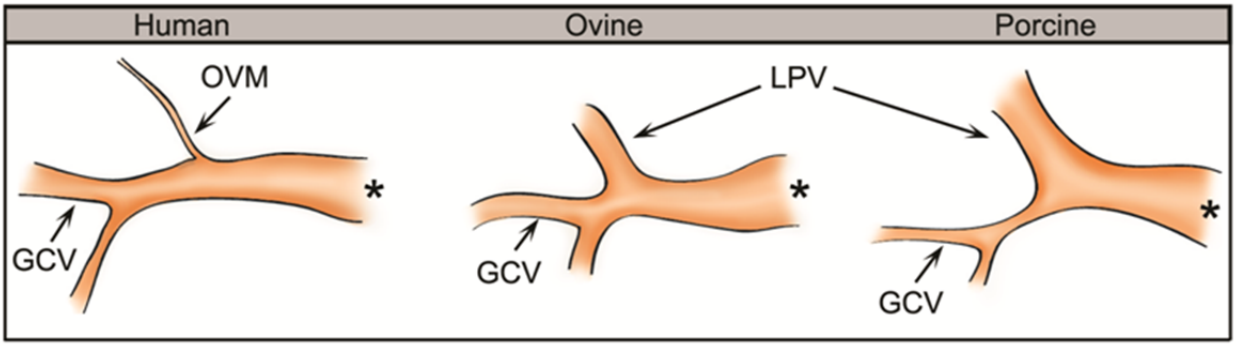

Figure 3-7 A sketch of the tributaries of the coronary sinus vessel, showing the tapered oblique vein of Marshall (**OVM**) in human and the patent left precaval vein (**LPV**) in ovine and porcine tissues. The great cardiac vein (**GCV**) of porcine is narrowest among the three species. (*****) indicates the ostium of the CS vessel.

3.4.2 Mechanical properties and implications of PTMA intervention.

Our results showed that the excised human CS stress-strain relationship is non-linear and anisotropic with the circumferential direction being more compliant. When comparing with ovine and porcine CS tissues, human tissues were found to be stiffer and highly anisotropic. High stiffness of human CS tissues might be accounted for by the advanced age of the patients selected in this study (86.5 ± 9.7 years). Tissue stiffness has been shown to increase with age due to the degeneration and fragmentation of elastin fibers [119] and an increase of collagen content [120, 121] which were observed in our human CS tissues. Therefore, it is possible that the mechanical properties of older porcine and ovine CS tissues more closely resemble those of an aged human, although this has not been assessed.

Animal models were first tested to evaluate the feasibility of the PTMA devices for the treatment of MR. Previous studies using ovine models demonstrated the feasibility of PTMA devices in reducing MR. However, for the human trials of three PTMA devices reported in 2006 and 2007, the results were suboptimal. Specifically, Webb et al. [72] reported fracture of the device bridge element in three of four patients implanted with a permanent Monarc PTMA device. Duffy et al. [73] observed that the distal anchor of a Carillon PTMA device did not hold tension during device traction in two of five temporarily

implanted patients. Dubreuil et al. [79] reported temporary placements of a Viacor PTMA device in patients with an ischemic MR and MA dilation. They found that the MA diameter after the device implantation remained large compared to the surgical annuloplasty results. A more recent study in 2010 on the second generation Monarc PTMA device reported a reduction in MR by ≥ 1 grade at 12 months in 50% of 22 implanted patients [80]. Unsuccessful implantations were associated with the lack of appropriately-sized devices (n = 13), inaccurate device positioning resulting in no MR reduction (n = 4), device migration (n = 1) and fracture of the proximal anchor (n = 4). Thus, the success of PTMA animal trials was not reflected in human trials. Even though doubts always exist regarding the validity of animal models and their applicability to humans, there is clearly a lack of scientific evidence and engineering quantification of the discrepancy between animal and human trials.

In this chapter, we observed substantial differences in material properties between the animal and human CS, where the animal CS tissues were more compliant and deformable than the human ones. This indicated that the biomechanical environment in which the PTMA device is embedded was different in animals and humans. Therefore, the PTMA device might function well in animal models due to a relatively low tissue-stent interaction force. In contrast, under the stiffer mechanical environment in humans, the PTMA device may experience a higher interaction force which could possibly affect its durability. This observation underscores the importance of having an appropriate animal model for evaluating device function for its ultimate use in human.

3.4.3 Limitations and future study

The age range for the majority of MR patients is 60-70 years. In this study, our patient group is 87 ± 10 years old. The material properties of soft tissues were known to be stiffer with age and diseased cardiac tissues are age-related. However, in this study, we did not study the influence of age on the human CS tissues and only compared the available aged human group to animal types. In addition, due to limited access to fresh human tissues, in this study, we used fresh frozen human tissues. To facilitate the

comparison of human, porcine and ovine tissues, we also froze fresh porcine and ovine tissues at -80°C prior to biaxial mechanical testing. Thus, by utilizing a similar freezing protocol for all of our samples, we could avoid inconsistency in tissue storage. Nonetheless, the fact that we do not have fresh human tissue is a limitation of this study.

Our histological analysis showed that CS is non-homogenous and composed of layers of constituents (elastin, collagen, and striated myocardial fibers). In this study, the CS was modeled as a single-layer homogenous structure. A multiple layered material model incorporating structure-motivated phenomenon might provide a more accurate estimate of layer-specific material properties [122]. Other imaging methodologies such as scanning electron and two-photon laser scanning confocal microscopy might be helpful for collagen and fiber structural analysis (e.g., the fiber diameter and undulation period), to further correlate the structural findings with the mechanical properties of the vessel. Moreover, PTMA devices interact with the CS wall as well as the surrounding tissues, i.e., the mitral annulus, leaflets, chordae tendineae and the adjacent myocardium. To fully evaluate the PTMA device function, the mechanical properties of these interposed tissues, besides the CS wall, need to be quantified as well. Lastly, the sample size for each species in this study was relatively small; a larger sample size would provide more conclusive results.

3.5 Summary

We observed a discrepancy in mechanical and microstructural properties of CS vessels in aged human, ovine and porcine species. Overall, the human CS vessels were stiffer in both the circumferential and longitudinal directions than the ovine and porcine CS vessels. Higher collagen, lesser SMF, and fragmented elastin fibers found in human CS tissues demonstrated the effects of aging. This study also showed that the mechanical properties of CS tissues varied largely among patients. PTMA device studies involving animal models should be evaluated carefully given the distinguishable mechanical and structural differences between aged human, ovine, and porcine CS vessels obtained in this study.

4 Quantification of Tension to Cinch the Mitral Annulus Through the Coronary Sinus*

As mentioned in Chapter 1, PTMA device's main function is to shrink or cinching the mitral annulus to reduce the dilated mitral annulus, thus improve MR. Currently, there is a lack of information on the magnitude of the cinching force required to shrink the mitral annulus. In addition to the structural and material property characterizations of the CS vessel conducted in Chapter 2 and Chapter 3, in this chapter, an ex vivo whole heart study was performed. An novel experimental setup was developed to obtain the relation between cinching force, via the CS vessel imbedded in the heart, and mitral annular area reduction, using a ovine model.

4.1 Introduction

Previous investigation on MA mechanics demonstrated the tension was lower in the commissural section (17.8 N/m) compared to anterior (40.0 N/m) or posterior (30.6 N/m) sections of the annulus [123-126]. These studies offered insights into the underlying mechanism of annular dilatation. Annuloplasty complicates the annular mechanics by undersizing the dilated MA geometry [127]. Some studies measured the forces generated by the myocardium on a prosthetic device and correlated them with changes in MA geometry. The maximum in-plane MA force generated by the myocardium on a rigid annulplasty ring in a porcine mitral valve was 6 – 8 N at mid-systole[128]. The influence of a flexible ring was studied in swine models and the maximum force was in a range of 4.4 – 13.9 N [129]. Later, the development of saddle-shape bioprosthetic valve represented a novel advance in design to reduce the leaflet stress [130-133]. In a comparative study, the forces on the anterior and commissural annular

* The contents of this chapter were partially published in:
S. Bhattacharya, T. Pham, Z He, W Sun, "Tension to passively cinch the mitral annulus through coronary sinus access: an ex vivo study in ovine model", Journal of Biomechanics, (submitted).

segments of the flat ring were 0.72 ± 0.14 N and 1.38 ± 0.27 N, respectively, while the saddle-shaped ring exhibited nearly zero[134].

These studies, however, only provided knowledge of cyclic forces that a device could experience during implantation, e.g. myocardial forces acting on the device, but not the force generated by devices necessary to reduce the dilated MA. A fundamental question arises: what are the contributions from active myocardial contraction, passive myocardial deformation, hydrostatic blood pressure and leaflet annulus tension to the forces on the devices? The answer will not only facilitate the design and increase safety of annuloplasty devices but help to understand myocardial function and MA dilatation mechanism. In this chapter, an *ex vivo* technique was developed to quantify the CS cinching tension. The goal is to form a baseline value of cinching tension needed to correct dilated MA. The ovine model has been used extensively in experimental mitral valve mechanics studies [135, 136] and pre-clinical studies of TMVR [137-139]. The impact of cinching tension on the MA area, septal-lateral (S-L) and commissure-commissure (C-C) diameters and leakage in dilated valves were investigated.

4.2 Materials and Methods

4.2.1 Specimen Preparation

Ten fresh adult ovine hearts (mean weight: 313.5 ± 51.90 gram) were obtained from a local slaughter house. The hearts, which were not tested within 48 hours upon arrival, were cryopreserved at -80°C [110]. Studies have shown that a short period of cryopreservation do not induce significant changes in vascular tissue mechanical properties [140-143]. For each heart, the left atrium was carefully removed to expose the mitral valve (MV), the MA, the CS vessel and CS ostium. Small graphite markers were affixed to the MA to demarcate the area to be measured (**Fig. 4-1c**). A suture was inserted within the CS vessel with one end tied at the GCV end and the other end exited the CS ostium. The coronary arteries and CS attributes were occluded by sutures.

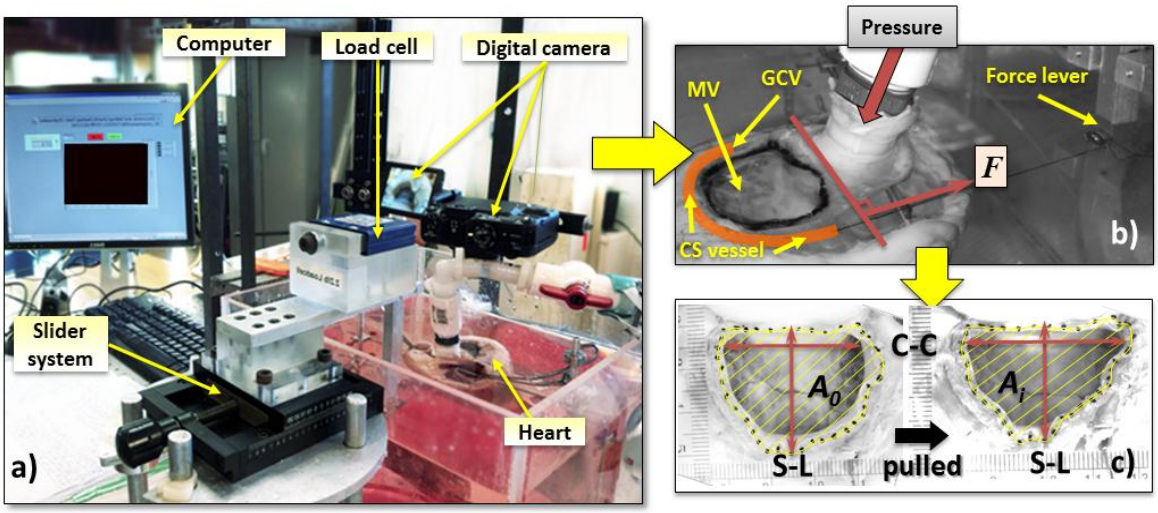

Figure 4-1: a) An image of the mitral valve (MV) cinching system consists of a computer acquisition system, a force transducer connects to a slider and a digital camera; b) a top view of a representative heart showing the location of the MV, the tissue dye highlighting the measured MV area, the coronary sinus (CS) vessel, the Great Cardiac Vein (GCV) vessel and the cinching force, F; c) the representative captured digital images of the reference area, A_0 and the area after pulled at a distance, A_i.

4.2.2 The MV cinching system setup

The experimental system consists of a water column, a pump, a clear Plexiglas solution chamber, a custom-made rigid supporting structure, a slider system, one digital camera and a computerized data acquisition system (Fig.4-1a). Each heart was stabilized by fixing the right ventricle to the custom-made supporting structure placed inside the Plexiglas chamber. The left ventricle (LV) pressurization was achieved by injecting saline solution into the LV through a cannula, which was inserted into the ascending aorta vessel and passed the aortic leaflets. The water column, fabricated with a large-bore tubing attached to the aortic cannula. Ethylene-Glycol-Tetraacetic acid (EGTA, 2.0 mM) and papaverine (0.1M) were added to the saline solution (37ºC) to minimize the active contraction of muscle fibers in order to obtain the passive mechanical properties of the heart. The LV pressure was controlled by the height between the saline level in the water column and the mitral annular plane [144]. A quasi-static system was chosen as the MV experiences highest force during peak systole or when the valve is fully

closed. A peak hydrostatic systolic pressure of 90 mmHg is chosen for the physiological pressure of an ovine heart [145, 146]. The leakage volume was measured by an amount of fluid regurgitated back into the left atrium during pressurization. The testing chamber was threaded with an outlet tube that drained the regurgitated fluid into a graduated cylinder for leakage measurements.

The slider system consists of a force lever, which was connected to a 10 N force transducer mounted on a linear stage. The handle of the linear stage can be manually rotated to linearly displace the force lever with an accuracy of ± 0.01 mm. The force transducer was connected to high-performance data acquisition device (National Instrument,NI SCC-68/SCC-SG24, NI 6351). A custom-made LabVIEW program was created to record the force transducer data at each displacement. The force transducer was calibrated prior to each experiment. The MA measurements were obtained from a digital camera mounted perpendicular to the MA plane.

4.2.3 Experimental protocol

Each heart was preconditioned by applying 10 consecutive pressure loading (90 mmHg) cycles. The experimental measurements including the MV cinching tension, MV area, leakage and MA area measurements were obtained during the three phases when the mitral valve was: 1) open (no pressure, P0), 2) close (pressurize at 90 mmHg, P90), and 3) altered or dilated at 90 mmHg pressure (P90-D). The P0 was performed to measure the cinching force generated by the suture inside the CS vessel during the passive relax state. The P90 was chosen as a baseline value for normal valve function during left ventricular filling. For P90-D, the MV dilation was achieved by injecting phenol (95%), into the muscular MA using a needle. The toxic substance in phenol can damage the structure and function of the muscle and has been utilized in an *in vivo* study to simulate the dilation of the mitral annulus [147]. To cinch the MA, the suture end at the CS ostium was pulled in the direction perpendicular to the C-C direction of the MA (Fig. 4-1b). For each pull, a linear displacement, d, of 2 mm for a total of 9 displacements in each phase was achieved (d_i, i = 0, 2, 4…12, 16 and 20 mm).

4.2.4 Data acquisition and analysis

The cinching tension (**T**) and the corresponding image of MA were measured simultaneously at an instant of a displacement. All the MA dimensions were measured using ImageJ (National Institute of Health). The MA area, A, was defined as the area encompassed by the markers. The S-L diameter was calculated as the distance between the two markers placed on the mid-septal and mid-lateral mitral annulus, and the C-C diameter was measured as the distance between the two markers placed on the commissures (**Fig. 4-1c)**. The leakage (L/min) was measured after visualization of full expansion of the LV and closing of the MV for 20 seconds.

4.2.5 Statistics

All measurements are shown as mean ± standard deviation (SD). The analysis of variance (ANOVA) test followed by the Holm-Sidak test and the Dunn's Method test were used to compare measurements between the three phases. Data were tested for normality using the Shapiro-Wilk test. The Student's t-test was used to determine significant differences. The paired Student's t-test was employed to determine the significant changes in parameters at a certain pull distance. Correlations between the parameters were determined using the Pearson's (for normal) and Spearman (for non-parametric data) correlation coefficient (r). A probability value less than 0.05 was considered statistical significant, with high significance indicated by $p < 0.001$. All statistical analyses were performed using SigmaPlot (Systat Software Inc., San Jose, CA) and SYSTAT (Systat Software, Chicago, IL).

4.3 Results

The MA deformation after each incremental load increase of a representative ovine heart during the three phases is shown in Fig. 4-2. The decrease in the mean MA area after each pull in each phase is

shown in Fig. 4-3a. Prior to pulling, the MA area increased 23.34 ± 18.02% from P0 to P90 and dilated further by 22.83 ± 0.06% in P90-D. Upon pulling about 16 mm (d_{16}), the dilated MA area was reduced by 26.17% (from 8.35 ± 2.00 cm^2 to 6.62 ± 1.85 cm^2) and similar to the baseline value (6.80 ± 1.89 cm^2). From Fig. 4-3b, at d = 16 mm, T required to reduce the dilated MV area to the baseline was 2.10 ± 0.47 N. It can also be seen that T generated by the suture (P0) alone without pressurization was 0.38 ± 0.10 N.

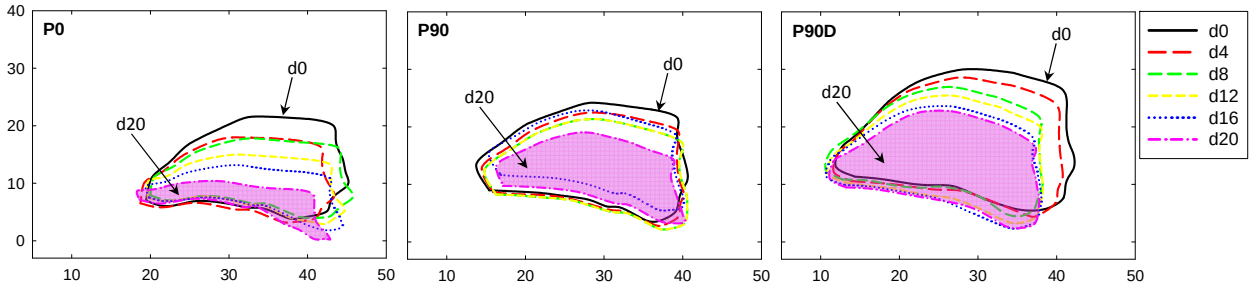

Figure 4-2: Images of a representative mitral valve deformation at d = 0, 4, 8, 12, 16 and 20 mm during the three phases: (P0) when the mitral valve was open at zero pressure), (P90) close or pressurized at 90 mmHg, and (P90D) after the mitral annulus was dilated and pressurized. (Dimension is in millimeter)

The mean S-L diameter increased significantly by 26% from the baseline to dilation (from 2.23 ± 0.31 cm to 2.81 ± 0.25 cm, $p < 0.001$). At d_{16}, the mean S-L diameter was significantly lower than d_0 (2.14 ± 0.27 versus 2.81 ± 0.25, $p < 0.001$) and below the baseline value (2.14 ± 0.27 cm to 2.23 ± 0.31 cm, $p = 0.485$). The C-C diameter was increased by 11% after dilation. However, the C-C diameters obtained during P90-D remained unaffected throughout the experiment (Fig. 4-3c). The mean C-C diameter in P90 at d_0 was 3.09 ± 0.39 cm and in P90-D at d_{16} was 3.36 ± 0.36 cm, $p = 0.121$. A summary of comparisons of the MV area, the S-L and C-C diameters and the leakage rate between baseline at no pull (d = 0) and dilated condition at 16 and 20 mm pulling distances (d = 16 and 20) are listed in Table 4-1.

Table 4-1. Summary of ovine heart data showing the mean and standard deviation (SD) of the mitral valve area (MV), septal-lateral (SL) and commissure-commissure (CC) diameters, leakage at 90 mmHg pressure and the change in pressure during the experiment.

During pressurization of 90 mmHg				
	Baseline	Dilated		
	at d=0	at d=0	at d=16	at d=20
MV (cm^2)	6.80 ± 1.89	8.35 ± 2.00	6.62 ± 1.85	6.27 ± 1.77
S-L dia (cm)	2.23 ± 0.31	2.81 ± 0.25*	2.14 ± 0.27†	2.01 ± 0.26†
C-C dia (cm)	3.09 ± 0.39	3.42 ± 0.36	3.36 ± 0.36	3.38 ± 0.35
Leakage (L/min)	0.09 ± 0.07	0.18 ± 0.09	0.09 ± 0.07	0.08 ± 0.05‡

* compared to baseline d=0, $P < 0.001$, † compared to dilated d=0, $P < 0.001$, ‡ compared to dilated d=16, $P < 0.05$

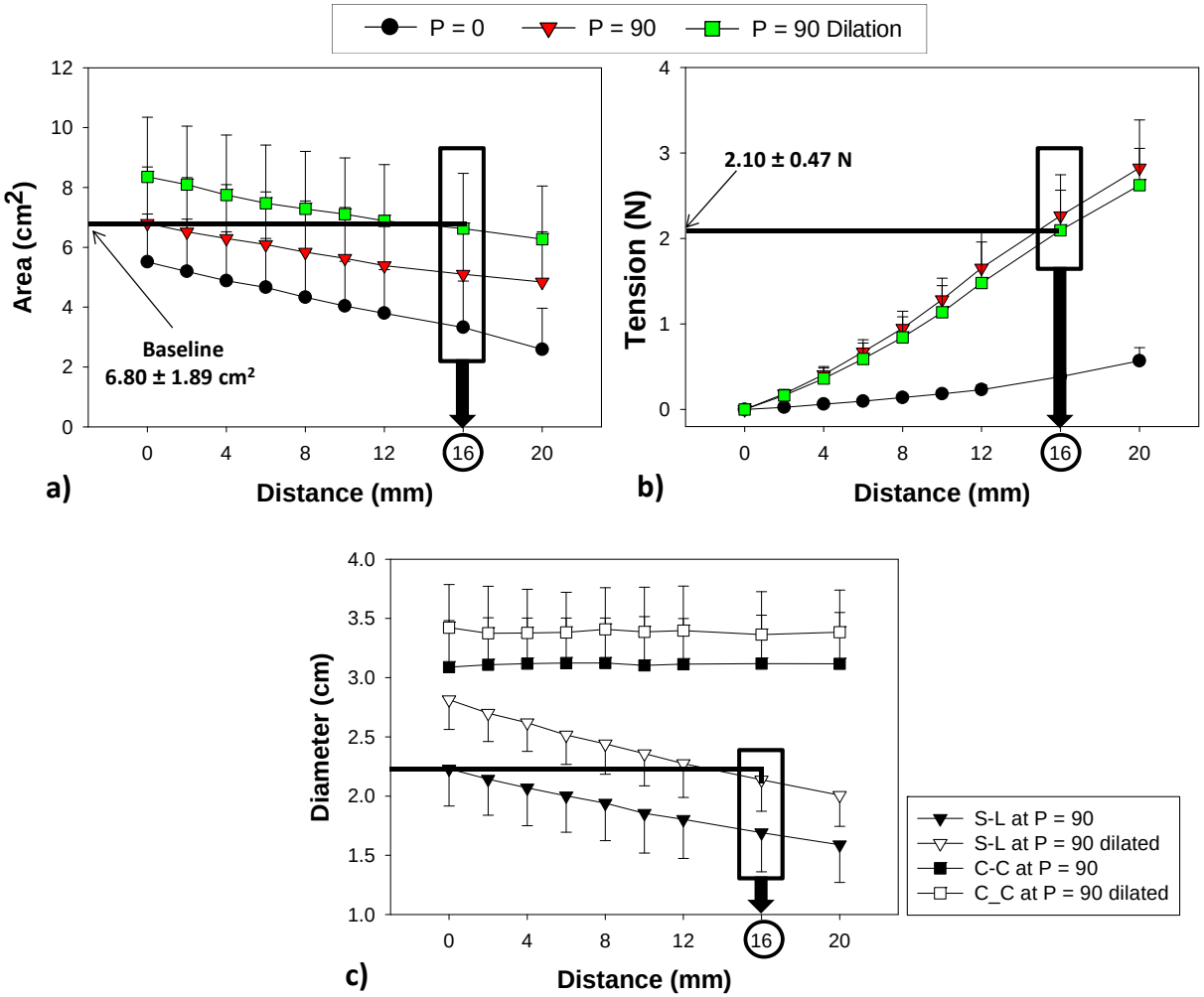

Figure 4-3: The relations between distance pulled and a) area (cm^2), b) force (N) and c) septal-lateral (S-L) and commissure-to-commissure (C-C) diameter of the ovine hearts in three phases of valve open (P=0), valve close at 90 mmHg pressure (P=90) and valve dilation at 90 mmHg (P=90 Dilation). Data are shown as mean ± standard deviation.

The relation between MA area and **T** in each phase is shown in Fig. 4-4a. At a maximum pulling distance (d_{20}), a small tension of 0.6 N was required to shrink 58% of the MA area during P0. At the same tension, as expected, only 9% and 11% MA reduction were achieved for P90 and P90-D, respectively. At 15% MA area reduction, the tension of both P90 and P90-D was 1 N. After this point, the P90-D response curve shifted down slightly, indicating a larger tension would be required to shrink the MA area. The decrease in the MA area was accompanied by the reduction in the S-L and C-C diameters, and no difference was observed between P90 and P90-D, see Fig. 4-4b. At 2.10 ± 0.47 N, when the dilated MA area returned back to the baseline value, a 21.30 ± 5.6% reduction in the MA area and a 24.18 ± 5.28% reduction in the S-L diameter were achieved.

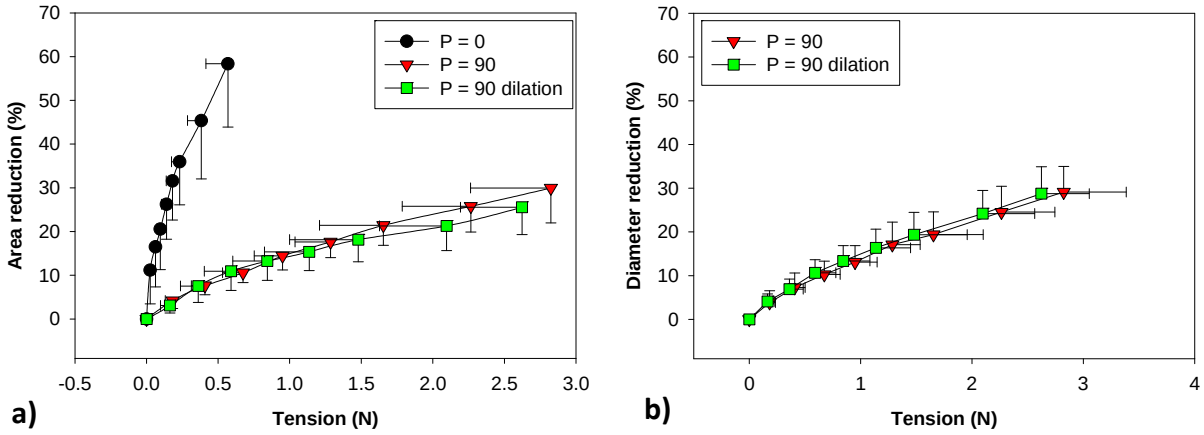

Figure 4-4: The relation between (a) mitral annulus area and cinching tension, and between (b) S-L and C-C diameters and cinching tension. Data are shown as mean ± standard deviation.

Figure 5-5 shows the changes in the MA area, the tensions and the leakage rates from the initial (d_0) to the final (d_{24}) pulling distances. In the normal hearts, we observed a small leakage of 0.094 ± 0.070

L/min. After phenol application, the leakage rate increased to 0.181 ± 0.008 L/min or by 93%. The progression of annular cinching caused the MA area to decrease progressively with leakage rate ($r = 0.992$, $p < 0.001$ for P90 and $r = 0.957$, $p < 0.001$ for P90-D). The T was reversely correlated with leakage rate ($r = -0.983$, $p < 0.001$ for P90 and $r = -0.912$, $p < 0.001$ for P90-D). Leakage was reduced to normal leakage rate at 1.71 N, and the MV area approached to normal at 6.76 cm^2.

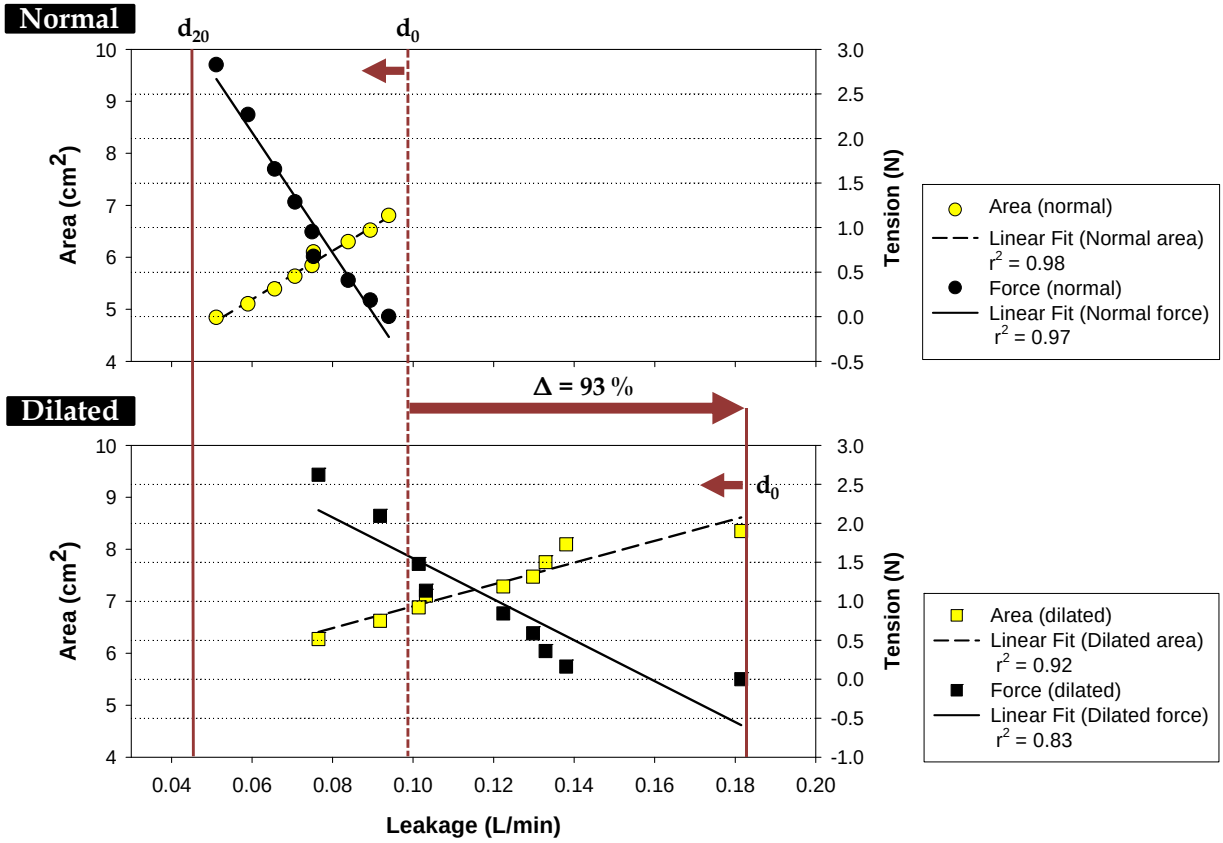

Figure 4-5: The correlations between the mean leakage rate and mean mitral area and mean cinching tension in the a) normal and b) dilated conditions. Solid and dashed lines are the linear fits of the data. The d_0 indicates no pull, and d_{20} is 20-mm pulling distance.

4.4 Discussion

Despite the increase in the development of TMVR devices, limited information is available on device forces required to restore normal valve function. An *ex vivo* technique developed in this study aims

to quantify the cinching tension (**T**) needed to restore normal MA from dilation in the passive ovine heart model. The MA dilation was achieved up to 22.83% and the S-L and C-C diameters were increased by 26% and 11% upon dilation, respectively. Various studies have demonstrated significant changes of MA in either ischemic or acute cardiomyopathy that resulted in significant MR. An *in vivo* animal study demonstrated that in chronic ischemic MR condition, the entire mitral annular regions, including the fibrous (anterior) and muscular (posterior) sections, dilates proportionally [148]. Timek *et al.* [149] showed that the progression of acute ischemic MR in ovine models was characterized as 20% - 28% (mild/moderate – moderate/severe) increase in MA area and 14% - 19% increase in S-L diameter. For human study, significant MR caused by ischemic cardiomyopathy was characterized as 31% increase in MA area and 17% and 11% increase in S-L and C-C diameters [150]. Thus, the increase in both MA area and S-L and C-C diameters in this study showed an indication of MA dilation.

The loading condition on the MA is primarily due to the LV pressurization achieved by the hydrostatic pressure. The T from the suture is, therefore, an additional force on the LV wall and the leaflets connecting to the MA to balance the hydrostatic pressure force. From **Fig. 4-3**, during the P0, **T** generated by the suture was 0.06 ± 0.01 N (P0, d = 4 mm), resulting in MA area of 4.88 ± 1.63 cm^2. The **T** required to reduce to a similar MA area with a presence of the hydrostatic pressure was 2.80 ± 0.56 N (P90, d = 20 mm). Thus, the increase in **T** as the result of hydrostatic pressure can be calculated as P90 – P0, approximately 2.74 N or increased by 4557%. This drastic increase in **T** between P0 and P90 indicates that LV pressure is an important factor in determining the effective **T** of the device. To determine the change in **T** with the presence of MA dilation, the difference between **T** at P90 and P90D was obtained. At a MA area of 6.3 ± 1.8 cm^2, **T** of P90 and P90D were 0.41 ± 0.09 N and 2.62 ± 0.43 N, respectively, resulting in 2.21 N, or increased by 539%. Since the pressure was constant for both phases, this increase in tension directly relates to the impaired muscular tissue around the MA due to phenol injection. Thus, we can view this suture cinching tension as a compensation force in MA reduction. In other words, **T** indicates the maximum force to be generated by the device necessary to restore normal

MA geometry without active myocardial contraction, and usually depends on severity of annular dilatation.

The cinching tension, however, can be less in magnitude during LV contraction. An *in vivo* ovine study of Siefert *et al.* [151], they measured the MA forces using a custom-made device with strain gauges placed directly on the MA in S-L and C-C directions [151]. The mean S-L and C-C forces of normal ovine group at 90 mmHg were 3.9 ± 0.8 N and 2.6 ± 0.6 N, respectively. In another study [152], the same group found a significant decrease in the S-L forces as the result of ischemic MR with inferior left ventricular infarction. Their findings support the notion that the active contraction mechanism might have been impaired in ischemic MR [153-155]. Daimon *et al.* [153] found that their IMR patient group had an attenuated mitral annular motion and a reduction in MA contraction by 23.0 ± 6.5% compared to the normal group of 42.6 ± 7%. In addition, their analysis showed that annular contraction was the strongest determinant of the severity of MR among the annular measurement. The hydrostatic pressure in this study is not considering *in vivo* annular contraction and expansion of myocardial fibers. Thus, the active contraction properties of the MA might relieve this suture tension. However, active contraction in relation to cinching tension is remained to be determined.

The experimental technique used in this study for MA restoration only allowed a significant reduction in the S-L dimension while the C-C dimension remained unchanged, which can be seen in Figs. 5-3&5-4. The impact of C-C dimension in restoring MV competency, however, is still a debate. Several clinical and experimental studies have shown that S-L dimension has a prominent role in functional MR [156] and that reduction in S-L diameter alone is sufficient to restore leaflet coaptation [157, 158].

Restoration of normal MV by cinching the MA was adopted by several novel methods. A device called the cerclage, was designed and tested in swine subjects to shrink the entire annular circumference and S-L diameter [159]. The device is made of a braided non-absorbable suture that encircles the mitral annulus via the CS vessel, septal myocardicum, right ventricle and atrium path, and tying the two ends. Using 16 swine subjects, the S-L diameter reduction was measured at three tension forces (200g, 400g

and 600g), and a maximum of 20% of the reduction in both systole and diastole at 600 g (~6 N) of tension was observed. This high magnitude of tension could be the result of shrinking a massive muscular structure that included both MA and right ventricle. Timek *et al.* demonstrated that S-L diameter reduction was achieved by more than one trans-annular sutures connected from locations on the anterior fibrous region to the posterior annulus[160, 161] but no force was measured. Recently, Jensen *et al.* [162] found that at 32% of trans-annular trigone-posterior annulus distance reduction at three different location, the peak forces were 1.2 ± 0.9 N, 1.5 ± 1.0 N, and 0.8 ± 0.2 N with no significant difference between them. Interestingly, the sum of the forces ranged from 0.12 ± 0.03 N to 3.5 ± 1.3 N, which matches our results even though force directions and suture techniques were different. Their cyclic traction suture forces increased with increasing levels of downsizing as our cinching tensions increased with increasing MA area reduction. It should be noted that the magnitude of forces measured is dependent on the type of device [162] and how it shapes the MA. Difference in the locations of device implantation (e.g. within the CS vessel or directly on the MA) and various hemodynamic and boundary condition could affect both MA geometry and mechanics.

Currently, there is a lack of understanding of biomechanics involved in the device design and optimization of TMVR devices, possibly due to the complex MV geometries. Fortunately, in the past decade, the mechanical testing techniques and constitutive modeling in cardiovascular mechanics have improved tremendously. Human tissue material properties can now be tested extensively [163], modeled and implemented in computational studies [45]. Improved computational models of MV has evolved [31, 46, 164-167] and predicted several diseased states [43, 168-170]. Thus, the data in this study can be used in validation of computational models to predict the functionality of TMVR devices.

There are several limitations in this study. The data are valid for isolated MA dilation model which is distinctly different from ischemic MR model [171]. The mitral valve closure due to the hydrostatic pressure could alter the native MA mechanics by the expansion of the global LV. Leaflet coaptation height, depth and tethering length were not recorded as the result of 2D imaging, thus, MR

grade was not classified. Future study using 3D echocardiography as an imaging acquisition technique will provide a new insight into the 3D dynamic behavior of the MV during cinching. This study did not account for global expansion and contraction of left ventricle, *in vivo* annular contraction and expansion of myocardial fibers. Thus, the active contraction properties of the MA and left ventricle may relieve this suture cinching tension.

4.5 Summary

This chapter investigated the cinching tension required to reduce MA dilation in passive ovine heart model. The MA was dilated up to 22.83%. A mean force of 2.1 ± 0.47 N was required for 21.30 ± 5.6% in MA area reduction, reduced leakage by 51.72 ± 16.19% and restored the normal condition with a significant reduction in the S-L dimension. The cinching tension generated by the suture acts as a compensation force in MA reduction, implying the maximum tension to be generated by annuloplasty device to restore normal MA geometry. Several approaches that utilize the CS to rectify MA dilation have been developed, but long-term durability is yet to be achieved due to current fatigue and fracture events. Therefore, knowledge of the cinching force with the corresponding MA geometry will greatly contribute to the development and design of future TMVR devices and understanding of myocardial contraction function.

5 Simulated Biomechanical Interaction between Coronary Sinus and PTMA proximal anchoring stent*

In previous chapters, we have collected experimental data and obtained material parameters from various constitutive models to characterize the mechanical properties of mitral tissues. From this chapter and onwards, we will implement the tissue properties and material models into Finite Element (FE) simulation and analysis. In this chapter, we will first introduce a method to analyze the biomechanical interaction between stent and tissue model using only a proximal section of the PTMA and a simplified CS geometry. As we performed and compared tissue properties between human and animal models in previous chapters, we will also applied different tissue properties and elucidate any difference between the human and animal models in the assessment and prediction of PTMA intervention. The FE software, ABAQUS (Pawtucket, RI), will be used throughout the dissertation as the finite element implementation platform due to its wide commercial availability.

* The contents of this chapter were partially published in:
T Pham, M Deherrera and W Sun, "Biomechanical interaction between coronary sinus and proximal anchoring stent in percutaneous treatment of mitral regurgitation", ***Computer Methods in Biomechanics and Biomedical Engineering*** 6(11): 4336–4344, 2012.

5.1 Introduction

5.1.1 Nitinol stent and application

Nickel Titanium or Nitinol (NiTi) material is known for its superelasticity or the ability to return to original shape after severe deformation. NiTi can be stretched over 10% and still return to its original length [172]. Figure 6-1a shows the loading and unloading cycle of Nitinol relative to other living tissues that is characterized by a pronounced hysteresis. Compare to stainless steel, NiTi is much weaker and exhibits a lower ultimate tensile strength. However, the loading and unloading curves exhibit plateau regions, which a large strain can be gained on loading and the same strain can be relieved upon unloading, without significant increase or decrease in loads or stress. Macroscopically, when stress is applied to NiTi, the superelastic NiTi changes its crystal structure from austenite to martensite. The Austensite (A) structure is cubic in nature, while the martensite (M) structure is complex monoclinic structure. When stress is removed, the material returns to the original structure and recovers its original shape.

While superelasticity is the result of a stress induced phase transformation, shape memory is the result of a thermal phase transformation [173]. The transformation temperature of NiTi is characterized by four transformation temperatures: the martensite start temperature (Ms) which is the temperature at which the material starts transforming from austenite to martensite, martensite finish temperature (Mf), at which the transformation is complete and the material is fully in the martensite phase; austenite start temperature (As) at which the reverse transformation from austenite to martensite starts; and austenite finish temperature (Af) at which the reverse phase transformation is completed and the material is fully in the austenite phase. When cooling and in absence of applied load, the material transforms from austenite into twinned martensite with no shape change (Fig. 5-1c-phase A). At this stage, NiTi loses its stiffness. By applying a pure mechanical load, a full phase transformation from twinned martensite to fully detwinned martensite can be observed (Fig. 5-1c-phase B). Upon the presence of temperature Af, a complete shape recovery is observed upon unloading, resembling elastic material behavior (Fig. 5-1c-

phase C). The effect of shape change and temperature dependency of NiTi is known as Pseudoelastic Effect, which described in a stress-strain relationship as shown in Fig. 5-1d.

Nitinol is one of very few alloys that is both pseudo-elastic, thermal shape memory and biocompatible. Thus, NiTi has become suitable material for a variety of self-expanding (SE) stents. These SE stents are manufactured with a targeted diameter larger than the vessel diameter, so that they can be crimped and restrained in a delivery system, then elastically released into the vessel. Early design of NiTi stent was used in non-vascular applications, in a form of round or flat wire. For instance, Endocare s Horizon Stent was used for the relief of bladder outlet obstruction and IntraCoil Stent for treatment of patients with superficial femoral artery and popliteal artery lesions [173]. One advantage of simple wire coil is the capability to retrieve the stent. As mentioned earlier, NiTi stent loses its stiffness at cooler temperature, thus, retrieving can be easily done by a cold saline.

In the mid-1990s, the laser cutting tubular NiTi stents become popular in many peripheral and vascular treatments. Early examples of laser-cut tubular NiTi stents are Angiomed Memotherm and the Scimed Radius stents. The Memotherm was a rigid, closed-cell design with a diamond shaped pattern, and the Radius is a flexible open-cell design with sequential rings and periodic peak-to-peak non-flex bridges. More recent designs employ variations and/or combinations of these basic design features, e.g. SMART Stent (from Cordis), Jostent SelfX Stent (Jomed) and Dynalink Stent (Guidant).

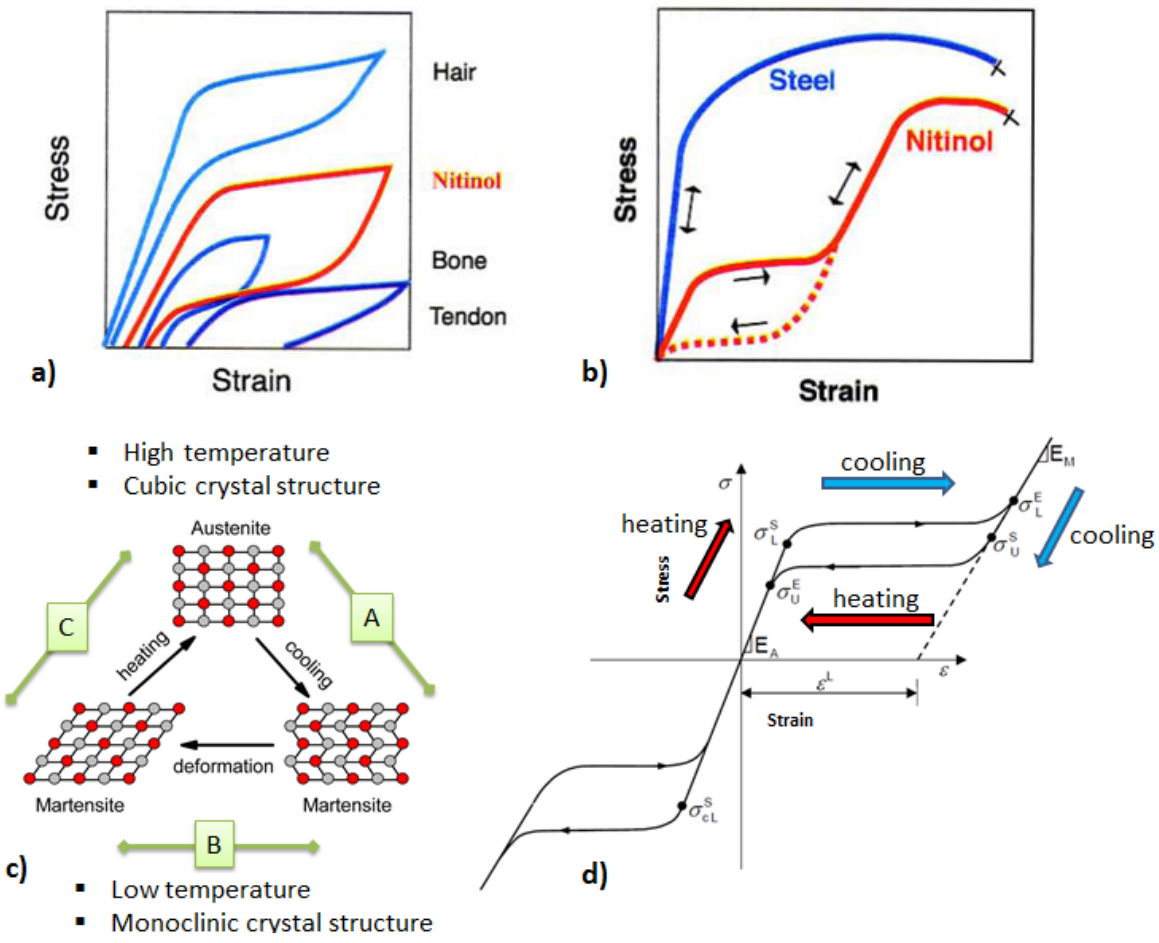

Figure 5-1: a) Biomechanical compatibility of Nitinol: deformation characteristics of Nitinol and living tissues, adopted from; b) schematic stress-strain diagram for Nitinol and stainless steel; c) macrostructure of NiTi showing the Austenite and Martensite phases; and d) stress-strain curve of NiTi material. Images from (a) and (b) are adopted from [174].

A distinctive feature of NiTi tubular stents is its nonlinear response and hysteresis. These unique features create such a great advantage for endovascular stenting applications. To illustrate this, the schematic stress-strain curve for NiTi can be described in the cycle of crimping a stent into a delivery system, deploying, releasing it into the vessel, as shown in Fig. 5-2 [173]. The stress axis is put as the hoop force and the strain axis as stent diameter. Since the stent is always manufactured in a way such that the final expanded diameter is larger than the vessel diameter, it needs to be crimped into the delivery catheter, from point a to point b, then packaged, sterilized and shipped. During the implantation, stent will

be released into the targeted vessel, expanding from point b until further expansion is prevented by impingement with the vessel (point c). Since the stent did not expand to its pre-set shape, it continues to exert a low outward force, called chronic outward force (COF). From point c to point d, stent will exhibit a force that will resist recoil pressures or any other external compression forces. This force is much stronger than the unloading force (point c to point e), which is called the radial resistive force (RRF). In summary, the stress hysteresis of NiTi allows a very low radial force, or COF, even stent is oversizing. The stent generates forces that resist compression, or RRF, until plateau stress is reached. It has been shown that the low COF allows vessel to remodel with less intimal hyperplasia [175].

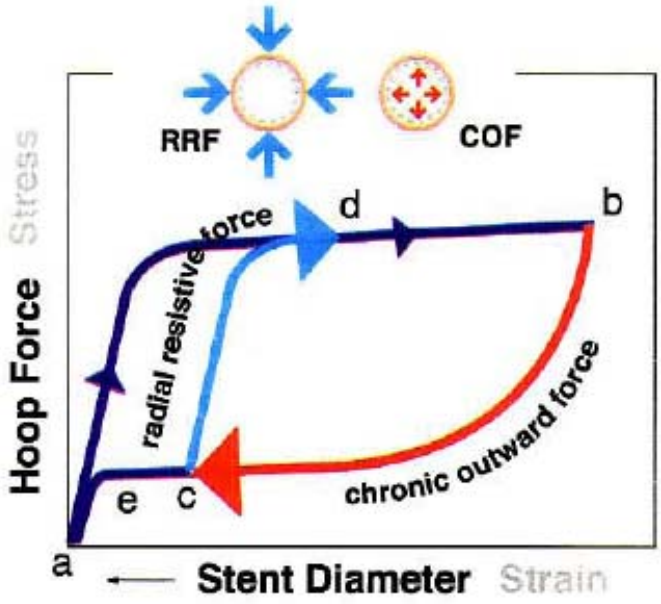

Figure 5-2: Schematic stress hysteresis and concept of biased stiffness as demonstrated with the cycle insertion into delivery system/deployment/compression of a tubular stent. Adopted from [173].

5.1.2 Tissue-stent interaction (TSI) studies using Finite Element Analysis (FEA)

Upon delivered, the stent comes into contact with the vessel wall, thus the COFs impose mechanical stresses on the vessel wall. In return the hemodynamic conditions (e.g. blood pressure) in the

vessel generate cyclic pulsating load that accounts for the fatigue life of the device and eventually result in mechanical failures. The schematic of this cycle is illustrated in Fig. 5-3. As self-expanding stents have proven to reduce vessel recoil and restenosis as compared to balloon expandable stents and provide a less invasive alternative for the treatment of endovascular disease [176], adverse events as the result of stent mechanical fatigue could result in undesirable clinical events such as thrombosis and intimal hyperplasia [175] and particularly reoccurrence of MR in PTMA intervention. In order to prevent these adverse events, it is important to understand the tissue-stent interaction (TSI) and their mechanical factors that contribute to adverse outcomes during stent deployment process and after stent implantation.

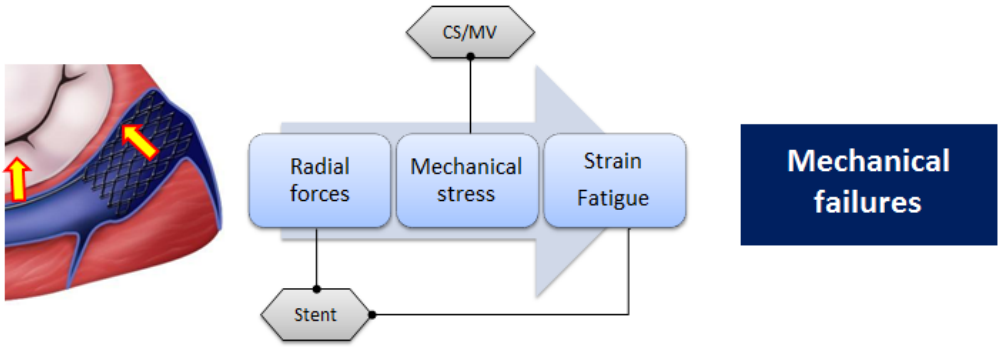

Figure 5-3: Biomechanical interaction between stent and tissue schematic

Studies on the mechanical behaviors of NiTi stents and their interaction with surrounding vessels have been conducted by many researchers. Wu et al. [177] evaluated the biomechanical properties of NiTi carotid stents and their interactions with carotid arteries using FEA. Their TSI results showed that stent with shorter struts may have better clinical results and that stent geometries have an impact on vessel geometrical changes. Kleinstreuer et al. [178 studied the mechanical behavior (e.g. vessel stresses, stent strain and radial forces) and fatigue performance of different NiTi materials and grafts during crimping, deployment and cyclic pressure loading within the abdominal aortic aneurysm (AAA). Using the fatigue-life diagram, they were able to predict the acceptable AAA stent-graft design during crimping and cyclic pressure loading. Azaouzi et al. {Azaouzi, 2012 #209] used Finite Element analyses (FEAs) to simulate

the deployment of self-expanding NiTi stent into the artery under pulsatile loading. The authors analyzed the impact of stent geometries on the arterial and to assess the influence of artery on the deformation field within the stent. They concluded that stent geometries (e.g. length, width and thickness of strut) have an influence on stent strength and the amount of stent oversizing has an impact on stent fatigue life. Auricchio et al. [179] expanded FEA studies of self-expanding stent by evaluating three different stent designs (e.g. laser-cut open-cell, laser-cut closed-cell and braided closed-cell) in a patient-specific carotid artery. The authors found that stent design with closed-cell provides higher lumen gain and stent configuration and size have a limited impact on the vessel straightening.

Although extensive work has been done to evaluate the self-expanding NiTi stents, little or no attention has been focused on characterizing the biomechanical interaction between the NiTi PTMA stent and the CS vessel. In this chapter, we present FEA of stent deployment within the CS vessel, considering the realistic material models of CS vessels. Our FEA provides quantitative measures of stress and strain of both stent and vessel and estimates fatigue life of stent, a very important key issue for medical implants.

5.1.3 Human versus animal models

Animal studies have demonstrated the effectiveness of PTMA devices to reduce MR in heart failure induced by rapid pacing in the short- term [7-9]. However, initial human trials were suboptimal. The adverse events included compression of the left circumflex artery, perforation of vessel branches, device migration and device fracture [10-14]. Some of these issues may be improved by a detailed anatomical assessment of the CS and its tributaries prior to the procedure using imaging modalities such as multidetector computed tomography. Device dysfunctions involving device migration and fracture, however, are mainly associated with the biomechanical interaction between CS tissues and the device that is largely unexplored in the literature. In pre-clinical trials of cardiovascular interventional devices, animal results are often used as a guide for device design and development. However, without a

quantitative understanding of the difference between animal and human tissues and the associated device-CS tissue interactions, the development of these devices based on ad hoc and trial-and-error approaches can be time-consuming and costly. In the present study, we first established a finite element (FE) study to evaluate the biomechanical responses of the proximal anchor of this PTMA device when interacted with the human and porcine CS walls. In addition, we chose two Nitinol stent materials to investigate the impact of stent material stiffness. The biomechanical interactive properties between the stents and the CS vessels were quantified by measuring the contact forces, vessel wall stresses, strains and fatigue safety factor of stents were analyzed.

5.2 Materials and Methods

5.2.1 Model Geometries

The complete FE model for the stent deployment simulation consists of the proximal stent, the CS vessel, and the stent expanding and crimping sheaths. Geometrical and numerical details of the models are listed in Table 5-1. The proximal anchor can be thought of as an elastic lattice, deriving its strength from the joints and bending action of component struts. Because of the lack of symmetry in this part, the entire anchor has been modeled. The stent geometry, after the laser cut from a cylindrical Nitinol tube and electroplishing, was 21 mm in length with an inner diameter (ID) of 1.6 mm and a thickness of 0.3 mm, as shown in Fig. 5-4a. This stent geometry was further deformed, through a series of expansion and annealing process, to an expanded shape as shown in Fig. 5-4b. Typically, the stent anchor's diameter is oversized and larger than the CS's diameter by 2 – 4 mm [180]. Therefore, it was expanded from an ID of 1.6 mm to a targeted ID of 14.90 mm, assuming the CS's ID is 12 mm. The radial expansion was carried out in the FE simulation by displacing the expanding sheath that placed inside the stent anchor in increments of 3, 4, 6, 8, 12 and 15.50 mm in outer diameter (OD), each followed by an annealing step. The annealing process was simulated using a built-in function in ABAQUS (*anneal) where stent stresses and strains were set to zero. By dividing one large deformation step into several steps of small

deformations with an annealing process, the potential damages to the stent that may be caused by large deformations can be effectively reduced. The final deformed geometry of the stent anchor is shown in Fig. 5-4b, in which it was composed of two strut cells in the axial and twelve in the circumferential directions. The two pairs of stent struts were joined by a strut link (Fig. 5-4c). Crimping and release of the stent anchor were achieved by displacing the cylindrical crimping sheath located externally of the stent anchor inwardly and outwardly, respectively.

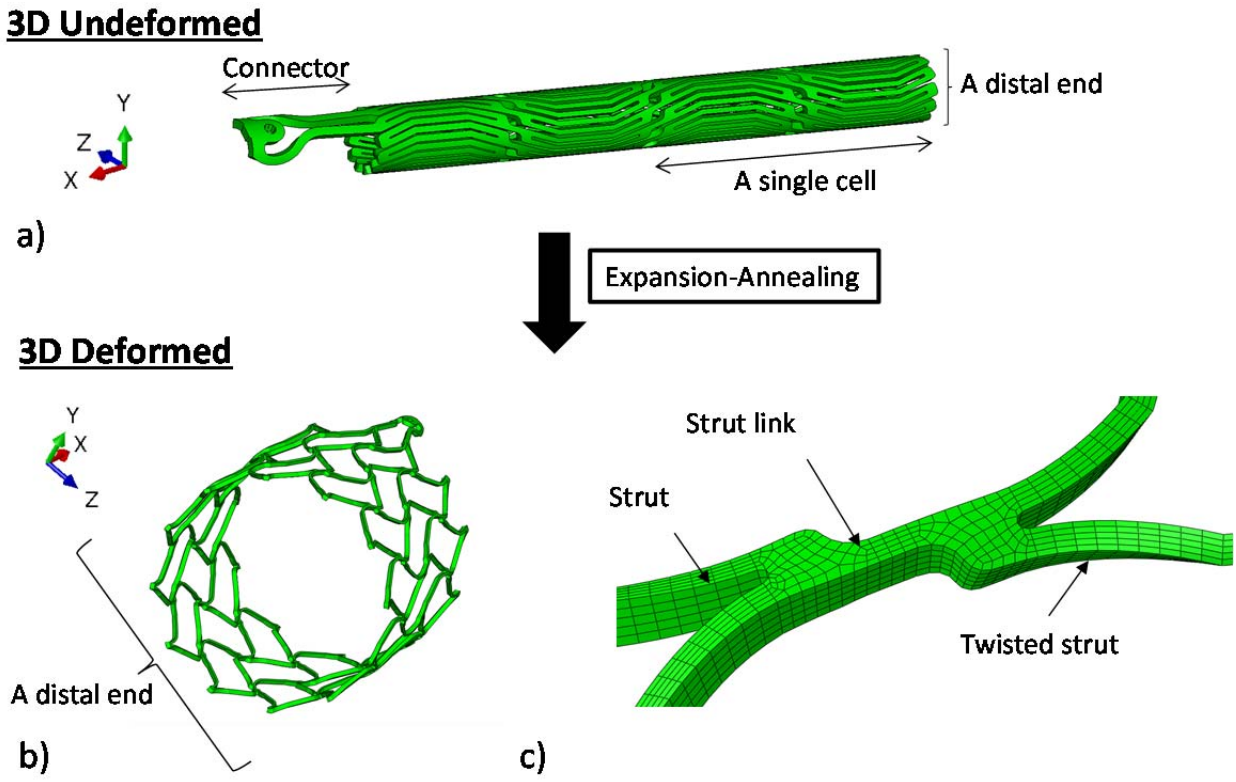

Figure 5-4: a) The 3D undeformed shape of the stent prior to expansion-annealing process, showing the connector and the stent body that is composed of 12 struts in the circumferential (z) and 2 in the axial (x) directions; b) the 3D deformed shape of the stent after expansion-annealing process; and c) the two struts of the stent are united by a strut link. The strut is twisted asymmetrically after the process.

Table 5-1. Geometrical and Finite Element modeling measures of all models

Models	Dimension (mm)	Undeformed	Element type	No. of elements
CS	ID Thickness Length	12 0.74 60	C3D8I *	43,199
Stent	ID Thickness Length	1.60 0.30 21	C3D8I *	114,219
Sleeve_expand	ID Thickness Length	11 - 41.5	M3D4R †	2,231
Sleeve_crimp	ID Thickness Length	15.52 - 41.50	M3D4R †	2,231

A study by El-Maasarany et al. [85] on the anatomy of the CS vessel showed that 80% (32/40 patients) of human specimens had coronary sinus as a cylindrical shape near the opening into the right atrium. Thus, we simplified our CS vessel model to a cylindrical tube, with an inner diameter of 12 mm and a thickness of 0.74 mm [181], to facilitate the comparison between different CS tissues and stent materials.

The 8-node hexahedral linear incompatible mode element (C3D8I) was chosen to mesh both the CS vessel and the stent as C3D8I is preferred for stent analysis due to the nature of bending during loading. The 4-node quadrilateral element (M3D4R) was modeled for the expansion and crimping sheaths. A mesh sensitivity analysis was performed, see appendix A for more details.

5.2.2 Material properties and constitutive modeling

The two different Nitinol materials, Nitinol 1 (N1) and Nitinol 2 (N2), were utilized in the simulations, adopted from Kleinstreuer et al. [182] with modifications. For an isothermal analysis as the

one presented here, the stent material model can be defined by a stress-strain curve and "breakpoint" stresses, as shown in Fig. 5-5a. The inputs to this model are the two moduli of Elasticity, the plateau transformation strain and the five stress breakpoints. From Table 5-2, it can be seen that N1 material is stiffer than N2 material with higher austenite (E_A) and martensite (E_M) moduli.

Table 5-2. The material parameters of CS vessels and stents

	μ_1 (MPa)	a_1	μ_2(MPa)	a_2	μ_2(MPa)	a_2					
Human	127.653	5.928	-63.082	11.851	4.674	19.317					
Porcine	8.213	10.608	22.689	-5.748	-12.515	9.184					
	E_A(MPa)	ν_A	E_M (MPa)	ν_M	ε_L	$\sigma^S{}_L$	$\sigma^E{}_L$	$\sigma^S{}_U$	$\sigma^E{}_U$	$\sigma^S{}_{CL}$	T
Nitin-1	70,000	0.3	47,800	0.3	0.063	600	670	288	254	900	37
Nitin-2	40,000	0.3	18,554	0.3	0.04	390	425	140	135	585	37

The mechanical properties of the coronary sinus of both human and porcine were obtained from the pressure-inflation tests of porcine (n = 7, 6-9 months old) [183] and human (n = 4, 85.25 ± 7.41 years old) CS vessels. Briefly, the human CS vessels were subjected to the mechanical test while they were intact (i.e. the CS vessel was not dissected out of the heart). After 10 preconditioning cycles, the vessels were incrementally dilated up to 80 mmHg of pressure. The dilated CS diameters were measured to obtain the CS pressure-radius curve, from which the hoop/axial stress-stretch relation were calculated [183]. We chose the Ogden isotropic nonlinear hyperelastic model [184] to characterize the experimental data,

$$W = \sum_{i=1}^{N} \frac{2\mu_i}{a_i^2}(\lambda_1^{a_i} + \lambda_2^{a_i} + \lambda_3^{a_i} - 3), \tag{6.1}$$

where μ_i and a_i are the material constants and λ_i are the principal stretches. The mean data from four human and seven porcine specimens were fitted with the Eq.6.1 to obtain the material parameters. The goodness of fit was determined using R-square value based on the Levenberg-Marquardt nonlinear

regression algorithm using SYSTAT 10 (Systat Software Inc., Chicago, IL). The Ogden model curve fitting results for both human and porcine tissues are illustrated in Fig. 5-5b & c.

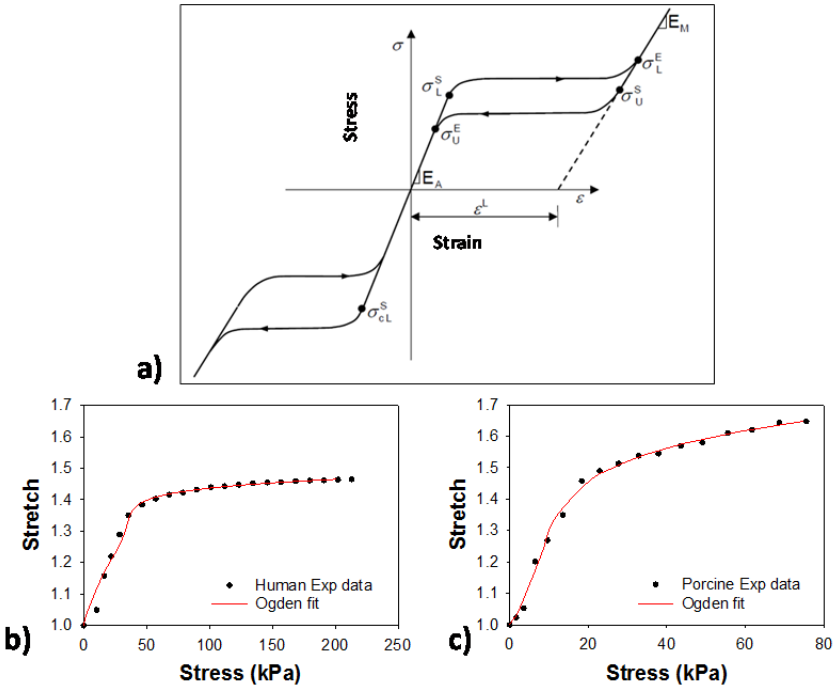

Figure 5-5: a) A typical stress-strain curve for Nitinol material, mean b) human and c) porcine CS stress-stretch curves fitted with the Ogden model.

5.2.3 Boundary and loading conditions

The expanded geometry of the stent was crimped in a catheter prior to the PTMA deployment. In the simulation, the stent was crimped to an OD of 11.98 mm using a displacement-controlled deformation of the crimping sheath, see Fig. 5-6. After the stent release and deployment in the CS vessel, the biomechanical interaction between the device and the CS wall is rather complex. Here, we briefly described the procedure and interactive forces involved: The proximal stent anchor is released from the delivery catheter and deployed into the CS ostium. The expansion of the stent generates contact forces between the CS tissue and the stent, which enable anchoring of the stent to the CS wall. A biodegradable suture keeps the bridge links "open" and elongated; upon dissolution, the links close, the bridge length is

reduced and the proximal and distal stent anchors are brought closer together, reshaping and reducing the mitral annulus in the septal-lateral distance. Therefore, the bridge segment will impose an axial force on the proximal stent. In addition, an internal venous pressure of 10 mmHg will also deform the CS wall and affect the stent-tissue interaction. The major biomechanical loading steps in this process are illustrated in Fig. 5-6. In the simulation, we developed three corresponding steps as follows:

Step 1 – Contact between CS wall and stent anchor during the stent deployment. The contact was established by removing the crimping sheath to release the proximal anchor to contact with the CS inner wall.

Step 2 – Effect of axial contraction force due to the bridge contraction. An axial load with a magnitude of 2.45 N in the axial direction was applied to the connector elements to approximate the pulling force generated by the contraction of the bridge section that occurs upon dissolving of the biodegradable suture [185].

Step 3 – Deformation due to the pulsatile blood pressure in the CS vessel. An incremental pressure, from 0 to 10 mmHg, was imposed on the luminal surface of the CS wall to mimic the physiological condition.

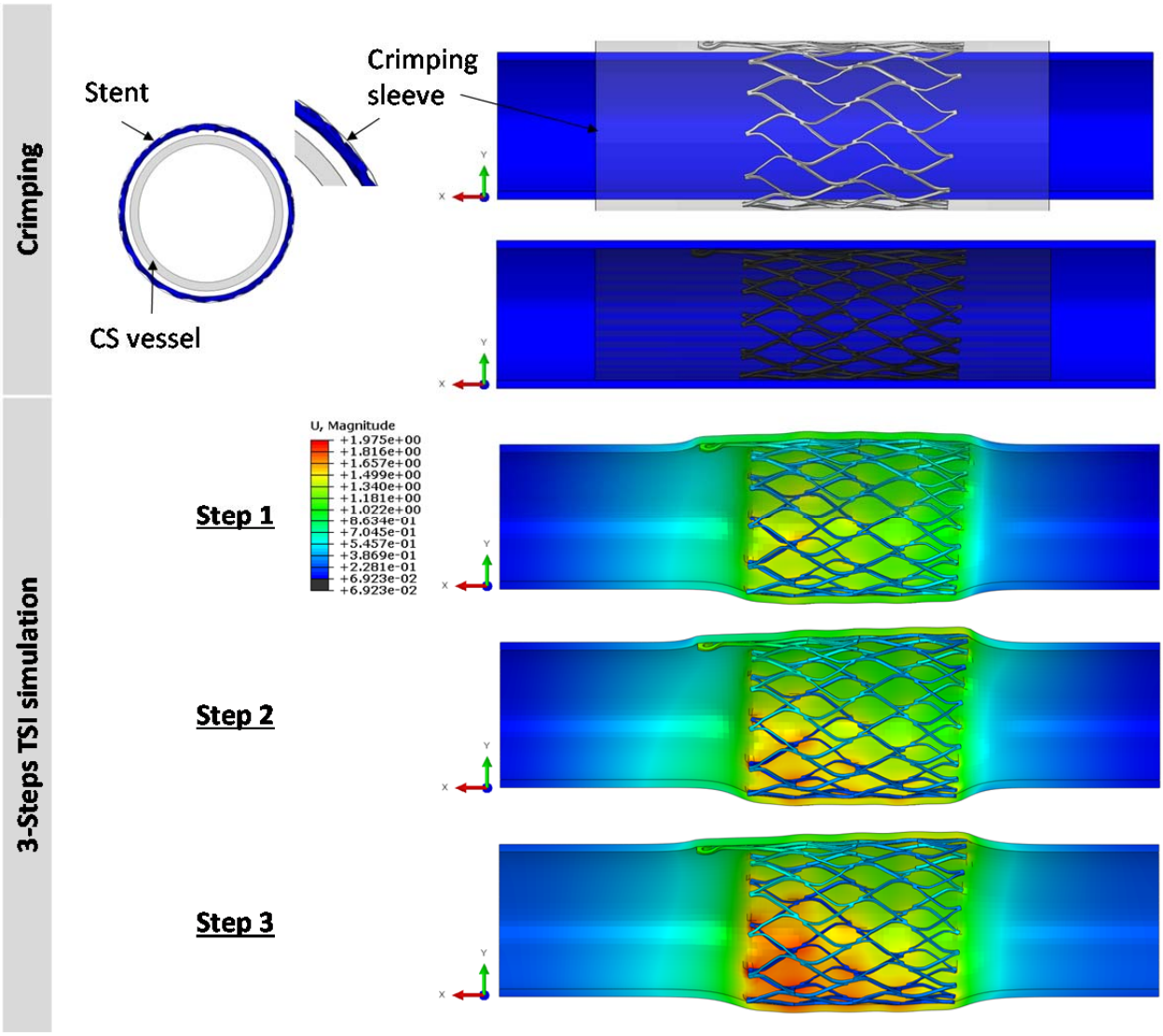

Figure 5-6: (Top) The crimping process was carried out by applying displacement control on the crimping sheath to decrease the diameter of the stent to less than 12 mm. (Bottom) The 3-step TSI simulation: step-1: release the crimping sheath, step-2: apply an axial load of 2.45 N, and step-3: apply a pressure of 10 mmHg to the inner wall of CS.

The coefficient of friction between the stent and CS inner wall contact surfaces was set to 0.1 in steps 1 and 2. For step 3, the contact definition was set as a non-slipping condition (an ABAQUS option: ROUGH) to imitate the effect of long-term tissue in-growth in-between the stent struts. The FE analysis was performed with the ABAQUS/Explicit release 6.11 on a high performance computing (HPC) Linux

cluster with Intel Xeon X5650 Westmere cores. The following output variables were analyzed in each of the three steps.

5.2.4 Finite Element output variables

1) Stress and strain. The von Mises stress was used to report the magnitude of peak stresses induced by stents on the vessel wall. To facilitate comparison between different models and avoid the bias caused by local high stress concentration, the 99-percentile values of the peak stresses of the CS vessel wall were evaluated [186, 187]. The 99-percentile values were computed by excluding 1% of all nodes containing the highest values (See Appendix A Table A2 for comparison between maximum (MAX) peak and 99-percentile stresses). Stent strains were analyzed with the maximum tensile strain variable (SDV24).

2) Contact forces. Contact forces between the outer stent surface and the inner surface of the CS vessel were extracted from the model. Elevated contact forces in the vicinity of stent struts may lead to injury of the CS inner wall, or ultimately causes tears of the posterior CS wall. Conversely, insufficient radial contact forces will prevent proper device anchoring. The contact forces have normal and shear components, denoted by *CNF* and *CSF*, respectively, and are expressed as:

$$CNF = \sum_{n=1}^{n_c} NF_{n,post},$$
$$CSF = \sum_{n=1}^{n_c} SF_{n,post} \qquad (6.2)$$

where n_c is the total number of nodes of the stent cell that are in contact with the CS inner wall, and $NF_{i,post}$ and $SF_{i,post}$ are the normal contact force and shear contact forces, respectively, at each node after deployment.

3) Stent fatigue analysis and safety factor [182]. Quantitative studies of metal fatigue often utilize the well-established Goodman-Haigh diagram [188], which is recommended by the FDA for stent fatigue

analysis [188, 189]. In Goodman diagrams, a pair of the mean stress or strain and its amplitude (or half-amplitude) at a particular point is plotted and compared with constant life curves [189] for that particular material. The mean tensile strain, ε, and the half-amplitude oscillating strain, Δε, at a given node are calculated by:

$$\varepsilon_{mean} = (\varepsilon_{\max} + \varepsilon_{\min})/2$$
$$\Delta\varepsilon = (\varepsilon_{\max} - \varepsilon_{\min})/2 \quad , \tag{6.3}$$

where ε_{max} and ε_{min} are the maximal and minimal strains, upon the application of 10 mmHg at a node on the PTMA stent after deployment. For a Nitinol material, the constant life curves from Pelton *et al.* [190] were used. Using the 0.4% strain amplitude delineated by the constant life line [190], the stent fatigue safety factor can be predicted using the equation: safety factor = 0.4%/half-amplitude strain. Four cases were analyzed: human-N1 (human CS vessel interacts with N1 stent), human-N2 (human with N2), porcine-N1, and porcine-N2.

5.2.5 Impact of stent strut thickness

The evaluation of PTMA device performance was performed based on two criteria: 1) inducing a minimal vessel injury and 2) enabling stent mechanical function (i.e., anchoring and fatigue life). The mechanical stress on the vessel wall induced by the stent strut cells often provokes vascular wall injury that stimulates the intimal hyperplasia [191]. Therefore, to minimize the vessel wall stress, the structural compliance of the stent needs to be low to meet the compliance of the vessel wall. In the meantime, the stent itself also needs to have enough structural strength to withstand the cyclic mechanical changes induced by cardiac pulsatile pressures, and have enough radial force for its anchoring mechanism.

The purpose of this study is to alter the stent design to reduce radial interactive forces. The approach includes maintain the same material properties of the stent and varying the strut thickness. Two stents models with different strut thickness values were developed. The results from these models include peak stresses and strains, interaction forces (shear and normal) of the CS wall and the stent, as well as the

device fatigue life and safety factor were compared to the original design, and differences between these design can provide insights into the stent designs that may help to reduce future device failure in the PTMA intervention.

Table 5-3. Values of undeformed design parameters of different stents

	No. of strut				
	Length	**Thickness**	**Circ.**	**Axial**	**No. of elements**
Original	26	0.30	12	2	114,000
Mod1	26	0.23	12	2	91,370
Mod2	26	0.18	12	2	68,532

5.3 Results

5.3.1 Vessel wall stress

The von Mises stress distributions on the CS vessel wall in Step 1 are illustrated in Fig. 5-7. It can be seen that peak stresses were located on the regions of the CS wall that were in contact with the strut links of the stent. The N1 stent induced the highest peak stresses on the human model, whereas N2 stent had the lowest peak stresses on the porcine model. The 99-percentile peak stress in the human CS induced by N1 stent was about two-fold higher than that in the porcine tissue, i.e., 31.40 kPa in human vs. 13.36 kPa in porcine. The stresses induced by N2 stent were slightly lower than those of N1 stent for both human (30.97 kPa) and porcine (12.57 kPa) tissues. In steps 2 and 3, as shown in Fig. 5-8a, there was a slight increase of the stresses in both human and porcine CS walls. The application of the axial force at the connector end and the internal pressure could result in the loss of wall apposition at the proximal end of the stent. As illustrated in the Fig. 5-8c, the porcine model had a gap between the vessel wall and the stent, whereas a better stent apposition was achieved in the human vessel, as shown in Fig. 5-8b.

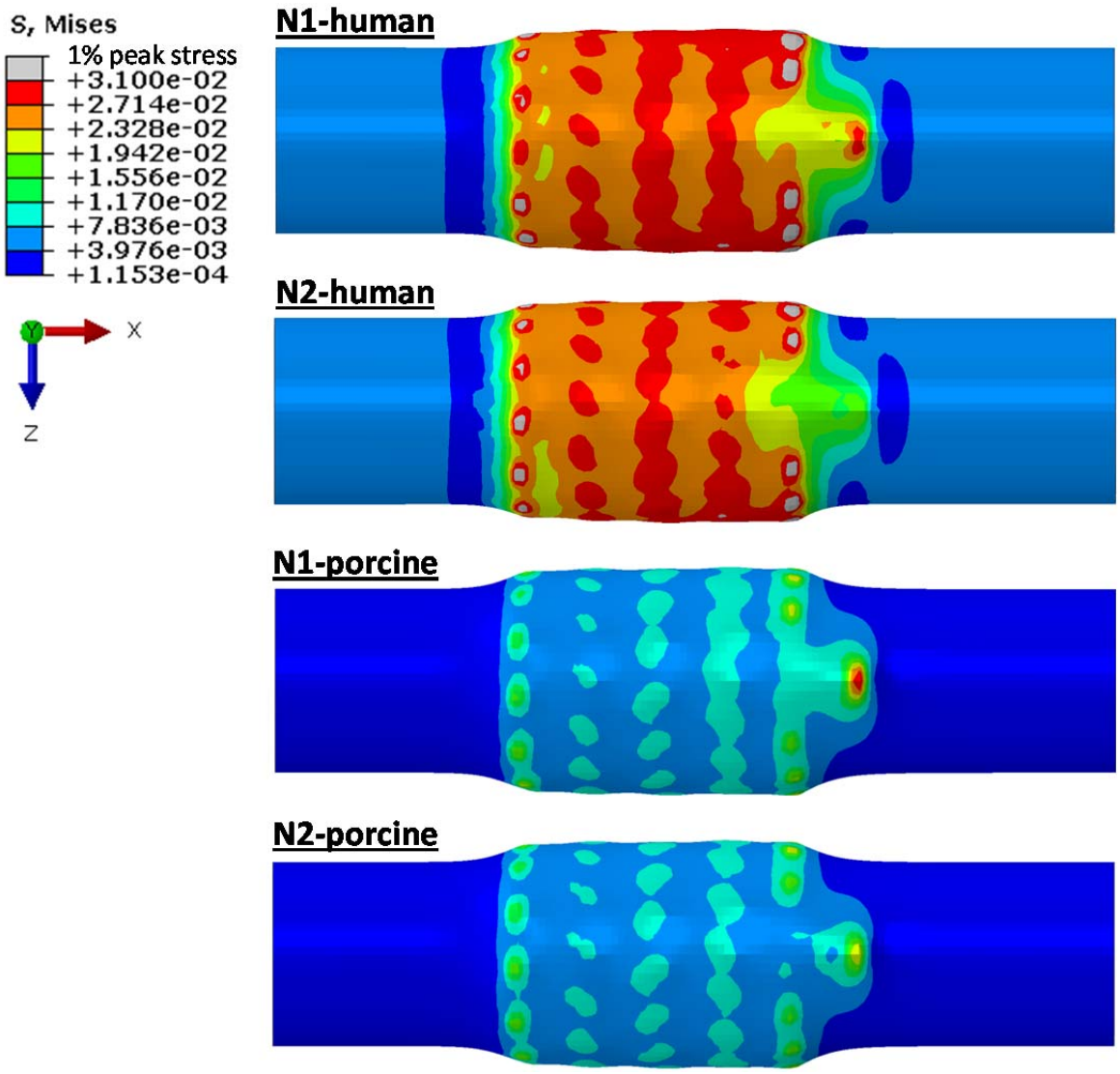

Figure 5-7: Contour plots of von Mises stress distribution on the human and porcine coronary sinus walls after initial contact with Nitinol stents (N1 and N2).

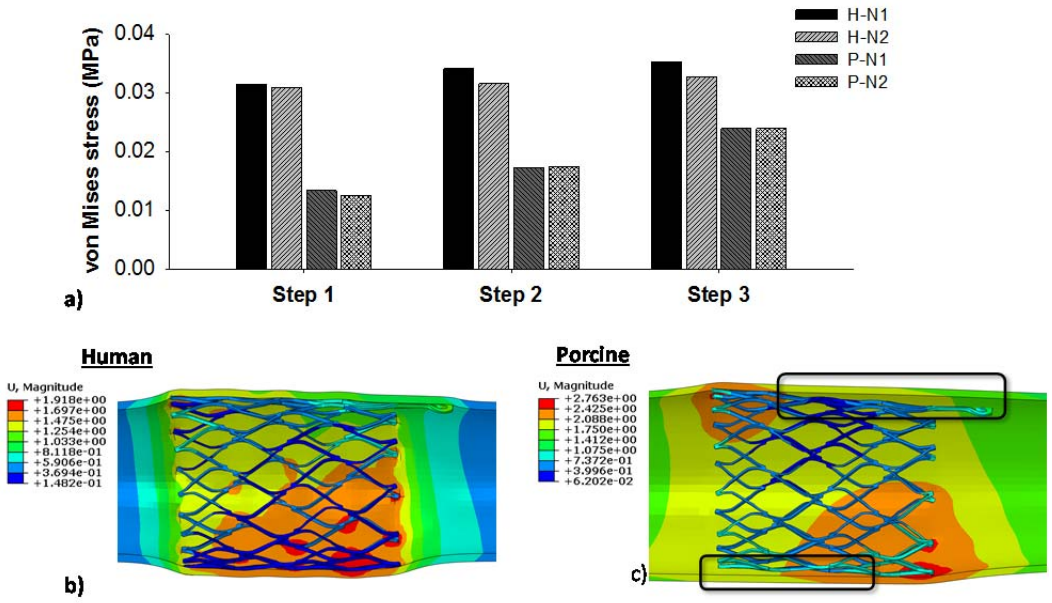

Figure 5-8: a) The 99-percentile peak von Mises stresses on human and porcine vessel walls imposed by N1 and N2 stents in the 3-step TSI simulation, b) the human-N1 interaction with a good stent apposition, and c) the porcine-N1 interaction where stent is separated from the vessel wall.

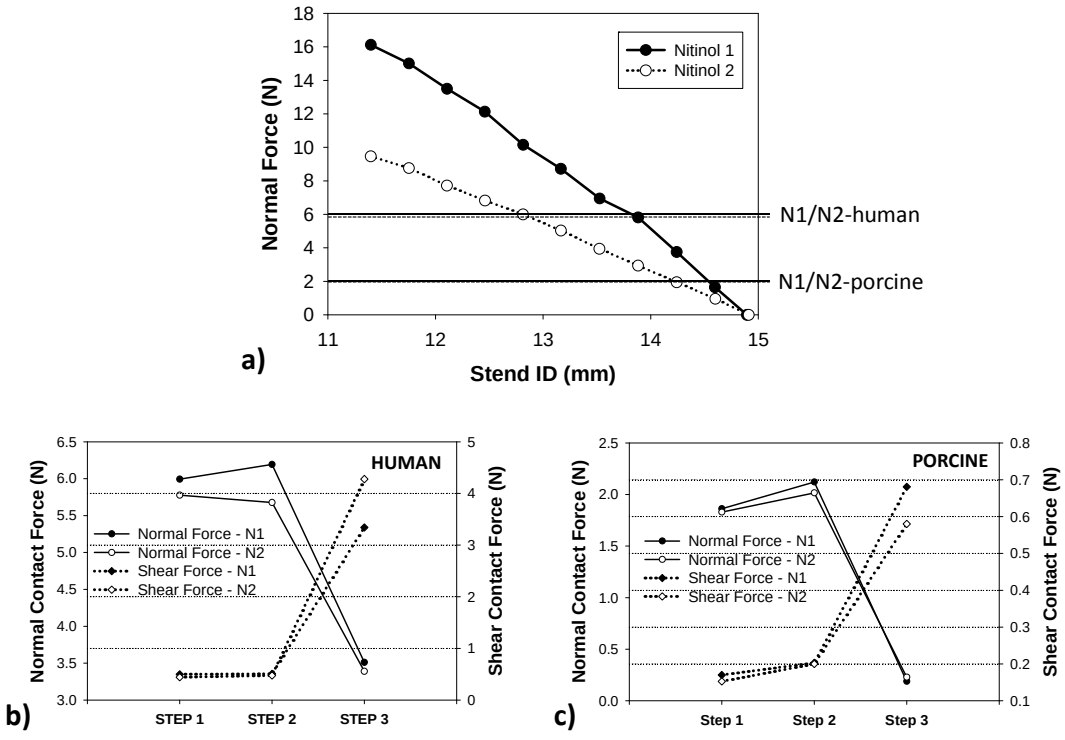

Figure 5-9: a) The relation between stents' inner diameter and radial force during crimping. Lines across the graph represented the maximum normal forces generated from stent N1 in human and porcine and dotted lines presented the N2 after step 1; the normal and shear forces in the 3-step TSI simulation for b) human and c) porcine in the 3-step TSI simulations.

5.3.2 Contact forces

Maximum interactive radial forces of 16 N and 9.5 N were needed to crimp N1 and N2 stents from the ID of 14.90 mm to 11.98 mm, respectively, as shown in Fig. 5-9a. In Step 1, the maximum radial forces imposed by the stents on the human CS wall were about three times larger than those in the porcine model, i.e., 5.99 N versus 1.86 N. It can be seen that in Fig. 5-9b & c, the stent N1 generated slightly higher normal and shear forces than the stent N2 at the initial contact in step 1, i.e., 5.99 N and 0.50 N vs. 5.78 N and 0.44 N for human and 1.86 N and 0.17 N vs. 1.83 N and 0.15 N for porcine, respectively. Both normal and shear forces slightly increased when applied an axial force of 2.45 N. In step 3, when a

pressure was exerted to the inner vessel wall, shear forces increased while normal forces dropped due to the tissue in-growth contact condition.

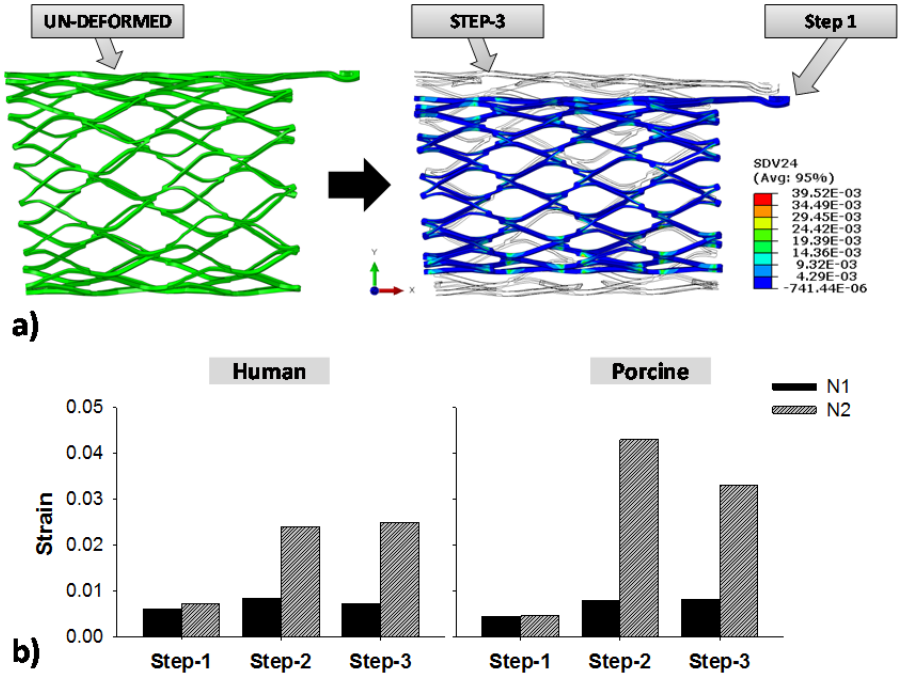

Figure 5-10: a) Visualization of the stent N1's undeformed geometry prior to crimping (left) and of the shape and strain contour of the stent after crimping overlapping with the shape after the step-3 (right); b) the maximum tensile strains in each step of both stents in the human and porcine TSI simulations.

5.3.3 Stent strain and fatigue analysis

Stent strain. Fig. 5-10a illustrates the un-deformed and crimped stent shapes, as well as the shape after step 3 for the N1 stent. The stent deformed nearly back to its original configurations at the end of the step 3. As shown in Fig. 5-10b, the peak strains of stent N1 stent did not fluctuate much throughout the 3-step simulation in both human and porcine models whereas they increased significantly in the N2 stent after step 1. The maximum strain on the stent in Fig. 5-11a was found to be at twisted struts near strut

links in all simulations. During steps 2 and 3, high strain regions were observed mostly at the strut link locations near the connector region (Fig. 5-11b).

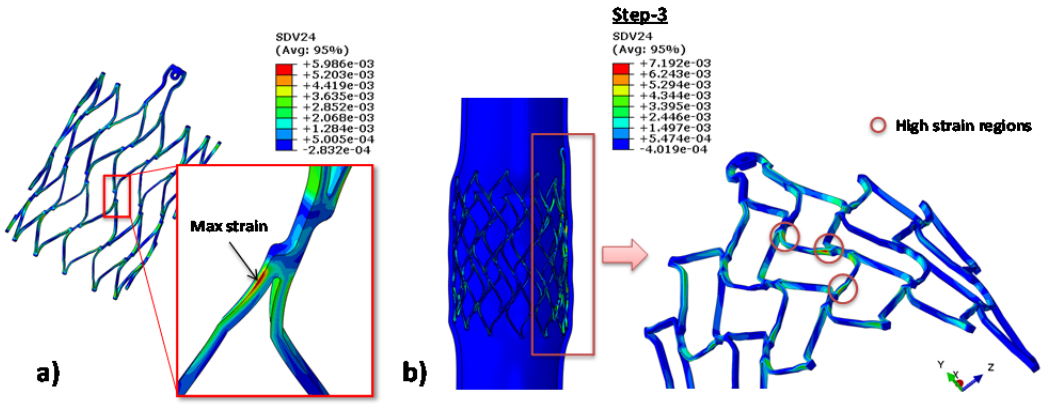

Figure 5-11: a) Common maximum local strain observed on the stent strut in all steps (N1 stent is shown), and b) regions that are under high strain after applied a pressure to the inner vessel wall for stent N1.

Fatigue analysis of stents. The Goodman diagrams in Fig. 5-12 plotted the fatigue-life responses of the two stents under a cyclic loading pressure of 0-10 mmHg. Although all strain values of the N2 stent in human and porcine tissues were below the constant life line curve of 0.4%, they were more scattered and wide-spread compared to the N1 stent. The maximum oscillating strain of the N1 stent in the human model was 0.23%, and its safety factor was 1.72. The safety factor of the N2 stent was higher, 2.98, with the oscillating strain of 0.13%. When deployed in porcine tissue, the N1 stent had a safety factor of 4.07. In contrast, a very high cyclic strain of 0.34% observed in the N2 stent resulted in a relatively low safety factor of 1.17.

5.3.4 Impact of stent strut thickness

Stress and strain analysis. It can be seen in Fig. 5-4 that the stent strut was twisted after expansion and annealing. The stent outer surface is not smooth. Thus, it is necessary to perform the expansion and annealing procedure to obtain accurate per-deployment stent geometries. Table 6.4 lists all

the maximum Von mises stresses and strains of the vessel wall, as well as three stent models. Both Mod1 and Mod2 stents are softer than the original stent model, resulted in higher maximum strains on the stent after releasing the stents. Stresses on the stent increased as strains increased.

Table 5-4 Maximum von Mises stresses and strains of CS wall and stent models

		STRESS (MPa)			STRAIN		
	Steps	**Original**	**Mod1**	**Mod2**	**Original**	**Mod1**	**Mod2**
CS WALL	1	3.47E-02	3.44E-02	3.30E-02	0.23	0.23	0.23
	2	3.66E-02	3.55E-02	3.52E-02	0.26	0.23	0.28
	3	3.58E-02	3.55E-02	3.46E-02	0.27	0.25	0.25
STENT	1	1001.00	955.00	947.40	2.49E-02	2.40E-02	2.38E-02
	2	358.60	380.00	371.60	4.96E-03	5.40E-03	5.32E-03
	3	444.70	480.30	525.90	6.37E-03	6.88E-03	7.54E-03

Normal and shear forces. Because stiffer stent generated a higher normal force, Mod1 and Mod2 stents exerted less forces compared to the original stent, as shown in **Fig. 5-9a**. There is a slight difference in forces between the stent models in steps 1 and 2 but no difference was observed in step 3. No device slippage was observed in step 2. Shear forces, illustrated in **Fig. 5-9b**, increased in step 3demonstrating the tissue in-growth over time.

5.3.5 Stent fatigue analysis

The strain amplitude of the original model is 8.43E-2% and the safety factor is 4.75. Decreasing in strain amplitudes of Mod1 and Mod2 (6.61E-2% and 6.68E-2%) resulted in higher safety factors of 6.05 and 5.98, respectively. Changing stent thickness does not reduce the fatigue life of the stent in the PTMA intervention. As shown in Fig. 5-12, strain points on the Goodman diagram of Mod1 and Mod2 are similar to the strain points of the original design, and all are condensed and below 0.1% strain amplitude and 1% mean strain.

This computational study indicated that PTMA device performance can be improved by altering the stent thickness. By reducing the stent thickness at a particular value, stress on the vessel wall can be reduced without compromising the stent anchoring forces and fatigue life.

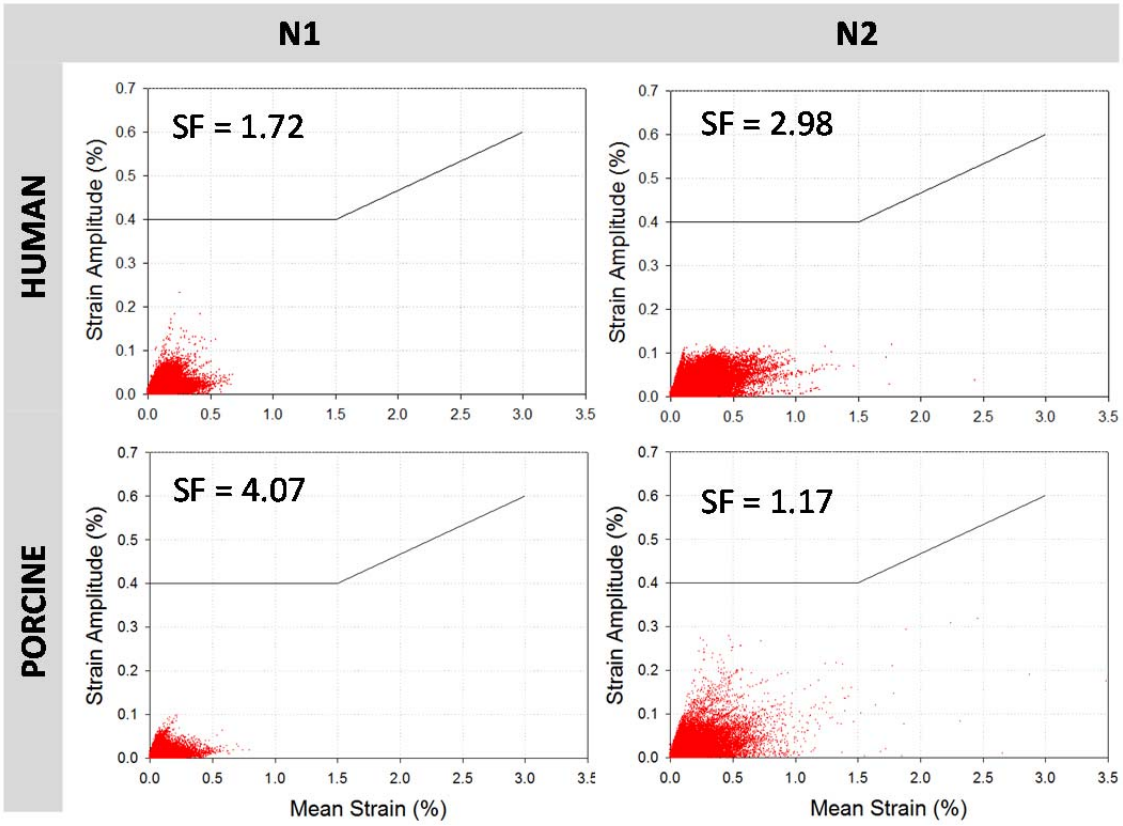

Figure 5-12: Goodman diagrams presenting the fatigue life of stents N1 and N2 after applied a 10 mmHg of pressure in the vessel walls, the black line represents the predicted fracture above 0.4 % strain amplitude for a range of mean strains.

5.4 Discussion

5.4.1 Interaction forces and stent migration implication

In this study, we simulated and compared the biomechanical interactions between two anchoring stents and two CS vessels – the human and porcine CS vessels. Under the same loading and boundary conditions, the stents deployed into the stiffer human vessel underwent much higher interactive normal contact forces than when deployed into the porcine vessel. In addition, a larger gap between the porcine wall and the stents was observed, suggesting that the potential for stent migration is much higher in the porcine model than in the human model. This result underscored the importance of the CS tissue

mechanical properties, and also brought up questions on the validity of using animal models to evaluate the device performance. We recently performed biaxial mechanical testing of CS tissues from three species: aged human (86.5 ± 9.7 years old), porcine (6 - 9 months old) and ovine (1 year old) tissues. It was also found that there were substantial mechanical property differences among these three species [192], with the aged human tissue being much stiffer than animal tissues. Older animals may provide stiffer tissue properties that are similar to aged humans, although this hypothesis has not been assessed.

In step 3, the contact definition between the CS wall and the stent was set as a non-slipping condition to imitate the effect of long-term tissue in-growth in-between the stent struts. This contact condition was designed mainly to study the long-term stent fatigue damage, during which tissue in-growth would occur. It should be also noted that the axial pull mechanism from the bridge elements of the PTMA device occurred gradually and would not be fully active until the imbedded suture dissolved completely over approximately 1 month. During this period of time, stent anchoring inside the vessel may be enhanced because of the tissue in-growth. In the immediate post-deployment period, the normal contact force would be the dominant force. Without the axial pull the chance of stent migration is low. Moreover, the PTMA procedure is a beating heart operation, any immediate migration of the device may be corrected immediately in the operation.

Additionally, to investigate the no tissue in-growth condition, we further investigated the normal and shear forces in step 3 by setting the coefficient of friction between the stent N1 and the human CS inner wall as 0.1. From the simulation results, no stent migration was observed in step 3. The normal force of 3.55 N was similar to the original (rough, non-slipping) model of 3.52 N. The shear force, though, was reduced to 0.34 N while the shear on the original model is 3.34 N, as one would expect.

Another factor that could impact the stent migration is the CS geometry. We assumed the CS vessel was a cylindrical tube at the anchoring location. The actual anatomic geometry of the CS vessel has a larger diameter at the ostium and becomes narrower towards the GCV vessel, which may help prevent the stent from migrating towards the GCV vessel. However, this effect was not investigated in this study.

5.4.2 Vessel and stent fatigue damage implication

Vessel wall stress. Stent migration and perforation of CS vessel wall are the two competing factors that require a delicate balance of the expansion force of the deployed stent. A higher interactive force will facilitate the stent anchoring but may also cause damage to the CS vessel wall. The maximum peak stresses on the CS wall were about 0.5 – 1 MPa for the human model and about 20 – 200 kPa in the porcine model. Currently, the published data on the ultimate tensile strengths (UTS) of human CS wall tissues are limited. One study reported the UTS of porcine CS vessel, which are in the range of 1.66 – 2.57 MPa [193].Thus, based on the simulated peak stresses and the reported UTS of porcine CS tissue, the perforation of porcine CS wall would not occur. Moreover, we noticed that the peak stresses were concentrated on a very small number of nodal points, which represented less than 0.06% of total nodal points of the CS wall and were mainly located at the regions of the proximal and distal ends of the stent. The high stress concentration might be due to the excessive bending of the elements as a result of geometrical changes from expanded tissue-stent contact region to the non-tissue-stent contact region. Thus, to avoid local stress concentrations, the 99-percentile peak stress was adopted for the comparison among the four models [187, 194].

Stent fatigue analysis. In this study, we investigated the stents made of two different Nitinol materials. We found that the interactive forces induced by the two stents were similar; however, the fatigue safety factors of the four models were quite different. The stent N1 had a lower safety factor when deployed in human than porcine, while stent N2 had a better safety factor in human than porcine model. This result suggested that the stent material properties could have an impact on stent durability, but not significantly on its interactive responses with the CS tissues. Thus, a greater impact on the biomechanical interactions may be achieved by changing the structural design of the stent. Computational and clinical studies [195, 196 , 197] have shown that decreasing the stent strut thickness has favorable outcomes in terms of lower chronic vessel stresses and lower clinical restenosis rate, which may be a direction for further improving the stent design.

5.4.3 Clinical relevance

Currently, there are several percutaneous devices utilizing a similar trans-coronary sinus concept to reduce the dilated mitral annulus. For instance, the CARILLON device (Cardiac Dimensions, Kirkland, Washington), which consists of distal and proximal anchors (Nitinol and titanium) and joined by a Nitinol ribbon connector, could reduce the dilated annulus by manually pulling the proximal anchor toward the CS ostium. Due to the difficulty in anchoring to the CS wall, a second generation device was developed with a twist at the distal anchor. The device was implanted in humans for up 6 months of follow-up [77]. A total of 30 out of 40 patients successfully received the device with an average of 23% MR reduction. However, three patients suffered from CS perforation and dissection. Another device, Viacor (Viacor, Wilmington, Massachusetts), consists of up to three rigid Nitinol rods. Various rod sizes and stiffness are used to achieve the desired MR reduction. The issues with this device were associated with fracture, migration and delivery failures due to the vast difference in CS structures and geometries [27, 78]. Patients not only have high variability in CS anatomical structures, the mechanical properties of CS also varied greatly, as shown previously by Pham and Sun [192].

The current adverse events are associated with vessel injury (e.g. perforation and dissection) and device malfunctions (e.g. migration and fractures), which possibly are the results of mechanical mismatch between the implanted devices and the CS tissues. For instance, the CARILLON anchors were formed by two wires twisted together. Hence, lack of a sufficient stent-tissue contact surface might result in high stress concentration leading to perforation of the CS wall, as well as high possibility of device slippage. Fractures of the VIACOR device might be due to its lack of flexibility and stress reduction (due to its rod structure) to accommodate the dynamic motion of the CS vessel wall. Clearly, rigorous engineering analysis is warranted for the investigation of these device malfunctions.

6 Simulation of Complete PTMA Device Deployment into Patient-specific CS*

In the previous chapter, we have introduced a FE method to analyze the biomechanical interaction between the proximal stent and the ostial region of the CS vessel. In this chapter, we added several key components of the delivery systems which are essential to the final deployed configuration as seen clinically. It is well known that human anatomy is highly variable and the procedural outcomes of any medical devices are essentially related to anatomic considerations. In this study, for the first time, we will introduce FEA of a complete PTMA device being deployed within a selected patient-specific CS model. Several techniques used to reconstruct 3D patient-specific model will be first reviewed in Sections 6.1.1-2 and a technique of reconstructing the CS will be introduced in Section 6.2.1. Next, the analysis of tissue-stent interaction (TSI) will be divided into two phases. In phase 1 in Section 6.2, three patient-specific CS models were selected and PTMA stents were modeled with a simplified bridge section. A complete PTMA stent with bridge section and the entire deployment process will be introduced in Section 6.3. Evaluation of the stent and its interaction with the CS vessel as well as the predicted clinical outcomes were analyzed for each phase.

* Some of the contents of this chapter are taken from:

W. Sun, C, Martin and **T Pham**, "Computational Modeling of Heart Valve Function and Intervention ", ***Annual Review of Biomedical Engineering,*** accepted.

6.1 Introduction

6.1.1 Patient-specific noninvasive imaging modalities

Much of the recent advancement in valvular heart disease evaluation and treatment can be attributed to the advent of noninvasive cardiac imaging modalities, such as echocardiography (Echo), magnetic resonance imaging (MRI), and computed tomographic imaging (CT), which are now being used extensively for diagnostics and risk evaluation. Clinicians rely heavily on Echo for evaluating aortic and mitral valve morphology. In particular, transesophageal echocardiography (TEE) is used extensively for the evaluation and diagnosis of MV pathology as well as the feasibility of repair. The 2D TEE provides high quality images of the MV, yet sometimes the site and degree of prolapse can be incorrectly identified from 2D images [198-200]. Consequently, 3D TEE is being increasingly adopted. However, as TEE has a relatively poor spatial resolution compared to MRI and CT, MRI is preferred for analyzing valvular flow characteristics. Because CT has been shown to facilitate accurate and reproducible AV annular measurements compared to Echo [201], it is more relevant in geometric measurement applications, particularly in transcatheter aortic valve (TAV) intervention where AV geometries are of importance.

6.1.2 Valvular imaging process and segmentation

The precise patient-specific geometry and location of valvular features is of critical importance for the proper diagnosis and treatment of valvular diseases. Recently, several research groups have obtained in vivo AV and MV geometries using Echo [57, 202-204], MRI [33, 46, 58] and multi-slice CT scans [44, 45, 205-207] to reconstruct patient-specific aortic and mitral valve models. From these images, it is often difficult to identify the more delicate valvular substructures such as the leaflet free edge and chordae tendineae. A more accurate description of the valve structures is achievable, but these methods often employ manual tracing or manual geometrical reconstruction by point selection and interpolation [57]. Now, many groups are using semi-automatic methods to segment the valve structures

from clinical images through standard image processing techniques such as intensity-based thresholding to distinguish the valve structures from the surrounding blood pool [32, 44, 58, 207].

Many of the segmentation methods discussed previously are static or at one time snap-shot. The segmentation process would have to be repeated for additional time points in order to analyze the dynamic valve geometries through the cardiac cycle. Real-time visualization of the 3D valve geometries throughout the cardiac cycle could also greatly benefit clinicians. There are now a couple dynamic valve models in the literature to address this need. Veronesi *et al.* [208] were among the first group to quantify the 3D AV and AV dynamics from matrix array transesophageal images. The AV and MV features were semi-automatically detected and then automatically tracked through the cardiac cycle. Ionasec *et al.* [209] have also developed a dynamic model of the aortic and mitral valves with the ability to capture morphologic and pathologic differences over an entire cardiac cycle based on the trajectories of landmark points. The robustness and accuracy of the method was demonstrated by extensive experiments on 1516 TEE and 690 cardiac CT volumes with an average processing time of 4.8 seconds and an average accuracy within 1.45 mm of the expert defined ground-truth. The use of subject-specific dynamic valve models for pre-operative planning holds great promise; however, an automated, fast, and user-friendly method to load 3D imaging data, refine them into nonlinear FE models, and from there to further visualization and simulation processing has not yet been accomplished.

In this Chapter, we adopted the semi-automation method to reconstruct the geometry of the CS vessel for the purpose of analyzing the tissue response after PTMA stent deployment. Full phase cardiac MSCT scans were collected from patients at Hartford Hospital (Hartford, CT). Institutional Review Broad approval to review de-identified images was obtained for this study. Selected patients with very good visualization of the CS geometry were selected and digitized at our laboratory.

6.2 Modeling the biomechanical interaction of a whole PTMA deployment into the CS

6.2.1 Patient-specific model of the CS vessel

Del Valle-Fernandez et al. [84] studied the dynamic anatomy and the relationships of the CS/GCV and its spatial relation with the MA using multi-detector computed tomography angiography (MDCTA). Through the injection of nonionic contrast media through a peripheral vein, CS vasculature could be visualized and at various phases of a cardiac cycle (40%, 75% and 0% of the RR interval presenting the end-systole, mid-diastole and end-diastole, respectively) were analyzed using the EKG signal. They found that the geometries of the CS/GCV were statistically significant different among the 3 phases of the cardiac cycle, with the largest diameter and area observed at phase 40% (end-systole) and the smallest dimensions observed at phase 0% (end-diastole). Therefore, the reference (initial) geometry of the CS/GCV was reconstructed at the end-diastole phase.

The MSCT examination was performed on a GE LightSpeed 64-channel volume computed tomography scanner. In general, a total of 2000 slices of images with thickness of 0.625 mm were collected for the whole cardiac cycle [205]. A collimation of 25-30 × 0.625 mm and a rotation time of 375 ms were used resulting in a temporal resolution of less than 200 ms depending on the heart rate and pitch. Typically, 10 phases can be obtained for each cardiac cycle. MSCT images of the CS at end-systole and end-diastole were imported into Avizo 6.7 software (VSG, Burlington, MA) for 3D reconstruction and evaluated using a selected range of Hounsfield units. The end-systole was identified on a frame after mitral valve closing and before mitral valve opening, while the end-diastole was identified prior to mitral valve closing and after mitral valve opening. For each phase, the CS ostium was first identified at the right atrium in view 3 in Figure 6-1, which shows the curved planar geometry of the vessel. Upon manually tracing the CS in several frames, the cross section of the CS were automatically marked in views 1 and 2, which show the CS relative position to the mitral valve. The 3D presentation of the vessel was formed after generating a surface and formulating tetrahedral mesh in Avizo.

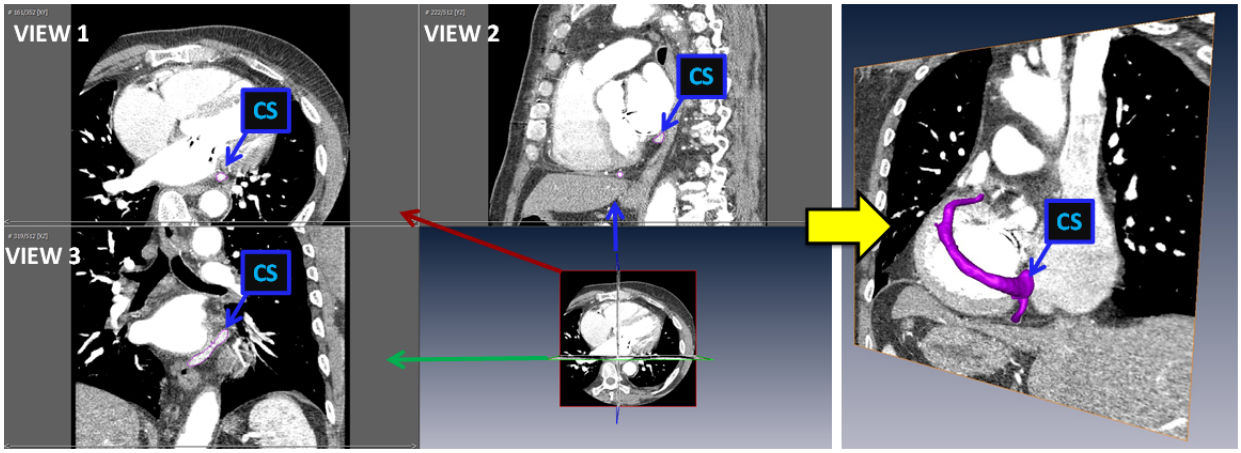

Figure 6-1: The 3D reconstruct of the coronary sinus (CS) using three views, xy (view 1), YZ (view 2) and XZ (View 3) using Avizo image-processing software and meshed using Hypermesh software.

6.2.2 Patient selection

From the 14 CS vessel reconstructed models, three CS models were selected for the analysis of PTMA stent deployment. The geometrical measurements of the CS vessel includes the CS and GCV diameters, the length of septal-lateral and anterioposteior mitral annulus, the distances between the CS ostium and middle cardiac vein, between the middle cardiac vein and left marginal vein, between the great cardiac vein and the left marginal vein, see Figure 6-2. Table 6-1 summarizes the CS and GCV's diameters and their respective proximal and distal anchor's diameters.

Table 6-1. Patient CS geometries and their respective stent geometrical measurements.

	Length (mm)		Thickness (mm)				Inner Diameter (mm)			
	CS	Stent	CS	GCV	Prox	Dist	CS	Prox	GCV	Dist
P1	103.67	82.45	0.61	0.51	0.30	0.30	10.53	14.88 (+4)	4.71	8.47 (+4)
P2	108.20	76.00	0.74	0.37	0.30	0.25	6.76	12.00 (+5)	5.21	6.83 (+2)
P3	118.70	89.20	0.74	0.37	0.30	0.30	10.04	14.88 (+4)	4.24	8.47 (+4)

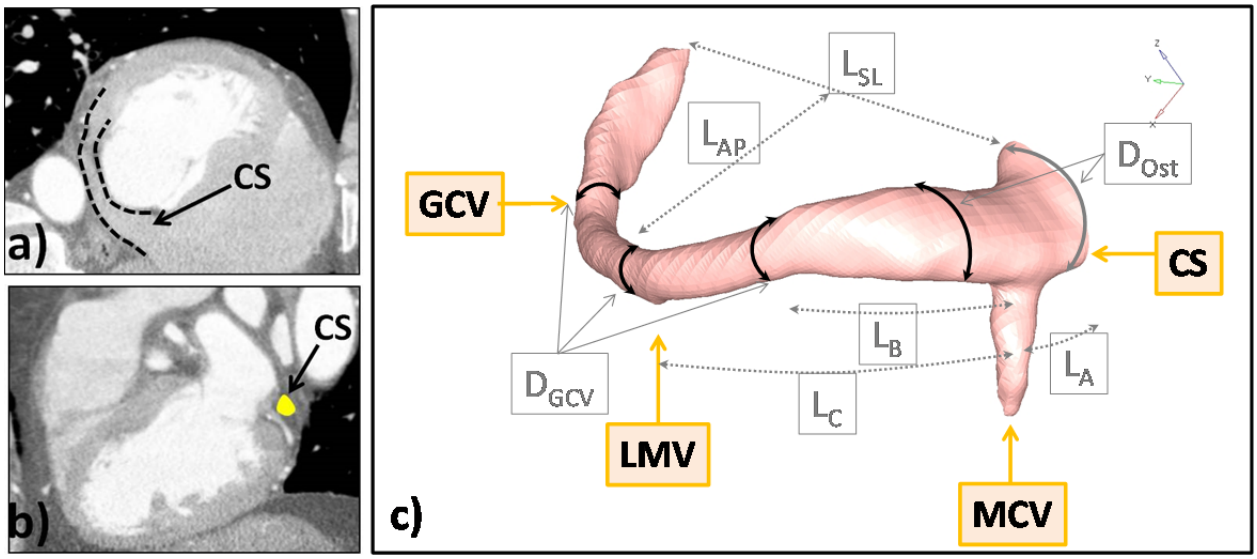

Figure 6-2: Representative CS vessel identified from a patient CT images in a) short-axis and b) long-axis views, and c) the CS vessel geometrical measurements. L_{sl} – length of septo-laterol mitral annulus, L_{ap} – anteroposterior length, D_{gcv} – Great Cardiac Vein dia., D_{ost} – CS ostium dia., MCV – Middle Cardiac Vein, LMV – Left Marginal Vein

6.2.3 Tissue properties and modeling techniques

The CS material parameters were obtained from fitting the experimental pressure-inflation data collected from four cadaver CS vessels to the nonlinear hyperelastic Ogden model as specified in Chapter 5. Please refer to Table 5-2 and Fig. 5-5 for the mean values of material parameters and mechanical behaviors of human CS vessels and of a Nitinol stent material, respectively.

The simulation process was divided into three steps: Step 1: Releasing both anchors into contacts with the CS wall. Step 2: Connecting the bridge element to the distal anchor connector. Step 3: Applying the CS pressure in the vessel wall. The analysis was run with ABAQUS/Explicit v6.9 on a Linux cluster using 12 2.8GHz CPUs. The tissue-stent interaction (TSI) was evaluated based on the following parameters: 1) the normal and shear contact forces between both of the stents and the corresponding vessel wall, 2) the maximum tensile strain of the stents and maximum principal strain imposed on the CS vessel wall, and 3) Von Mises stresses of CS wall.

6.2.4 Finite element simulation results

Figure 6-3 a&b show the CS and GCV strain and stress distributions in the three-step simulation. Due the smaller size of the GCV, all GCVs were overstretched more than the CS ostium. As the result, the GCVs exhibited significantly higher stresses and strains compared to the CS ostial regions. It could be that the tortuosity of the CS vessel plays a role in the overall wall stress. For instance, for the less tortuous vessel, stent can conform well to the vessel curvature and no local high strain to be observed. Patient 3 has a very tortuous CS geometry where the GCV section was constricted, as shown in Figure 6-4. As the result, highest wall stress was observed, see Figure 6-3b. The radial forces generated by the distal anchors were greater than by the proximal anchors after stent release and come in contact with the vessel wall in step 1, Figure 6-3c. The normal forces were greater than the shear forces in all simulation, which indicated a less likely of stent migration. From Figure 6-3c, it can be seen that patient 2 exhibited lower distal normal force than proximal normal force. It could be that the GCV was only 11% over dilated while patients 1 and 3 were 32.22% and 38.29% over dilated, respectively.

We approximated the mitral annulus area by measuring the change in the region encircled by the CS vessel from the undeformed to the final step. The results show that on average, 15% of the area was reduced in three patients.

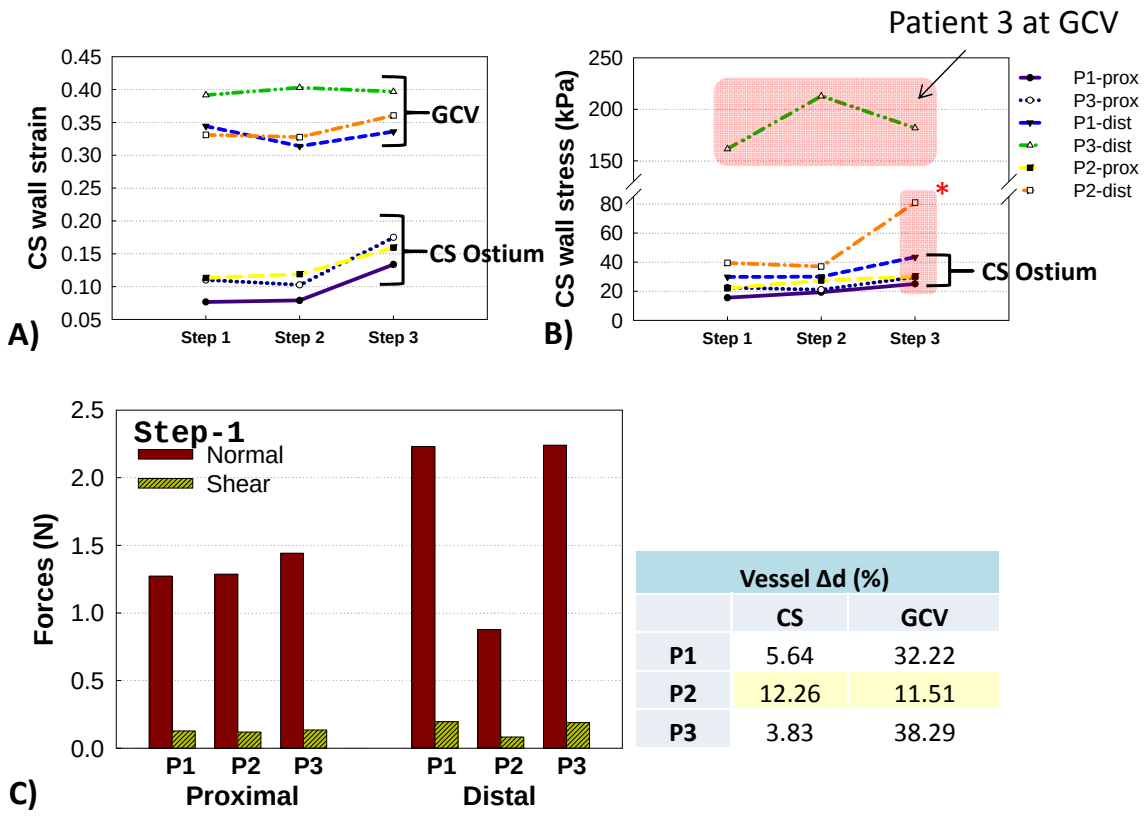

Vessel Δd (%)		
	CS	GCV
P1	5.64	32.22
P2	12.26	11.51
P3	3.83	38.29

Figure 6-3: a) CS vessel stress and strain results and the normal in the three simulation steps; and b) normal and shear forces of the proximal and distal anchors after stent release and come in contact with the CS vessel wall in Step 1.

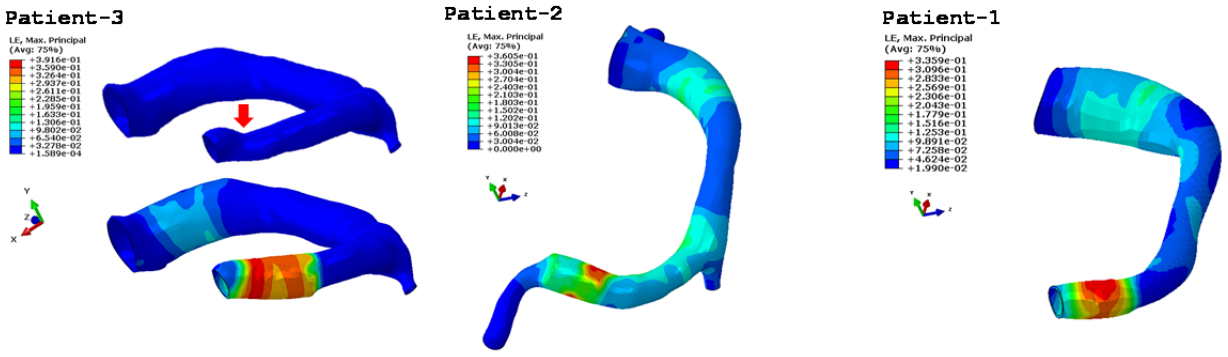

Figure 6-4: Strain distribution on the cs ostial and Great Cardiac Vein sections after step 3.

A consistent increase and decrease pattern of normal contact forces was observed in all patient results, see Figure 6-5. Shear forces were very low in step-1 due to the stent expansion. The shear forces increased dramatically in step 2 as the bridge section connected to the distal stent. Shear forces become greater in step 3 in patients 2 and 3 after applied a CS pressure of 20 mmHg. However, because it was not significantly greater than the normal force, no stent migration was observed. In patient 3, the shear force was smaller than the normal force. This could be that the bridge section is slightly longer.

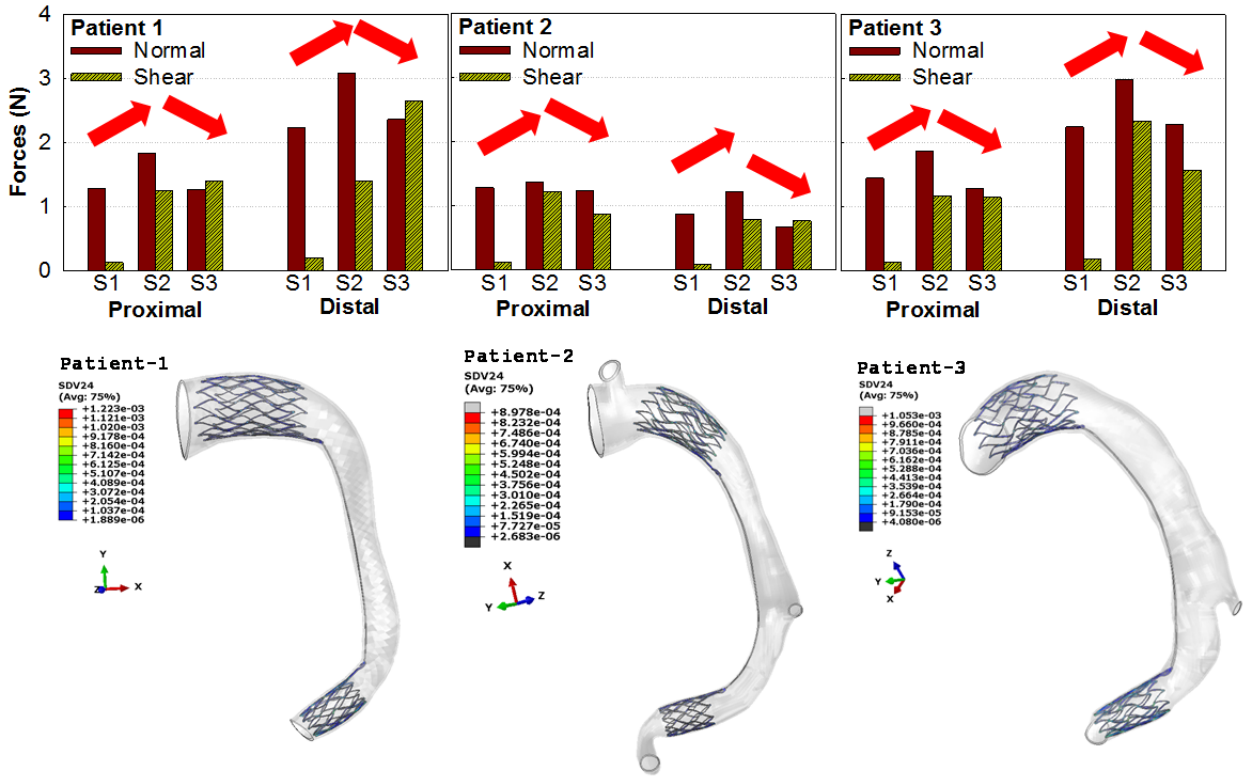

Figure 6-5: The reactive forces in each of the three deployment steps for three patients, and the CS/stent deformed shapes of the three patients.

A longer bridge section in patient 3 could affect the functionality of PTMA stent. It can be seen in Table 6-2 that the stent length for patient 3 is 89.20 mm or bridge length of 48.96 mm, which is longer than patients 1 and 2. As the result, patient 3 has a lower reduction in mitral annular area compared to patient 1, 13.88% versus 16.75%. For patient 2, although the bridge length is shorter than patient 1, it's CS length is 5 mm greater, which resulted in smaller mitral annular area reduction. To summarize the

results, the shorter the stent is relative to the CS length, the more reduction is in mitral annular area, although too short stent might increase the chance of stent slippage. Table 6-2 also shows the change in the left ventricle end-systolic (LVES) from patients undergo PTMA intervention in Harnek *et al.* study. It has been shown that the mitral annular size linearly correlates with the changes in left ventricle end-systolic (LVES)/end-diastolic (LVED) volume. Therefore, this study showed that a reduction in mitral annular area is within the range reported in clinical study.

Table 6-2. The reduction in mitral area and the left ventricle end-systolic (LVES) and the corresponding stent length.

	CS_L (mm)	Stent_L (mm)	Bridge_L (mm)	ΔA (%)		Δ-LVESV (%)	Follow-ups
P1	103.67	82.45	41.50	-16.75	**Harnek et al.**	-6	3 mo
P2	108.22	80.63	43.13	-7.91		-4	6 mo
P3	118.80	89.20	48.96	-13.88		-17	12 mo

6.3 Modeling of a complete PTMA device deployment with a delivery catheter system

In this section, we selected a patient from our database to study the TSI incorporating two additional features: (1) a complete PTMA stent model with 'spring-like' bridge section incorporating the effect of bio-degradable material and (2) a complete stent deployment process including the stent delivery catheter components. By adding these two features, PTMA stent deployment and its interaction with the CS vessel wall will be more accurately simulated and analyzed.

6.3.1 Patient selection

The patients chosen for this study was a 49 years old female. She was selected for CT scans for suspicion of coronary artery disease. However, from her full-heart CT scans, there was no sign of calcification in her coronary arteries, as well as no indication of calcification elsewhere. Her left ventricle size was normal and the mitral leaflets coapt properly at mid-systole phase. Therefore, this patient is considered healthy.

6.3.2 Modeling of complete PTMA device with pre-stretch biodegradable materials

The PTMA device consists of three components: the proximal, distal and bridge. Details on the modeling method of the proximal anchor were previously mentioned in Chapter 5. The structure of the distal anchor is similar to the proximal anchor but smaller in size and the number of strut cells. There are 9 and 2 cells in the circumferential and axial directions, respectively. The bridge section is a 'spring-like' section that can be elongated and retracted. A biodegradable material (BMD) is incorporated within the bridge section and maintains the device in an elongated form before and during implantation. The 8-node hexahedral linear incompatible mode element (C3D8I) was chosen to mesh the stent as C3D8I is preferred for stent analysis due to the nature of bending during loading without experiencing hourglass effect for relatively coarse mesh. The proximal and distal anchors were modeled with 2,251 and 1,371 elements and 8,432 and 5,048 nodes, respectively. The 8-node hexahedral linear reduce-integration mode element (C3D8R) was chosen to mesh the bridge with 1,723 elements and 6,264 nodes. The biodegradable component was modeled using 468 C3D8R elements with 1664 nodes. The CS vessel was also modeled using 18,630 C3D8R elements and 25,020 nodes with four layers through the thickness. For the C3D8R element, hourglass control stiffness was utilized to mitigate the strain-free hourglass modes when loaded in bending. In order to ensure proper hourglass control was used, the kinetic energy was carefully monitored and kept below internal energy.

The tension of the bridge is determined by prestretching the entire bridge. To prestretch the bridge, displacement control was used to extend the bridge about 20 mm. According to the manufacture standard, PTMA device length is 20 mm shorter than the CS implantation length. In order to retain the tension of the bridge after the bridge was prestretched and throughout the simulation, BDM, which is modeled as brick element, was incorporated within the bridge cells, as shown in Figure 6-6. Contacts between the BDM and the bridge elements were enabled after the first prestretch step with a rough surface interaction (*friction, rough).

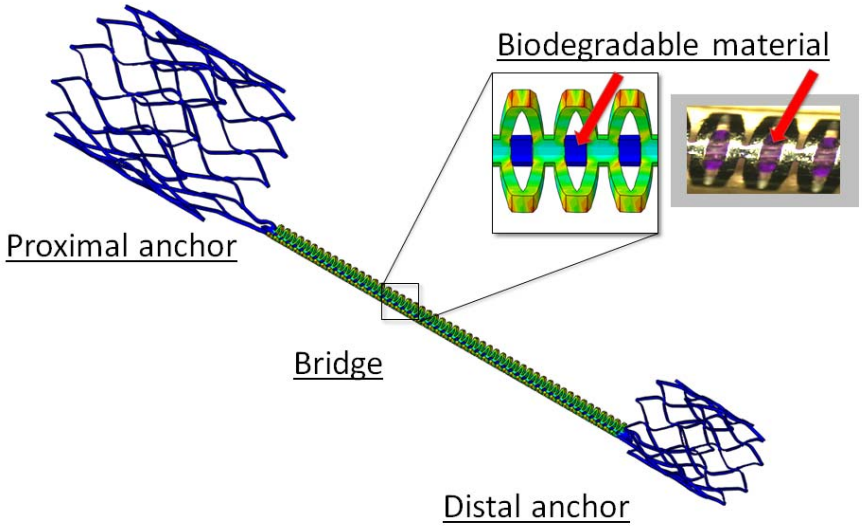

Figure 6-6: Proximal and Distal Anchors and the bridge section with biodegradable material (BDM). The popup window shows a realistic and simulation demonstration of three bridge cells with three BDM's sandwiched in-between.

6.3.3 Delivery catheter system and process

6.3.3.1 Components of the delivery catheter system

The delivery catheter system consists of several components. In this study, we did not include a complete delivery system. We mainly focused on the biomechanical interaction between the device and the CS vessel, therefore, we simplified the system to include: the crimper, guide wire and catheter. Other anchoring components were also used during stent crimping and releasing within the catheter: inner tube and plate components are to stabilize the bridge section and the distal stent during crimping, respectively. Figure 6-7 shows the delivery components as well as their respective locations.

6.3.3.2 Stent crimping process

Both the proximal and distal anchors were crimped to a 3 mm ID catheter. The crimper was modeled as a cylindrical tube with shell elements. Displacement-controlled deformation of the crimper

was utilized to crimp the stent to the diameter smaller than 3 mm. The inner-tube component, modeled as cylindrical tube with shell elements, was also radially displaced during this step to stabilize the bridge element during crimping. The 4-node quadrilateral element (M3D4R) was used to mesh the crimper, catheter and inner tube with 966, 12426 and 2173 elements and 987, 9752 and 2214 nodes, respectively.

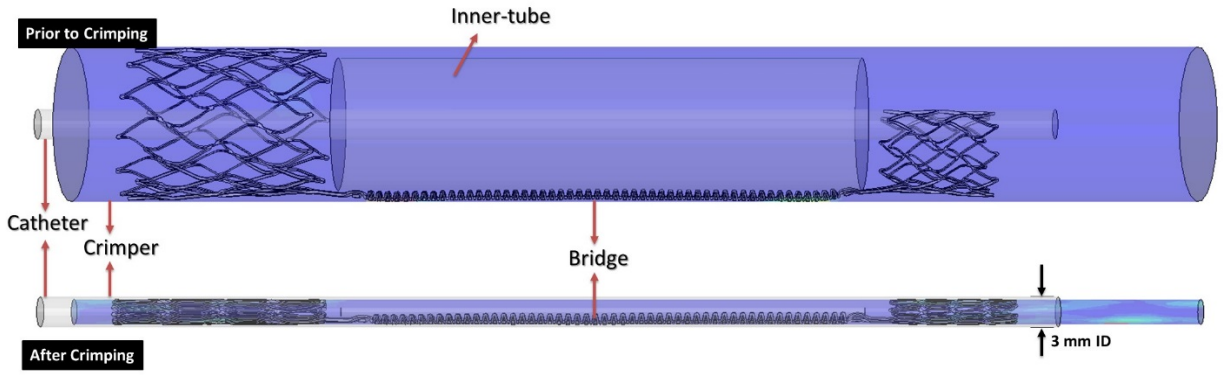

Figure 6-7: Prior and after crimping process showing the geometries of the PTMA stent, crimper, catheter and inner tube.

6.3.3.3 Deployment of PTMA stent and boundary conditions

Deployment of the PTMA stent was first achieved by delivering a catheter into the CS vessel. The delivering route of the catheter was specified by a motion path along the CS vessel. Clinically, the geometry of the CS vessel can be visualized by injecting a contrast agent and imaging with echocardiography. A practitioner then can have a visualization of a CS geometry and then maneuver the catheter through the vessel. The motion path is formulated and carried out by a set of unit vectors, their angles of rotation and velocities.

The unit vectors were selected at various locations within the CS vessel. The angles of rotation between two unit vectors were calculated from their rotational matrix. According to Euler's rotation theorem, any rotation of a rigid body may be described using three angles: φ, θ, ϕ. A rotation of an angle of φ about x-axis is defined as:

$$R_x(\varphi) = \begin{bmatrix} 1 & 0 & 0 \\ 0 & \cos(\varphi) & -\sin(\varphi) \\ 0 & \sin(\varphi) & \cos(\varphi) \end{bmatrix} \tag{6.1}$$

A rotation of an angle of θ about the y-axis is defined as:

$$R_y(\theta) = \begin{bmatrix} \cos(\theta) & 0 & \sin(\theta) \\ 0 & 1 & 0 \\ -\sin(\theta) & 0 & \cos(\theta) \end{bmatrix} \tag{6.2}$$

A rotation of an angle of ϕ about the z-axis is defined as:

$$R_z(\phi) = \begin{bmatrix} \cos(\phi) & -\sin(\phi) & 0 \\ \sin(\phi) & \cos(\phi) & 0 \\ 0 & 0 & 1 \end{bmatrix} \tag{6.3}$$

A generalized rotation matrix can be described as:

$$R = R_x(\varphi)R_y(\theta)R_z(\phi) = \begin{bmatrix} R_{11} & R_{12} & R_{13} \\ R_{21} & R_{22} & R_{23} \\ R_{31} & R_{32} & R_{33} \end{bmatrix} \tag{6.4}$$

To solve for ψ, we know that

$$\frac{R_{32}}{R_{33}} = \tan(\varphi) \tag{6.5}$$

Then

$$\psi = \text{atan2}(R_{32}, R_{33}) \tag{6.6}$$

Where atan2(y,x) is the arc tangent of the two variables x and y. When $\cos(\theta) < 0$, then $\psi = \text{atan2}(-R_{32}, -R_{33})$. To prevent this, the equation 6.6 can be modified as

$$\psi = \text{atan2}\left(\frac{R_{32}}{\cos(\theta)}, \frac{R_{33}}{\cos(\theta)}\right) \tag{6.7}$$

A similar calculation holds for finding ϕ. We know that

$$\frac{R_{21}}{R_{11}} = \tan(\phi) \tag{6.8}$$

To solve for ϕ

$$\phi = \text{atan2}\left(\frac{R_{21}}{\cos(\theta)}, \frac{R_{11}}{\cos(\theta)}\right) \tag{6.9}$$

To solve for θ, we know that

$$R_{31} = -\sin\theta \tag{6.9}$$

Then,

$$\theta = -\arcsin(R_{31}) \tag{6.10}$$

The motion path was controlled by applying the kinematic coupling constraint between a node and the tip of the catheter. Basically, a kinematic coupling constraints the tip of the catheter (i.e. a set of slave nodes) to the translation and rotation of a master node in a specified manner. It is useful in this case since a larger number of slave nodes are constrained to the rigid body motion of a single master node. Each slave node of the tip of the catheter has a unique relationship with the master node, therefore, the kinematic coupling constraint can be considered as a combination of general master-slave constraints {ABAQUS}. The motion of the catheter can be described as turning, twisting and rotating. Therefore, a kinematic coupling constraint can be used to prescribe a twisting and turning motion without constraining radial motion. Due to the tortuosity of the CS, a total of 12 locations were selected from the ostium to the entrance of GCV, as shown in different views of CS vessel Figure 6-8. The translational and rotational boundary conditions were imposed on the master node, preferred as refnode, in each step to perform the concerted maneuver through the CS vessel.

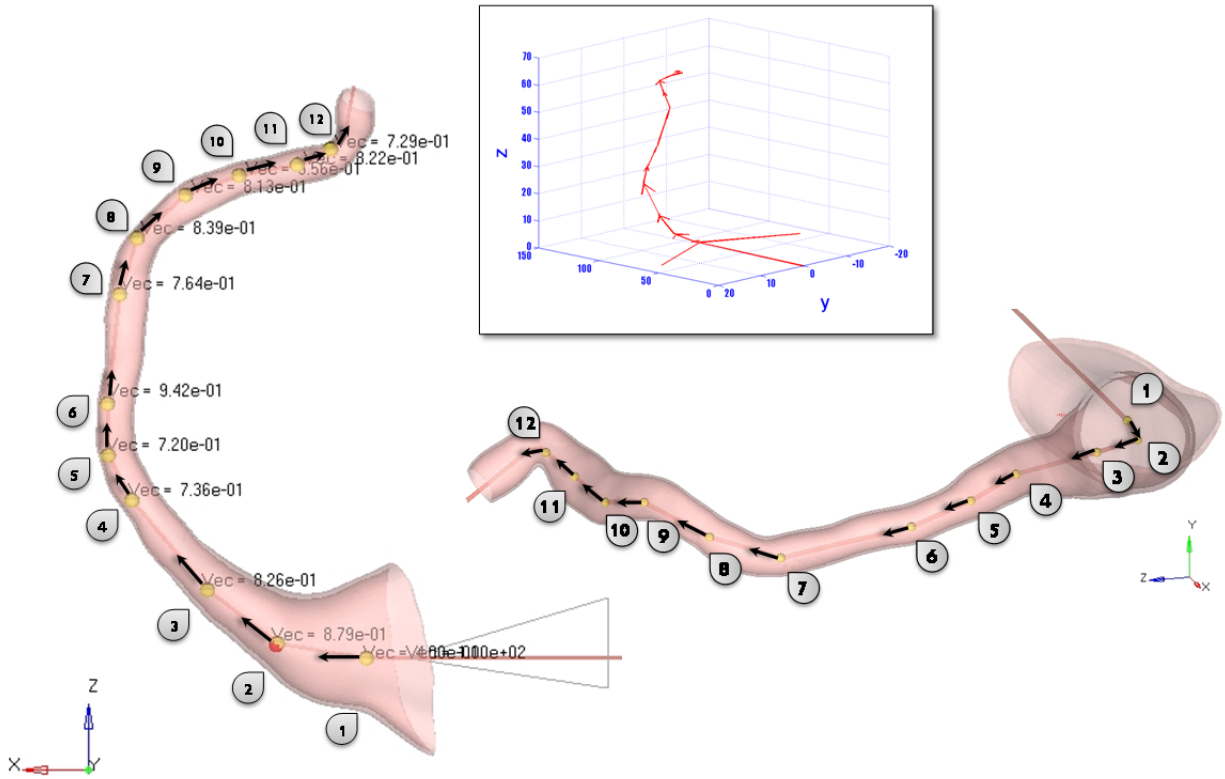

Figure 6-8: A representative CS vessel shows different views of the virtual deployment of the PTMA device performed by generating a delivery pathway along the guidewire positioning within CS vessel, and the graph shows the vectors in 3D space.

The CS pressure waveform is assumed to be mimicking the atrial pressure prior to mitral valve closure. Since the simulation process was treated as quasi-static and only analyze at the end-diastole, a range of pressure was chosen to simulate the CS pressure, as demarcated in red box in Figure 6-9a. This pressure wave was applied to each step during the deployment process to simulate the pulsatile blood flow inside the CS. As shown in the pressure waveform of the entire cardiac cycle in Figure 6-9a, pressure within the CS does not exceed 20 mmHg. Therefore, we generalized the CS pressure as shown in the Figure 6-9b.

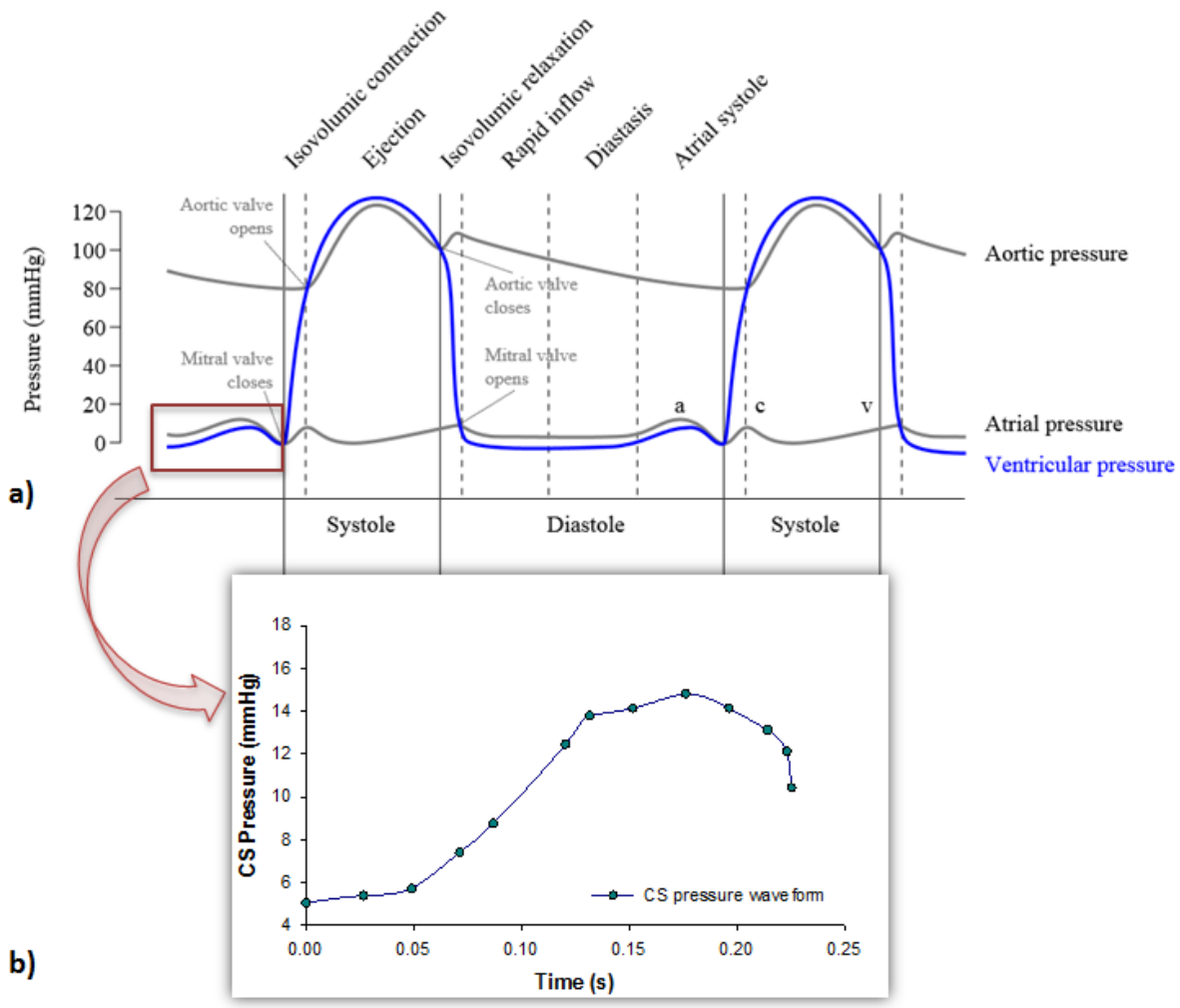

Figure 6-9: The CS pressure waveform obtained from a) standard physiological pressure waveform and b) extracted CS pressure.

The guide wire was modeled as a hollow cylindrical tube that has a curvature similar to the CS geometry. To simplify the process, deployment of the guide wire will not be simulated; instead, it was created and meshed according to the CS curvature. Contact between the outer surface of guide wire and the inner surface of the catheter was enabled in order to prevent catheter from penetrating the CS vessel wall.

Next, the deployment of the PTMA stent was carried out by retracting the delivery catheter. Basically, additional 12 steps were performed in which the magnitude of displacement were equal and opposite direction of the forward delivery route. The distal anchor was first deployed into the CS vessel

by retracting the catheter at position 11 and the proximal anchor at position 4 (Figure 6-8). According to the procedure in the instructor manual of PTMA device, the stent needs to be pulled back until the proximal anchor is at the desired target site. This strategy is numerically implemented as follows. At position 5, the contact between the proximal anchor and the catheter was set to 'rough' so that as the proximal anchor is pulled back to the direct of the CS ostium, the entire device was also dragged towards the same direction. Because the distal anchor was already expanded at the GCV end, the friction helps to resist the anchor slippage. However, if the distal anchor's diameter is undersized, stent migration is inevitable. After this step, the rough contact between the proximal anchor and the catheter was released and proximal anchor release continued at the position 4.

The final step was of the simulation is the contraction of the bridge to cinch the CS vessel. This step involved removing the contacts between BDM and bridge elements. This step might result in high inaccuracy due to the high kinetic energy as the stent bounced back to its contracted and non-stretched geometry. To minimize this affect, viscous damping was added to the bridge section.

Most contact algorithms were performed using either 'general contact' or 'contact pair' algorithms. The 'general contact' was set for stent only due to unspecified surface interactions, which automatically detects and computes all interactions within the domain. The 'contact pair' algorithm was modeled as master-slave surfaces which were specified by users. Table 6-3 list all the contact surfaces and their algorithm and friction coefficients.

Table 6-3. Contact surfaces and their contact algorithms and friction coefficients

Contact bodies	ABAQUS contact algorithm	Friction coefficient Or rough (no slippage)
Bridge/Biodegradable	Contact pair	Rough
Crimper/Stent	Contact pair	0.1
Stent/Catheter	Contact pair	0.9, 1.0
Catheter/Guidewire	Contact pair	0.01
CS/Guidewire	Contact pair	0.01
CS/Catheter	Contact pair	0.05
Stent/CS	Contact pair	0.1, 0.9
Stent	General contact	0.1

6.3.4 Post-processing

The simulation was similar to the data analysis methods performed in Chapter 5, in this simulation process, CS stress, stent strain, interactive forces and stent fatigue were analyzed throughout the process. Figure 6-10 shows which components of the model were analyzed during particular steps. Particularly, only the bridge section was analyzed during the stent pre-stretch step. In this step, the distal anchor was fixed and displacement controlled was applied to stretch the bridge and its cell with a total of 20 mm. The tension of the bridge was measured at the proximal stent connector as total reaction forces. Peak stress and strain of the bridge was analyzed for potential failure. In the stent crimping step, both proximal, anchor and bridge sections were analyzed for peak stress/strain, though bridge section was expected to exhibit minimum stress since only displacement was imposed with no deformation. For the catheter deliver steps, peak stress/strain of the stent was checked only in the initial deliver step to ensure no high localized stress. It is assumed that stress will not significantly highly than the peak stress in the previous crimping step since only displacement control was imposed on the catheter to move the stent into the CS vessel. However, kinematic energy with respect to strain energy of the stent was monitored throughout the entire deliver process. The interaction between the CS and the catheter was carefully monitored in the catheter delivery steps to ensure no CS peak stress or damage. In the stent release in the CS vessel step and the last step of the stent contraction, all components were analyzed in details. Additionally, the mitral annular area was measured to determine the functionality of the PTMA device.

	Stent pre-stretch	Stent crimping	Stent release in catheter	Catheter delivery	Stent release in CS vessel	Stent contraction
		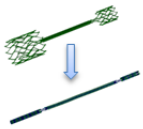	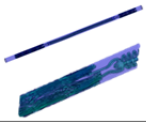	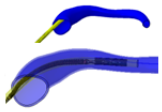	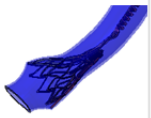	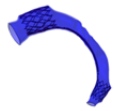
CS vessel	✗	✗	✗	✓	✓	✓
Proximal Anchor	✗	✓	✓	✓	✓	✓
Distal Anchor	✗	✓	✓	✓	✓	✓
Bridge Section	✓	✓	✓	✓	✓	✓
Catheter	✗	✗	✗	✓	✗	✗

Figure 6-10: Schematic of stent deployment process and selected (checked) components to be analyzed.

6.3.5 Results

6.3.5.1 Stent prestretch, crimping, release in catheter and delivery process

As shown in Figure 6-11, an uniform expansion of the bridge section of the PTMA stent can be observed. With the imbedded bio-degradable material, the PTMA stent bridge has a peak strain of 10.2%. The reaction force has a steep increase at the displacement of less than 9 mm and then levels from 9 – 16 mm of the displacement.

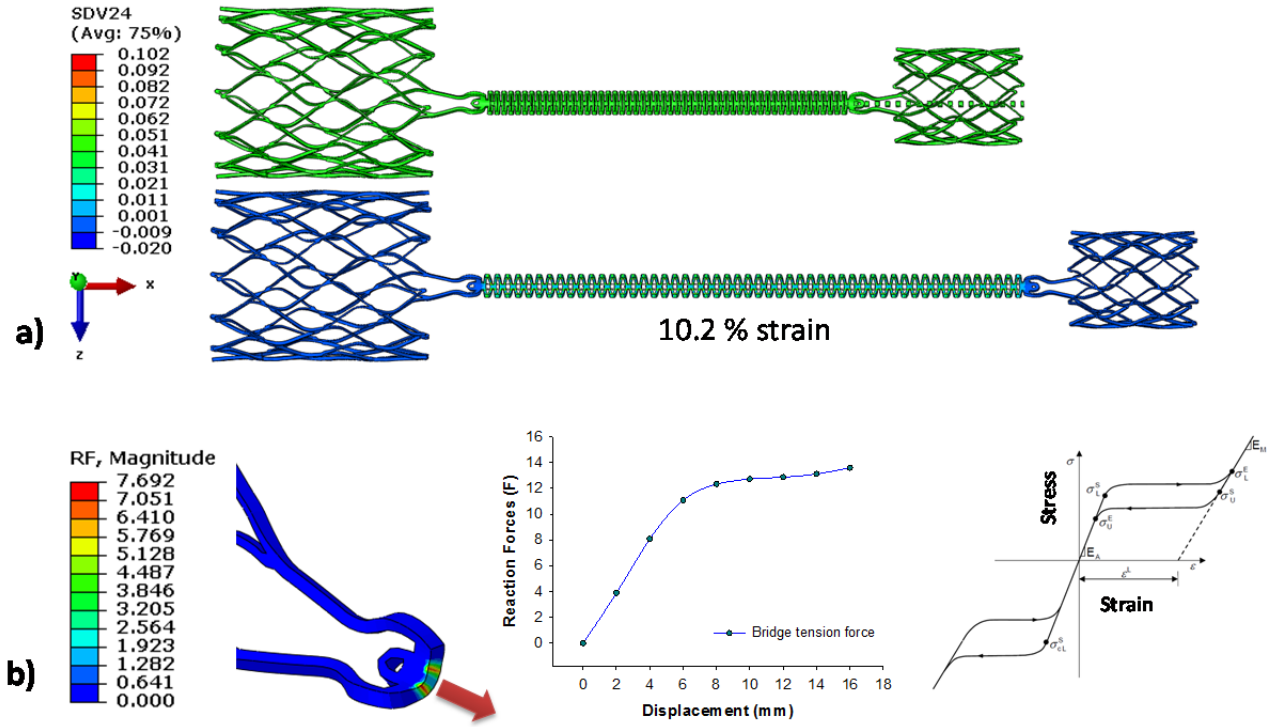

Figure 6-11: a) The stent pre-stretch step where the bridge is prestretched to obtain the bridge tension, maximum strain on the stent at the end of the step is 10.2%; b) the measurement of reaction forces (RF) or bridge tension force after prestretched, showing the RF and displacement relationship, which correspond to the stress-strain Nitinol characteristics.

With the crimping catheter reducing its diameter, the anchoring stents (both proximal and distal anchoring stents) were crimped into a small diameter, as shown in Figure 6-12. Note that upon the release of the stent into the delivery catheter, the bridge stent is not straight, but wavy due to the force balance of

between anchoring stents and the bridge. The proximal anchor has a peak strain of 14.9%, whereas the distal anchor has a peak strain of 17%. It is clear that the distal anchor has a relatively larger oversize than the proximal stent. Note the maximum strains did not increase after release into the catheter.

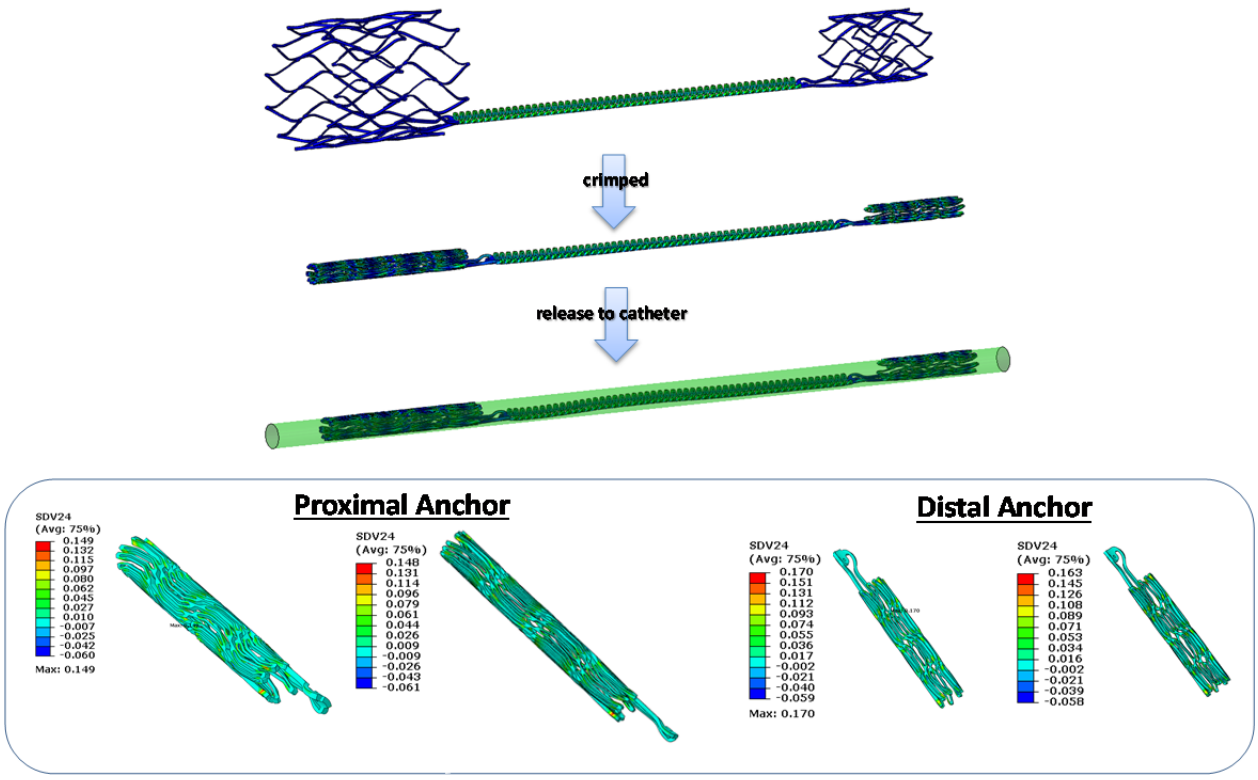

Figure 6-12: The geometry of the stent prior and post crimping process and release into the catheter. The strain distribution (SDV24) of proximal and distal anchors. Maximum strains did not increase after release into the catheter.

During the stent delivery process, it can be seen from Figure 6-13 that the delivery catheter would not induce additional stress and strain on the CS and anchoring stents. At the start of the catheter delivery, the CS wall stress is about 0.029MPa. When it is delivered about half way into the CS, the CS wall stress is about 0.031, and the end of the delivery, it is about 0.032

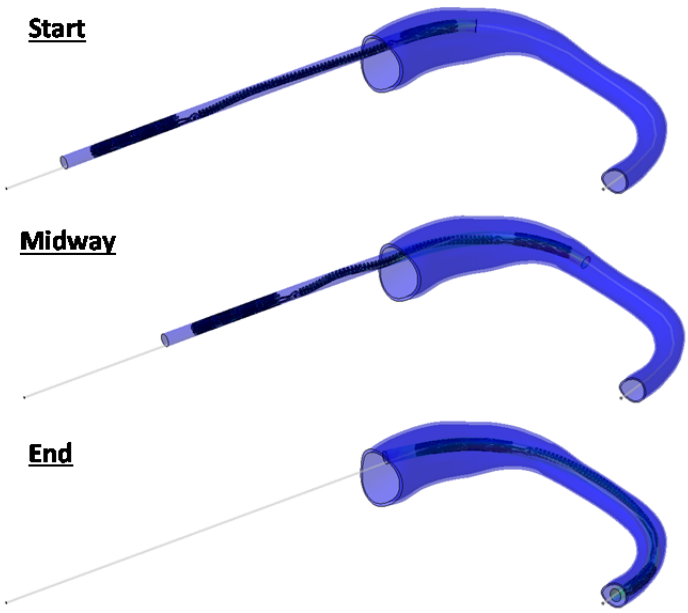

Peak stress (MPa)			
	Start	Midway	End
CS	0.029	0.031	0.032
Catheter	3387.89	1980.29	1907.73
Stent strain (SDV24)			
Proximal anchor	0.151	0.151	0.149
Distal anchor	0.166	0.159	0.161
Bridge	0.101	0.142	0.141

Figure 6-13: Peak stress and strain of CS, catheter, proximal and distal anchors and bridge section during the catheter deployment steps.

Due to the shape-memory characteristics of Nitinol material, both anchors spring open during the release steps. Figure 6-14 and Table 6-4 show the maximum stent strains of selected increments during the simulated release steps. The spring-open shape of the stent is similar to the realistic shape of Nitinol stent during release step that observed clinically. Maximum strains of both proximal and distal anchors are similar, between 0.138 – 0.161. Strain reduced significantly from 0.153 to 0.048 and from 0.138 to 0.024 for distal and proximal anchors after completely removed from the catheter, respectively. The bridge section strain remained between 0.10 – 0.14 during the entire release step. This demonstrates that during release step, stent will not experience any critical peak stress that could eventually result in fatigue damage.

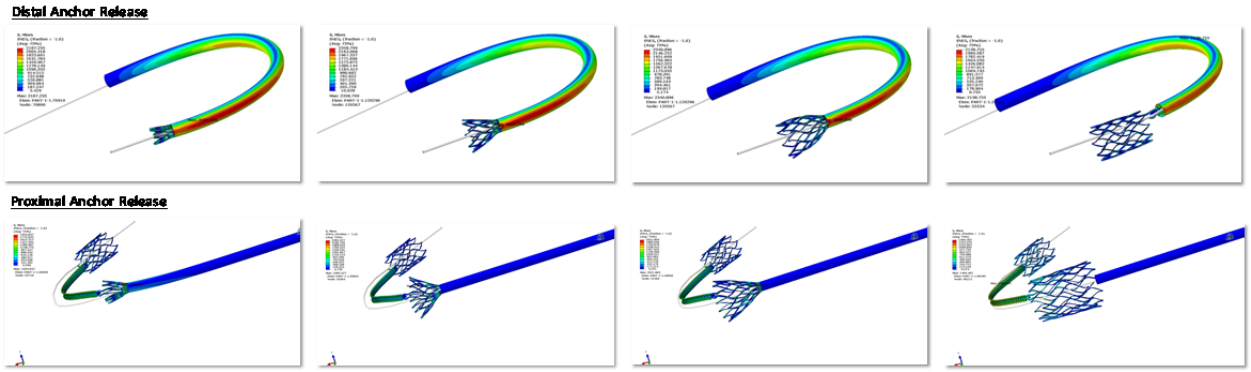

Figure 6-14: Distal and proximal anchor releasing steps: strain distribution of the entire stent during the selected ten releasing increments.

Figure 6-15 shows the peak von Mises stresses of both CS ostial region and GCV during the proximal and distal anchor release steps. The peak stress on GCV was 1.41 MPa after complete distal anchor release and decreased below 0.8 MPa following proximal anchor release. The proximal anchor release did not cause high stress at the CS ostium, peak stresses were below GCV stresses. The highest stress was during half-way release at a value of 0.73 MPa. It could be that GCV was over dilated, at 69.1% while CS ostium was only dilated by 24%. It is interesting that although both anchors were selected so that they are 2 mm oversize, the GCV showed much over-dilation compared to the CS ostium. One reason could be the thickness—GCV thickness is half of CS ostium thickness (0.37 versus 0.74 mm, measured in Chapter 1).

Table 6-4. The maximum strains during release steps for distal and proximal anchors.

Maximum Stent Strain (SDV24)			
Steps	**Proximal anchor**	**Distal Anchor**	**Bridge**
1 (Start)	--	0.161	0.14
2	--	0.159	0.14
3	--	0.153	0.10
4	--	0.048	0.10
6 (Bridge pulling)	--	--	0.10
7	0.149	--	0.10
8	0.160	--	0.10
9	0.138	--	0.10
10 (End)	0.024	--	0.10

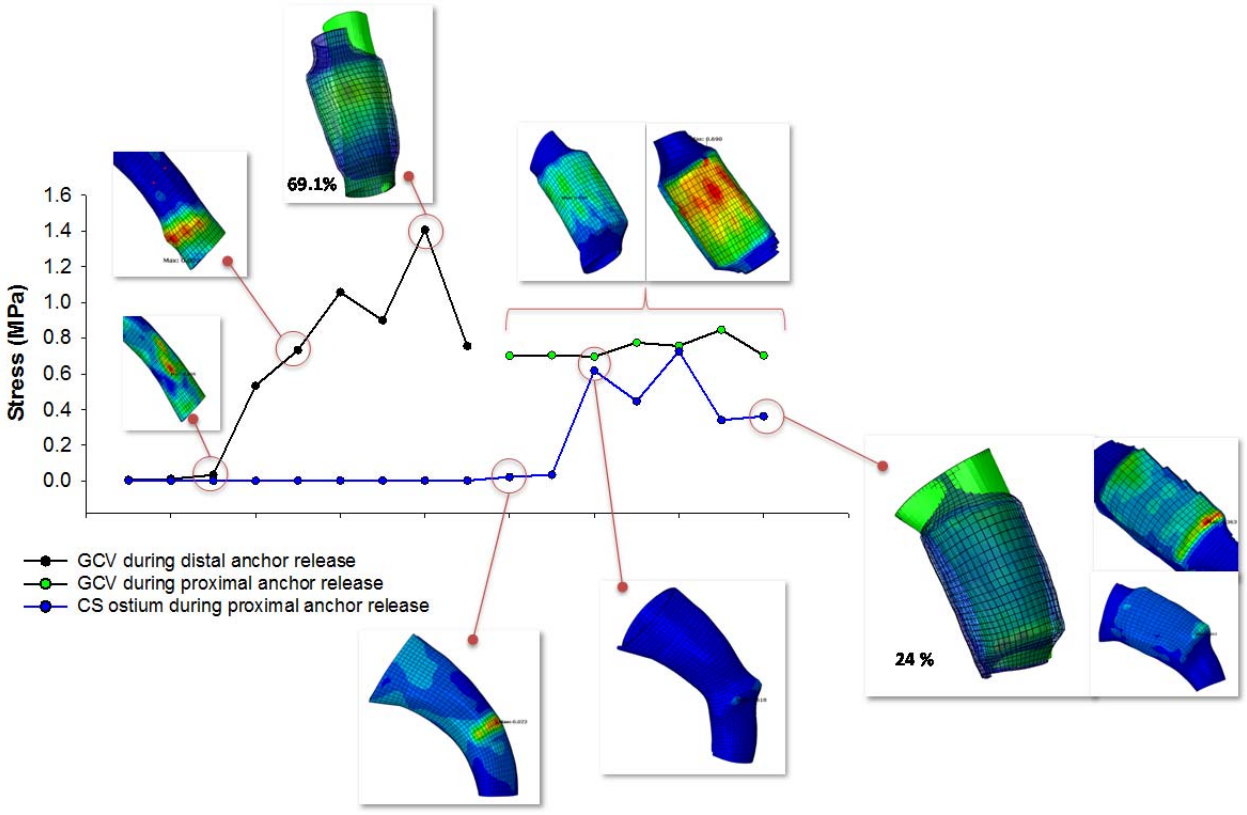

Figure 6-15: Peak von Mises stresses on CS ostium and GCV regions due to stent release.

The final form of the PTMA stent after deployed within the CS vessel is shown in Figure 6-16a. It can be seen that the distal anchor is not circular, while the proximal anchor is more uniformly expanded and conformed to the CS ostium. This could be due to the aggressive oversize of the stent anchor to the GCV section. At about 6.9 mm extension from the proximal anchor connector, maximum strain of 0.31 was observed. Although the magnitude is relative low compare to maximum 8-10% strain value for Nitinol to reach to plastic deformation range, this peak could be higher due to stent fatigue overtime. It has been reported in the first clinical study by Webb *et al.* that bridge separation is observed at 9-mm gap between the proximal anchor and the shortened bridge at 22 days in one patient, 30 mm gap at 28 days and 41-mm gap at day 81 with the return of grade 3 MR. This could be due to the bridge length which could be too short for this particular patient. However, note that shorter bridge length might produce a better MR reduction. One possibility that could relieve high strain is increase the strut width of the bridge. In addition, strains on the stent strut along the connector direction were higher, similar to the observation in Stent strain and fatigue analysis.

Figure 6-16b shows the reduction in mitral annular area after stent deployment. In Section 6.2.4, from the same patient, using the simplified bridge model, the MA area was reduced by 16.75%. In this section, the MA area reduced from 15.21 to 13.45 cm^2, by 13.09%. The difference in MA reduction could be due to the simplified bridge model and delivery process. The results from this section show a more accurate CS curvature and stent conformity compared to Section 6.2.4. The addition of bridge section incorporating the biodegradable material and the delivery process could also produce more accurate responses.

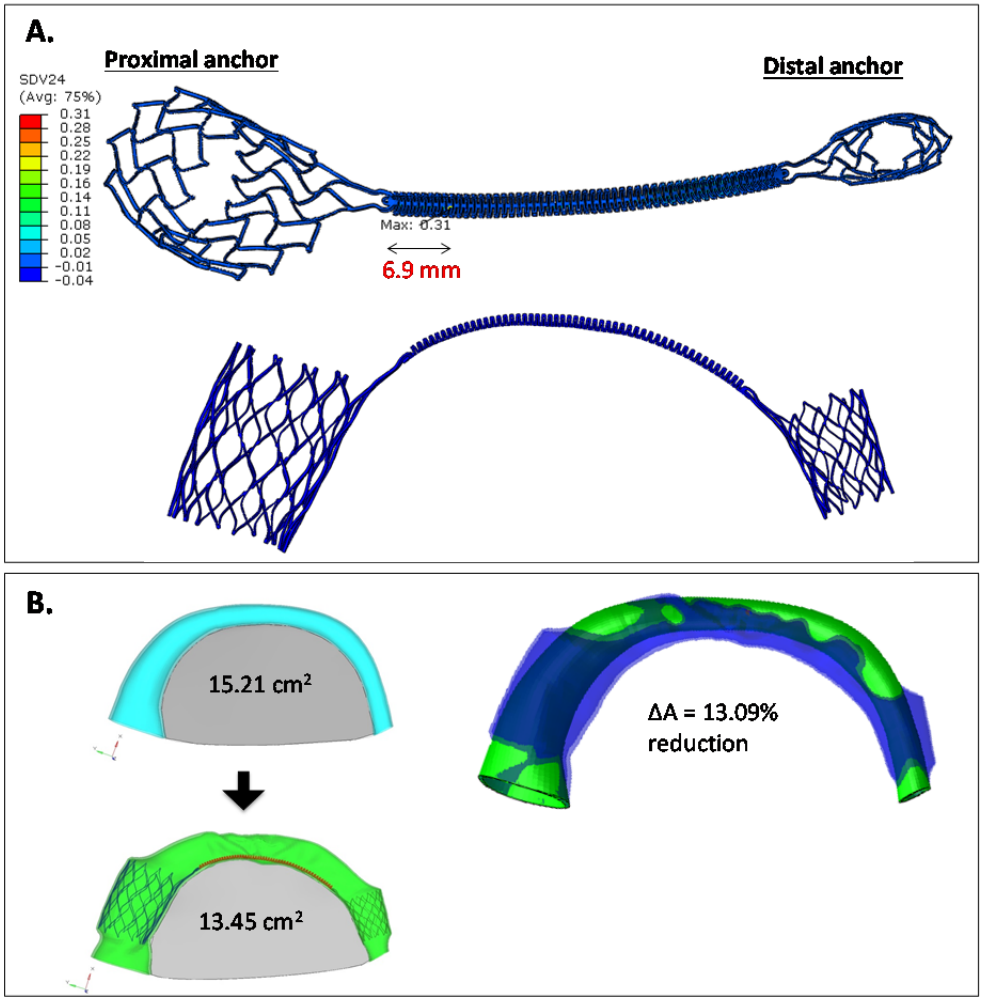

Figure 6-16: A) A final deformed shape of the PTMA stent in two views and b) reduction in mitral area after stent deployment.

6.4 Discussion

6.4.1 Tissue-stent interaction in PTMA intervention

PTMA stent was selected based on patient geometries. Currently, both anchors were 2 – 4 mm larger in diameter than the CS and GCV diameters, and the bridge's effective length is 20 mm shorter than the CS length. Our simulation result from this particular patient showed that the current criteria for PTMA stent selection might not be appropriate, such that the GCV section might need to be less oversized compared to the CS ostial section. From the preliminary study of the CS ultimate tensile strength (UTS), it shows that the human GCV samples were weaker than human CS samples, 1.0 versus 1.5 MPa. By comparing the UTS with the peak stresses observed in this chapter, it can be seen that the GCV section is most likely ruptured due to its maximum stress (1.41 MPa) exceeding the UTS of 1.0 MPa. However, the CS region's maximum stress (< 0.8 MPa) was well below the UTS of 1.5 MPa. This demonstrates that sizing using diameter alone might not provide confidence on tissue damage, as the tissue properties are of important factor that could greatly affect the outcome of the procedure.

Our study shows the regions of high strain distribution on PTMA stent that are similar to clinical observation. To prevent stent fracture at the bridge section, the second generation of PTMA device incorporated suture reinforcement. However, in the second clinical study by Harnek *et al.*, they observed several stent fractures along the stent anchors, which were observed in our simulations. This information could shed some lights into the current PTMA stent problems of high strain and fatigue.

6.4.2 Clinical significance of the study

The TSI during catheter delivery and stent release cannot be visualized and analyze by practitioners during PTMA procedure. Thus, adverse events such as endothelial cell damage, vessel perforation and stent fatigue could eventually result in device failure and mortality. Quantitative understanding of the biomechanics is clearly an enabling step for science-based design of the devices.

This approach will avoid the currently observed disasterous fatigue failure and move towards patient-specific sizing of the implants.

6.4.3 Limitations

There are several limitations of this study. First, the CS vessel was assumed to be fixed at both ends. The CS vessel starts at the right atrium and ends at the GCV which continues to descend into the left ventricle wall. Thus, it is appropriate that both ends of the CS will be fixed. Second, there is no surrounding tissues (i.e., connective tissues, myocardial tissues and mitral annulus) surround the CS vessel. The cinching force, due to lack of surrounding tissues, could be under estimated. Therefore, in this study, cinching force was not measured. The mitral annular area could also be overestimated due to the same assumption. However, this study focused mainly on the interaction between the device and CS tissues, the measurement of MA area was for the purpose of evaluating the simulation of the bridge after contraction and comparison between the two bridge models. Third, the material properties of human CS were not patient-specific and CS model was not obtained from MR patients. A database of human CS tissues was obtained in Chapter 2, which will be utilized in future studies in combination with a more robust material model. Currently, CT scan is not standard of care for patients with MR condition. However, such protocol can be developed and CT scan information will be valuable for MR geometries. Lastly, the simulation model was not validated with experimental data due to lack of imaging data from post-procedural patients. In Chapter 4, a method was developed to cinch the ovine MV ex vivo to obtain the cinching force and MA area. Thus, the computational model in this chapter can be validated by replicating this experiment using ovine heart model in place of human heart and PTMA stent in place of the suture. Future validation work will be further discussed in the next section.

6.4.4 Future works

In the future validation study, we will be developing a Nitinol material PTMA stent and the delivery process. There are several steps to achieve this: 1) obtain the laser cut stent geometry of the PTMA stent. The laser cut sent geometry is needed for stent manufacturers/vendors such as NDC, or

Memory, to laser cut the stent from a standard 10 mm or 6 mm Nitinol tube. We will first generate SolidWork geometry files for various final PTMA stent designs. Afterwards, the FE models of the stents will be generated from the SolidWork files using the software HyperMesh (Altair Engineering, MI). Computational simulations will be performed to study the stent forming process from the laser cut geometry to the fully expanded final shape. The laser cut geometry of the stent will be sent out to either NDC or Memory for fabrication. Once physical laser cut stents are obtained from vendors, we will prepare the necessary tools for the heat treatment and forming process to expand the laser cut tube to the fully expanded shape. 2) Deploy of the PTMA stents into an ovine heart via the coronary sinus (CS) vessel and measure deformation at passive state (i.e. vessel diameter and mitral annulus reduction) using ultrasound and 3D digital image correlation system. We will set up an ex vivo ovine heart model to perform the delivery of the stent into the CS vessel. Mitral valve annulus deformation, mitral valve orifice area and stent deformation will be obtained and correlated with the FE simulation results of the whole system stent. In vivo implantation of the PTMA stents is also an option.

7 Summary and Future Studies*

In this chapter, I will summarize main findings of the previous Chapters (1 to 7). Major contributions from this dissertation will be highlighted. Then, I will discuss the areas for future studies.

7.1 Summary

In **Chapter 1**, a brief review of the heart and heart valves, and normal mitral valve structure and function was provided. Main clinical issues and current clinical treatment techniques for mitral valve disease were also summarized. Following it, I gave a brief overview of current mitral valve biomechanical studies on experimentally characterizing mitral valve tissue properties, constitutive modeling of valve elastic tissue, and computational studies of mitral valve function and intervention. Finally, I reviewed the recent mitral valve treatment techniques, in particularly the minimally invasive, percutaneous, transcatheter mitral valve repair, which leaded to the motivation of my research on the modeling of minimally invasive PTMA intervention for mitral valve repair.

Since coronary sinus (CS) vessel serves as a conduit for the deployment of the PTMA device for the treatment of functional mitral regurgitation. Characterization of CS mechanical response is an important step toward an understanding of tissue-device interaction in the PTMA intervention. The purpose of the study in **Chapter 2** is to investigate mechanical properties of the porcine CS vessel using pressure-inflation test and constitutively model the wall behavior using a four-fiber family strain energy function (SEF). My results showed that CS vessel exhibited a S-shape pressure-radius response and could be dilated up to 88% at a pressure of 80 mmHg. Excellent results from model fitting indicated that the four-fiber family SEF could capture the experimental data well and could be used in future numerical simulations of tissue-device interaction. In addition, histology study was performed to identify the

---

* Some of the contents of this chapter are taken from:

W. Sun, C, Martin and **T Pham**, "Computational Modeling of Heart Valve Function and Intervention ", ***Annual Review of Biomedical Engineering,*** accepted.

microstructure of the CS vessel wall. I found a high content of striated myocardial fibers (SMFs) surrounded the CS vessel wall, which was also mainly composed of SMFs, while the smooth muscle cells are very low in content. The elastin and collagen fibers are highly concentrated in the luminal and outer layers and sparsely distributed in the medial layer of the CS wall. These structural and mechanical properties of the CS should be taken into consideration for future PTMA device designs.

There are two limitations in the study of Chapter 2: 1) the experiment was conducted under relatively simple pressure inflation loading conditions, and 2) only the porcine CS was examined. Due to complex tissue-device interactions, quantification of tissue behaviors under multi-axial loading conditions may be needed. Moreover, a study of CS tissue properties from different species (i.e., porcine, ovine and human) may be helpful in understanding the outcomes among animal trials and human studies, and establishing a proper animal model to evaluate the device efficacy. Thus, in **Chapter 3**, I studied the mechanical properties of the CS wall from porcine, ovine and human models. The human cadaver CS tissues were selected from an age group of 86.5 ± 9.7 years old. The CS tissues were subjected to multi-protocol biaxial tests and characterized by the Fung-type elastic model. Histological analysis was also performed to compare the difference in tissue microstructure among porcine, ovine and aged human CS tissues. My results showed that the aged human CS tissues exhibited much stiffer and highly anisotropic behaviors compared to the porcine and ovine. Both of the porcine and ovine CS vessel walls were thicker and mainly composed of striated muscle fibers (SMF), whereas the thinner aged human CS had higher collagen, lesser SMF, and more fragmented elastin fibers, which are possibly due to the aging effects. I also observed that the anatomical features of porcine CS vessel might be not suitable for the PTMA deployment. These differences between animal and human models raise questions for the validity of using animal models to investigate the biomechanics involved in the PTMA intervention. Therefore, caution must be taken in future studies of PTMA stents using animal models.

Since the PTMA technique uses a stent to cinch a segment of the mitral annulus (MA) and reduces mitral regurgitation. The cinching mechanism results in septal-lateral annular shrinkage.

However, the mechanism has not been characterized completely. In **Chapter 4**, a method was developed to quantify the relation between cinching tension and MA area in an *ex vivo* ovine model. The cinching tension was measured from a suture inserted within the coronary sinus (CS) vessel with one end tied to the distal end of the vessel and the other end exited to the CS ostium where it was attached to a force transducer on a linear stage. The cinching tension, MA area, septal-lateral (S-L) and commissure-commissure (C-C) diameters and the leakage were simultaneously measured in normal and dilated condition, under a hydrostatic left ventricular pressure of 90 mmHg. From the experimental results, it can be seen that the mitral annulus area was increased up to 22.83% after MA dilation. A mean tension of 2.1 ± 0.47 N reduced the MA area by 21.30 ± 5.6% and S-L diameter by 24.18 ± 5.28%. Thus, leakage was improved by 51.72 ± 16.19% following by restoration of normal MA geometry. In conclusion: The cinching tension generated by the suture acts as a compensation force in MA reduction, implying the maximum tension needed to be generated by annuloplasty device to restore normal annular size. The relationship between cinching tension and the corresponding MA geometry will contribute to the development of future PTMA devices and understanding of myocardial contraction function.

With the quantification and modeling of CS material properties, in **Chapter 5**, a finite element analysis was performed to investigate the biomechanical interaction between the proximal anchor stent of a PTMA device and the coronary sinus (CS) vessel in three steps including i) the stent release and contact with the CS wall, ii) the axial pull at the stent connector and iii) the pressure inflation of the vessel wall. To investigate the impact of the material properties of the CS tissues and of the stent on the interactive responses, the CS vessel was modeled with human and porcine CS material properties, and the proximal stent was modeled with two different Nitinol material properties with one being stiffer than the other. The simulation results indicated that the vessel wall stresses and contact forces imposed by the stents were much higher in human than porcine models. However, the mechanical differences induced by the two stent types were relatively small. The softer stent exhibited a better fatigue safety factor when deployed in the human model than in the porcine model. These results underscored the importance of the CS tissue

mechanical properties. Higher vessel wall stress and stent radial force were obtained in human model than those in porcine model, which also brought up questions as to the validity of using porcine model to assess device mechanical function. The quantification of these biomechanical interactions can offer scientific insight into the development and optimization of PTMA device design.

In **Chapter 6**, I added several key components of the delivery catheter systems which are essential to the final deployed configuration clinically. Furthermore, the outcome of the procedure depends on a proper selection of device that is specific to a patient and his/her anatomical structure. It is well known that human anatomy is highly variable and the procedural outcomes of any medical devices are essentially related to anatomic considerations. In this chapter, for the first time, we introduced FEA of a complete PTMA device being deployed within a selected patient-specific CS model. Three patient-specific CS models were selected and PTMA stents were first modeled with a simplified bridge section. Evaluation of the stent and its interaction with the CS vessel as well as the predicted clinical outcomes were analyzed for each phase. To accurately study the functionality of the device and its interaction with the CS vessel, the bridge section of the PTMA stent was modeled with a spring-like structure, similar to the realistic one, and with a built-in biodegradable material to allow the bridge to remain extended prior to its contraction. The entire stent crimping and deployment process was simulated that allowed detailed analysis of tissue-stent interaction: high stress concentration in the stent and on vessel wall, oversizing of the CS vessel and possible fracture locations of the stent based on peak strain value.

Major contributions of this dissertation are:

1. Reported, to our knowledge, the first study of the structural compliance of the porcine coronary sinus using pressure-inflation tests
2. Reported, to our knowledge, the first study of the biaxial mechanical properties of the porcine, ovine and aged human coronary sinus using planar biaxial mechanical tests
3. Reported, to our knowledge, the first study of aged human mitral leaflet mechanical properties.

4. Quantified the relation between cinching tension and mitral annulus area in an *ex vivo* ovine model
5. Simulated the deployment of PTMA proximal stents into the CS using porcine and human models and with two different nitinol materials.
6. Simulated the deployment of a complete PTMA device into a patient-specific CS.

7.2 Future Studies

7.2.1 Quantification of in vivo human tissue properties

Although the use of aged-matched human tissue properties in valve simulations is a substantial improvement over animal tissue properties, there are also limitations to using *ex vivo* tissue properties from human cadaveric hearts. First of all, ex vivo tissue properties are not patient specific. Rather the tissue properties are selected from a cadaveric heart with similar characteristics (age, sex, etc.) to the patient of interest. This requires a thorough testing database of human tissue properties from an array of patients with differing ages [210], genders, and degrees of disease because all these factors can significantly impact the cardiovascular tissue properties. Furthermore, tissue property homogeneity is generally assumed over a particular region. Ex vivo testing data generally only represents the average response from the center region of a specimen. In reality, the tissue structure and the associated mechanical properties are heterogeneous. The ultimate goal would be to obtain the patient-specific tissue properties from non-invasive imaging modalities using either the inverse FE method or new techniques. It is possible to measure aortic tissue expansion over the cardiac cycle by utilizing time-elapsed non-invasive imaging modalities [210]. The difficulty is that the physiological stress/strain range is rather narrow. The challenge remains to be how to quantify the arterial material responses at low (0-80 mmHg) and high (>120mmHg) stress levels to obtain the complete material response from the un-stressed and un-loaded state to the state of tissue dissection, tear and rupture. Several groups have adopted an inverse FE procedure to perform stress analysis from *in vivo* imaging [211-213]; however, such approaches have not

been applied to valve tissues. A future effort could be to develop an inverse FE method which would utilize existing databases of human tissue properties to guide the inverse FE solution progress.

7.2.2 Incorporation of the mitral apparatus and left ventricle model

As mentioned in Chapter 1, the MV is a complex yet elegantly structured cardiac valve that consists of four anatomic components working congruently during a cardiac cycle: an annulus, two leaflets, approximately 25 chordae tendineae, two papillary muscles, and the underlying left ventricular myocardium. To complete understand the biomechanics involved in the PTMA treatment of MR, one needs to incorporate the complete MV apparatus into the computational model.

Currently, the tissue model is greatly simplified to only CS vessel without surrounding structure. In order to fully analyze the functionality of the PTMA device, it is important to incorporate the surrounding structure, which consists of the mitral valve, part of the left atrium, left ventricle and the surrounding connective tissues of the CS vessel. I am in the process of constructing such a computational model, as shown in Figure 7-1. However, there are still many fundamental studies that remain to be done, including the characterization of material properties of each of those anatomic components. I have completed, to my knowledge, the first study on the characterization of 21 aged human mitral leaflets. The results have been published and incorporated into this dissertation in the Appendix B.

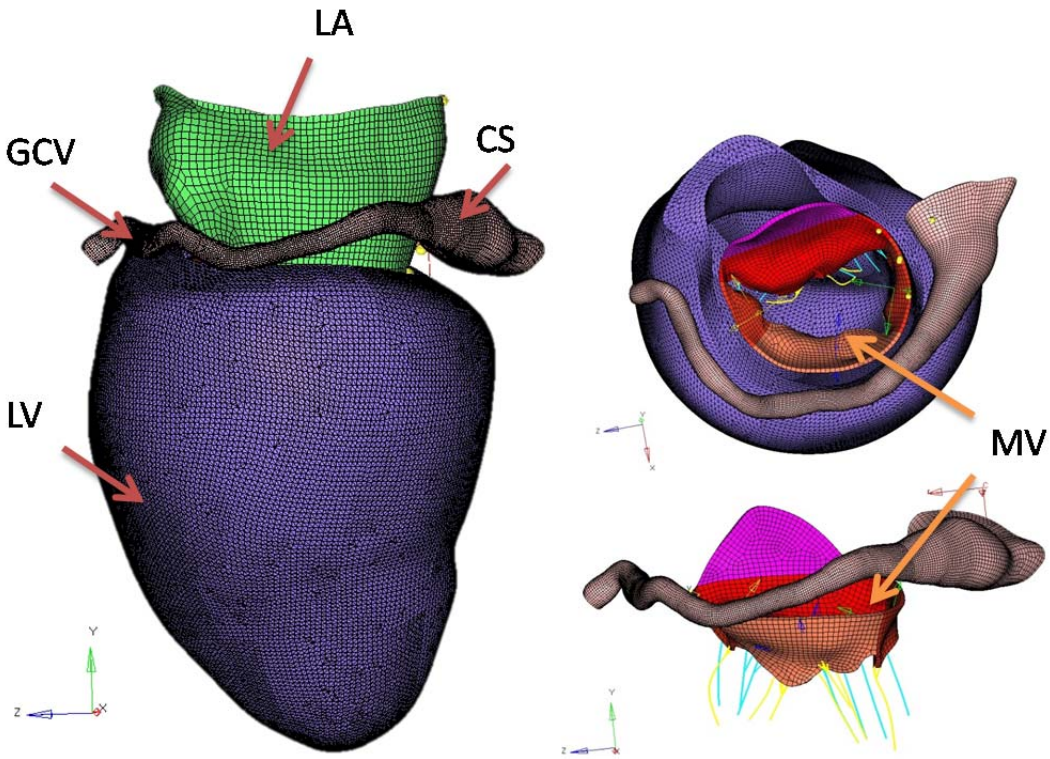

Figure 7-1: A FEM model of a whole MV apparatus together with the CS, left atrium and left ventricle.

7.2.3 Image-based fluid dynamic and fluid structural interaction simulation

Structural FEA, as conducted in this dissertation, can provide a full and detailed quantitative stress and strain analysis of regions of interest, while computational fluid dynamics (CFD) can provide a quantitative description of the flow characteristics, which was not performed here. Fully-coupled fluid-structure interaction (FSI) methods are also emerging to more comprehensively model valvular biomechanics. However, the accuracy of computational simulations depends heavily on the valve geometry, material properties, and the loading and boundary conditions used. Due to the complexity of the mitral valve, most of the early valve models utilized idealized, symmetric geometries of the valve structures and adopted linear elastic material properties. Only in the past several years have clinical images been utilized to develop patient-specific valve models with improved accuracy. Most of the imaging modalities offer 3D volumetric, time-resolved data that encompass comprehensive structural and fluid flow information. Such 3D data, although largely unexploited in clinical settings, offers researchers

the possibility to reconstruct the 3D geometry of heart valves and study MV function and intervention at a patient-specific level, and pre-operative planning tools can be developed for a specific patient. Nonetheless, much more remains to be done in the areas of CFD and FSI studies of mitral valve intervention.

7.2.4 Multi-scale modeling

A normal heart valve functions at multiple length-scales, including organ, tissue, cell and molecular scales [214]. Since the overall behavior of the heart valve is linked to every length scale, alteration of one scale would trigger and activate changes in another. Thereby, one cannot fully describe the heart valve biomechanics from a single length-scale. Mechanical stimuli, such as transvalvular pressures, impose stretches on the organ-scale that translate to the tissue-scale [215]. It has been shown that such dynamic deformation in-vitro can mediate the responses of valvular interstitial cells (VICs), which serve to maintain tissue structural integrity via protein synthesis and enzymatic degradation. The aortic VIC deformation under a quasi-static physiological pressure was quantified by Huang *et al.* [216]. They found that the nuclear aspect ratios, measured as an index of overall cellular strain, increased substantially from 4 to 90 mmHg, with the fibrosa layer exhibiting a greater rate of change compared to the ventricular layer. Owing to the heterogeneity of the leaflet structure, Vesely and Noseworthy [217] studied the layer-specific mechanical properties of the porcine AV leaflet, by separating the fibrosa and the ventricularis from fresh and glutaraldehyde-fixed porcine aortic leaflets, they found that although the two layers differ structurally, mechanically, they complement each other during AV function, e.g. more radial extensibility to facilitate valve closure. Later, Stella and Sacks [218] characterized the material properties of the layers using strip biaxial tests. Their mechanical data were later implemented in a series of computational studies by Weinberg *et al.* [219], who developed a computational model to simulate the mechanical behaviors of valves across the range of length scales. In their most recent study [220], a multi-scale simulation in both solid and fluid domains was performed to analyze whether the geometric difference or the mechanical deformation difference causes the major differences in function and

pathology (e.g. calcification) between normal tricuspid and BAV valves. Interestingly, the model predicts that cell-scale deformations were similar in both valves regardless of organ-scale differences, suggesting calcification may instead be due to a genetic difference which gives rise to a difference in matrix constituents. Limitations of the study that may have affected their results include modeling both tissue- and cell-scales using isotropic constitutive relations, the use of homogenized BAV tissue structures, and the lack of BAV tissue properties. Although their cell-scale model was greatly simplified, their simulation was the first to link across the length scales to create a multi-scale model. Clearly, much more computational work remains to be done at cellular and molecular levels, and innovative methods linking both the spatial and temporal scales to simulate the development of pathological events remains to be developed.

7.3 Conclusion

Minimally invasive percutaneous transvenous mitral annuloplasty (PTMA) devices have been shown to be promising in correcting MR in several animal studies, however, device dysfunction and fatigue fracture have been reported in the human clinical trials. These adverse events reflect a pressing need for a better understanding of the biomechanical interaction between a device and mitral valve apparatus. In this work, integrated experimental and computational studies were performed to apply engineering analysis of a minimally invasive mitral valve repair to study the biomechanical interaction between a PTMA device and surrounding tissues (i.e., CS vessel). A series of experimental methods were performed to characterize the biomechanics of the CS vessel, which have not been published in the current literature. Constitutive formulations were introduced to accurately model the tissue properties and apply to the finite element (FE) simulations. Realistic patient-specific geometries of the CS vessel were obtained from clinical imaging data and reconstructed into three-dimensional (3D) FE model. By incorporating patient material properties and 3D patient-specific geometries, FE simulation of the device deployment into the vessel could be achieved to investigate the tissue-stent interaction (TSI) and the associated biomechanics involved in the system. The results from experimental and computational data showed that the mechanical properties of human CS and valvular tissues were significantly stiffer than ones from animal models and also varied largely among the aging population. These results underscored the need for carefully evaluating the biomechanics involved in the PTMA intervention and the importance of having an appropriate animal model for evaluating device function for its ultimate use in human. From the TSI simulation, detailed analysis include proper sizing of the device, high stress concentration in the stent and on the vessel wall during delivery and upon deployment, contact forces between the stent and tissues for tissue damage analysis and possible stent fracture based on fatigue analysis. It is hoped that the approaches developed in this work will provide a valuable tool that will allow one to virtually assess and predict the clinical outcomes of PTMA intervention and to facilitate optimal device design and development.

8 APPENDIX A: PTMA Element Selection and Mesh Sensitivity Analysis

Element Selection. In this study, we used the C3D8I element that has 8-integration points with a 5x5 layers of elements cross the stent and CS walls. For most of the stent analyses, due to the bending-dominated loading nature of the stent, the maximum stresses/strains are usually detected at the stent surface. The incompatible mode eight-node brick element (C3D8I) is preferred for stent analysis because it provides a good estimation on peak stress and strain and does not suffer from the hourglassing phenomenon if the integration points are closer to the surface. Although the quality of the C3D8I element is far from the fully integrated brick element, of which the best results are usually obtained with quadratic elements, they are relatively low in computation cost. For the current analysis, the computation time takes about 14 hours with 50 CPUs running on Intel Xeon X5650 Westmere cores.

Mesh Sensitivity Analysis. A selection of different mesh sizes was used to perform a mesh sensitivity analysis on the interaction of the CS vessel and PTMA proximal stent. Both of the CS wall and stent meshes were refined, and the results are shown in Table 9-1. The small differences (results from the end of step-1) between the three meshes suggest that mesh density has low impact on the simulation results. For the CS model, the mesh 3 achieved the smallest high stress compare with meshes 1 and 2. Therefore, the finest mesh 3 was chosen for both CS and stent models in this study. Table 9-2 shows all the maximum (MAX) and 99% stress values in each TSI step for all four models.

Table 8-1: Mesh sensitivity analysis

Variables (Step-1)	Mesh 1	Mesh 2	Mesh 3
No. of element – CS vessel	25,920	34,561	43,199
von Mises Stress at 99% (Mpa)	0.044	0.035	0.031
von Mises Stress at 1% (Mpa)	1.109	1.097	0.884
No. of element – Stent	68,532	91,375	114,219
Strain (SDV24)	5.39E-03	5.82E-03	5.99E-03
Normal forces (N)	6.514	6.071	5.993
Shear forces (N)	0.551	0.523	0.498

Table 8-2 : Maximu (Max) and 99% peak stress of CS vessel wall

	STEP 1		STEP 2		STEP 3	
	99 %(MPa)	MAX (MPa)	99 %(MPa)	MAX(MPa)	99 %(MPa)	MAX(MPa)
N1-human	0.031	0.884	0.034	1.345	0.035	1.268
N2-human	0.031	0.507	0.032	0.951	0.033	1.074
N1-porcine	0.013	0.056	0.017	0.175	0.024	0.239
N2-porcine	0.013	0.039	0.017	0.076	0.024	0.118

9 APPENDIX B: Material Characterization of Mitral Valve Leaflets*

A complete study of the material properties of human mitral leaflets is reported in this section. The study characterized human mitral valve leaflets using biaxial testing method and fitted with Fung's elastic model. Information obtained in this chapter will be useful for future incorporation of mitral valve into the left heart model, to study the patient-specific material properties of mitral valve with more accurate prediction of valvular mechanical responses.

9.1 Introduction

The prevalence of MV disease has been shown to be strongly associated with age of the patients, particularly in mitral regurgitation patients, increasing from 0.5% in patients aged 18 to 44 years to 9.3% in patients aged ≥75 years [15, 221]. Clearly, MV disease mainly affects the aged population. It is well known that aging has a substantial impact on soft tissue mechanical properties. Studies have shown that the stiffness of aortic vessels is much higher in aged patients compared with that of young patients [222-226]. However, our knowledge on the mechanical properties of mitral valve tissues in aged patients has been very limited. Quantification of native tissue properties has many implications in the development of medical treatment and prosthetic device, and the understanding of physiological function and disease progression. For example, mitral valve repair, benefited from the improved understanding of mitral valve biomechanics, has now been acknowledged as desirable and superior to mitral valve replacement in virtually all pathologies of mitral disease [227].

---

* The contents of this chapter were partially published in
T Pham, W Sun, Material properties of aged human mitral valve leaflets , **Journal of Biomedical Material Research Part A**, 2013, DOI: 10.1002/jbm.a.34939
.

Our current knowledge of mitral valve mechanical properties is mainly derived from that of porcine mitral valves [7, 228-235]. The assumption that porcine MV is similar to that of human ones is frequently adopted, even though it has not been rigorously validated. Indeed, there are numerous computational models of human mitral valve that had utilized porcine MV tissue properties [31, 46, 164-167, 236]. Moreover, for prosthetic valve device approval, the Food and Drug Administration (FDA) mandates pre-clinical animal trials, using either porcine or ovine models, to demonstrate sufficient safety including performance and handling, as well as to study the efficacy of new valve devices [237]. While many disparate results between human and animal trials have been observed, the current assumption taken for heart valve device trials (such as for transcatheter valve intervention [137, 138, 238-241]) - porcine and ovine animal models are similar to those of aged humans – is still prevailing.

In this chapter, the mechanical properties of aged human MV tissues, both mitral anterior (AML) and posterior (PML) leaflets, were characterized using the planar biaxial testing method. The MV tissues were obtained from individuals above 65 years old with no prior history of valvular disease. The material stiffness, extensibility and degree of anisotropy of the leaflet samples were quantified. Histological analysis was performed to examine tissue microstructural properties. The presence of abnormal valvular structures such as calcific deposits and disrupted fiber structure was assessed. Finally, the material properties of aged human mitral leaflets were compared with those of animal mitral leaflets published in the literature.

9.2 Materials and Methods

9.2.1 Materials and sample preparation

A total of 21 hearts from 82.62 ± 8.77 years old human cadavers were obtained from the National Disease Research Interchange (NDRI, Philadelphia, PA). An approval was obtained from the Institutional Review Board at the University of Connecticut for human tissue research in this study. The selection criteria for the hearts were no history of valvular disease or any valvular repair or replacement. See Table

9-1 for characteristics and medical history of all patients. All hearts were fresh frozen within a post-mortem recovery of less than 24 hours and kept frozen during delivery. Upon arrival, the hearts were defrosted in a hot water bath, and the MV leaflets were dissected out. A total of 20 AML and 18 PML specimens were removed from the hearts and used in this study. All chordae tendineae were carefully cut off from the leaflets. The MV leaflets that could not be tested immediately were cryopreserved in 10% DMSO [110] and stored in the -80˚C freezer until testing. It has been showed that connective tissues can preserve their structural architecture [242] and mechanical properties [110, 243, 244] when store in a cryoprotectant agent at low temperature (-80°C). The cryopreserved specimens were thawed using a four-step process [110] to remove cryoprotectant agent prior to testing. Specimen thickness was measured and averaged at three locations in the belly region and two in the free-edge region (Fig. 9-1) using a thickness gauge (Mitutoyo, Model 7301).

Table 9-1. Patients' medical history

Specimen	Age	Gender	Smoking	Diabetes	Heart Weight (g)	Cause of death	Heart related disease(s)	Calcification grade	
								AML	PML
1	69	M	Unknown	Unknown	733	CPA secondary to HA	HTN	1	1
2	88	F	n	Unknown	342	Alzheimer	CAD	2	no data
3	78	M	Unknown	Unknown	396	CPA secondary to HA	HBP, HA	1	0
4	79	F	y*	Unknown	545	Respiratory failure	CHF	2	1
5	81	F	n	y	330	Unkonwn	Stroke	2	1
6	96	F	y	n	545	CPA	None	2	1
7	95	F	y*	n	330	Respiratory arrest	None	2	1
8	79	F	n	Unknown	404	CPA	HTN	1	1
9	98	F	n	y	303	Respiratory arrest	None	1	1
10	82	M	y*	y	714	COPD	HTN, CHF, CAD	2	1
11	75	M	y*	n	425	HA	None	1	1
12	63	M	y*	n	369	Unknown	HTN	2	0
13	75	F	y*	n	575	CPA	HTN	2	1
14	82	M	y*	n	510	CPA	HTN	2	1
15	83	M	y	n	412	Vascular Dementia	HTN, CHF	2	no data
16	87	F	y*	n	295	Unknown	None	2	no data
17	80	F	y*	n	397	Unknown	None	1	1
18	82	M	y	n	544	Aspiration Pneumonia	None	3	3
19	95	M	y	n	425	Natural Causes (Age)	None	2	1
20	87	F	n	n	490	Unknown	None	1	1
21	81	F	y*	n	621	Alzheimer's related	None	1	0
Mean	82.00	F:10	--	--	464.00	--	--	--	--
SD	8.51	M:7	--	--	130.86	--	--	--	--

COPD - Chronic obstructive pulmonary disorder, **HTN** - Hypertension, **HBP** – High blood pressure, **CAD** - coronary artery disease, **CHF** - Congestive heart failure, **CPA** - chronic pulmonary aspergillosis, **HA** - heart attack.

*Smoking = quit more than 5 years prior to death.

Calcification 1 = focal, calcification 2 = densely distribution over the belly region, calcification 3 = complete calcification

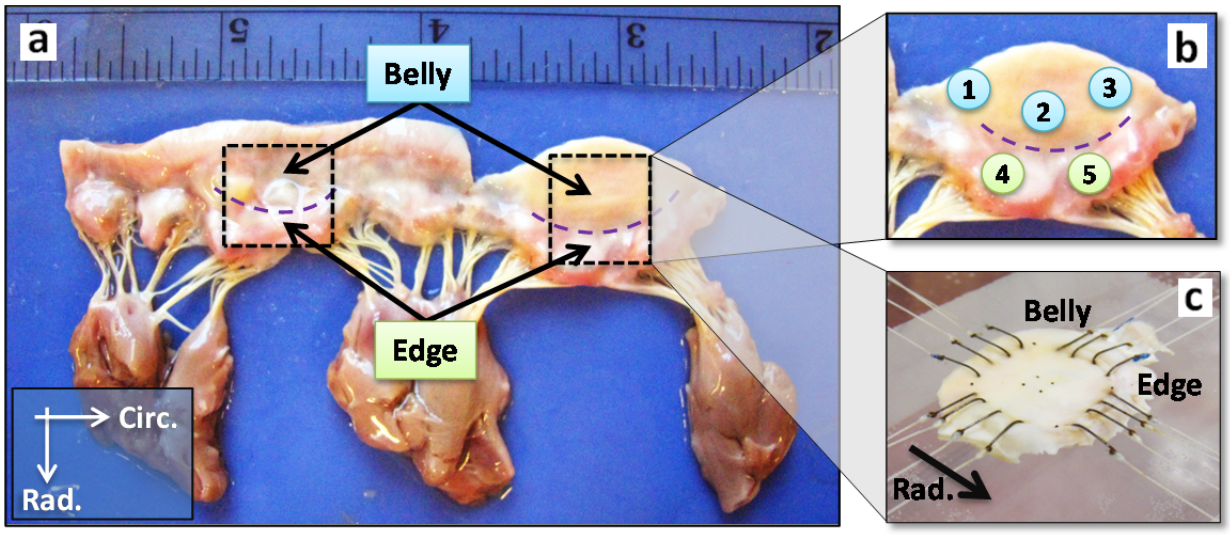

Figure 9-1. a) An image of one excised mitral valve from a cadaver heart. The testing regions are located in the dash square boxes and above and below regions of the dashed curved lines on each leaflet are belly and edge, respectively; b) five regions of thickness measurements; and c) mounting position and alignment of the leaflet specimen.

9.2.2 Biaxial mechanical test

Details on planar biaxial mechanical testing techniques and methods of analysis can be found in Sacks and Sun 2003 [38]. Briefly, all specimens were mounted in a trampoline fashion by continuous strands of silk suture looped along each of the four specimen sides, with the circumferential (CIRC) and radial (RAD) directions aligned to the loading axes of the biaxial test fixtures. In each specimen side, four barbless fish hooks (size 22) were punctured through the tissue thickness and spaced out evenly near the leaflet edge (Fig. 9-1-c**)**. All specimens were tested in a phosphate buffered saline solution bath at 37°C. The four markers were affixed to the lower-belly region of the tissue above the line demarcating the edge and the belly regions (Fig. 9-1-b). This region was chosen due to its relatively homogenous fiber structure where collagen fibers are aligned to the circumferential direction. A stress-controlled test protocol was utilized [117], wherein the ratio of the normal Lagrangian stress components T_{11} : T_{22} was kept constant

with $T_{12} = T_{21} = 0$. Preconditioning was performed to minimize tissue hysteresis. Each tissue specimen was preconditioned for at least 40 continuous cycles with $T_{11} : T_{22} = 1 : 1$. The seven successive protocols were performed using the ratios $T_{11} : T_{22} = 1 : 0.3$, 1 : 0.5, 1 : 0.75, 1 : 1, 0.75 : 1, 0.5 : 1, and 0.3 : 1. The unloaded reference markers were obtained after preconditioning cycles and used to analyze all the consecutive protocols.

9.2.3 Biomechanical analysis

The mechanical properties of valve leaflets were compared by means of secant modulus at three equibiaxial membrane tension levels: 1) at 10 N/m for tissue responses under small load, 2) at 60 N/m to produce responses at physiological level [245], and 3) at high load of 120 N/m for high stress state. From the equibiaxial protocols, the areal strain, e, was also obtained , $e = \lambda_{\theta\theta} * \lambda_{zz} - 1$, where $\lambda_{\theta\theta}$ and λ_{zz} are the CIRC and RAD stretch values at the three equibiaxial membrane tension levels, respectively. In addition, the degree of anisotropy (DA) was calculated as the ratio of CIRC strain to RAD strain under equibiaxial stretching. With the value of DA approaching 1, the tissue response is considered isotropic, while others represent various degrees of anisotropy. The correlations between the mechanical property data and clinical variables were also examined.

9.2.4 Microstructural analysis

The microscopic anatomy of representative AML and PML tissues used in mechanical testing were examined. Specimens were fixed in 10% formalin for 24 hours prior to histological process and analysis. After dehydrated and embedded in paraffin, the specimens were sectioned into 5 μm thick sections. Tissues were stained with Verhoeff Van-Gieson (VVG) for elastic fiber (as black), collagen fiber (as pink) and muscle cell (as dark brown/gray) visualization. Crimping of collagen fibers were also assessed using Picro-sirius red stain. The calcified deposits on the leaflets were identified with von-Kossa stain. Histological images were obtained from an Olympus U-TVO.5xC digital camera coupled to an Olympus BX40 light microscope.

9.2.5 Constitutive Modeling

The valve leaflet materials are assumed to be homogeneous and incompressible, and exhibited nonlinear, hyperelastic and anisotropic responses. The Fung-type model was utilized to model the biaxial mechanical responses of these valve samples. The in-plane 2nd Piola-Kirchhoff stresses, S_{ij}, were derived from a strain energy function (SEF), W,

$$S_{ij} = \frac{\partial W}{\partial E_{ij}} \tag{9.1}$$

where E_{ij} is the Green-Lagrange strain tensor and W is expressed as:

$$W = \frac{c}{2}\left(e^{Q} - 1\right) \tag{9.2}$$

$$Q = A_1 E_{11}^2 + A_2 E_{22}^2 + 2A_3 E_{11} E_{22} + A_4 E_{12}^2 + 2A_5 E_{11} E_{12} + 2A_6 E_{22} E_{12} \tag{9.3}$$

with c and $A_{1\text{-}6}$ are material parameters. The constitutive model was fit to the seven stress controlled protocols for each individual specimen to obtain the material parameters. The goodness of the fit was determined by a correlation coefficient, R-square value, based on the nonlinear regression Levenberg-Marquardt algorithm in SYSTAT 10 (Systat Software Inc., Chicago, IL).

9.2.6 Statistical analysis

Data were tested for normality prior to statistical tests. Statistical differences between the AML and PML variables were determined using the Student's t-test. A paired-sample t-test was performed to compare the directional responses. Non-parametric tests, including the Wilcoxon signed-rank test (for paired data) and Mann-Whitney rank sum test, were used for non-normal distributed sample groups. Correlations between the parameters and clinical variables were determined using the Pearson's (for normal) and Spearman (for non-parametric data) correlation coefficient (r), and p-values were calculated based on the aforementioned statistical tests. A p-value less than 0.05 was considered statistical significant, with high significance indicated by $p < 0.001$. Statistical analyses were performed using SigmaPlot (V11.0, Systat Software Inc., San Jose, CA) and SYSTAT 10 (Systat Software Inc., Chicago, IL). All measurements were presented as mean ± standard deviation (SD).

9.3 Results

9.3.1 Valve leaflet thickness and degree of calcification

The general observations of the leaflet samples were: thickening of leaflets, calcification and chordae tendineae fusion. As showed in Fig. 9-2, calcified regions on the leaflets were classified into four groups: 1) no calcification, defined as CALC 0, 2) focal or spotted dense mass of calcium deposition, defined as CALC 1, 2) dense and uniform calcium deposition over a large continuous region, defined as CALC 2, and 3) completely calcified and thickened leaflet, defined as CALC 3. From the 20 AML samples, 35% (n = 7) had CALC 1, 60% (n = 12) had CALC 2, and 0.05% (n = 1) had a complete calcification or CALC 3. Therefore, all AML samples had some degree of calcification. The CALC 2 or a uniform and continuous distribution of calcification in the AML samples were observed mainly at the aortomitral curtain or the anterior annular region that is anatomically coupled to the aortic annulus [246], and focal calcified spots were observed at the regions of chordal insertions. There was no uniform calcification in 18 PML samples, 78% (n = 14) exhibited CAL 1, 0.06% (n = 1) with CAL 2 and 17% (n = 3) with no calcification. Similar to the AML samples, the focal calcification in PML samples were mostly found at the annular and chordal insertion regions.

One valve had AML and PML thickness of 4.28 mm and 4.0 mm, respectively, due to severe calcification, which was identified as outliers and removed from the subsequent data analysis. The mean thickness of AML and PML samples were then 1.74 ± 0.37 (n = 19) and 1.83 ± 0.34 (n = 17) mm, $p = 0.51$, respectively. Both the interquartile and overall ranges of both leaflet data sets are similar, see Fig. 9-3. The mean belly and free-edge thickness values are also examined. It can be seen in Fig. 9-3 that the belly (denoted as AB) regions were significantly thinner than the free-edge (denoted as AE) regions of AML samples, 1.62 ± 0.34 mm versus 2.00 ± 0.54 mm, $p < 0.05$. Fusion of the chords and calcification most likely contributed to a higher value in thickness in the free-edge regions of all AML samples. No

difference between the free-edge (PE) and belly (PB) regions of the PML leaflets, 1.90 ± 0.44 mm versus 1.70 ± 0.39 mm, p = 0.09. No correlation between age and thickness was observed in both leaflet groups.

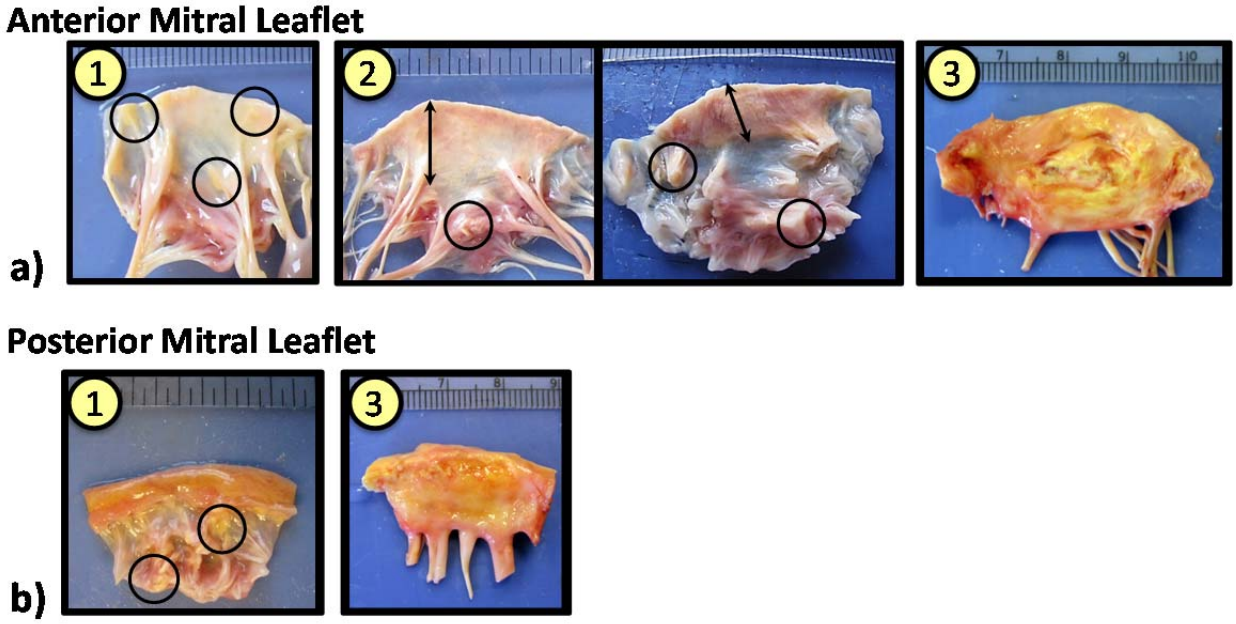

Figure 9-2: a) The anterior and b) posterior mitral valve leaflets showing calcification (CALC) degrees: (1) - focal or spotted dense mass of calcium deposit, (2) - dense and uniform calcium deposition over large continuous regions, and (3) completely calcified and thickened leaflet.

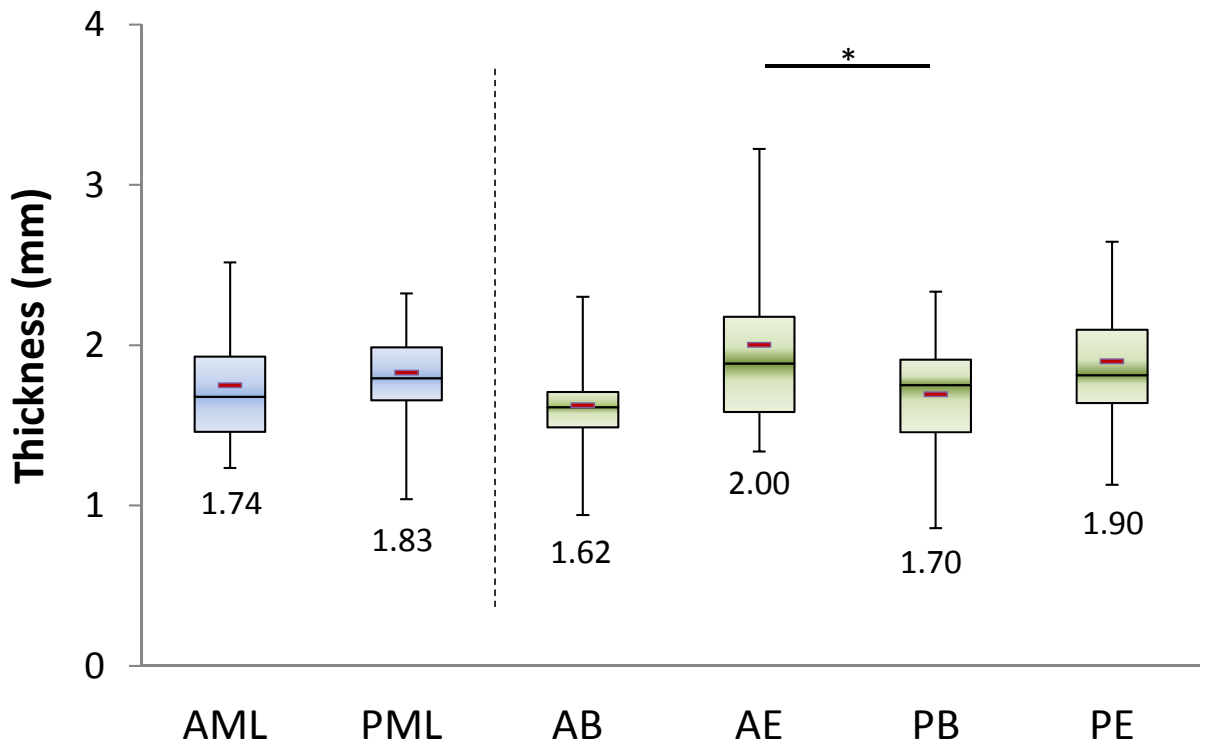

Figure 9-3: Boxplots of the thickness of AML (n = 19) and PML (n = 17) samples (left side) and of thicknesses of belly and edge regions of AML and PML samples (right side). The black lines inside the boxes represent the median. The red dashes and the numbers represent the mean values. (*) indicates a statistical significant difference between two groups. **AB** – Anterior Belly, **AE** – Anterior Edge, **PB** – Posterior Belly, **PE** – Posterior Edge.

9.3.2 Biomechanical responses

In general, the stress-strain response curve of leaflet tissues exhibits an anisotropic behavior, with the CIRC direction being the stiffer one. This MV leaflet characteristic has been observed and reported in studies of porcine [228] and human [43, 247] mitral leaflets. However, in our sample set, several AML (n = 6) samples had the RAD direction being stiffer than the CIRC direction, see Fig. 9-4b. This reverse directional response could be possibly due to the calcium deposits within the leaflet, which might dominate these leaflet responses. In our data analysis, we considered the samples with reverse directional response atypical for normal aged mitral leaflet tissues, and thus, they was excluded the subsequent data

analysis. The mean equibiaxial membrane tension-strain curves for the AML (n = 13) and PML (n = 14) samples in the CIRC and RAD directions after removal of reverse response data at 60 N/m are illustrated in Fig. 9-4a.

The mean secant moduli of mitral leaflet samples were calculated (Fig. 9-5). The AML samples were significantly stiffer than the PML samples at the three membrane tension levels (10 and 60 N/m, p = 0.002, and 120 N/m, p = 0.006), see Fig. 9-6a. Similarity in the mean areal strains at 60 and 120 N/m membrane tensions indicated that both AML and PML samples reached to a high stiffening region on a stress-strain curve at 60 N/m, where the collagen fibers may have already been straightened. Both leaflet groups were anisotropic with mean DA values of 0.46 ± 0.25 and 0.47 ± 0.26 at 10 N/m, respectively, and the values did not change significantly at higher membrane tension levels, 0.48 ± 0.18 and 0.48 ± 0.27 at 60 N/m and 0.53 ± 0.13 and 0.46 ± 0.20 at 120 N/m, respectively, as shown in Fig. 9-6b.

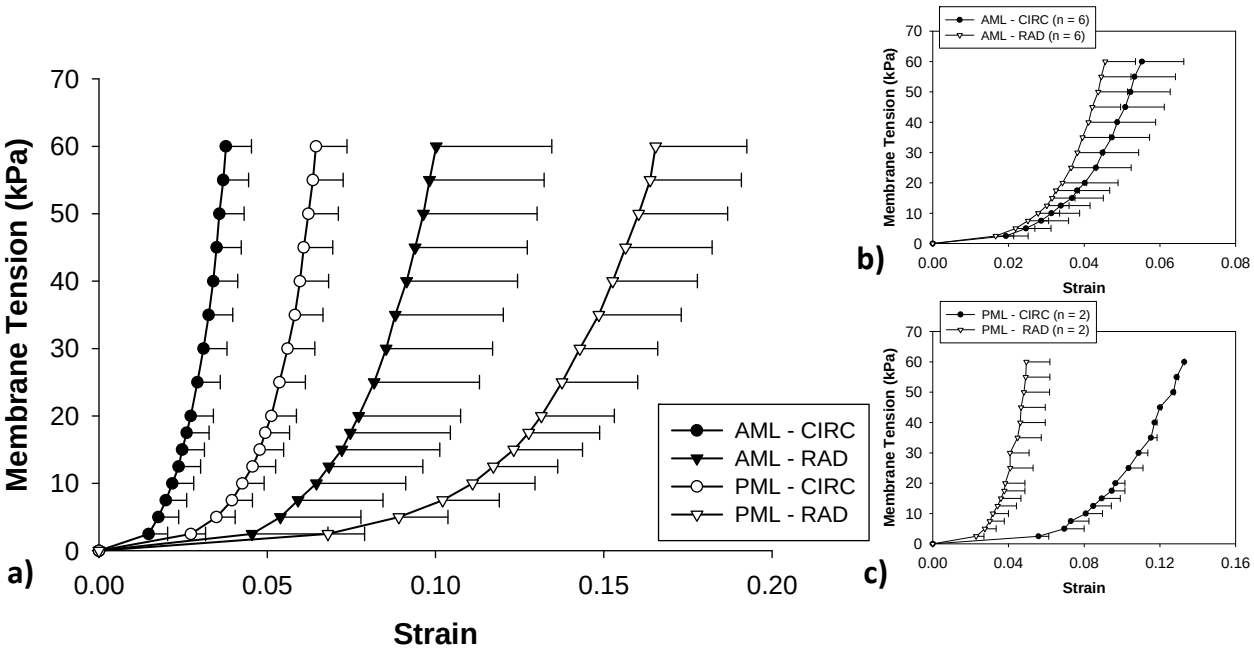

Figure 9-4: a) Mean equibiaxial protocols of the anterior (AML) and posterior (PML) mitral leaflet samples in circumferential (CIRC) and radial (RAD) directions prior to data removal, b) the AML (n = 6) and c) PML (n = 2, one sample had stiffness lower than 10 N/m) samples with reverse directions.

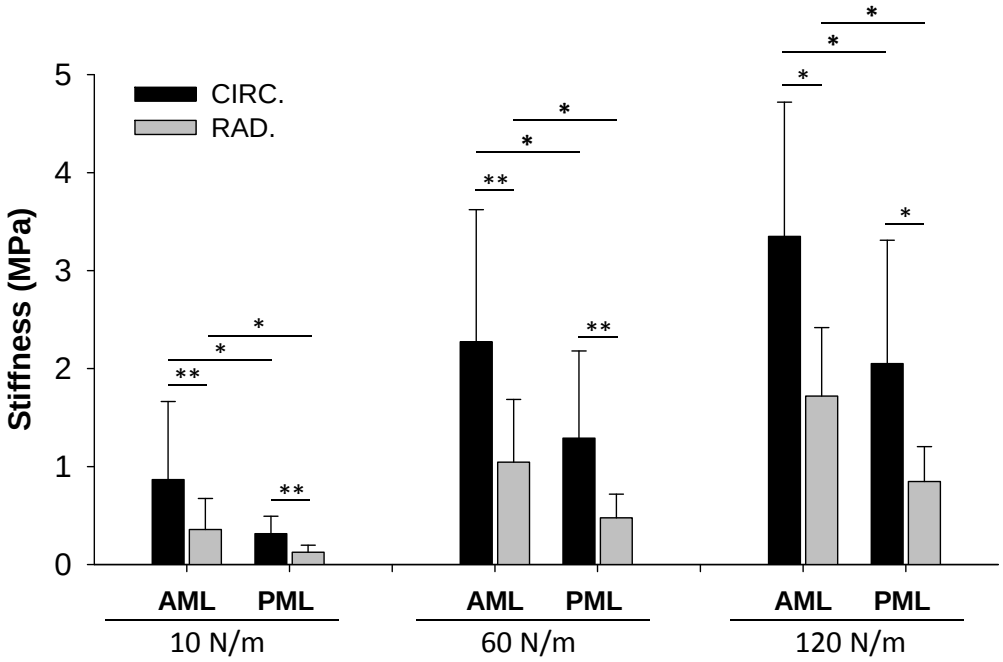

Figure 9-5: Comparing stiffness between the circumferential and radial directions (short bar) and between the AML and PML samples (long bar) (*) $p < 0.05$ and (**) $p < 0.001$.

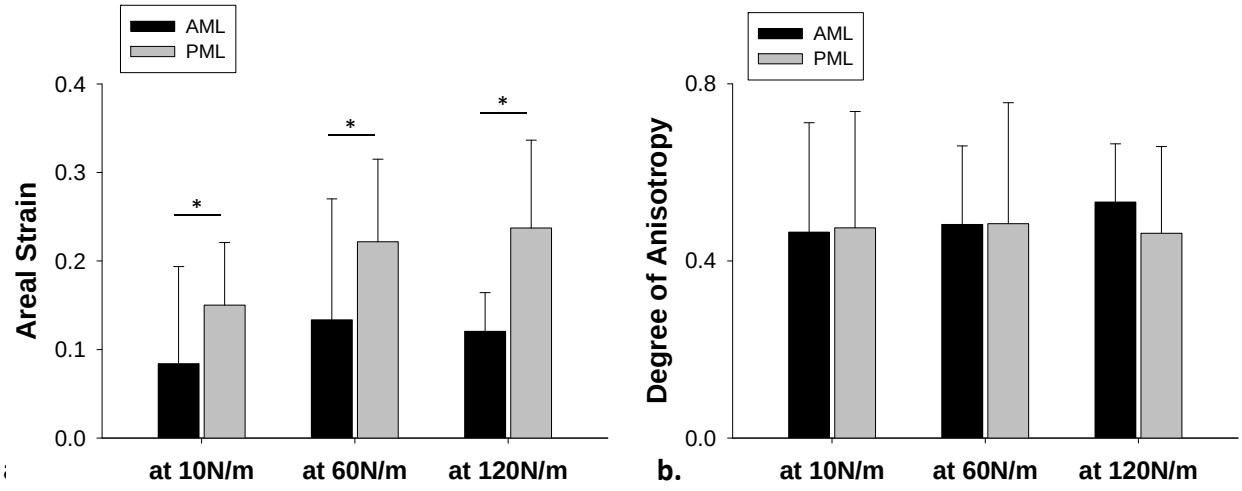

Figure 9-6: Comparison of a) the extensibility and b) the degree of anisotropy at 10, 60 and 120 N/m for the AML and PML samples, no significant variation in degree of anisotropy was found. (*) indicates statistical significant difference with $p < 0.05$.

9.3.3 Correlation with patients' medical history

No correlation was observed between the mechanical properties and patients' characteristic data (Table 9-1) of age, smoking, and diabetes. The leaflet samples were further divided into subgroups of hypertension (HTN) versus normotensive (NTN), and calcification levels, and compared between the groups. Of note, for calcification levels, we compared CALC 1 versus CALC 2 for the AML samples, and CALC 0 versus CALC 1 for the PML samples. Table 9-3 listed the stiffness, the areal strain and the DA values of each subgroup at 60 N/m membrane tension. An increase in tissue stiffness was observed when CALC 1 was increased to CALC 2 and when NTN was increased to HTN. All samples remained anisotropic in all disease states.

9.3.4 Constitutive modeling

A representative seven-protocol stress-strain curves with the Fung-elastic model fits in each direction of a set of leaflet samples are illustrated in Fig. 9-7-a&b. The patient-specific material parameters obtained from fitting the multi-protocol experiment data to the seven-parameter Fung-elastic model of Eq. 9.2 for both leaflet groups are shown in Table 9-2. The model demonstrated an excellent fit with the mean R^2 values of about 0.93 for AML and 0.92 for PML.

Table 9-2. Material parameters of mitral valve leaflets.

Specs	c	A_1	A_2	A_3	A_4	A_5	A_6	R^2	c	A_1	A_2	A_3	A_4	A_5	A_6	R^2
1	0.87	328.54	220.00	58.72	270.79	-26.74	15.92	0.98	0.71	145.59	65.70	42.81	104.35	-8.67	-10.32	0.96
3	0.85	354.72	294.61	115.29	13.94	0.59	4.96	0.98	-	-	-	-	-	-	-	-
4	1.55	371.86	328.02	37.72	339.71	-33.78	65.17	0.95	5.30	389.56	66.31	92.15	13.65	-1.57	-4.02	0.82
5	0.37	672.03	94.99	80.02	42.72	-7.12	-4.07	0.93	0.33	99.93	85.12	0.03	13.85	4.33	1.81	0.97
6	-	-	-	-	-	-	-	-	0.58	30.75	37.56	8.26	-28.74	5.34	-11.22	0.88
7	-	-	-	-	-	-	-	-	0.76	227.88	57.53	7.95	13.80	-31.37	17.13	0.88
8	0.26	292.65	250.12	112.10	66.92	7.42	28.11	0.88	0.73	147.93	54.29	-20.76	10.39	-2.65	-3.97	0.98
9	0.61	188.25	74.98	1.68	1.21	0.01	0.71	0.96	0.65	26.67	23.90	8.94	5.47	1.26	1.71	0.89
10	-	-	-	-	-	-	-	-	1.21	391.98	34.42	37.73	84.78	48.47	-5.05	0.79
11	-	-	-	-	-	-	-	-	0.28	326.87	62.51	50.23	94.13	0.61	2.53	0.95
12	-	-	-	-	-	-	-	-	0.46	83.72	19.45	11.85	1.39	-2.59	0.23	0.95
13	2.22	168.85	72.49	42.84	13.90	-8.62	1.89	0.98	0.71	327.54	163.94	35.08	34.74	5.47	7.39	0.95
14	0.98	974.11	221.35	-23.19	449.04	17.23	32.84	0.86	-	-	-	-	-	-	-	-
15	1.10	351.79	1017.67	344.84	178.34	75.48	-9.12	0.85	-	-	-	-	-	-	-	-
16	0.30	368.61	329.88	12.17	34.12	8.36	-3.04	0.93	-	-	-	-	-	-	-	-
17	0.13	56.48	11.50	3.77	8.61	-8.30	-1.57	0.98	0.84	7.80	246.06	24.88	15.57	-1.89	-7.91	0.87
20	3.01	484.73	452.11	251.34	60.38	-41.49	32.19	0.86	0.34	228.46	201.21	0.65	11.11	3.87	-17.88	0.97
21	0.71	460.83	159.80	1.11	183.35	60.34	51.44	0.96	0.22	223.13	57.99	27.18	39.44	-5.10	1.58	0.96
Mean	**1.00**	**390.26**	**271.35**	**79.88**	**127.92**	**3.34**	**16.57**	**0.93**	**0.94**	**189.84**	**84.00**	**23.36**	**29.57**	**1.11**	**-2.00**	**0.92**
SD	0.83	233.15	256.84	107.55	145.67	33.40	23.49	0.05	1.28	133.21	69.15	27.74	38.59	16.48	8.68	**0.06**

Table 9-3. Differences in stiffness, areal strain and degree of anisotropy (DA) between tissue valve leaflets.

		n	SM-CIRC (MPa)	*p*	SM-RAD (MPa)	*p*	Areal strain	*p*	DA	*p*
AML	**NTN**	6	2.03 ± 1.51	0.30	0.77 ± 0.57	0.10	0.19 ± 0.19	0.07	0.42 ± 0.20	0.24
	HTN	7	2.48 ± 1.28		1.28 ± 0.64		0.08 ± 0.03		0.54 ± 0.15	
	CALC 1	7	1.96 ± 1.27	0.45	0.88 ± 0.55	0.35	0.17 ± 0.18	0.45	0.46 ± 0.18	0.65
	CALC 2	6	2.64 ± 1.46		1.23 ± 0.73		0.09 ± 0.03		0.51 ± 0.19	
PML	**NTN**	8	1.22 ± 0.99	0.57	0.42 ± 0.20	0.30	0.25 ± 0.09	0.29	0.52 ± 0.32	0.63
	HTN	6	1.39 ± 0.81		0.56 ± 0.29		0.19 ± 0.10		0.44 ± 0.21	
	CALC 0	2	0.94 ± 0.35	/	0.28 ± 0.09	/	0.29 ± 0.09	/	0.30 ± 0.01	/
	CALC 1	12	1.35 ± 0.95		0.51 ± 0.24		0.21 ± 0.09		0.52 ± 0.28	

NTN – normotensive, **HTN** – hypertensive, **CALC** – calcification, **SM** – Secant Modulus, **CIRC** – circumferential, **RAD** – radial, **DA** – Degree of Anisotrophy, **AML** – Anterior Mitral Leaflet, **PML** – Posterior Mitral Leaflet.

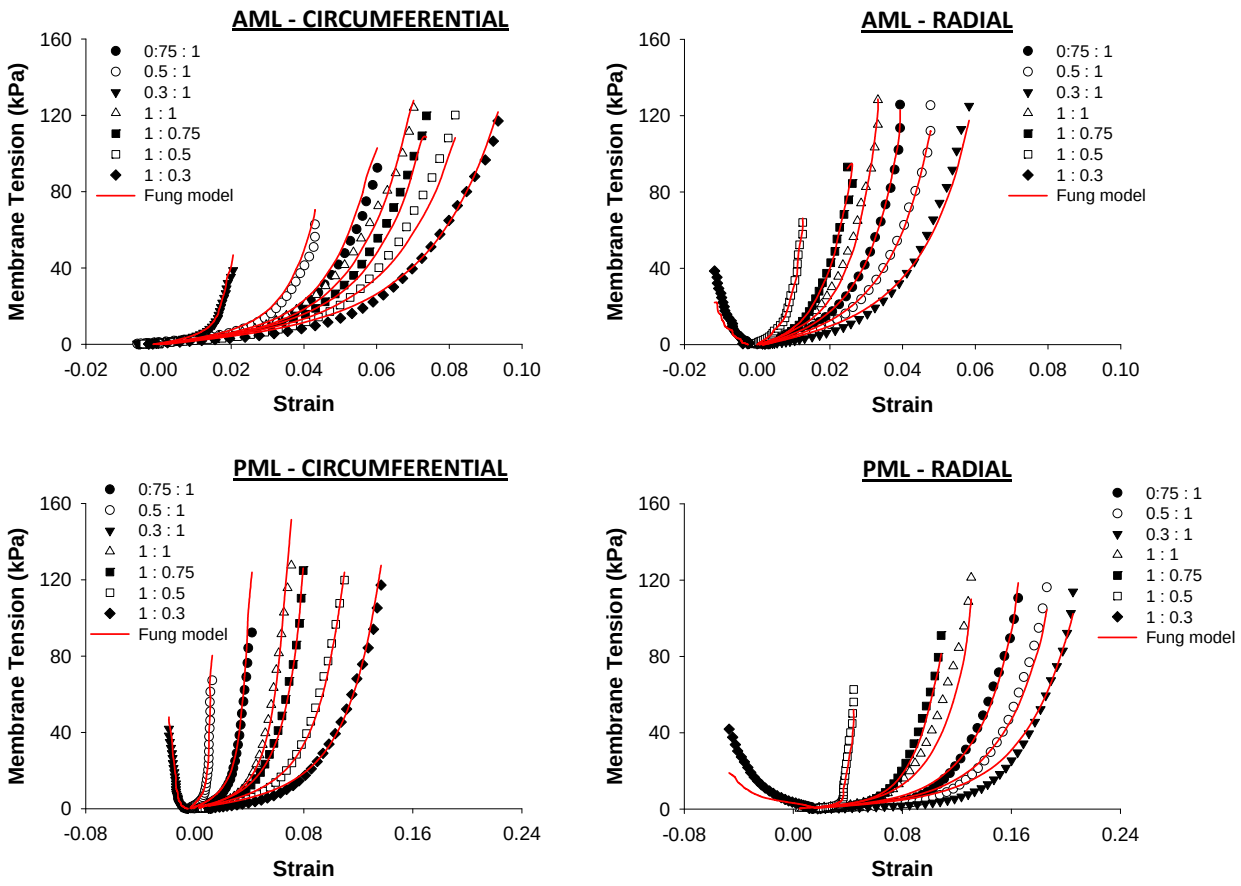

Figure 9-7: Representative experimental data and Fung's model fit of multiple biaxial in the circumferential (CIRC) and radial (RAD) of the AML (top) and PML (bottom) samples.

9.3.5 Microstructural analysis

Figure 4-8 illustrates the Movat stain sections of the belly and free-edge regions of the representative AML and PML samples in both CIRC and RAD directions. Both AML and PML samples appeared to undergo the pathological changes: accumulation of fibrous components (arrows in Fig. 9-8), multiple replicated elastic lamellae in the atrialis layer and disorganized and fragmented elastin fibers (Fig. 9-8b). In the belly region, infiltration of the massive amount of proteoglycan (PG) and glycosaminoglycan (GAG) (Fig. 9-8a) together with disorientation of the collagen networks, appeared as marble-like structure as reported by Stephens *et al.* [248] in aged porcine mitral valve leaflets, were observed in both leaflet groups. In the free-edge region, collagen content was abundant in the fibrosa layer and also evident in spongiosa layer of the AML sample while the amount of PG/GAG was merely visible in the same region. Fibrin was also evident within the fibrosa layer and highly expressed in the belly regions in both AML and PML samples. In addition, the von Kossa stains showed the calcified deposits in the belly regions with a high distribution in the fibrosa layer of the AML sample, see Fig. 9-9. The calcification content decreased toward the free-edge region and disappeared near the belly and free-edge junction. For the PML samples, only small calcified spots were observed, which scattered in the spongiosa layer along the radial direction of the valve leaflet.

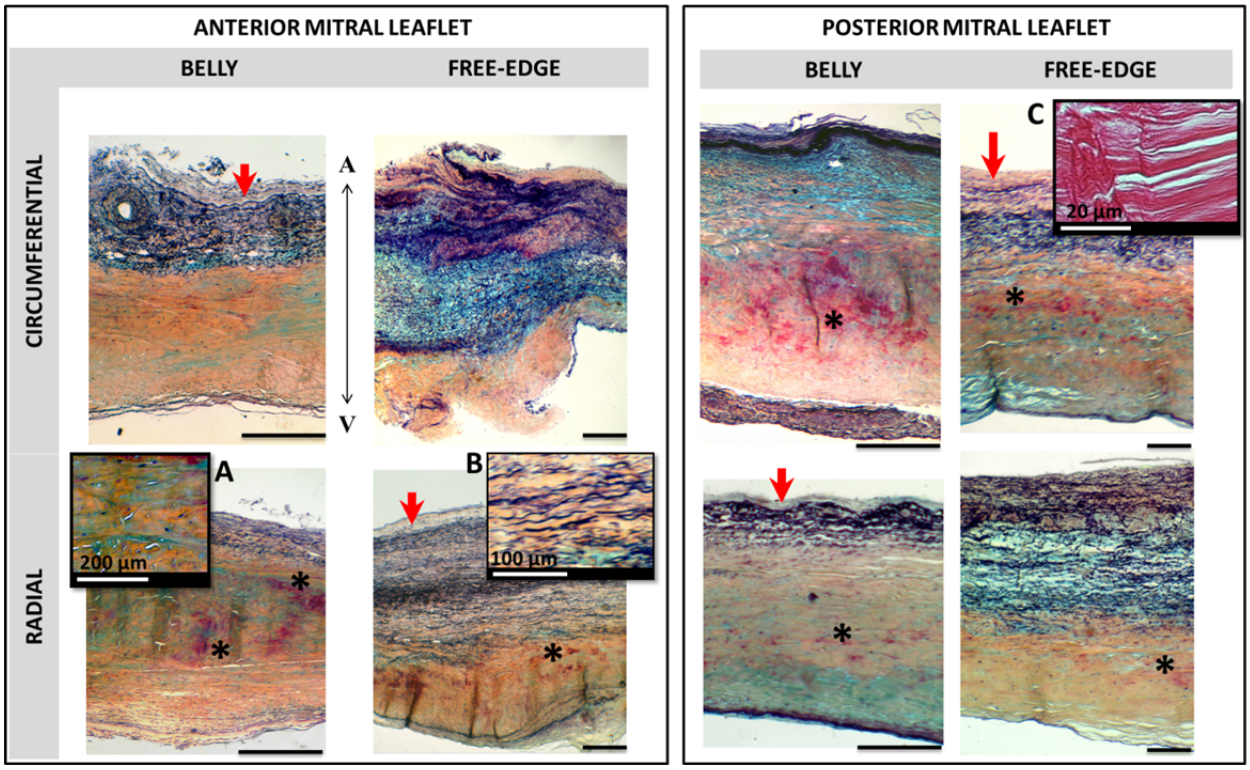

Figure 9-8: Representative histological results of the AML and PML samples from one patient. The images on the top row show the cross sections through thickness in the circumferential (CIRC) direction, the one on the left is at the belly and the right is at the free-edge region. The bottom row displays images of sections cut in the radial direction. The pop-up image A on the bottom left shows the proteoglycan (PG) and glycosaminoglycan (GAG) infiltration in the belly region, and the pop-up image B on the right shows fragmented elastin fibers in the radial direction within the atrialis layer. The pop-up image C shows the reduction in undulation of collagen fibers stained with Picrosirius red stain 100x. Red arrows indicate the accumulation of fibrous layers in the atrialis layers. Asterisk (*) indicate the presence of fibrin (intense red color) in the fibrosa layers. Movat-pentachrome stains: collagen – yellow, elastin – black, PG/GAG – blue/greenish, red – muscle fibers, intense red – fibrinoid, fibrin. All histology slides were captured with 10x magnification under the light microscope. Bar = 400 um.

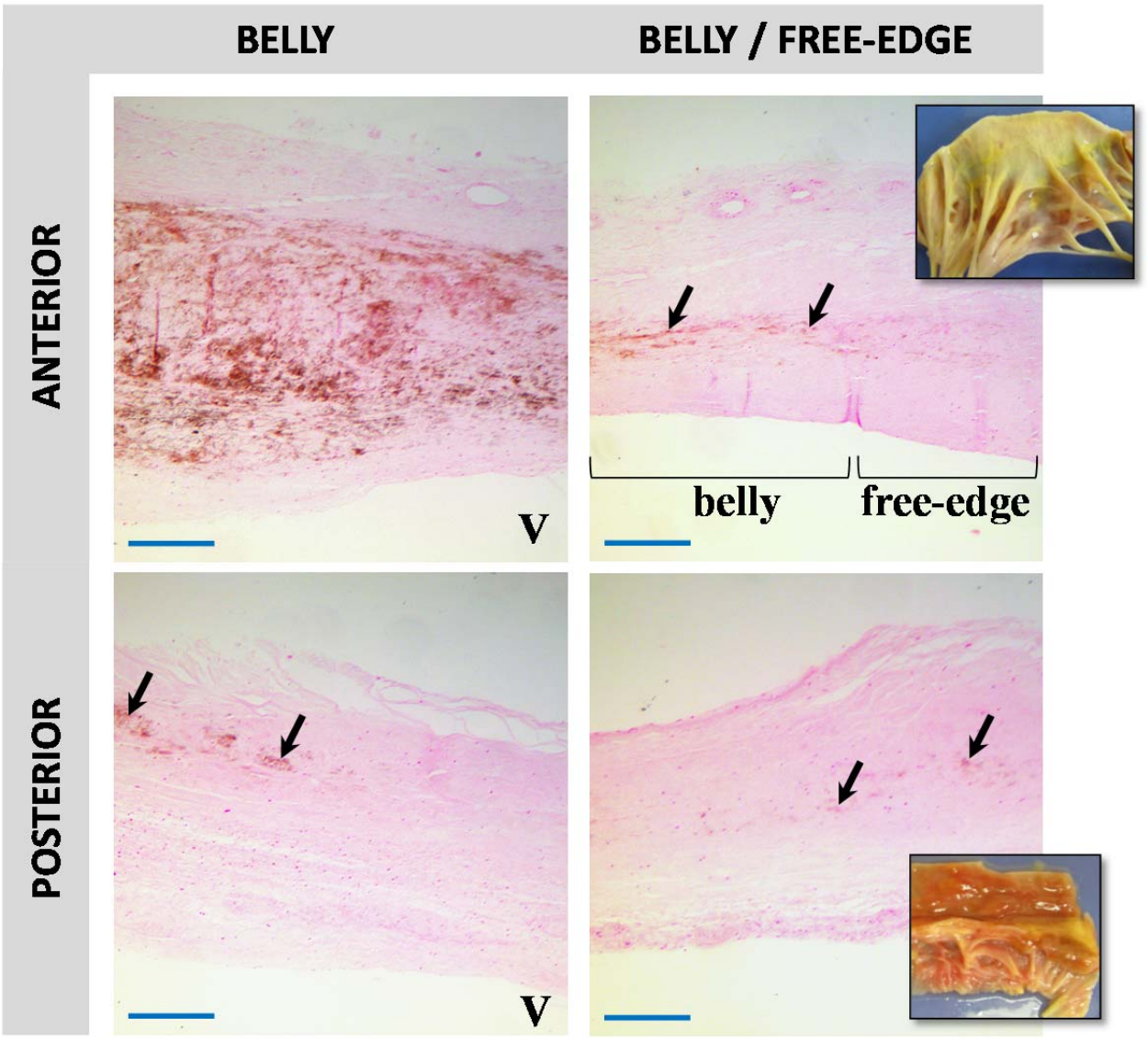

Figure 9-9: Representative histological results for calcification (dark brown color indicated by the arrows) in the belly and belly/free-edge regions in the radial direction. Dense and thick calcified deposits were seen on the AML belly region covered the spongiosa and fibrosa layers and spots on belly/free-edge region in the fibrosa. Calcification were scattered throughout the thickness and along the radial direction of PML sample. Von Kossa stains. Bar is 400 μm.

9.4 Discussion

9.4.1 Tissue properties related to aging

Heart valve disease mainly affects senior patients. Therefore, a study of normal and diseased valve tissue properties in advance aged patients is more relevant than a study of younger age groups, and it could enhance our understanding of the heart valve disease progression and the development of clinical treatment techniques. In this study, we presented, to our knowledge, the first comprehensive biaxial characterization of aged (82.62 ± 8.77 years old) human MV leaflets using a relatively large sample size (n = 21). A comparative study of age-dependent valve property changes was conducted by Stephens *et al.* [248] using a porcine model. They compared the three age groups, i.e., 6 weeks, 6 months and 6 years old of porcine mitral and aortic valves and observed an elevated stiffness and a higher collagen fiber distribution with increasing age. Another animal study by Stephen *et al.* [249] showed that changes in valve PGs and GAGs with age are complex and distinct within valve type. In human mitral valve leaflets, the GAG content and many different PG subclasses were found to be significantly decreased with advancing age [250]. Other studies have also shown that age has a significant impact on the composition of soft tissues [251, 252], resulting in significant differences in both material and microstructural properties of human aortic tissues [253]. Interestingly, our results suggest that the mechanical properties of leaflet tissues remain unchanged for persons older than 65 years of age. A broad age range of 30 – 90 years could possibly reveal significant differences as previously reported by others [253].

9.4.2 Comparison with human MV tissue properties reported in the literature

An early study of human mitral leaflet mechanics performed in 1970s by Clark [254] showed the unidirectional non-linear stress-strain behavior of generalized leaflets, though with unknown leaflet types, patient background and medical history. Recently, the uniaxial data of mitral valve tissues from a 88 year-old patient in the study by Prot *et al.* [43] showed the CIRC and RAD maximum stretches were approximately 4% and 12% for the AML sample and 23% and 69% for the PML sample, respectively. Our mean maximum strains were similar to their data for the AML samples, 4% and 10% for CIRC and RAD directions, respectively, but our PML samples were much stiffer, with 6% and 17% for CIRC and RAD directions, respectively. Barber and coworkers [247] showed that normal posterior mitral valve leaflets could stretch up to 15.5 ± 6.2% and 24.1 ± 4.0% strain in the CIRC and RAD directions, respectively. They cut the tissues into strips, stretched until failure (with higher load range 200-400g) and reported the maximum tangent modulus as stiffness, which were 6.1 ± 1.6 kN/m (CIRC) and 6.4 ± 0.3 kN/m (RAD). Because of different testing methods (i.e., uniaxial versus biaxial tests), a direction comparison cannot be made across studies. However, in general, the mechanical behaviors of our samples seem to be stiffer than others. In our biaxial testing protocols, we performed rigorous pre-conditioning of at least 40 cycles and analyzed the experimental data using the post-preconditioning reference state. As shown in the studies by Martin and Sun [255] and Carew *et al.* [256], valve tissues exhibited significant residual strains upon unloading, even after 20 cycles of preconditioning. Therefore, in this study, the tissue response was evaluated after 40 cycles of preconditioning to obtain reproducible mechanical testing data. By applying rigorous preconditioning, the residual strain was removed when analyzed using the post-preconditioning state. Thus, the tissue responses obtained in this study were stiffer than ones analyzed using a less number of pre-conditioning cycles, as shown in the Figure 8 in Martin and Sun [255].

9.4.3 Valve microstructure

Even though the hearts collected from patients who were not diagnosed with valvular diseases, we observed that all AML samples and 88% of the PML samples exhibited a certain degree of calcification, some with severe calcification. Several retrospective studies of mitral valve calcification found that it is a degenerative process that commonly occurring in elderly [257, 258]. Woodring and West [259] found a prevalence of valvular calcification increased with increasing age, 36% of patients over 70 years and 75% over 80. Hence, the mean age of our samples was 83 which could explain the present of calcification in all of our valves. Mechanically, the samples with more calcified deposits had higher stiffness and lower areal strain comparing to ones with less calcification. Furthermore, calcification was mostly found on the annulus and chordae insertion points. Recently, a computational study of mitral leaflet dynamics has shown that the annulus and chordae insertion locations are associated with high stress concentration [35]. Thus, the high stress could be one of the factors contributing to tissue calcification.

Our histological data shows that the microstructure of our human MV leaflets was altered with evidences of massive calcified deposition, marbling of PG/GAGs, straightened collagen fibers, high collagen contents and fragmented elastin fibers. Similar observations were reported by Martin *et al.* [260] who compared porcine and human aortic valve leaflets and also found straighter collagen fibers that corresponding to higher stiffness in human tissues compared to porcine ones. The study by Pham and Sun [261] also found significantly stiffer mechanical properties of their human coronary sinus vessels, which exhibited a high collagen content in the intima layer, compared to those of porcine and ovine models.

We also examined the difference in mechanical properties of MV tissues between individuals with and without hypertension. Hypertension has been shown to alter the structure and function of valve leaflets to accommodate an increase in blood pressure and consequently correlates with valvular disease such as degenerative and calcification [262-265]. We found that MV leaflets from hypertensive hearts

exhibited a higher stiffness and lower extensibility values compared to that of normotensive hearts. Yap *et al.* [266] studied the dynamic deformation of aortic valve during hypertensive loading conditions and showed that valves experienced an increased diastolic stretch with high pressure conditions. A long-term exposure to an increased tensile strain may lead to structural damages resulting in high stiffness and low extensibility.

9.4.4 Modeling of MV leaflets

Although the overall thickness of the AML samples was similar to that of PML samples, AML free-edge regions were thicker compared to the belly regions, whereas PML tissues had a relatively uniform thickness. Mechanically, both of the AML and PML exhibited a nonlinear and anisotropic behavior. However, the AML leaflets were stiffer than the PML leaflets in both circumferential and radial directions. Differences between the anterior and posterior leaflets found in this study may indicate that AML and PML might need to be modeled with separate sets of material properties in computational studies. Finite element modeling (FEM) has been proven useful in predicting the biomechanics of mitral valve at pathological [43, 168-170] conditions as well as the mechanical behaviors in the edge-to-edge surgical repair [64 , 267, 268] and chordal replacement [53] techniques. Up to now, the patient-specific material properties of heart valve have yet to be assessed *in vivo*. Thus, our *ex vivo* human biaxial material properties data and the constitutive models will be useful in computational studies of aged human mitral valve and provide more accurate prediction of valvular mechanical responses.

9.4.5 Difference in the mechanical properties between animal and human MV leaflet tissues.

It is well known that some of bioprosthetic aortic valves are made from chemically-treated porcine aortic valve and the pre-clinical animal studies are required by the FDA. In addition, there are numerous studies in the literature that use either porcine or ovine valve tissue as a surrogate for human one to study MV tissue structure and mechanical properties. For example, planar biaxial mechanical data

of porcine mitral valve leaflets by May-Newman and Yin [228] and Kunzelman and Cochran [229] were widely used in constitutive material modeling [31, 164] and simulation of human mitral valve dynamics at physiological condition [46, 165-167, 236]. However, compared to our data, their tissue responses were much compliant. For instance, May-Newman and Yin [228] reported stretches of 17% and 20% for AML and 23% and 24% for PML at 20 N/m in the CIRC and RAD directions, respectively. This suggests that human MV leaflets were much stiffer than porcine ones and that porcine valve models might not reflect the functionality of aged human mitral valves.

9.4.6 Limitations

Studies in the literature have shown the differences between fresh and preserved tissues [269-277]. Particularly, Clark [254] showed that freezing at -70 °C without any medium markedly altered the mechanical behavior of mitral valve tissues such that an increase in pre-transition modulus and a markedly increase in post-transition modulus in frozen samples compared with fresh ones. Due to the limited access to fresh human tissues, the obtained data from frozen tissue samples could be different from those of fresh tissues. The additional freezing method using cryoprotectant at a very cold temperature at our laboratory, however, has been shown to provide a minimal effect in the mechanical properties [110]. The structures of both anterior and posterior valve leaflets were not homogeneous, particularly at the free-edge region where the tissue was thicker and exhibited disorganized fiber microstructures throughout the layers. An assumption of tissue homogeneity in the central region of the leaflet samples might not represent the material properties of the entire leaflet area. Thus, regional heterogeneity in mechanical properties of leaflet needs to be further studied. In addition, the degree of calcification was classified based on structural observation, thus no quantitative correlation with the mechanical data was assessed. A more detailed quantitative study of valvular pathogenesis including changes in the ECM components as well as immunohistochemical analysis is needed to further characterize and correlate with the mechanical data. Another limitation is our small range of ages. A larger sample size including younger human mitral valves would facilitate comparison and correlation data with age and further study the mechanics of pathologic valves. For instance, the myxomatous degenerative disease of the mitral valve leaflet is a common cause of mitral regurgitation [278, 279]. Myxomatous disease occurs more frequently in younger age group [280], and mitral valve repair is a common treatment technique [281]. Thus, material property data obtained for a younger patient population with myxomatous disease would be more valuable in FE simulations for evaluating diseased valvular structure and the efficacy of various surgical procedures.

9.5 Summary

In this chapter, the mechanical properties of the human mitral valve leaflet tissues aged older than 65 years of age were characterized using a multiple planar biaxial testing method. The overall nonlinear anisotropic valve leaflet tissue properties were quantified. We found that for mitral leaflets, the radial direction was significantly more compliant than the circumferential direction. The anterior leaflets were significantly stiffer and less compliant than the posterior leaflets in both directions. From the histological results, the changes in the elastic components including the fragmented and disorganized elastin network, high collagen content and the presence of fibrosis and PGs/GAGs infiltration were observed, suggesting possible valvular degenerative characteristics in the valve samples. Additionally, calcification was observed in most of the leaflet samples. Overall, stiffness increased and areal strain decreased with calcification severity. Leaflet tissues from hypertensive hearts also exhibited a higher stiffness and low areal strain than normotensive hearts. This study showed that the mechanical properties of aged human mitral tissues might not be equivalent to that of animal tissues. The anterior and posterior leaflet mechanical data herein could be implemented into finite element models to study the structure and function of aged human mitral valve tissues.

References

[1] AHA, 2010, "American Heart Association: Heart Disease and Stroke Statistics—2010 Update."

[2] Rausch, M. K., Bothe, W., Kvitting, J. P. E., Swanson, J. C., Ingels Jr, N. B., Miller, D. C., and Kuhl, E., 2011, "Characterization of mitral valve annular dynamics in the beating heart," Annals of Biomedical Engineering, 39(6), pp. 1690-1702.

[3] Yanagishita, M., 1993, "Function of proteoglycans in the extracellular matrix," Acta pathologica japonica, 43(6), pp. 283-293.

[4] Scott, J. E., 2003, "Elasticity in extracellular matrix 'shape modules' of tendon, cartilage, etc. A sliding proteoglycan-filament model," The Journal of physiology, 553(Pt 2), pp. 335-343.

[5] Kinsella, M. G., Bressler, S. L., and Wight, T. N., 2004, "The regulated synthesis of versican, decorin, and biglycan: extracellular matrix proteoglycans that influence cellular phenotype," Critical reviews in eukaryotic gene expression, 14(3), pp. 203-234.

[6] Liao, J., Yang, L., Grashow, J., and Sacks, M. S., 2007, "The relation between collagen fibril kinematics and mechanical properties in the mitral valve anterior leaflet," Journal of Biomechanical Engineering, 129(1), pp. 78-87.

[7] Chen, L., Yin, F. C. P., and May-Newman, K., 2004, "The Structure and Mechanical Properties of the Mitral Valve Leaflet-Strut Chordae Transition Zone," Journal of Biomechanical Engineering, 126(2), pp. 244-251.

[8] Sacks, M. S., He, Z., Baijens, L., Wanant, S., Shah, P., Sugimoto, H., and Yoganathan, A. P., 2002, "Surface strains in the anterior leaflet of the functioning mitral valve," Annals of Biomedical Engineering, 30(10), pp. 1281-1290.

[9] Lam, J. H., Ranganathan, N., Wigle, E. D., and Silver, M. D., 1970, "Morphology of the human mitral valve. I. Chordae tendineae: a new classification," Circulation, 41(3), pp. 449-458.

[10] Timek, T., Dagum, P., Lai, D. T., Green, G. R., Glasson, J. R., Daughters, G. T., Ingels, N. B., Jr., and Miller, D. C., 2001, "The role of atrial contraction in mitral valve closure," J Heart Valve Dis, 10(3), pp. 312-319.

[11] Timek, T. A., Green, G. R., Tibayan, F. A., Lai, D. T., Rodriguez, F., Liang, D., Daughters, G. T., Ingels Jr, N. B., and Miller, D. C., 2003, "Aorto-Mitral Annular Dynamics," Annals of Thoracic Surgery, 76(6), pp. 1944-1950.

[12] Marzilli, M., Sabbah, H. N., Lee, T., and Stein, P. D., 1980, "Role of the papillary muscle in opening and closure of the mitral valve," The American journal of physiology, 238(3), pp. H348-354.

[13] Madu, E. C., and D'Cruz, I. A., 1997, "The vital role of papillary muscles in mitral and ventricular function: echocardiographic insights," Clin Cardiol, 20(2), pp. 93-98.

[14] Goldberg, S. L., and Feldman, T., 2010, "Percutaneous mitral valve interventions: overview of new approaches," Curr Cardiol Rep, 12(5), pp. 404-412.

[15] Lloyd-Jones, D., Adams, R. J., Brown, T. M., Carnethon, M., Dai, S., De Simone, G., Ferguson, T. B., Ford, E., Furie, K., Gillespie, C., Go, A., Greenlund, K., Haase, N., Hailpern, S., Ho, P. M., Howard, V., Kissela, B., Kittner, S., Lackland, D., Lisabeth, L., Marelli, A., McDermott, M. M., Meigs, J., Mozaffarian, D., Mussolino, M., Nichol, G., Roger, V. L., Rosamond, W., Sacco, R., Sorlie, P., Stafford, R., Thom, T., Wasserthiel-Smoller, S., Wong, N. D., and Wylie-Rosett, J., 2010, "Executive summary: Heart disease and stroke statistics-2010 update: A report from the american heart association," Circulation, 121(7), pp. e46-e215.

[16] Nkomo, V., Gardin, J., Skelton, T., Gottdiener, J., Scott, C., and EnriquezSarano, M., 2006, "Burden of valvular heart diseases: a population-based study," Lancet., 368, pp. 1005-1011.

[17] Hickey, M. S., Smith, L. R., Muhlbaier, L. H., Harrell, F. E., Jr., Reves, J. G., Hinohara, T., Califf, R. M., Pryor, D. B., and Rankin, J. S., 1988, "Current prognosis of ischemic mitral regurgitation. Implications for future management," Circulation., 78(3 Pt 2), pp. I51-59.

[18] Lamas, G. A., Mitchell, G. F., Flaker, G. C., Smith, S. C., Jr., Gersh, B. J., Basta, L., Moye, L., Braunwald, E., and Pfeffer, M. A., 1997, "Clinical significance of mitral regurgitation after acute myocardial infarction. Survival and Ventricular Enlargement Investigators," Circulation., 96(3), pp. 827-833.

[19] Grigioni, F., Enriquez-Sarano, M., Zehr, K. J., Bailey, K. R., and Tajik, A. J., 2001, "Ischemic mitral regurgitation: long-term outcome and prognostic implications with quantitative Doppler assessment," Circulation., 103(13), pp. 1759-1764.

[20] Carpentier, A., 1983, "Cardiac valve surgery--the "French correction"," J Thorac Cardiovasc Surg, 86(3), pp. 323-337.

[21] David, T. E., 2004, "Artificial chordae," Semin Thorac Cardiovasc Surg, 16(2), pp. 161-168.

[22] Privitera, S., Butany, J., Silversides, C., Leask, R. L., and David, T. E., 2005, "Artificial chordae tendinae: long-term changes," J Card Surg, 20(1), pp. 90-92.

[23] Feldman, T., Foster, E., Glower, D. G., Kar, S., Rinaldi, M. J., Fail, P. S., Smalling, R. W., Siegel, R., Rose, G. A., Engeron, E., Loghin, C., Trento, A., Skipper, E. R., Fudge, T., Letsou, G. V., Massaro, J. M., and Mauri, L., 2011, "Percutaneous repair or surgery for mitral regurgitation," New England Journal of Medicine, 364(15), pp. 1395-1406.

[24] Di Donato, M., Frigiola, A., Menicanti, L., Boghdabi, A., Badia, T., Neagu, A., Montericcio, V., and Ranucci, M., 2003, "Moderate ischemic mitral regurgitation and coronary artery bypass surgery: effect of mitral repair on clinical outcome," J Heart Valve Dis., 12(3), pp. 272-279.

[25] Gillinov, A. M., Wierup, P. N., Blackstone, E. H., Bishay, E. S., Cosgrove, D. M., White, J., Lytle, B. W., and McCarthy, P. M., 2001, "Is repair preferable to replacement for ischemic mitral regurgitation?," J Thorac Cardiovasc Surg., 122(6), pp. 1125-1141.

[26] Grossi, E. A., Goldberg, J. D., LaPietra, A., Ye, X., Zakow, P., Sussman, M., Delianides, J., Culliford, A. T., Esposito, R. A., Ribakove, G. H., Galloway, A. C., and Colvin, S. B., 2001, "Ischemic mitral valve reconstruction and replacement: comparison of long-term survival and complications," J Thorac Cardiovasc Surg., 122(6), pp. 1107-1124.

[27] Dubreuil, O., Basmadjian, A., Ducharme, A., Thibault, B., Crepeau, J., Lam, J. Y., and Bilodeau, L., 2007, "Percutaneous mitral valve annuloplasty for ischemic mitral regurgitation: first in man experience with a temporary implant," Catheter Cardiovasc Interv., 69(7), pp. 1053-1061.

[28] Sacks, M. S., 2000, "Biaxial mechanical evaluation of planar biological materials," Journal of Elasticity, 61, pp. 199-246.

[29] Fung, Y. C., 1993, Biomechanics: Mechanical Properties of Living Tissues, Springer Verlag, New York.

[30] Cataloglu, A., Clark, R. E., and Gould, P. L., 1977, "Stress analysis of aortic valve leaflets with smoothed geometrical data," Journal of Biomechanics, 10, pp. 153-158.

[31] Kunzelman, K. S., Cochran, R. P., Chuong, C., Ring, W. S., Verrier, E. D., and Eberhart, R. D., 1993, "Finite element analysis of the mitral valve," The Journal of heart valve disease, 2(3), pp. 326-340.

[32] Pouch, A. M., Xu, C., Yushkevich, P. A., Jassar, A. S., Vergnat, M., Gorman, J. H., 3rd, Gorman, R. C., Sehgal, C. M., and Jackson, B. M., 2012, "Semi-automated mitral valve morphometry and computational stress analysis using 3D ultrasound," J Biomech, 45(5), pp. 903-907.

[33] Stevanella, M., Krishnamurthy, G., Votta, E., Swanson, J. C., Redaelli, A., and Ingels, N. B., Jr., 2011, "Mitral leaflet modeling: Importance of in vivo shape and material properties," J Biomech, 44(12), pp. 2229-2235.

[34] Votta, E., Maisano, F., Bolling, S. F., Alfieri, O., Montevecchi, F. M., and Redaelli, A., 2007, "The Geoform Disease-Specific Annuloplasty System: A Finite Element Study," Annals of Thoracic Surgery, 84(1), pp. 92-101.

[35] Krishnamurthy, G., Ennis, D. B., Itoh, A., Bothe, W., Swanson, J. C., Karlsson, M., Kuh, E., Miller, D. C., and Ingels Jr, N. B., 2008, "Material properties of the ovine mitral valve anterior leaflet in vivo from inverse finite element analysis," American Journal of Physiology - Heart and Circulatory Physiology, 295(3), pp. H1141-H1149.

[36] Humphery, J. D., 2002, Cardiovascular Solid Mechanics, Springer Verlag.

[37] Sun, W., Abad, A., and Sacks, M. S., 2005, "Simulated bioprosthetic heart valve deformation under quasi-static loading," J Biomech Eng, 127(6), pp. 905-914.

[38] Sacks, M. S., and Sun, W., 2003, "Multiaxial Mechanical Behavior of Biological Materials," Annu Rev Biomed Eng.

[39] Labrosse, M. R., Lobo, K., and Beller, C. J., 2010, "Structural analysis of the natural aortic valve in dynamics: From unpressurized to physiologically loaded," Journal of Biomechanics, 43(10), pp. 1916-1922.

[40] Labrosse, M. R., Boodhwani, M., Sohmer, B., and Beller, C. J., 2011, "Modeling leaflet correction techniques in aortic valve repair: A finite element study," Journal of Biomechanics, 44(12), pp. 2292-2298.

[41] Weiss, J. A., Maker, B. N., and Govindjee, S., 1996, "Finite element implementation of incompressible, transversely isotropic hyperelasticity," Comput Method Appl M, 135(1-2), pp. 107-128.

[42] Holzapfel, G. A., Gasser , T. C., and Ogden, R. W., 2000, "A new constitutive framework for arterial wall mechanics and a comparative study of material models," J. Elasticity, 61, pp. 1–48.

[43] Prot, V., Skallerud, B., Sommer, G., and Holzapfel, G. A., 2010, "On modelling and analysis of healthy and pathological human mitral valves: two case studies," Journal of the mechanical behavior of biomedical materials, 3, pp. 167-177.

[44] Wang, Q., Sirois, E., and Sun, W., 2012, "Patient-specific modeling of biomechanical interaction in transcatheter aortic valve deployment," Journal of Biomechanics, 45(11), pp. 1965-1971.

[45] Wang, Q., and Sun, W., 2013, "Finite element modeling of mitral valve dynamic deformation using patient-specific multi-slices computed tomography scans," Annals of Biomedical Engineering, 41(1), pp. 142-153.

[46] Stevanella, M., Maffessanti, F., Conti, C. A., Votta, E., Arnoldi, A., Lombardi, M., Parodi, O., Caiani, E. G., and Redaelli, A., 2011, "Mitral Valve Patient-Specific Finite Element Modeling from Cardiac MRI: Application to an Annuloplasty Procedure," Cardiovascular Engineering and Technology, 2(2), pp. 66-76.

[47] May-Newman, K., and Yin, F. C., 1998, "A constitutive law for mitral valve tissue," J Biomech Eng, 120(1), pp. 38-47.

[48] Conti, C. A., Votta, E., Della Corte, A., Del Viscovo, L., Bancone, C., Cotrufo, M., and Redaelli, A., 2010, "Dynamic finite element analysis of the aortic root from MRI-derived parameters," Med Eng Phys, 32(2), pp. 212-221.

[49] Auricchio, F., Conti, M., Morganti, S., and Reali, A., 2013, "Simulation of transcatheter aortic valve implantation: a patient-specific finite element approach," Computer Methods in Biomechanics and Biomedical Engineering.

[50] Kunzelman, K. S., Quick, D. W., and Cochran, R. P., 1998, "Altered collagen concentration in mitral valve leaflets: Biochemical and finite element analysis," Annals of Thoracic Surgery, 66(6 SUPPL.), pp. S198-S205.

[51] Kunzelman, K. S., Reimink, M. S., and Cochran, R. P., 1997, "Annular dilatation increases stress in the mitral valve and delays coaptation: a finite element computer model," Cardiovasc Surg, 5(4), pp. 427-434.

[52] Reimink, M. S., Kunzelman, K. S., Verrier, E. D., and Cochran, R. P., 1995, "The effect of anterior chordal replacement on mitral valve function and stresses. A finite element study," ASAIO Journal, 41(3), pp. M754-M762.

[53] Reimink, M. S., Kunzelman, K. S., and Cochran, R. P., 1996, "The effect of chordal replacement suture length on function and stresses in repaired mitral valves A finite element study," Journal of Heart Valve Disease, 5(4), pp. 365-375.

[54] Maisano, F., Redaelli, A., Soncini, M., Votta, E., Arcobasso, L., and Alfieri, O., 2005, "An annular prosthesis for the treatment of functional mitral regurgitation: finite element model analysis of a dog bone-shaped ring prosthesis," Ann Thorac Surg, 79(4), pp. 1268-1275.

[55] Wong, V. M., Wenk, J. F., Zhang, Z., Cheng, G., Acevedo-Bolton, G., Burger, M., Saloner, D. A., Wallace, A. W., Guccione, J. M., Ratcliffe, M. B., and Ge, L., 2012, "The Effect of Mitral Annuloplasty Shape in Ischemic Mitral Regurgitation: A Finite Element Simulation," The Annals of Thoracic Surgery, 93(3), pp. 776-782.

[56] Xu, C., Jassar, A. S., Nathan, D. P., Eperjesi, T. J., Brinster, C. J., Levack, M. M., Vergnat, M., Gorman, R. C., Gorman, J. H., 3rd, and Jackson, B. M., 2012, "Augmented mitral valve leaflet area decreases leaflet stress: a finite element simulation," Ann Thorac Surg, 93(4), pp. 1141-1145.

[57] Votta, E., Caiani, E., Veronesi, F., Soncini, M., Montevecchi, F. M., and Redaelli, A., 2008, "Mitral valve finite-element modelling from ultrasound data: A pilot study for a new approach to understand mitral function and clinical scenarios," Philosophical Transactions of the Royal Society A: Mathematical, Physical and Engineering Sciences, 366(1879), pp. 3411-3434.

[58] Wenk, J. F., Zhang, Z., Cheng, G., Malhotra, D., Acevedo-Bolton, G., Burger, M., Suzuki, T., Saloner, D. A., Wallace, A. W., Guccione, J. M., and Ratcliffe, M. B., 2010, "First Finite Element Model of the Left Ventricle With Mitral Valve: Insights Into Ischemic Mitral Regurgitation," Annals of Thoracic Surgery, 89(5), pp. 1546-1553.

[59] Itoh, A., Krishnamurthy, G., Swanson, J. C., Ennis, D. B., Bothe, W., Kuhl, E., Karlsson, M., Davis, L. R., Miller, D. C., and Ingels Jr, N. B., 2009, "Active stiffening of mitral valve leaflets in the beating heart," American Journal of Physiology - Heart and Circulatory Physiology, 296(6), pp. H1766-H1773.

[60] Skallerud, B., Prot, V., and Nordrum, I. S., 2011, "Modeling active muscle contraction in mitral valve leaflets during systole: A first approach," Biomechanics and Modeling in Mechanobiology, 10(1), pp. 11-26.

[61] Boekstegers, P., Hausleiter, J., Baldus, S., von Bardeleben, R. S., Beucher, H., Butter, C., Franzen, O., Hoffmann, R., Ince, H., Kuck, K. H., Rudolph, V., Schäfer, U., Schillinger, W., and Wunderlich, N., 2013, "Percutaneous interventional mitral regurgitation treatment using the Mitra-Clip system," Clinical Research in Cardiology, pp. 1-12.

[62] Redaelli, A., Guadagni, G., Fumero, R., Maisano, F., and Alfieri, O., 2001, "A computational study of the hemodynamics after "edge-to-edge" mitral valve repair," Journal of Biomechanical Engineering, 123(6), pp. 565-570.

[63] Fiore, G. B., Guadagni, G., Putignano, G., Redaelli, A., Fumero, R., Maisano, F., and Alfieri, O., 2001, "Experimental and computational simulation of the haemodynamic conditons after edge-to-edge mitral valve repair," R. D. Kamm, G. W. Schmid-Schoenbein, G. A. Atesian, and M. S. Hefzy, eds.Snowbird, UT, pp. 429-430.

[64] Votta, E., Maisano, F., Soncini, M., Redaelli, A., Montevecchi, F. M., and Alfieri, O., 2002, "3-D computational analysis of the stress distribution on the leaflets after edge-to-edge repair of mitral regurgitation," Journal of Heart Valve Disease, 11(6), pp. 810-822.

[65] Avanzini, A., 2008, "A computational procedure for prediction of structural effects of edge-to-edge repair on mitral valve," Journal of Biomechanical Engineering, 130(3).

[66] Lau, K. D., Díaz-Zuccarini, V., Scambler, P., and Burriesci, G., 2011, "Fluid-structure interaction study of the edge-to-edge repair technique on the mitral valve," Journal of Biomechanics, 44(13), pp. 2409-2417.

[67] Dal Pan, F., Donzella, G., Fucci, C., and Schreiber, M., 2005, "Structural effects of an innovative surgical technique to repair heart valve defects," Journal of Biomechanics, 38(12), pp. 2460-2471.

[68] Kunzelman, K. S., Einstein, D. R., and Cochran, R. P., 2007, "Fluid-structure interaction models of the mitral valve: Function in normal and pathological states," Philosophical Transactions of the Royal Society B: Biological Sciences, 362(1484), pp. 1393-1406.

[69] Ma, X., Gao, H., Griffith, B. E., Berry, C., and Luo, X., 2013, "Image-based fluid-structure interaction model of the human mitral valve," Computers and Fluids, 71, pp. 417-425.

[70] Dahl, S. K., Vierendeels, J., Degroote, J., Annerel, S., Hellevik, L. R., and Skallerud, B., 2012, "FSI simulation of asymmetric mitral valve dynamics during diastolic filling," Computer Methods in Biomechanics and Biomedical Engineering, 15(2), pp. 121-130.

[71] Kische, S., Nienaber, C., and Ince, H., 2012, "Use of four MitraClip devices in a patient with ischemic cardiomyopathy and mitral regurgitation: "zipping by clipping"," Catheter Cardiovasc Interv, 80(6), pp. 1007-1013.

[72] Webb, J. G., Harnek, J., Munt, B. I., Kimblad, P. O., Chandavimol, M., Thompson, C. R., Mayo, J. R., and Solem, J. O., 2006, "Percutaneous transvenous mitral annuloplasty: initial human experience with device implantation in the coronary sinus," Circulation., 113(6), pp. 851-855. Epub 2006 Feb 2006.

[73] Duffy, S. J., Federman, J., Farrington, C., Reuter, D. G., Richardson, M., and Kaye, D. M., 2006, "Feasibility and short-term efficacy of percutaneous mitral annular reduction for the therapy of functional mitral regurgitation in patients with heart failure," Catheter Cardiovasc Interv., 68(2), pp. 205-210.

[74] Siminiak, T., Hoppe, U. C., Schofer, J., Haude, M., Herrman, J. P., Vainer, J., Firek, L., Reuter, D. G., Goldberg, S. L., and Bibber, R. V., 2009, "Effectiveness and Safety of Percutaneous Coronary Sinus-Based Mitral Valve Repair in Patients With Dilated Cardiomyopathy (from the AMADEUS Trial)," Am J Cardiology, 104, pp. 565-570.

[75] Hoppe, U. C., Brandt, M. C., Degen, H., Dodos, F., Schneider, T., Stoepel, C., Kroener, A., and Haude, M., 2009, "Percutaneous Mitral Annuloplasty Device Leaves Free Access to Cardiac Veins for Resynchronization Therapy," Catheterization and Cardiovascular Interventions, 74.

[76] Siminiak, T., Firek, L., Jerzykowska, O., Katmucki, P., Wotoszyn, M., Smuszkiewicz, P., and Link, R., 2007, "Percutaneous valve repair for mitral regurgitation using the Carillon(TM)-Mitral Contour System(TM). Description of the method and case report," Kardiologia Polska, 65(3), pp. 272-278.

[77] Schofer, J., Siminiak, T., Haude, M., Herrman, J. P., Vainer, J., Wu, J. C., Levy, W. C., Mauri, L., Feldman, T., Kwong, R. Y., Kaye, D. M., Duffy, S. J., Tübler, T., Degen, H., Brandt, M. C., Van Bibber, R., Goldberg, S., Reuter, D. G., and Hoppe, U. C., 2009, "Percutaneous mitral annuloplasty for functional mitral regurgitation: Results of the CARILLON mitral annuloplasty device european union study," Circulation, 120(4), pp. 326-333.

[78] Sack, S. e. a., 2009, "Percutaneous Transvenous Mitral Annuloplasty: Initial Human Experience With a Novel Coronary Sinus Implant Device," Circ Cardiovasc Interv, 2, pp. 277-284.

[79] Dubreuil, O., Basmadjian, A., Ducharme, A., Thibault, B., Crepeau, J., Lam, J. Y. T., and Bilodeau, L., 2007, "Percutaneous mitral valve annuloplasty for ischemic mitral regurgitation: First in man experience with a temporary implant," Catheterization and Cardiovascular Interventions, 69(7), pp. 1053-1061.

[80] Harnek, J., Webb, J. G., Kuck, K. H., Tschope, C., Vahanian, A., Buller, C. E., James, S. K., Tiefenbacher, C. P., and Stone, G. W., 2010, "Transcatheter implantation of the MONARC coronary sinus device for mitral regurgitation," JACC: Cardiovascular Interventions, 4(1), pp. 115-122.

[81] Barceló, A., Fuente, L. M. D. l., and Stertzer, S. H., 2004, "Anatomic And Histologic Review of The Coronary Sinus," Int. J. Morphol., 22(4), pp. 331-338.

[82] Chauvin, M., Shah, D. C., Haïssaguerre, M., Marcellin, L., and Brechenmacher, C., 2000, "The Anatomic Basis of Connections Between the Coronary Sinus Musculature and the Left Atrium in Humans," Circulation 101, pp. 647-652.

[83] Loukas, M., Bilinsky, S., Bilinsky, E., El-Sedfy, A., and Anderson, R. H., 2009, "Cardiac Veins: A Review of the Literature," Clinical Anatomy, 22, pp. 129-145.

[84] del Valle-Fernandez, R., Jelnin, V., Panagopoulos, G., and Ruiz, C. E., 2009, "Insight into the dynamics of the coronary sinus/great cardiac vein and the mitral annulus: implications for percutaneous mitral annuloplasty techniques," Circ Cardiovasc Interv, 2(6), pp. 557-564.

[85] El-Maasarany, S., Ferrett, C. G., Firth, A., Sheppard, M., and Henein, M. Y., 2005, "The coronary sinus conduit function: Anatomical study (relationship to adjacent structures)," Europace 7, pp. 475-481.

[86] Kunzelman, K. S., Cochran, R. P., Verrier, E. D., and Eberhart, R. C., 1994, "Anatomic basis for mitral valve modelling," J Heart Valve Dis, 3(5), pp. 491-496.

[87] Prince, J. L., and Links, J., 2005, Medical Imaging Signals and Systems Prentice Hall.

[88] Wicker, B., Hutchens, H., Wu, Q., Yeh, A., and Humphrey, J., 2008, "Normal basilar artery structure and biaxial mechanical behaviour," Comput Methods Biomech Biomed Engin., 11(5), pp. 539-551.

[89] Humphrey, J. D., 2002, Cardiovascular solid mechanics : cells, tissues, and organs, Springer, New York.

[90] Holzapfel, G. A., and Gasser, T. C., 2000, "A new constitutive framework for arterial wall mechanics and a comparative study of material models," Journal of Elasticity, 61, pp. 1-48.

[91] Baek, S., Gleason, R. L., Rajagopal, K. R., and Humphrey, J. D., 2007, "Theory of small on large: potential utility in computations of fluid-solid interactions in arteries. ," Computer Methods Appl Mech Eng, 196, pp. 3070-3078.

[92] Monos, E., Contney, S., Cowley, A. J., and Stekiel, W., 1989, "Effect of long-term tilt on mechanical and electrical properties of rat saphenous vein," Am J Physiol., 256(4 Pt 2), pp. H1185-1191.

[93] Stooker, W., Gok, M., Sipkema, P., Niessen, H., Baidoshvili, A., Westerhof, N., Jansen, E., Wildevuur, C., and Eijsman, L., 2003, "Pressure-diameter relationship in the human greater sapheneous vein," Ann Thorac Surg, 76, pp. 1533– 1538.

[94] Wesly, R., Vaishnav, R., Fuchs, J., Patel, D., and Greenfield, J. J., 1975, "Static linear and nonlinear elastic properties of normal and arterialized venous tissue in dog and man," Circ Res, 37(4), pp. 509-520.

[95] Hayashi, K., Mori, K., and Miyazaki, H., 2002, "Biomechanical response of femoral vein to chronic elevation of blood pressure in rabbits," Am J Physiol. Heart Circ Physiol, 284, pp. H511-H518.

[96] Eberth, J. F., Taucer, A. I., Wilson, E., and Humphrey, J. D., 2009, "Mechanics of carotid arteries in a mouse model of marfan syndrome," Annals of Biomedical Engineering, 37(6), pp. 1093-1104.

[97] Gleason, R. L., Dye, W. W., Wilson, E., and Humphrey, J. D., 2008, "Quantification of the mechanical behavior of carotid arteries from wild-type, dystrophin-deficient, and sarcoglycan-Î´ knockout mice," Journal of Biomechanics, 41(15), pp. 3213-3218.

[98] Hansen, L., Wan, W., and Gleason, R. L., 2009, "Microstructurally motivated constitutive modeling of mouse arteries cultured under altered axial stretch," Journal of biomechanical engineering, 131(10), p. 101015.

[99] Wicker, B. K., Hutchens, H. P., Wu, Q., Yeh, A. T., and Humphrey, J. D., 2008, "Normal basilar artery structure and biaxial mechanical behaviour," Computer Methods in Biomechanics and Biomedical Engineering, 11(5), pp. 539-551.

[100] Criscione, J. C., 2004, "A constitutive framework for tubular structures that enables a semi-inverse solution to extension and inflation," Journal of Elasticity, 77(1), pp. 57-81.

[101] Criscione, J. C., 2008, "Kinematics framework optimized for deformation, growth, and remodeling in vascular organs," Biomechanics and Modeling in Mechanobiology, 7(4), pp. 285-293.

[102] Lanir, Y., 1979, "A Structural Theory for the Homogeneous Biaxial Stress-Strain Relationships in Flat Collageneous Tissues," Journal of Biomechanics, 12, pp. 423-436.

[103] Holzapfel, G. A., and Gasser, T. C., 2001, "A viscoelastic model for fiber-reinforced composites at finite strains: Continuum basis, computational aspects and applications," Computer Methods in Applied Mechanics and Engineering, 190(34), pp. 4379-4403.

[104] Gasser, T. C., Ogden, R. W., and Holzapfel, G. A., 2006, "Hyperelastic modelling of arterial layers with distributed collagen fibre orientations," Journal of the Royal Society Interface, 3(6), pp. 15-35.

[105] Sacks, M. S., 2003, "Incorporation of experimentally-derived fiber orientation into a structural constitutive model for planar collagenous tissues," J Biomech Eng, 125(2), pp. 280-287.

[106] Condado, J. A., and Velez-Gimon, M., 2003, "Catheter-based approach to mitral regurgitation," J Interv Cardiol., 16(6), pp. 523-534.

[107] Kaye, D. M., Byrne, M., Alferness, C., and Power, J., 2003, "Feasibility and short-term efficacy of percutaneous mitral annular reduction for the therapy of heart failure-induced mitral regurgitation," Circulation., 108(15), pp. 1795-1797. Epub 2003 Oct 1796.

[108] Maniu, C. V., Patel, J. B., Reuter, D. G., Meyer, D. M., Edwards, W. D., Rihal, C. S., and Redfield, M. M., 2004, "Acute and chronic reduction of functional mitral regurgitation in experimental heart failure by percutaneous mitral annuloplasty," J Am Coll Cardiol., 44(8), pp. 1652-1661.

[109] Pham, T., and Sun, W., 2010, "Characterization of the mechanical properties of the coronary sinus for percutaneous transvenous mitral annuloplasty," Acta Biomaterialia (in press).

[110] Bia, D., Pessana, F., Armentano, R., Perez, H., Graf, S., Zocalo, Y., Saldıas, M., Perez, N., Alvarez, O., Silva, W., Machin, D., Sueta, P., Ferrin, S., Acosta, M., and Alvarez, I., 2006, "Cryopreservation procedure does not modify human carotid homografts mechanical properties: an isobaric and dynamic analysis," Cell and Tissue Banking, 7, pp. 183–194.

[111] García, A., Peña, E., Laborda, A., Lostalé, F., De Gregorio, M. A., Doblaré, M., and Martínez, M. A., 2011, "Experimental study and constitutive modelling of the passive mechanical properties of the porcine carotid artery and its relation to histological analysis: Implications in animal cardiovascular device trials," Medical Engineering and Physics, 33(6), pp. 665-676.

[112] Alastrué, V., Peña, E., Martínez, M. A., and Doblaré, M., 2008, "Experimental study and constitutive modelling of the passive mechanical properties of the ovine infrarenal vena cava tissue," Journal of Biomechanics, 41(14), pp. 3038-3045.

[113] Carboni, M., Desch, G. W., and Weizsäcker, H. W., 2007, "Passive mechanical properties of porcine left circumflex artery and its mathematical description," Medical Engineering & Physics, 29(1), pp. 8-16.

[114] Desch, G. W., and Weizsäcker, H. W., 2007, "A model for passive elastic properties of rat vena cava," Journal of Biomechanics, 40(14), pp. 3130-3145.

[115] Schulze-Bauer, C. A. J., Morth, C., and Holzapfel, G. A., 2003, "Passive Biaxial Mechanical Response of Aged Human Iliac Arteries," Journal of Biomechanical Engineering, 125, pp. 395-406.

[116] Tritthart, H., P., M. D., Stierle, H. E., and Krause, H., 1973, "Effects of Ca-Free and EDTA-Containing Tyrode Solution on Transmembrane Electrical Activity and Contraction in Guinea Pig Papillary Muscle," Pfliigers Arch. , 338, pp. 361--376.

[117] Sun, W., Sacks, M. S., Sellaro, T. L., Slaughter, W. S., and Scott, M. J., 2003, "Biaxial Mechanical Response of Bioprosthetic Heart Valve Biomaterials to High In-plane Shear," Journal of Biomedical Engineering, 125, pp. 372-380.

[118] Sun, W., and Sacks, M. S., 2005, "Finite element implementation of a generalized Fung-elastic constitutive model for planar tissues," Biomechanics and Modeling in Mechanobiology, 4(Nov.,(2-3)), pp. 190-199.

[119] Kohn, R., 1977, Heart and cardiovascular system, Nostrand Reinhold New York.

[120] Laurent, S., Boutouyrie, P., and Lacolley, P., 2005, "Structural and Genetic Bases of Arterial Stiffness," Hypertension, 45, pp. 1050-1055.

[121] Pezet, M., Mariko, B., Jacob, M., and Faury, G., 2009, "The elastic fibres: A regulator of normal and pathological ageing of elastic blood vessels," Medecine et Longevite 1(2), pp. 64-75.

[122] Holzapfel, G. A., Sommer, G., Gasser, C. T., and Regitnig, P., 2005, "Determination of layer-specific mechanical properties of human coronary arteries with nonatherosclerotic intimal thickening and related constitutive modeling " Am J Physiol Heart Circ Physiol, 289, pp. 2048-2058.

[123] Bhattacharya, S., and He, Z., 2012, "Annulus tension of the prolapsed mitral valve corrected by edge-to-edge repair," J Biomech, 45(3), pp. 562-568.

[124] He, Z., and Bhattacharya, S., 2010, "Mitral valve annulus tension and the mechanism of annular dilation: an in-vitro study," J Heart Valve Dis, 19(6), pp. 701-707.

[125] Bhattacharya, S., and He, Z., 2009, "Role of annulus tension in annular dilatation," J Heart Valve Dis, 18(5), pp. 481-487.

[126] He, Z., and Bhattacharya, S., 2008, "Papillary muscle and annulus size effect on anterior and posterior annulus tension of the mitral valve: an insight into annulus dilatation," J Biomech, 41(11), pp. 2524-2532.

[127] Rabbah, J. P. M., Saikrishnan, N., Siefert, A. W., Santhanakrishnan, A., and Yoganathan, A. P., 2013, "Mechanics of healthy and functionally diseased mitral valves: A critical review," Journal of Biomechanical Engineering, 135(2).

[128] Hasenkam, J. M., Nygaard, H., Paulsen, P. K., Kim, W. Y., and Hansen, O. K., 1994, "What force can the myocardium generate on a prosthetic mitral valve ring? An animal experimental study," Journal of Heart Valve Disease, 3(3), pp. 324-329.

[129] Shandas, R., Mitchell, M., Conrad, C., Knudson, O., Sorrell, J., Mahalingam, S., Fragoso, M., and Valdes-Cruz, L., 2001, "A general method for estimating deformation and forces imposed in vivo on bioprosthetic heart valves with flexible annuli: In vitro and animal validation studies," Journal of Heart Valve Disease, 10(4), pp. 495-504.

[130] Jensen, M. O., Jensen, H., Levine, R. A., Yoganathan, A. P., Andersen, N. T., Nygaard, H., Hasenkam, J. M., and Nielsen, S. L., 2011, "Saddle-shaped mitral valve annuloplasty rings improve leaflet coaptation geometry," Journal of Thoracic and Cardiovascular Surgery, 142(3), pp. 697-703.

[131] Padala, M., Hutchison, R. A., Croft, L. R., Jimenez, J. H., Gorman, R. C., Gorman Iii, J. H., Sacks, M. S., and Yoganathan, A. P., 2009, "Saddle Shape of the Mitral Annulus Reduces Systolic Strains on the P2 Segment of the Posterior Mitral Leaflet," The Annals of Thoracic Surgery, 88(5), pp. 1499-1504.

[132] Gorman, J. H., 3rd, Jackson, B. M., Enomoto, Y., and Gorman, R. C., 2004, "The effect of regional ischemia on mitral valve annular saddle shape," Ann Thorac Surg, 77(2), pp. 544-548.

[133] Salgo, I. S., Gorman, J. H., 3rd, Gorman, R. C., Jackson, B. M., Bowen, F. W., Plappert, T., St John Sutton, M. G., and Edmunds, L. H., Jr., 2002, "Effect of annular shape on leaflet curvature in reducing mitral leaflet stress," Circulation, 106(6), pp. 711-717.

[134] Jensen, M. ÿ., Jensen, H., Nielsen, S. L., Smerup, M., Johansen, P., Yoganathan, A. P., Nygaard, H., and Hasenkam, J. M., 2008, "What forces act on a flat rigid mitral annuloplasty ring?," Journal of Heart Valve Disease, 17(3), pp. 267-275.

[135] Randall Green, G., Dagum, P., Glasson, J. R., Francisco Nistal, J., Daughtersii, G. T., Ingels Jr, N. B., and Craig Miller, D., 1999, "Restricted posterior leaflet motion after mitral ring annuloplasty," Annals of Thoracic Surgery, 68(6), pp. 2100-2106.

[136] Gorman Iii, M. D. J. H., Gorman Md, R. C., Jackson Ms, B. M., Hiramatsu Md, Y., Gikakis Bse, N., Kelley Md, S. T., St. John Sutton Mbbs, M. G., Plappert Cvt, T., and Edmunds Jr, M. D. L. H., 1997, "Distortions of the Mitral Valve in Acute Ischemic Mitral Regurgitation," The Annals of Thoracic Surgery, 64(4), pp. 1026-1031.

[137] Kaye, D. M., Byrne, M., Alferness, C., and Power, J., 2003, "Feasibility and Short-Term Efficacy of Percutaneous Mitral Annular Reduction for the Therapy of Heart Failure–Induced Mitral Regurgitation," Circulation, 108, pp. 1795-1797.

[138] Byrne, M. J., Kaye, D. M., Mathis, M., Reuter, D. G., Alferness, C. A., and Power, J. M., 2004, "Percutaneous mitral annular reduction provides continued benefit in an ovine model of dilated cardiomyopathy," Circulation, 110(19), pp. 3088-3092.

[139] Liddicoat, J. R., Mac Neill, B. D., Gillinov, A. M., Cohn, W. E., Chin, C. H., Prado, A. D., Pandian, N. G., and Oesterle, S. N., 2003, "Percutaneous Mitral Valve Repair: A Feasibility Study in an Ovine Model of Acute Ischemic Mitral Regurgitation," Catheterization and Cardiovascular Interventions, 60(3), pp. 410-416.

[140] Bia, D., 2006, "Cryopreservation procedure does not modify human carotid homografts mechanical properties: an isobaric and dynamic analysis," Cell and Tissue Banking, 7, pp. 183-194.

[141] Langerak, S. E., Groenink, M., Van der Wall, E. E., Wassenaar, C., Vanbavel, E., Van Baal, M. C., and Spaan, J. A. E., 2001, "Impact of current cryopreservation procedures on mechanical and functional properties of human aortic homografts," Transplant International, 14(4), pp. 248-255.

[142] Delgadillo, J. O. V., Delorme, S., El-Ayoubi, R., Diraddo, R., and Hatzikiriakos, S. G., 2010, "Effect of freezing on the passive mechanical properties of arterial samples," Journal of Biomedical Science and Engineering, 3(7), pp. 645-652.

[143] Stemper, B. D., Yoganandan, N., Stineman, M. R., Gennarelli, T. A., Baisden, J. L., and Pintar, F. A., 2007, "Mechanics of Fresh, Refrigerated, and Frozen Arterial Tissue," Journal of Surgical Research(139), pp. 236–242.

[144] Yamauchi, H., Vasilyev, N. V., Marx, G. R., Loyola, H., Padala, M., Yoganathan, A. P., and Del Nido, P. J., 2012, "Right ventricular papillary muscle approximation as a novel technique of valve repair for functional tricuspid regurgitation in an ex vivo porcine model," Journal of Thoracic and Cardiovascular Surgery, 144(1), pp. 235-242.

[145] Siefert, A. W., Jimenez, J. H., West, D. S., Koomalsingh, K. J., Gorman, R. C., Gorman Iii, J. H., and Yoganathan, A. P., 2012, "In-vivo transducer to measure dynamic mitral annular forces," Journal of Biomechanics, 45(8), pp. 1514-1516.

[146] Sakamoto, H., Parish, L. M., Hamamoto, H., Enomoto, Y., Zeeshan, A., Plappert, T., Jackson, B. M., St John-Sutton, M. G., Gorman, R. C., and Gorman, J. H., 3rd, 2006, "Effects of hemodynamic alterations on anterior mitral leaflet curvature during systole," J Thorac Cardiovasc Surg, 132(6), pp. 1414-1419.

[147] Green, G. R., Dagum, P., Glasson, J. R., Daughters, G. T., Bolger, A. F., Foppiano, L. E., Berry, G. J., Ingels Jr, N. B., and Miller, D. C., 1999, "Mitral annular dilatation and papillary muscle dislocation without mitral regurgitation in sheep," Circulation, 100(19 SUPPL.), pp. II95-II102.

[148] Tibayan, F. A., Rodriguez, F., Langer, F., Zasio, M. K., Bailey, L., Liang, D., Daughters, G. T., Ingels Jr, N. B., and Miller, D. C., 2003, "Annular Remodeling in Chronic Ischemic Mitral Regurgitation: Ring Selection Implications," The Annals of Thoracic Surgery, 76(5), pp. 1549-1555.

[149] Timek, T. A., Lai, D. T., Liang, D., Daughters, G. T., Ingels Jr, N. B., and Miller, D. C., 2010, "Determinants of evolution and progression of acute ovine ischemic mitral regurgitation," Journal of Heart Valve Disease, 19(4), pp. 420-425.

[150] Kwan, J., Shiota, T., Agler, D. A., Popovi─ç, Z. B., Qin, J. X., Gillinov, M. A., Stewart, W. J., Cosgrove, D. M., McCarthy, P. M., and Thomas, J. D., 2003, "Geometric differences of the mitral apparatus between ischemic and dilated cardiomyopathy with significant mitral regurgitation: Real-time three-dimensional echocardiography study," Circulation, 107(8), pp. 1135-1140.

[151] Siefert, A. W., Jimenez, J. H., Koomalsingh, K. J., West, D. S., Aguel, F., Shuto, T., Gorman, R. C., Gorman, J. H., 3rd, and Yoganathan, A. P., 2012, "Dynamic assessment of mitral annular force profile in an ovine model," Ann Thorac Surg, 94(1), pp. 59-65.

[152] Siefert, A. W., Jimenez, J. H., Koomalsingh, K. J., Aguel, F., West, D. S., Shuto, T., Snow, T. K., Gorman, R. C., Gorman, J. H., 3rd, and Yoganathan, A. P., 2012, "Contractile mitral annular forces are reduced with ischemic mitral regurgitation," J Thorac Cardiovasc Surg.

[153] Daimon, M., Saracino, G., Fukuda, S., Koyama, Y., Kwan, J., Song, J. M., Agler, D. A., Gillinov, A. M., Thomas, J. D., and Shiota, T., 2010, "Dynamic change of mitral annular geometry and motion in ischemic mitral regurgitation assessed by a computerized 3D echo method," Echocardiography, 27(9), pp. 1069-1077.

[154] Yiu, S. F., Enriquez-Sarano, M., Tribouilloy, C., Seward, J. B., and Tajik, A. J., 2000, "Determinants of the degree of functional mitral regurgitation in patients with systolic left ventricular dysfunction: A quantitative clinical study," Circulation, 102(12), pp. 1400-1406.

[155] Kaplan, S. R., Bashein, G., Sheehan, F. H., Legget, M. E., Munt, B., Li, X. N., Sivarajan, M., Bolson, E. L., Zeppa, M., and Martin, R. W., 2000, "Three-dimensional echocardiographic assessment of annular shape changes in the normal and regurgitant mitral valve," American Heart Journal, 139(3), pp. 378-387.

[156] Timek, T. A., Dagum, P., Lai, D. T., Liang, D., Daughters, G. T., Ingels N.B, Jr., and Miller, D. C., 2001, "Pathogenesis of mitral regurgitation in tachycardia-induced cardiomyopathy," Circulation, 104(SUPPL. 1), pp. i47-i53.

[157] Glasson, J. R., Komeda, M., Daughters, G. T., Bolger, A. F., Karlsson, M. O., Foppiano, L. E., Hayase, M., Oesterle, S. N., Ingels N.B, Jr., Miller, D. C., and Bolling, S. F., 1998, "Early systolic mitral leaflet 'loitering' during acute ischemic mitral regurgitation," Journal of Thoracic and Cardiovascular Surgery, 116(2), pp. 193-205.

[158] Lai, D. T. M., Timek, T. A., Dagum, P., Green, G. R., Glasson, J. R., Daughters, G. T., Liang, D., Ingels Jr, N. B., and Miller, D. C., 2000, "The effects of ring annuloplasty on mitral leaflet geometry during acute left ventricular ischemia," Journal of Thoracic and Cardiovascular Surgery, 120(5), pp. 966-975.

[159] Kim, J. H., Kocaturk, O., Ozturk, C., Faranesh, A. Z., Sonmez, M., Sampath, S., Saikus, C. E., Kim, A. H., Raman, V. K., Derbyshire, J. A., Schenke, W. H., Wright, V. J., Berry, C., McVeigh, E. R.,

and Lederman, R. J., 2009, "Mitral cerclage annuloplasty, a novel transcatheter treatment for secondary mitral valve regurgitation: initial results in swine," J Am Coll Cardiol, 54(7), pp. 638-651.

[160] Timek, T. A., Lai, D. T., Tibayan, F., Liang, D., Daughters, G. T., Dagum, P., Ingels, N. B., Jr., and Miller, D. C., 2002, "Septal-lateral annular cinching abolishes acute ischemic mitral regurgitation," J Thorac Cardiovasc Surg, 123(5), pp. 881-888.

[161] Timek, T. A., Lai, D. T., Liang, D., Tibayan, F., Langer, F., Rodriguez, F., Daughters, G. T., Ingels, N. B., Jr., and Miller, D. C., 2004, "Effects of paracommissural septal-lateral annular cinching on acute ischemic mitral regurgitation," Circulation, 110(11 Suppl 1), pp. II79-84.

[162] Jensen, M. O., Honge, J. L., Benediktsson, J. A., Siefert, A. W., Jensen, H., Yoganathan, A. P., Snow, T. K., Hasenkam, J. M., Nygaard, H., and Nielsen, S. L., 2013, "Mitral valve annular downsizing forces: Implications for annuloplasty device development," Journal of Thoracic and Cardiovascular Surgery.

[163] Pham, T., and Sun, W., 2013, "Material properties of aged human mitral valve leaflets," Journal of Biomedical Materials Research - Part A.

[164] Weinberg, E. J., and Kaazempur Mofrad, M. R., 2007, "A finite shell element for heart mitral valve leaflet mechanics, with large deformations and 3D constitutive material model," Journal of Biomechanics, 40(3), pp. 705-711.

[165] Pouch, A. M., Xu, C., Yushkevich, P. A., Jassar, A. S., Vergnat, M., Gorman Iii, J. H., Gorman, R. C., Sehgal, C. M., and Jackson, B. M., 2012, "Semi-automated mitral valve morphometry and computational stress analysis using 3D ultrasound," Journal of Biomechanics, 45(5), pp. 903-907.

[166] Krishnamurthy, G., Itoh, A., Bothe, W., Swanson, J. C., Kuhl, E., Karlsson, M., Craig Miller, D., and Ingels, N. B., Jr., 2009, "Stress-strain behavior of mitral valve leaflets in the beating ovine heart," J Biomech, 42(12), pp. 1909-1916.

[167] Prot, V., Haaverstad, R., and Skallerud, B., 2009, "Finite element analysis of the mitral apparatus: Annulus shape effect and chordal force distribution," Biomechanics and Modeling in Mechanobiology, 8(1), pp. 43-55.

[168] Xu, C., Jassar, A. S., Nathan, D. P., Eperjesi, T. J., Brinster, C. J., Levack, M. M., Vergnat, M., Gorman, R. C., Gorman Iii, J. H., and Jackson, B. M., 2012, "Augmented Mitral Valve Leaflet Area Decreases Leaflet Stress: A Finite Element Simulation," The Annals of Thoracic Surgery, 93(4), pp. 1141-1145.

[169] Kunzelman, K. S., Reimink, M. S., and Cochran, R. P., 1997, "Annular dilatation increases stress in the mitral valve and delays coaptation: A finite element computer model," Cardiovascular Surgery, 5(4), pp. 427-434.

[170] Wenk, J. F., Zhang, Z., Cheng, G., Malhotra, D., Acevedo-Bolton, G., Burger, M., Suzuki, T., Saloner, D. A., Wallace, A. W., Guccione, J. M., and Ratcliffe, M. B., 2010, "First Finite Element Model of the Left Ventricle With Mitral Valve: Insights Into Ischemic Mitral Regurgitation," The Annals of Thoracic Surgery, 89(5), pp. 1546-1553.

[171] Timek, T. A., and Miller, D. C., 2011, "Another multidisciplinary look at ischemic mitral regurgitation," Seminars in Thoracic and Cardiovascular Surgery, 23(3), pp. 220-231.

[172] Duerig, T. W., Tolomeo, D. E., and Wholey, M., 2000, "An overview of superelastic stent design," Min Invas Ther & Allied Technol, 9, pp. 235-246.

[173] Stoeckel, D., Pelton, A., and Duerig, T., 2004, "Self-expanding nitinol stents: material and design considerations," European radiology, 14(2), pp. 292-301.

[174] Shabalovskaya, S. A., 1996, "On the nature of the biocompatibility and on medical applications of NiTi shape memory and superelastic alloys," Bio-medical materials and engineering, 6(4), pp. 267-289.

[175] Harnek, J., Zoucas, E., Stenram, U., and Cwikiel, W., 2002, "Insertion of self-expandable nitinol stents without previous balloon angioplasty reduces restenosis compared with PTA prior to stenting," Cardiovascular and interventional radiology, 25(5), pp. 430-436.

[176] Duerig, T. W., and Wholey, M., 2002, "A comparison of balloon- and self-expanding stents," Minimally Invasive Therapy and Allied Technologies, 11(4), pp. 173-178.

[177] Wu, W., Qi, M., Liu, X. P., Yang, D. Z., and Wang, W. Q., 2007, "Delivery and release of nitinol stent in carotid artery and their interactions: A finite element analysis," Journal of Biomechanics, 40(13), pp. 3034-3040.

[178] Kleinstreuer, C., Li, Z., Basciano, C. A., Seelecke, S., and Farber, M. A., 2008, "Computational mechanics of Nitinol stent grafts," Journal of Biomechanics, 41(11), pp. 2370-2378.

[179] Auricchio, F., Conti, M., De Beule, M., De Santis, G., and Verhegghe, B., 2011, "Carotid artery stenting simulation: From patient-specific images to finite element analysis," Medical Engineering and Physics.

[180] Harnek, J., Webb, J. G., Kuck, K. H., Tschope, C., Vahanian, A., Buller, C. E., James, S. K., Tiefenbacher, C. P., and Stone, G. W., 2011, "Transcatheter implantation of the MONARC coronary sinus device for mitral regurgitation," JACC: Cardiovascular Interventions, 4(1), pp. 115-122.

[181] Pham, T., and Sun, W., 2012, "Comparison of biaxial mechanical properties of coronary sinus tissues from porcine, ovine and aged human species," Journal of the Mechanical Behavior of Biomedical Materials, 6, pp. 21-29.

[182] Kleinstreuer, C., Li, Z., Basciano, C., Seelecke, S., and Farber, M., 2008, "Computational mechanics of Nitinol stent grafts," J Biomech, 41(11), pp. 2370-2378.

[183] Pham, T., and Sun, W., 2010, "Characterization of the mechanical properties of the coronary sinus for percutaneous transvenous mitral annuloplasty," Acta Biomaterialia, 6(11), pp. 4336-4344.

[184] Ogden, R. W., 1997, Non-linear elastic deformations, Dover, Toronto.

[185] DeHerrera, M. A., and Sun, W., 2009, "Numerical Study of Metal Fatigue in a Superelastic Anchoring Stent Embedded in Coronary Sinus," Simulia Customer Conference ProceedingsLondon, England, pp. 713-726.

[186] Auricchio, F., Conti, M., De Beule, M., De Santis, G., and Verhegghe, B., 2011, "Carotid artery stenting simulation: From patient-specific images to finite element analysis," Medical Engineering and Physics, 33(3), pp. 281-289.

[187] Speelman, L., Bosboom, E. M. H., Schurink, G. W. H., Hellenthal, F. A. M. V. I., Buth, J., Breeuwer, M., Jacobs, M. J., and van de Vosse, F. N., 2008, "Patient-Specific AAA Wall Stress Analysis: 99-Percentile Versus Peak Stress," European Journal of Vascular and Endovascular Surgery, 36(6), pp. 668-676.

[188] FDA, 2010, "Guidance for Industry and FDA Staff: Non-Clinical Engineering Tests and Recommended Labeling for Intravascular Stents and Associated Delivery Systems," U. S. D. o. H. a. H. Services, ed., U.S. Department of Health and Human Services, Rockville, MD.

[189] Cavanaugh Jr., KJ, Holt, V., Goode, J., and Anderson, E., 2006, "FDA Recommendations for Nitinol Stent and Endovascular Graft Fatigue Characterization and Fracture Reporting," Journal of ASTM International, 3(6), pp. 8-18.

[190] Pelton, A. R., Schroeder, V., Mitchell, M. R., Gong, X. Y., Barney, M., and Robertson, S. W., 2008, "Fatigue and durability of Nitinol stents," Journal of the Mechanical Behavior of Biomedical Materials, 1(2), pp. 153-164.

[191] Rogers, C., and Edelman, E. R., 1995, "Endovascular stent design dictates experimental restenosis and thrombosis," Circulation, 91(12), pp. 2995-3001.

[192] Pham, T., and Sun, W., 2011, "Comparison of biaxial mechanical properties of coronary sinus tissues from porcine, ovine and aged human species," Journal of the Mechanical Behavior of Biomedical Materials, In press.

[193] Balazs, T., Bognar, E., Zima, E., and Dobranszky, J., 2008, "Mechanical properties of coronary veins.," GepeszetBudapest, Hungary.

[194] Heng, M. S., Fagan, M. J., Collier, J. W., Desai, G., McCollum, P. T., and Chetter, I. C., 2008, "Peak wall stress measurement in elective and acute abdominal aortic aneurysms," Journal of Vascular Surgery, 47(1), pp. 17-22.

[195] Zahedmanesh, H., and Lally, C., 2009, "Determination of the influence of stent strut thickness using the finite element method: Implications for vascular injury and in-stent restenosis," Medical and Biological Engineering and Computing, 47(4), pp. 385-393.

[196] Pache, J., Kastrati, A., Mehilli, J., Schühlen, H., Dotzer, F., Hausleiter, J., Fleckenstein, M., Neuman, F. J., Sattelberger, U., Schmitt, C., Müller, M., Dirschinger, J., and Schömig, A., 2003, "Intracoronary stenting and angiographic results: Strut thickness effect on restenosis outcome (ISAR-STEREO-2) trial," Journal of the American College of Cardiology, 41(8), pp. 1283-1288.

[197] Kastrati, A., Mehilli, J., Dirschinger, J., Dotzer, F., Schühlen, H., Neumann, F. J., Fleckenstein, M., Pfafferott, C., Seyfarth, M., and Schömig, A., 2001, "Intracoronary stenting and angiographic results: Strut thickness effect on restenosis outcome (ISAR-STEREO) trial," Circulation, 103(23), pp. 2816-2821.

[198] Mahmood, F., Karthik, S., Subramaniam, B., Panzica, P. J., Mitchell, J., Lerner, A. B., Jervis, K., and Maslow, A. D., 2008, "Intraoperative Application of Geometric Three-Dimensional Mitral Valve Assessment Package: A Feasibility Study," Journal of Cardiothoracic and Vascular Anesthesia, 22(2), pp. 292-298.

[199] Chauvel, C., Bogino, E., Clerc, P., Fernandez, G., Vernhet, J. C., Becat, A., and Dehant, P., 2000, "Usefulness of three-dimensional echocardiography for the evaluation of mitral valve prolapse: An intraoperative study," Journal of Heart Valve Disease, 9(3), pp. 341-349.

[200] Ahmed, S., Nanda, N. C., and Miller, A. P., 2003, "Usefulness of transesophageal three-dimensional echocardiography in the identification of individual segment/ scallop prolapse of the mitral valve," Echocardiography, 20, pp. 203-209.

[201] Jabbour, A., Barker, S., Davies, S., Prasad, S. K., Rubens, M., and Mohiaddin, R. H., 2011, "Multimodality imaging in transcatheter aortiv valve implantation and post-procedural aortic regurgitation: comparison among cardiovascular magnetic resonance, cardiac computed tomography, and echocardiography," Journal of the American College of Cardiology, 58(21), pp. 2165-2173.

[202] Xu, C., Brinster, C. J., Jassar, A. S., Vergnat, M., Eperjesi, T. J., Gorman, R. C., Gorman, J. H., 3rd, and Jackson, B. M., 2010, "A novel approach to in vivo mitral valve stress analysis," Am J Physiol Heart Circ Physiol, 299(6), pp. H1790-1794.

[203] Verhey, J. F., Nathan, N. S., Rienhoff, O., Kikinis, R., Rakebrandt, F., and D'Ambra, M. N., 2006, "Finite-element-method (FEM) model generation of time-resolved 3D echocardiographic geometry data for mitral-valve volumetry," Biomedical Engineering Online, 5, p. 17.

[204] Ryan, L. P., Jackson, B. M., Eperjesi, T. J., Plappert, T. J., St John-Sutton, M., Gorman, R. C., and Gorman, J. H., 3rd, 2008, "A methodology for assessing human mitral leaflet curvature using real-time 3-dimensional echocardiography," Journal of Thoracic & Cardiovascular Surgery, 136(3), pp. 726-734.

[205] Wang, Q., Book, G., Contreras Ortiz, S., Primiano, C., McKay, R., Kodali, S., and Sun, W., 2011, "Dimensional Analysis of Aortic Root Geometry During Diastole Using 3D Models Reconstructed from Clinical 64-Slice Computed Tomography Images," Cardiovascular Engineering and Technology, 2(4), pp. 324-333.

[206] Sirois, E., Wang, Q., and Sun, W., 2011, "Fluid Simulation of a Transcatheter Aortic Valve Deployment into a Patient-Specific Aortic Root," Cardiovascular Engineering and Technology, 2(3), pp. 186-195.

[207] Capelli, C., Bosi, G. M., Cerri, E., Nordmeyer, J., Odenwald, T., Bonhoeffer, P., Migliavacca, F., Taylor, A. M., and Schievano, S., 2012, "Patient-specific simulations of transcatheter aortic valve stent implantation," Med Biol Eng Comput, 50(2), pp. 183-192.

[208] Veronesi, F., Corsi, C., Sugeng, L., Mor-Avi, V., Caiani, E. G., Weinert, L., Lamberti, C., and Lang, R. M., 2009, "A Study of Functional Anatomy of Aortic-Mitral Valve Coupling Using 3D Matrix Transesophageal Echocardiography," Circulation: Cardiovascular Imaging, 2(1), pp. 24-31.

[209] Ionasec, R. I., Voigt, I., Georgescu, B., Yang, W., Houle, H., Vega-Higuera, F., Navab, N., and Comaniciu, D., 2010, "Patient-Specific Modeling and Quantification of the Aortic and Mitral Valves From 4-D Cardiac CT and TEE," Medical Imaging, IEEE Transactions on, 29(9), pp. 1636-1651.

[210] Martin, C., Sun, W., Primiano, C., McKay, R., and Elefteriades, J., 2013, "Age-dependent ascending aorta mechanics assessed through multiphase CT," Annals of Biomedical Engineering.

[211] Gee, M. W., Reeps, C., Eckstein, H. H., and Wall, W. A., 2009, "Prestressing in finite deformation abdominal aortic aneurysm simulation," Journal of Biomechanics, 42(11), pp. 1732-1739.

[212] Lu, J., Zhou, X., and Raghavan, M. L., 2008, "Inverse method of stress analysis for cerebral aneurysms," Biomechanics and Modeling in Mechanobiology, 7(6), pp. 477-486.

[213] Zhou, X., Raghavan, M. L., Harbaugh, R. E., and Lu, J., 2010, "Patient-specific wall stress analysis in cerebral aneurysms using inverse shell model," Annals of Biomedical Engineering, 38(2), pp. 478-489.

[214] Weinberg, E. J., Shahmirzadi, D., and Mofrad, M. R. K., 2010, "On the multiscale modeling of heart valve biomechanics in health and disease," Biomechanics and Modeling in Mechanobiology, 9(4), pp. 373-387.

[215] Sacks, M. S., David Merryman, W., and Schmidt, D. E., 2009, "On the biomechanics of heart valve function," Journal of Biomechanics, 42(12), pp. 1804-1824.

[216] Huang, H. Y. S., Liao, J., and Sacks, M. S., 2007, "In-situ deformation of the aortic valve interstitial cell nucleus under diastolic loading," Journal of Biomechanical Engineering, 129(6), pp. 880-889.

[217] Vesely, I., and Noseworthy, R., 1992, "Micromechanics of the fibrosa and the ventricularis in aortic valve leaflets," Journal of Biomechanics, 25(1), pp. 101-109+111-113.

[218] Stella, J. A., and Sacks, M. S., 2007, "On the Biaxial Mechanical Properties of the Layers of the Aortic Valve Leaflet," Journal of Biomechanical Engineering, 129(5), pp. 757-766.

[219] Weinberg, E. J., and Mofrad, M. R. K., 2007, "Three-dimensional, multiscale simulations of the human aortic valve," Cardiovascular Engineering, 7(4), pp. 140-155.

[220] Weinberg, E. J., and Kaazempur Mofrad, M. R., 2008, "A multiscale computational comparison of the bicuspid and tricuspid aortic valves in relation to calcific aortic stenosis," Journal of Biomechanics, 41(16), pp. 3482-3487.

[221] Nkomo, V. T., Gardin, J. M., Skelton, T. N., Gottdiener, J. S., Scott, C. G., and Enriquez-Sarano, M., 2006, "Burden of valvular heart diseases: a population-based study," Lancet, 368(9540), pp. 1005-1011.

[222] Hickson, S. S., Butlin, M., Graves, M., Taviani, V., Avolio, A. P., McEniery, C. M., and Wilkinson, I. B., 2010, "The relationship of age with regional aortic stiffness and diameter," JACC Cardiovasc Imaging, 3(12), pp. 1247-1255.

[223] Taviani, V., Hickson, S. S., Hardy, C. J., McEniery, C. M., Patterson, A. J., Gillard, J. H., Wilkinson, I. B., and Graves, M. J., 2011, "Age-related changes of regional pulse wave velocity in the descending aorta using Fourier velocity encoded M-mode," Magn Reson Med, 65(1), pp. 261-268.

[224] Rose, J. L., Lalande, A., Bouchot, O., Bourennane el, B., Walker, P. M., Ugolini, P., Revol-Muller, C., Cartier, R., and Brunotte, F., 2010, "Influence of age and sex on aortic distensibility assessed by MRI in healthy subjects," Magn Reson Imaging, 28(2), pp. 255-263.

[225] Gillessen, T., Gillessen, F., Sieberth, H., Hanrath, P., and Heintz, B., 1995, "Age-related changes in the elastic properties of the aortic tree in normotensive patients: investigation by intravascular ultrasound," Eur J Med Res, 1(3), pp. 144-148.

[226] Nelson, A. J., Worthley, S. G., Cameron, J. D., Willoughby, S. R., Piantadosi, C., Carbone, A., Dundon, B. K., Leung, M. C., Hope, S. A., Meredith, I. T., and Worthley, M. I., 2009, "Cardiovascular magnetic resonance-derived aortic distensibility: validation and observed regional differences in the elderly," J Hypertens, 27(3), pp. 535-542.

[227] Bolling, S. F., Li, S., O'Brien, S. M., Brennan, J. M., Prager, R. L., and Gammie, J. S., 2010, "Predictors of mitral valve repair: clinical and surgeon factors," Ann Thorac Surg, 90(6), pp. 1904-1911; discussion 1912.

[228] May-Newman, K., and Yin, F. C., 1995, "Biaxial mechanical behavior of excised porcine mitral valve leaflets," Am J Physiol, 269(4 Pt 2), pp. H1319-1327.

[229] Kunzelman, K. S., and Cochran, R. P., 1992, "Stress/strain characteristics of porcine mitral valve tissue: Parallel versus perpendicular collagen orientation," Journal of Cardiac Surgery, 7(1), pp. 71-78.

[230] Grashow, J. S., Yoganathan, A. P., and Sacks, M. S., 2006, "Biaixal Stress–Stretch Behavior of the Mitral Valve Anterior Leaflet at Physiologic Strain Rates," Annals of Biomedical Engineering, 34(2), pp. 315–325.

[231] He, Z., Ritchie, J., Grashow, J. S., Sacks, M. S., and Yoganathan, A. P., 2005, "In vitro dynamic strain behavior of the mitral valve posterior leaflet," Journal of Biomechanical Engineering, 127(3), pp. 504-511.

[232] He, Z., Sacks, M. S., Baijens, L., Wanant, S., Shah, P., and Yoganathan, A. P., 2003, "Effects of papillary muscle position on in-vitro dynamic strain on the porcine mitral valve," J Heart Valve Dis, 12(4), pp. 488-494.

[233] Sacks, M. S., Enomoto, Y., Graybill, J. R., Merryman, W. D., Zeeshan, A., Yoganathan, A. P., Levy, R. J., Gorman, R. C., and Gorman, J. H., 3rd, 2006, "In-vivo dynamic deformation of the mitral valve anterior leaflet," Ann Thorac Surg, 82(4), pp. 1369-1377.

[234] Sacks, M. S., He, Z., Baijens, L., Wanant, S., Shah, P., Sugimoto, H., and Yoganathan, A. P., 2002, "Surface strains in the anterior leaflet of the functioning mitral valve," Annals of Biomedical Engineering, 30(10), pp. 1281-1290.

[235] Chen, L., McCulloch, A. D., and May-Newman, K., 2004, "Nonhomogeneous deformation in the anterior leaflet of the mitral valve," Annals of Biomedical Engineering, 32(12), pp. 1599-1606.

[236] Stevanella, M., Votta, E., and Redaelli, A., 2009, "Mitral valve finite element modeling: Implications of tissues' nonlinear response and annular motion," Journal of Biomechanical Engineering, 131(12).

[237] FDA, 2010, "General Considerations for Animal Studies for Cardiovascular Devices," O. o. D. E. Center for Devices and Radiological Health, Division of Cardiovascular Devices, ed.

[238] Daimon, M., Shiota, T., Gillinov, A. M., Hayase, M., Ruel, M., Cohn, W. E., Blacker, S. J., and Liddicoat, J. R., 2005, "Percutaneous Mitral Valve Repair for Chronic Ischemic Mitral Regurgitation: A

Real-Time Three-Dimensional Echocardiographic Study in an Ovine Model," Circulation, 111(17), pp. 2183-2189.

[239] Liddicoat, J., R. , Briain, D. M. N., Gillinov, A. M., William, E. C., Chi-Hui, C., Aldo, D. P., Natesa, G. P., and Stephen, N. O., 2003, "Percutaneous mitral valve repair: A feasibility study in an ovine model of acute ischemic mitral regurgitation," Catheterization and Cardiovascular Interventions, 60(3), pp. 410-416.

[240] Maniu, C., V., Jeetendra, B. P., David, G. R., Donna, M. M., William, D. E., Charanjit, S. R., and Margaret, M. R., 2004, "Acute and chronic reduction of functional mitral regurgitation in experimental heart failure by percutaneous mitral annuloplasty," Journal of the American College of Cardiology, 44(8), pp. 1652-1661.

[241] Kimblad, P. O., Harnek, J., Roijer, A., Meurling, C., Brandt, J., and Solem, J. O., 2005, "Percutaneous Transvenous Mitral Annuloplasty (PTMA) with the Viking device reduces pacing-induced mitral regurgitation," EuroIntervention, 1(3), pp. 346-351.

[242] Gerson, C. J., Goldstein, S., and Heacox, A. E., 2009, "Retained structural integrity of collagen and elastin within cryopreserved human heart valve tissue as detected by two-photon laser scanning confocal microscopy," Cryobiology, 59(2), pp. 171-179.

[243] Rosset, E., Friggi, A., Novakovitch, G., Rolland, P. H., Rieu, R., Pellissier, J. F., Magnan, P. E., and Branchereau, A., 1996, "Effects of cryopreservation on the viscoelastic properties of human arteries," Ann Vasc Surg, 10(3), pp. 262-272.

[244] Song, Y. C., Pegg, D. E., and Hunt, C. J., 1995, "Cryopreservation of the common carotid artery of the rabbit: optimization of dimethyl sulfoxide concentration and cooling rate," Cryobiology, 32(5), pp. 405-421.

[245] Billiar, K. L., and Sacks, M. S., 2000, "Biaxial mechanical properties of the natural and glutaraldehyde treated aortic valve cusp - Part I: Experimental results," Journal of Biomechanical Engineering, 122(1), pp. 23-30.

[246] Goetz, W. A., Lansac, E., Lim, H. S., Stevens, S. A., Weber, P. A., and Duran, C. M. G., 2006, "Kinking of the atrioventricular plane during the cardiac cycle," Asian Cardiovascular and Thoracic Annals, 14(5), pp. 394-398.

[247] Barber, J. E., Kasper, F. K., Ratliff, N. B., Cosgrove, D. M., Griffin, B. P., and Vesely, I., 2001, "Mechanical properties of myxomatous mitral valves," Journal of Thoracic and Cardiovascular Surgery, 122(5), pp. 955-962.

[248] Stephens, E. H., De Jonge, N., McNeill, M. P., Durst, C. A., and Grande-Allen, K. J., 2010, "Age-related changes in material behavior of porcine mitral and aortic valves and correlation to matrix composition," Tissue Engineering - Part A, 16(3), pp. 867-878.

[249] Stephens, E. H., Chu, C.-K., and Grande-Allen, K. J., 2008, "Valve proteoglycan content and glycosaminoglycan fine structure are unique to microstructure, mechanical load and age: Relevance to an age-specific tissue-engineered heart valve," Acta Biomaterialia, 4(5), pp. 1148-1160.

[250] Grande-Allen, K. J., Clabro, A., Gupta, V., Wight, T. N., Hascall, V. C., and Vesely, I., 2004, "Glycosaminoglycans and proteoglycans in normal mitral valve leaflets and chordae: Association with regions of tensile and compressive loading," Glycobiology, 14(7), pp. 621-633.

[251] Sugimoto, T., Miyazaki, H., and Hayashi, K., 2003, "Age-related changes in the morphology and mechanics of arterial wall in the rat," JSME International Journal, Series C: Mechanical Systems, Machine Elements and Manufacturing, 46(4), pp. 1312-1320.

[252] Lanir, Y., 1979, "A structural theory for the homogeneous biaxial stress-strain relationships in flat collagenous tissues," Journal of Biomechanics, 12(6), pp. 423-436.

[253] Wuyts, F. L., Vanhuyse, V. J., Langewouters, G. J., Decraemer, W. F., Raman, E. R., and Buyle, S., 1995, "Elastic properties of human aortas in relation to age and atherosclerosis: A structural model," Physics in Medicine and Biology, 40(10), pp. 1577-1597.

[254] Clark, R. E., 1973, "Stress-strain characteristics of fresh and frozen human aortic and mitral leaflets and chordae tendineae. Implications for clinical use," J Thorac Cardiovasc Surg, 66(2), pp. 202-208.

[255] Martin, C., and Sun, W., 2012, "Biomechanical characterization of aortic valve tissue in humans and common animal models," Journal of Biomedical Materials Research - Part A, 100 A(6), pp. 1591-1599.

[256] Carew, E. O., Barber, J. E., and Vesely, I., 2000, "Role of Preconditioning and Recovery Time in Repeated Testing of Aortic Valve Tissues: Validation Through Quasilinear Viscoelastic Theory," Annals of Biomedical Engineering, 28(9), pp. 1093-1100.

[257] Toufan, M., Javadrashid, R., Paak, N., Gojazadeh, M., and Khalili, M., 2012, "Relationship between incidentally detected calcification of the mitral valve on 64-row multidetector computed tomography and mitral valve disease on echocardiography," Int J Gen Med, 5, pp. 839-843.

[258] Aronow, W. S., 1991, "Mitral annular calcification: significant and worth acting upon," Geriatrics, 46(4), pp. 73-75, 79-80, 85-76.

[259] Woodring, J. H., and West, J. W., 1989, "CT of aortic and mitral valve calcification," J Ky Med Assoc, 87(4), pp. 177-180.

[260] Martin, C., Pham, T., and Sun, W., 2011, "Significant differences in the material properties between aged human and porcine aortic tissues," Eur J Cardiothorac Surg, 40(1), pp. 28-34.

[261] Pham, T., and Sun, W., 2012, "Comparison of biaxial mechanical properties of coronary sinus tissues from porcine, ovine and aged human species," J Mech Behav Biomed Mater, 6, pp. 21-29.

[262] Orton, E. C., Lacerda, C. M. R., and MacLea, H. B., 2011, "Signaling pathways in mitral valve degeneration," Journal of Veterinary Cardiology.

[263] Guazzi, M., and Arena, R., 2010, "Pulmonary hypertension with left-sided heart disease," Nature Reviews Cardiology, 7(11), pp. 648-659.

[264] Manners, J. M., Monro, J. L., and Ross, J. K., 1977, "Pulmonary hypertension in mitral valve disease: 56 surgical patients reviewed," Thorax, 32(6), pp. 691-696.

[265] Gueron, M., Hirsch, M., Rosenman, E., and Borman, J., 1973, "Secondary mitral regurgitation and systemic hypertension," CHEST, 63(4), pp. 547-551.

[266] Yap, C. H., Kim, H. S., Balachandran, K., Weiler, M., Haj-Ali, R., and Yoganathan, A. P., 2010, "Dynamic deformation characteristics of porcine aortic valve leaflet under normal and hypertensive conditions," American Journal of Physiology - Heart and Circulatory Physiology, 298(2), pp. H395-H405.

[267] Mansi, T., Voigt, I., Georgescu, B., Zheng, X., Mengue, E. A., Hackl, M., Ionasec, R. I., Noack, T., Seeburger, J., and Comaniciu, D., 2012, "An integrated framework for finite-element modeling of mitral valve biomechanics from medical images: Application to MitralClip intervention planning," Medical Image Analysis, 16(7), pp. 1330-1346.

[268] Avanzini, A., 2008, "A computational procedure for prediction of structural effects of edge-to-edge repair on mitral valve," J Biomech Eng, 130(3), p. 031015.

[269] Venkatasubramanian, R. T., Grassl, E. D., Barocas, V. H., Lafontaine, D., and Bischof, J. C., 2006, "Effects of freezing and cryopreservation on the mechanical properties of arteries," Annals of Biomedical Engineering, 34(5), pp. 823-832.

[270] Devireddy, R. V., Neidert, M. R., Bischof, J. C., and Tranquillo, R. T., 2003, "Cryopreservation of Collagen-Based Tissue Equivalents. I. Effect of Freezing in the Absence of Cryoprotective Agents," Tissue Engineering, 9(6), pp. 1089-1100.

[271] Shi, X., Mukherjee, Y. X., Datta, A. K., and Capps, S. G., 1994, "Thermomechanics of biomaterials freezing process," pp. 57-69.

[272] Donovan, D. L., Schmidt, S. P., Townshend, S. P., Njus, G. O., and Sharp, W. V., 1990, "Material and structural characterization of human saphenous vein," Journal of Vascular Surgery, 12(5), pp. 531-537.

[273] Stemper, B. D., Yoganandan, N., Stineman, M. R., Gennarelli, T. A., Baisden, J. L., and Pintar, F. A., 2007, "Mechanics of Fresh, Refrigerated, and Frozen Arterial Tissue," Journal of Surgical Research, 139, pp. 236-242.

[274] Chow, M., and Zhang, Y., 2010, "Changes in the Mechanical and Biochemical Properties of Aortic Tissue due to Cold Storage," Journal of Surgical Research, Article In Press, pp. 1-9.

[275] Delgadillo, J. O. V., Delorme, S., Rouwayda, E., DiRaddo, R., and Hatzikiriakos, S. G., 2010, "Effect of freezing on the passive mechanical properties of arterial samples," J. Biomedical Science and Engineering, 3, pp. 645-652.

[276] Moon, D. K., Woo, S. L., Takakura, Y., Gabriel, M. T., and Abramowitch, S. D., 2006, "The effects of refreezing on the viscoelastic and tensile properties of ligaments," J Biomech, 6, pp. 1153–1157.

[277] Woo, S. L. Y., Orlando, C. A., Camp, J. F., and Akeson, W. H., 1986, "Effects of postmortem storage by freezing on ligament tensile behavior," J Biomech, 19, pp. 399–404.

[278] Gillinov, A. M., Cosgrove, D. M., Blackstone, E. H., Diaz, R., Arnold, J. H., Lytle, B. W., Smedira, N. G., Sabik, J. F., McCarthy, P. M., and Loop, F. D., 1998, "Durability of mitral valve repair for degenerative disease," J Thorac Cardiovasc Surg, 116(5), pp. 734-743.

[279] David, T. E., Armstrong, S., McCrindle, B. W., and Manlhiot, C., 2013, "Late outcomes of mitral valve repair for mitral regurgitation due to degenerative disease," Circulation, 127(14), pp. 1485-1492.

[280] Cohn, L. H., Couper, G. S., Aranki, S. F., Rizzo, R. J., Kinchla, N. M., and Collins, J. J., Jr., 1994, "Long-term results of mitral valve reconstruction for regurgitation of the myxomatous mitral valve," J Thorac Cardiovasc Surg, 107(1), pp. 143-150; discussion 150-141.

[281] Gillinov, A. M., and Cosgrove, D. M., 2002, "Mitral valve repair for degenerative disease," J Heart Valve Dis, 11 Suppl 1, pp. S15-20.